Survival Strategies for Unmanned Surface Vehicles in Harsh Ocean Environments

by

ⓒ*Zhi Li*, B. Eng., M. Eng.

A dissertation submitted to the School of Graduate Studies
in partial fulfillment of the requirements for the degree of

Doctor of Philosophy

Faculty of Engineering and Applied Science
Memorial University of Newfoundland

May, 2018

St. John's   Newfoundland

Abstract

Unmanned Surface Vehicles (USVs) have seen fast development in the past decades, and they have opened up new ways for observing the ocean. A USV can run autonomous missions on the water surface with different payload sensors for characterizing the chemical and physical properties of the water column. With a group of USVs operated simultaneously in a fleet, the ocean observation work can be extended to much larger areas to achieve diverse scientific objectives. The ocean has very challenging environments, and to enable a USV to successfully complete each survey mission under adverse weather conditions, it is of great importance to investigate accurate and robust path-following control algorithms. Further, the unexpected ocean disturbances on a USV can potentially lead to critical motions, which may cause a USV to capsize. Therefore, the safety analysis of a USV that runs a mission in the seaway becomes a particularly important subject.

This thesis provides a comprehensive investigation into the operation of a USV executing autonomous missions in adverse ocean environments. We investigate a USV's dynamic motion modeling and validation in 6 degrees of freedom (DOF), examine three path-following control algorithms and their real-world performance in adverse weather conditions, as well as establish the safe operational condition for a USV that operates in dynamic ocean environments. We hope that our accomplished work can assist the USV practitioners in choosing appropriate motion dynamics models and robust path-following control strategies, and potentially implementing our safety analysis results to improve a

USV's operational safety and survivability during its ocean exploration mission. The planar motion dynamics are derived from the 6 DOF rigid-body motion equations, based on which a hybrid identification method that combines the tow tank and field tests has been carried out to determine the model parameter values. Depending on the constructed planar dynamic motion model, we develop and test three path-following control algorithms, i.e. Vector Field Method (VF), Carrot Chasing Method (CC) and Line-of-Sight Method (LOS). Our investigation involves investigating their mathematical origins, performing simulation tests and carrying out field experiments in adverse weather conditions to examine each algorithm's robustness.

Understanding the uncontrollable oscillatory motions in heave, roll and pitch are critical for the safety of a USV that operates in harsh ocean environments. The major influence on a USV's oscillatory motion comes from the ocean waves. Since this highly nonlinear interactive dynamics are quite complicated, we implement three mathematical tools for the safety analysis, which includes the Analytical Method, Melnikov's Method and Erosion Basin Method. Using the approximated analytical solution, we demonstrate the well-known jump phenomenon for the nonlinear oscillatory motion. Using Melnikov's function, we determine a conservative critical condition to predict the occurrence of chaotic motion, which can be regarded as a USV's safe operation boundary condition. The erosion basin numerical analysis has been implemented as a supplement for the Melnikov's method, and the results show that the achieved Melnikov boundary condition corresponds to the 90% safe region proportion contour. The boundary condition has been successfully combined together with the wave excitation moments to determine the safe and unsafe operational regions for a USV. These results are summarized in a series of unsafe region contour plots in the 2D polar coordinates.

Acknowledgements

Table of Contents

List of Tables

x

List of Figures

xiv

Table of Symbols

The page numbers here indicate the place of first significant reference. Although not all symbols are explicitly referenced below, their definitions are obvious from the context.

Symbols

x, u, X Surge position, surge velocity, surge force (P. 23).

y, v, Y Sway position, sway velocity, sway force (P. 23).

z, w, Z Heave position, heave velocity, heave force (P. 23).

ϕ, p, K Roll angle, roll angular velocity, roll moment (P. 23).

θ, q, M Pitch angle, pitch angular velocity, pitch moment (P. 23).

ψ, r, N Yaw angle, yaw angular velocity, yaw moment (P. 23).

$\{I\}$, O_I Inertial North-East-Down frame, inertial frame origin (P. 23).

$\{B\}$, O_B Body frame, body frame origin (P. 23).

η Position and orientation vector (P. 24).

ν Linear and angular velocity vector (P. 24).

τ Forces and moments vector (P. 24).

m The total mass of a marine vehicle (P. 26).

M_{RB} Rigid-body inertia matrix (P. 26).

$C_{RB}(\nu)\nu$ Coriolis and centripetal forces and moments (P. 27).

M_A Added inertia matrix (P. 28).

$C_A(\nu)\nu$ Added mass Coriolis and centripetal forces and moments (P. 28).

$D(\nu)\nu$ Damping forces and moments (P. 29).

$g(\eta)$ Restoring forces and moments (P. 30).

ρ Water density (P. 30).

g Gravitational acceleration (P. 30).

∇ Displaced water volume (P. 30).

$\overline{GM}_T$ Transversal metacentric height (P. 30).

$\overline{GM}_L$ Longitudinal metacentric height(P. 30).

u_f Water flow speed (P. 37).

w_f Wake fraction coefficient (P. 37).

$T,\ T_p,\ T_s$ Propulsive force from one thruster, from port-side thruster, from starboard-side thruster (P. 38).

$\Omega,\ \Omega_p,\ \Omega_s$ Revolution rate of one propeller, of port-side propeller, of starboard-side propeller (P. 38).

T_a Available thrust force (P. 38).

t_d	Thrust deduction factor (P. 38).
k_1^*, k_2^*	Bilinear thruster model coefficients (P. 38).
k_1, k_2	Lumped bilinear thruster model coefficients (P. 38).
l	Perpendicular distance from one propeller's axle to the USV's centerplane (P. 38).
F_r	Froude number (P. 41).
L	Waterline length (P. 41).
X_t	External tow force along the surge direction (P. 41).
u_{ss}	Steady-state surge velocity (P. 44).
Ω_c	Commanded revolution rate for both port- and starboard-side propellers (P. 44).
V	Total velocity of the vehicle (P. 47).
β	Sideslip angle (P. 47).
χ	Vehicle's course angle (P. 47).
ψ_M	Magnetic heading angle (P. 47).
ψ_D	Local magnetic declination angle (P. 47).
$\Delta\Omega$	Differential rotational speed (P. 51).
wp_i	The ith waypoint position (P. 67).
p_c	The position of the circular path origin (P. 67).

R Circle radius (P. 67).

$p(t)$, p Time varying vehicle position in the North-East-Down frame (P. 67).

P The generalized followed path (P. 67).

$d(t)$, d_s, d_c The time-varying cross track error, the straight-line path cross track error, the circular path cross track error (P. 67).

χ_p The straight-line path direction with respect to true north (P. 69).

χ_{Orbit} The direction of the vector $\overrightarrow{p_c p}$ with respect to true north (P. 70).

V_d Desired or reference moving speed (P. 72).

K_{p1}, K_{i1}, K_{d1} Proportional gain, integral gain, derivative gain for the speed controller PID_1 (P. 73).

K_{p2}, K_{i2}, K_{d2} Proportional gain, integral gain, derivative gain for the course-keeping controller PID_2 (P. 73).

χ_d Desired course angle (P. 76).

k_s, k_c Vector field convergence rate control parameter for straight-line case and circular path case (P. 76).

χ_{Ms} Maximum approaching angle for straight-line path-following case (P. 76).

χ_{Mc} Maximum approaching angle for circular path-following case (P. 76).

ρ_d Circular path-following direction (P. 76).

Δ_s Straight-line path look-ahead distance (P. 80).

Δ_c Circular path look-ahead angle (P. 80).

K_{ps}, K_{is} Proportional gain, integral gain for the carrot chasing straight-line path-following control (P. 88).

K_{pc}, K_{ic} Proportional gain, integral gain for the carrot chasing circular path-following control (P. 88).

R_p The vehicle circle radius when implementing the line-of-sight method (P. 89).

T_c Path-following convergence time (P. 98).

U_1 Transition period total control energy (P. 99).

U_2 Transition period total steering energy (P. 99).

E Transition period total path tracking error (P. 99).

E_{AV} Steady-state period average path tracking error (P. 100).

E_{SD} Steady-state period path tracking error standard deviation (P. 100).

T_e The time it takes from the start to the end of a mission (P. 131).

D_{i1}, D_{i2} Linear, quadratic damping coefficients for heave, roll and pitch ($i = 3, 4, 5$) (P. 160).

R_{i1}, R_{i3} Linear, cubic restoring moment coefficients for heave, roll and pitch ($i = 3, 4, 5$) (P. 160).

v_i Decaying constant for heave, roll and pitch ($i = 3, 4, 5$) (P. 161).

ω_{di} Damped oscillation frequency for heave, roll and pitch ($i = 3, 4, 5$) (P. 161).

ω_{ni} Natural oscillation frequency for heave, roll and pitch ($i = 3, 4, 5$) (P. 161).

I_r, I_p Virtual roll, pitch moment of inertia (P. 162).

$T_{n4},\ T_{n5}$ Natural roll, pitch motion period (P. 162).

ζ Surface wave elevation (P. 175).

ζ_A Wave amplitude (P. 175).

ω_w Wave circular frequency (P. 175).

k Wave number (P. 175).

χ_w Wave direction with respect to the vehicle's heading direction (P. 175).

Z_0 The amplitude of the heave excitation force (P. 176).

ω_e Wave encounter frequency (P. 178).

K_0 The amplitude of the roll excitation moment (P. 181).

M_0 The amplitude of the pitch excitation moment (P. 181).

k_0 Non-dimensional roll excitation moment amplitude (P. 191).

ω_{ne} Normalized wave encounter frequency (P. 192).

m_0 Non-dimensional pitch excitation moment amplitude (P. 195).

K_{0c} Critical wave excitation amplitude for roll motion (P. 203).

M_{0c} Critical wave excitation amplitude for pitch motion (P. 204).

Abbreviations

USV Unmanned surface vehicle (P. 2).

GNC Guidance, navigation and control system (P. 6).

GPS Global positioning system (P. 7).

$AHRS$ Attitude and heading reference system (P. 7).

GC Guidance and control system (P. 9).

DOF Degrees of freedom (P. 11).

NED North-east-down frame (P. 23).

CG Center of gravity (P. 30).

CB Center of buoyancy (P. 30).

$RMSE$ Root mean square error (P. 45).

VF Vector field path-following control method (P. 66).

CC Carrot chasing path-following control method (P. 66).

LOS Line-of-sight path-following control method (P. 66).

PID Proportional-integral-derivative controller (P. 72).

VTP Virtual target point (P. 78).

CCI Carrot chasing method with integral gain (P. 93).

$MIMO$ Multiple-input-multiple-output system (P. 96).

HBM Harmonic balance method (P. 190).

Chapter 1

Introduction

This starting chapter introduces the motivation of this research, provides detailed litera-ture review and summarizes the main contributions.

1.1 Motivation

The ocean is of great importance for humankind. It covers 71 percent of Earth's surface and plays a key role in regulating the world's climate. Surrounded by the ocean, we build our civilization, and many of our businesses are dependent on the ocean such as fisheries and shipping. However, it is astounding that we still know so little about our ocean. Because the ocean is so vast, it is really difficult to explore. Traditionally, scientists rely on large research vessels and expensive equipment to do ocean surveys. This conventional method requires significant operational in-situ support, and therefore long time scientific data series and large area coverage are prohibitively expensive and very rare. Further, the ocean is very dynamic, and this challenging environment also makes it risky for human beings to carry out persistent ocean observations.

The fast advancement of robotic technology in the past few decades has dramatically changed the way we explore the ocean. In particular, Unmanned Surface Vehicles (USVs)

have opened up new ways of observing the ocean's processes across different time and length scales. USVs are robotic platforms that work on the water surface. They can be equipped with different payload sensors, which can be potentially employed for characterizing the chemical, physical and biological properties of the water surface and the water column. Such platforms are capable of performing long duration profiling missions, and their collected fine resolution ocean data surpass the traditional methods that are based on shipboard sampling or moored buoys. These vehicles are cost-effective and they can be remotely controlled by a team of scientists. Persistent ocean observations are enabled by their prolonged endurance, which is vital for monitoring and understanding the complex ocean phenomena, such as the ocean-atmosphere interaction [1]. With sufficient numbers of USVs operated simultaneously in a fleet, our observation work can be extended to much larger spatial coverage to achieve diverse scientific objectives.

With the aforementioned advantageous features, USVs have been successfully employed for a variety of missions, such as bathymetric mapping [2] and environmental monitoring [3], proving their considerable value for exploring the ocean. Nevertheless, to be suited for persistent observations in the ocean, a USV has to be able to survive harsh, fast-changing and often unpredictable ocean environments. Due to their small size and low inertia, USVs are easily influenced by environmental factors such as waves, winds and ocean currents. These disturbances will interact with a USV's hull and superstructure and potentially result in unfavorable motions in all degrees of freedom. Under the worst-case scenario, a USV will capsize or suffer complete destruction.

A typical scientific mission requires a USV to perform sensor data collection while following designated paths, and the path-following accuracy will directly influence the utility of the gathered data. However, precise path tracking control is quite challenging because of a USV's complicated hydrodynamic characteristics and unexpected environmental disturbances. There are many path-following control methods available in the

robotics community, but few of them have been implemented on a USV in real experiments under adverse weather conditions. Hence, their value and effectiveness are difficult to evaluate.

With the increasing interest for deployment of USVs for persistent ocean survey tasks, the safety of these platforms becomes a particularly important subject for ocean practitioners. The ocean is very dynamic and the adverse weather conditions could lead to an unsafe operational status for a USV. For example, excessive roll or pitch motion will cause a USV to capsize. Some open questions need to be answered: such as how we can determine a feasible path for a USV depending on the deteriorating environmental conditions, and is it possible for a USV to have self-awareness of its own safety so that more reliable and safer paths can be planned and executed on-line. The answers to these questions are vital for their future mission success.

Although we are still at the beginning stage of employing autonomous vehicles for ocean exploration missions, we can imagine the benefits of working with fully automated vehicles in the near future. These enormous improvements will further shape the way we study the ocean and deepen our understanding of this active hydrosphere.

1.2 Literature Review

1.2.1 Unmanned Surface Vehicles

Unmanned Surface Vehicles (USVs) have seen a large proliferation in the past two decades [4, 5]. In 1993, a mono-hull USV ARTEMIS was introduced by the MIT Sea Grant Program as a platform for initial testing of the guidance and control system [2]. Due to the limited endurance and seakeeping capability of ARTEMIS, a catamaran-type USV ACES, shown in Fig. 1.1a, was produced as a replacement for bathymetric mapping mission. The USV SESAMO [1], as shown in Fig. 1.1b, was designed for Antarctic sea surface micro-

layer sampling tasks, but it could only work in smooth sea and wind conditions. The USV Springer [3] was developed for pollutant tracking tasks and a research focus was on the development of a fault-tolerant guidance and control system. To fulfill the requirements of persistent observations, renewable energy has been utilised. In Fig. 1.1c, Wavegliders, for instance, have successfully travelled thousands of miles across the ocean without human intervention [6]. These platforms employ wave and solar energy to power their onboard sensors and propulsion systems. Similarly, the USV C-Enduro from ASV Ltd. (Fig. 1.1d) takes advantage of wind and solar energy for enduring ocean exploration missions.

(a) ACES [2]

(b) SESAMO [1]

(c) Wavegliders [4]

(d) C-Enduro (ASV Ltd.)

Figure 1.1: Different kinds of Unmanned Surface Vehicles (USVs).

There are a diversity of USVs, and they can be classified by their number of hulls, hull forms and applicable scenarios. Based on the number of hulls, we have mono-hull USVs and multi-hull USVs including catamaran and trimaran. The catamaran-type USVs have

attracted the most interest from different research institutions [4, 3, 7], and that is because they have good roll stability, provide sufficient payload capacity and are convenient to construct. The hull form is another factor that can be used to categorize USVs. The displacement-style USVs are supported exclusively or predominately by buoyant forces, and these platforms are widely employed for scientific missions. Under this category, semi-submersibles such as the buoy-type USV SeaDragon [8] can operate at low speeds and can be very stable in high sea states. The planing hull USVs are designed to operate at high speeds and are mainly used by coast guard for harbour patrol work [5]. Many USVs are designed for fresh water applications, and their small size and maneuverability make them suitable for missions in rivers and lakes [9]. Others are built with enhanced robustness and can be potentially deployed for persistent ocean observation missions even in the most dangerous weather conditions [8].

Effective ocean observations require a USV's persistent presence to monitor complicated ocean processes. For example, a recent field trial led by National Oceanography Center (NOC) is aimed at using autonomous vehicles to perform mapping of marine life for long duration in offshore environments. It is anticipated that there will be an increasing demand for the use of USVs for long duration ocean survey missions in the next few years [4]. A USV operating on the ocean surface has to survive the fast-changing ocean environments. A fundamental question is how users and the vehicle itself can assess its operational safety with respect to different adverse ocean influences. The safety of a USV has been an ongoing concern since the USV technology emerged. In [2], it is clearly stated that "large wave actions were a potential threat for the ACES USV's operational safety". After years of development, however, we are still restricted to the field experiments in an ideal environment and know little about a USV's actual performance in the ocean with adverse environmental influences.

1.2.2 Guidance, Navigation and Control

Unmanned Surface Vehicles (USVs) have demonstrated their utility in various marine applications, including seafloor mapping, environmental monitoring and sampling and harbour surveillance [1, 2, 3, 10]. Many of these applications require a USV to accurately follow designated paths in the survey environment. For example, while performing seafloor mapping using a side scanning sonar, a USV is commanded to follow the lawn-mower pattern to cover the studied ocean area. High-precision manoeuvring will notably improve the accuracy and quality of the constructed seafloor images.

The guidance, navigation and control (GNC) system is the key component to enable a USV to effectively carry out autonomous exploration missions. The block diagram in Fig. 1.2 shows a typical GNC system structure for an autonomous marine vessel, and the definition and functionality of each block have been summarized as follows [11]:
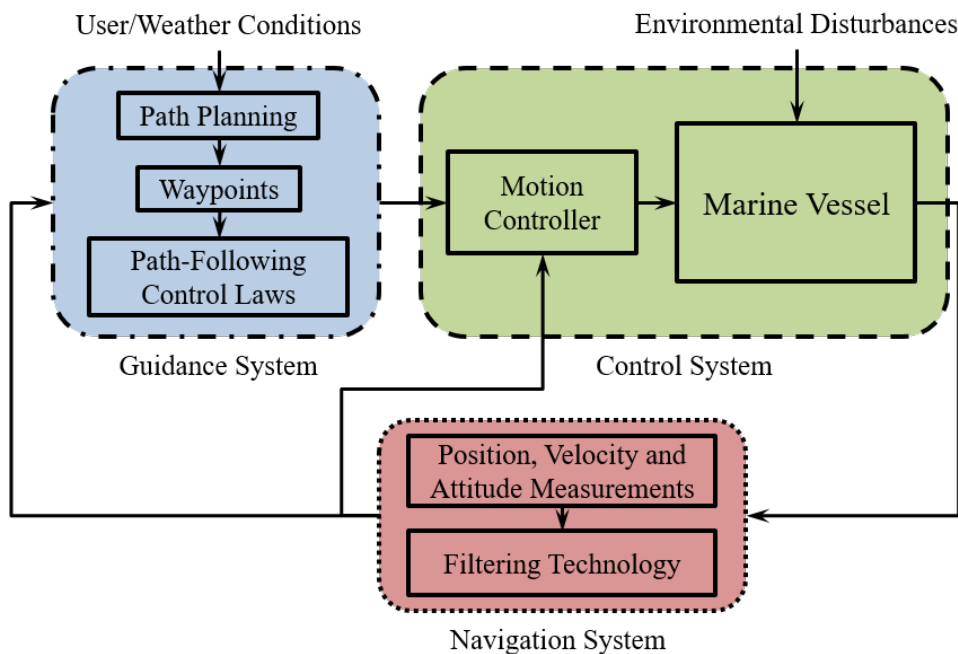
Figure 1.2: A typical guidance, navigation and control (GNC) system for an autonomous marine vessel.

1. **Guidance System** depends on the user input and weather conditions to plan the desired path for a marine vessel to follow. The vehicle position and velocity data are collected by the navigation system, and the path-following control laws act to provide the reference signals for the low level motion control system. It is important to note that enhanced autonomy, for example obstacle avoidance, involves the real-time replanning of the path based on data collected from auxillary perception sensors such as cameras and/or radar systems.

2. **Navigation System** collects the data from a marine vessel's onboard sensors, such as Global Positioning System (GPS) and Attitude and Heading Reference System (AHRS), to determine its position, velocity and course/heading angles. These real-time vehicle status data are fed into the guidance and control system to support the planning and motion control work. To provide an accurate estimation of the positions and velocities though, advanced filtering techniques like the Kalman Filter [12] need to be employed. Currently, all-in-one navigation solutions that combine GPS and AHRS sensor data and implement advanced filtering algorithms are available on the market.

3. **Control System** or the low-level motion controller is responsible for providing appropriate control commands for the vehicle actuators to achieve the desired control objectives. For instance, to accurately follow predefined paths, the guidance system provides the reference speed and heading angle for the motion controller. Through feedback or advanced control algorithm, the motion controller will act to keep up with the reference signal so that the vehicle can be successfully controlled to track desired survey paths.

Much effort has been put into the research of the GNC system for a USV. In the project of ACES [2], an initial design of the GNC system was completed. The navigation system

integrated a differential GPS and a compass, and the control strategy was developed using fuzzy logic. The guidance of ACES was based on waypoints, and the sea trial results demonstrated the successful execution of the waypoint-tracking mission. However, for vehicle safety reasons, the ACES was restricted to operations in the Charles River. In [7], an aluminum monohull USV equipped with a basic GNC system was built. The GNC system employed Line-of-Sight (LOS) guidance strategy, Kalman filter and a PD heading controller. The developed system was successfully tested in calm water conditions. Four monohull kayak-type USVs were developed as testbeds for high-level guidance strategy development and demonstration [13]. Each platform integrated fundamental navigation sensors that include a GPS and a compass, and the speed and heading were controlled by using PID controllers. A guidance strategy for collision avoidance [14] was tested with success. The Springer USV [3] implemented a new GNC system structure for its pollutant tracking missions. To deal with sensor failure, a fault-tolerant navigation algorithm based on fuzzy logic and Kalman filter was designed. The guidance system was based on a common Line-of-Sight (LOS) method, and a linear-quadratic regulator (LQR) controller was employed for motion control.

Although a variety of GNC systems have already been developed and tested on USVs with different levels of success, it turned out that most constructed systems were only tested in an ideal environment with minimum disturbances. Hence, it is difficult to determine the effectiveness of each method in adverse weather conditions. Environment-induced disturbances in a USV's dynamical motion could be a potential threat for safe operation. For instance, an excessive roll motion will cause capsizing. However, most researchers were not able to take into account this potential problem because they lacked the necessary safety analysis tools. Last but not least, although Line-of-Sight (LOS) guidance strategy has been widely implemented, there are other available methods, such as Vector Field Method or Carrot Chasing Method, that are potentially more efficient

and robust. It will be of great value to investigate these different algorithms and compare their performances in the real-world experiments.

In the scope of this research, we will mainly concentrate on the development of the guidance and control (GC) system for a USV because we know that accurate navigation solutions can be achieved by purchasing proper sensors. Our goal is to investigate and test different guidance and control algorithms and evaluate their performances.

1.2.3   Dynamical Modeling and Parameter Identification

The increasing need for high-performance control motivates the investigation of high-fidelity dynamic motion modeling and parameter identification for USVs. It is important to note that many advanced control strategies, such as H_∞ [15], sliding mode [16], backstepping [9] and adaptive control [17], are formulated relying on a USV's dynamic motion model. An accurate model and a proper estimation of the model parameter values are essential for the ultimate manoeuvring control performance.

A USV's planar dynamic motion model has been widely researched, because it is closely related to guidance and control algorithm development. The catamaran-type USV Springer [3] installed two independently controllable thrusters for its motion control. For simplicity, the vehicle was assumed to operate at constant speed, and the yaw motion was modeled as a black box single-input single-output (SISO) system. In this model, the input was the differential rotational speed of the two propellers, and the output was the heading angle. Although the simplified model could be conveniently used for control algorithm development, the model was restricted to only one operating speed and a physical propulsion system model was not included. The Charlie2005 [18] was also a catamaran-type USV, and it was equipped with two thrusters and two rudders for its motion control. The planar motion model was developed in surge and yaw direction, while neglecting the sway motion. The rudder dynamics was included into the model and the propulsion

system implemented a simplified affine thruster model. In [19], a complete planar motion model in surge, sway and yaw was derived from the 6 degrees of freedom rigid body motion equations [20]. Based on this complicated coupled nonlinear model, the paper introduced several methods to make model simplification for three kinds of USVs with different propulsion system configuration. The validation results indicated that the linear surge model was not able to capture the transient accelerating motion of each platform. Additionally, the experiments with the differential-driven USV showed the deficiency of the yaw model in capturing the relatively high turn rate. As a follow up, an improved planar motion model that incorporated the bilinear thruster model was presented [9]. This research was based on the Ribcraft USV from Virginia Polytechnic Institute and State University, and it employed one vectored thruster for riverine manoeuvring. The constructed and identified motion model was speed-dependent, and it was validated using the actual experimental data with satisfactory results.

To identify the hydrodynamic parameter values of a planar motion model, various methods have been reported. A conventional way includes using the tow tank facility to perform the standardized experiments, such as resistance, self-propulsion and planar motion mechanism tests [21]. Using the collected data, most unknown model parameter values can be accurately determined. However, this identification routine depends on the availability of the towing tank and related facility, and it is always costly and time-consuming. In addition, the strip theory and empirical methods are commonly used in the field of Naval Architecture for calculation of some hydrodynamic coefficients [22]. Currently, on-board sensor based model parameter identification techniques have been widely employed. The algorithms that have been implemented include least-squares fitting [9, 18, 23, 24], extended Kalman filter (EKF) [25], numerical optimization [26] and adaptive methodology [27]. These new techniques are cost-effective and enable potential in-field model parameter identification, which is important considering the normally

variable payloads for different USV missions.

A USV's horizontal motion modeling and analysis for control purposes has been extensively addressed, but it is the mostly uncontrolled motions, i.e. roll, pitch and heave, that are the most critical for a vehicle's safety. A USV operating in the seaway normally has 6 degrees of freedom (DOF) motion, and the oscillatory motions of roll, pitch and heave may cause capsizing or system failure. The oscillatory motions of roll, pitch and heave under the influence of environmental disturbances are complicated, and thus to make this problem tractable, the conventional decoupled nonlinear model structure [28, 29, 30, 31] is widely employed. This assumption is widely implemented for a ship's roll motion dynamics analysis, and many techniques, such as analytical approximation and Melnikov's method, are available to be used. To identify the oscillatory motion model parameters, the forced oscillation tests or free decay tests [32] are normally carried out.

1.2.4 Safety Analysis

Safety analysis of a marine craft is a very important subject, especially for those operating in harsh ocean environments. Nonlinear ship rolling motion analysis traces back to the 1970s [29], and it has been a research topic since then because it is closely related to the vessel stability against capsizing in the seaway. The rolling motion is conventionally decoupled from the other degrees of freedom, and the roll exciting moments are normally assumed to be from the harmonic waves. The nonlinearity in the roll motion leads to some well-known complicated phenomena. For instance, due to the nonlinearity of the roll restoring moments, the region around the roll resonant frequency may have multiple steady-state roll response solutions [33].

To investigate the nonlinear roll dynamics and perform the safety analysis, many approaches have been developed. In the early days, due to computational limitations, the analytical approximations of the steady-state rolling response solutions were formulated.

Some typical analytical methods include Perturbation Method and Harmonic Balance Method [34], and they have demonstrated their effectiveness in the main rolling resonance region. Melnikov's method [35, 28] has been widely accepted and employed for analysing ship rolling dynamics. As a global analysis technique, it assumes that the ship roll motion is subjected to a harmonic excitation. Through calculating the value of the Melnikov function, the distance between the stable and unstable manifolds can be determined as a criteria for prediction of the system chaotic behaviour, i.e. the case that potentially leads to capsizing. Recently, the Melnikov's method has also been extended to take into account strong damping effects [36]. Taking advantage of recent advances in computing power, the numerical method, i.e. erosion basin method, has been extensively employed for analysing a ship's nonlinear roll motion and even the complex coupled motions in the seaway. The erosion basin technique is commonly used to investigate the nonlinear roll dynamics in regular seas [30, 31]. In this method, the concept of the safe basin is used, which was first introduced in [37]. It has been demonstrated by several researchers [29] that with the increment of the wave exciting amplitude, the area of the safe basin will erode, and when this happens, the probability of a ship capsizing through rolling increases. Some other methods including Lyapunov and bifurcation analysis have also been introduced [29], but they are applied to limited scenarios.

In this research, we will investigate the commonly used safety analysis methods, i.e. analytical approximation, Melnikov's method and erosion basin, and try to extend them to analyse the roll, pitch and heave motion for a USV. Our main interest resides in finding out the relationship between a USV's operational safety and the primary disturbances from the ocean waves. Therefore, we will try to establish a safety criterion that links the wave amplitude and wave frequency to the operational status of a USV.

1.3 Research Platform

The Unmanned Surface Vehicle (USV) SeaCat shown in Fig. 1.3 is employed in this research. This platform was built at the Autonomous Ocean Systems Laboratory of Memorial University since 2010 for offshore scientific missions [38]. The vehicle itself is 1.5 *m* long and 1.0 *m* wide with a dry weight of 150 to 160 *kg* depending on the payload configurations.

As can be seen from Fig. 1.3a, SeaCat is a catamaran-type USV with two independently controllable propellers located at the rear part of each hull. It is powered by six 336 Wh lead-acid batteries, and they are enclosed in the main watertight compartments of the two hulls. The onboard distributed communication and control system is developed based on Controller Area Network (CAN) protocol [39], and all CAN node circuit boards and sensors are housed in rugged and waterproof enclosures. The default navigational sensors include an accurate GPS receiver with an external antenna installed on the superstructure and an Attitude and Heading Reference System (AHRS) for measuring the attitude of the vehicle. The weather station measures wind speed, wind direction, temperature and barometric pressure. The indoor localization sensors are needed when performing some indoor tests. As shown in Fig. 1.3b, depending on the mission requirements, other sensors such as sonar, camera and radar can also be integrated into the existing CAN bus network.

The USV SeaCat's wireless control and data logging system is developed so that the platform can be conveniently used for new algorithms testing and field experiments. A pair of long-range wireless communication modems are employed on the SeaCat and on the shore-side computer for transmission of the sensor data and vehicle control commands. As shown in Fig. 1.4, the shore-side configuration includes a laptop connected with the wireless modem and a gamepad for intuitive control of the vehicle. The graphical user interface (GUI) on the laptop is developed in the Matlab programming environment, and
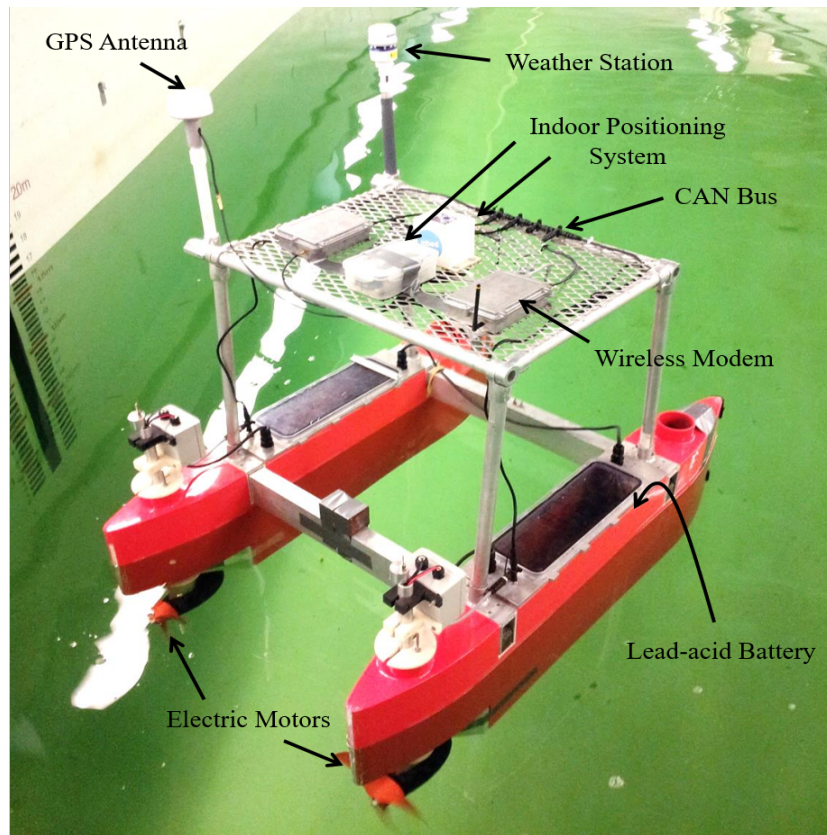
(a) The USV SeaCat in the preliminary tests
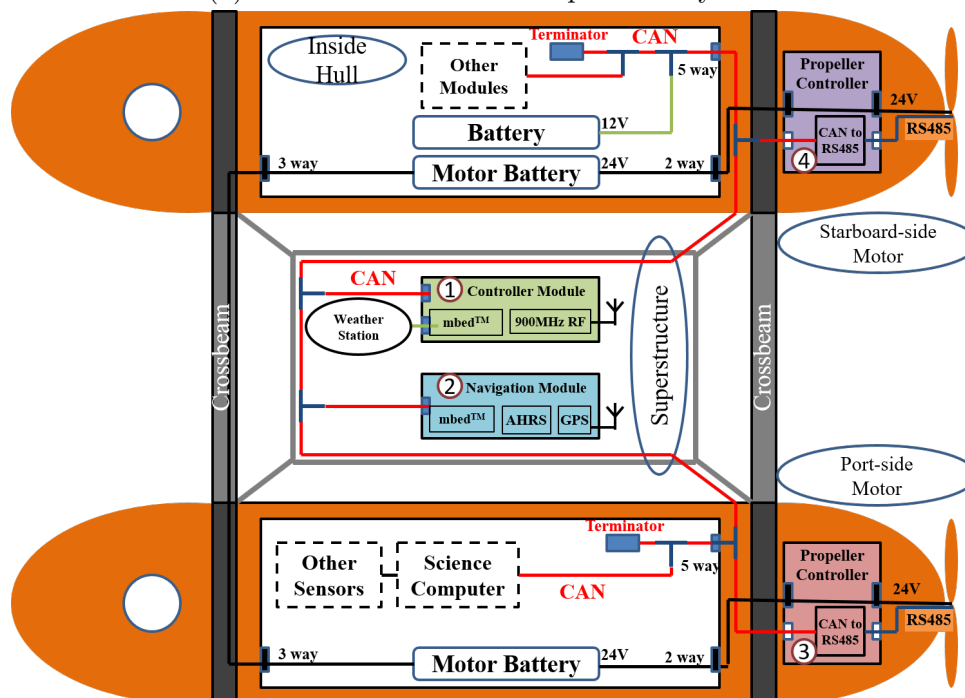
(b) The USV SeaCat's onboard communication and control system structure

Figure 1.3: The USV SeaCat system configuration.

all sensor data, time and propulsion system status can be visualized by the user in real time at 1 Hz update rate. Using the synchronized sensor data, the guidance and control algorithms can be developed on the shore-side computer on the backend of the GUI. The outputs from these algorithms are the vehicle control commands, and they will be transmitted to SeaCat through the wireless modem. This framework provides us with the freedom to develop and update the guidance and control algorithms while the USV has been deployed in the water, and it brings great convenience for users to tune different algorithms online. Further, in this research, we will develop different guidance and control algorithms in the simulation environments using Matlab, and thus the same programming environment will make it possible for us to directly implement the developed code for the real experiments. It is important to note that Matlab is not good at real-time data processing, and it restricts our sensor data update and controlling rate at 1 Hz. However, controlling SeaCat through 1 Hz wireless link is feasible due to the slow motion dynamics of the studied platform, which has been demonstrated during the field tests.
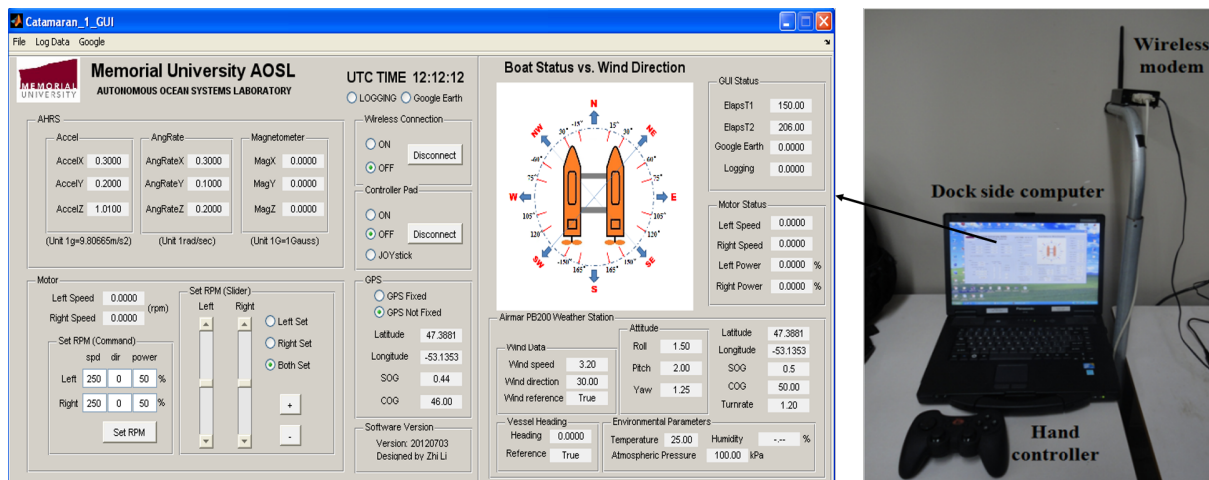
Figure 1.4: The USV SeaCat's shore-side control and data logging system.

The USV SeaCat has been successfully employed for a series of field experiments, and in this process we kept improving and modifying the system in order to fulfill different mission requirements. As shown in Fig. 1.5, we have summarised some typical appli-

cation scenarios for the USV SeaCat. The top left picture of Fig. 1.5 shows the USV SeaCat during the modeling and identification experiments, and it can be seen that the superstructure then is supported by four aluminum tubings. The top right picture shows the iceberg profiling experiment using SeaCat, and in order to increase the system pay-load capacity for fitting camera, multibeam and side-scan sonar, we installed additional fairings on the bottom of each hull. The two bottom figures of Fig. 1.5 show the configu-ration with the new arch superstructure. In these experiments, we evaluated the guidance and control algorithms and integrated a new sonar for the lakebed bathymetric mapping mission. The achieved lakebed map has been depicted as shown in Fig. 1.6. Note that we have defined a local origin and converted the distance to meters, and in the figure, we overlay the vehicle's lawn-mower type trajectory to indicate how we collect the lake depth information. Although the modifications make it difficult for consistency in our modeling and control algorithm development process, we try our best to keep the similar hydrostatic and hydrodynamic characteristics of the platform after each system change.

1.4 Contributions

This research presents the following contributions toward realizing enhanced safe opera-tion of a USV in dynamic and harsh ocean environments:

1. A USV's high fidelity planar motion dynamics model with model parameters iden-tified through performing tow tank and field experiments.

2. A comprehensive study and comparison of three well-accepted path-following con-trol algorithms, including investigation of their mathematical origins, performing simulation evaluations and carrying out field tests to examine their robustness un-der adverse weather conditions.

Figure 1.5: A series of USV field experiments with different system configurations.

3. An investigation of the linear and nonlinear oscillatory motion modeling and parameter identification methods for a USV's heave, roll and pitch motion.

4. A safety analysis of the studied USV in dynamic ocean environments through implementing three different kinds of analysis methodology.

5. An establishment of the safe operational condition that can be conveniently employed on a USV's path-planning system.

The control-related planar motion model is identified following a novel hybrid procedure. A precise bilinear thruster model is first identified by performing standardized tow tank tests, and then extensive field experiments are carried out for on-board sensor-based identification of the remaining model parameter values [18, 9]. The three path-following
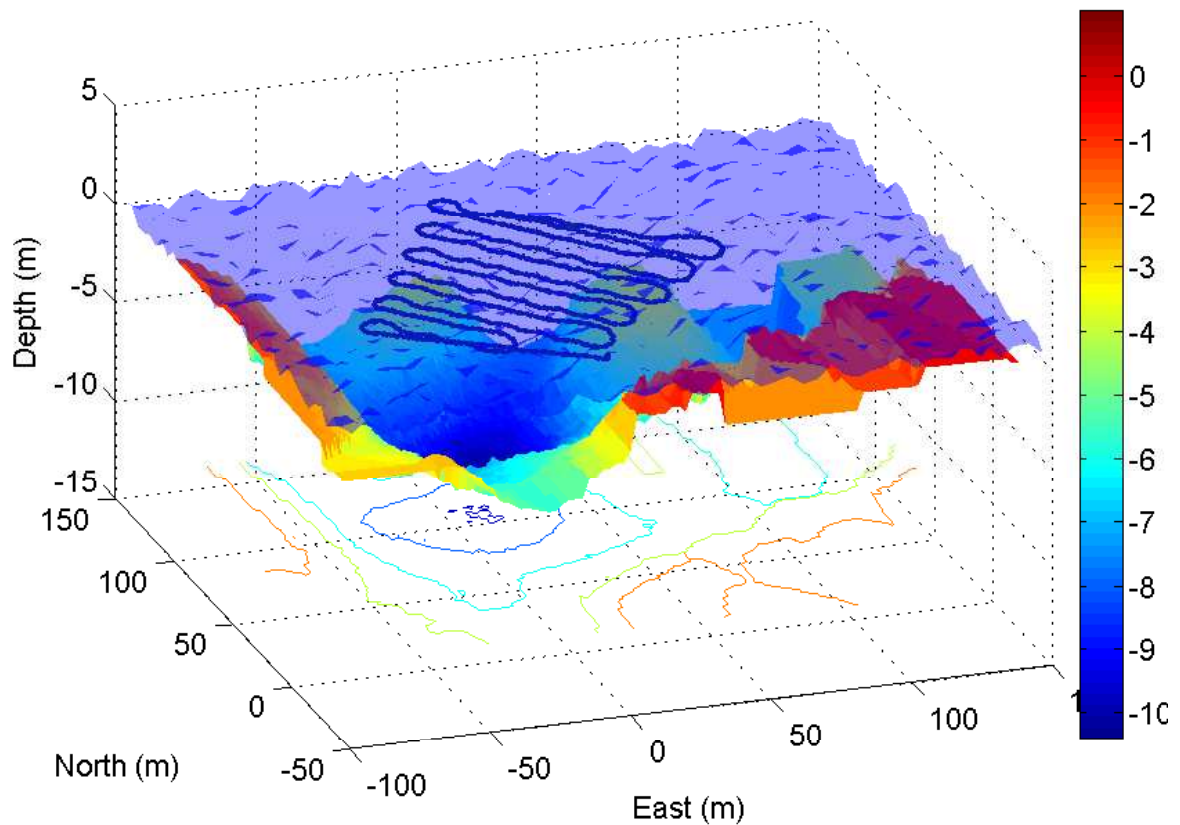
Figure 1.6: The achieved bathymetric map of the lakebed and the USV SeaCat's trajectory. It is important to note that the water surface is represented as with random waves (wave amplitude 0.2 m) as an indication of the operational environments of SeaCat.

control methods include Vector Field Method (VF), Carrot Chasing Method (CC) and Line-of-Sight Method (LOS), among which VF and CC have been introduced and implemented on a USV for the first time. We provide a novel insight into the theoretical origin of each algorithm, reveal the same mathematical origin for VF and CC and demonstrate the deficiency when using VF and LOS for tracking circular paths. Further analysis of each algorithm involves a comparison between simulation study and actual field experiments, which provides more convincing results than most existing associated researches. We also present a unique examination of the robustness of presented algorithms, where designated tests in adverse environmental conditions are performed. Uncontrolled oscil-

latory motion is critical for a USV's operation safety, however, this topic is not very well addressed in the current community [23, 3, 9]. We present the methods to build and identify the oscillatory motion model, depending on which the safety analysis of the the studied USV has been carried out using the available analyzing tools. A key contribution of this thesis is the establishment of a safe operational condition for a USV platform that operates in harsh ocean environments. We have demonstrated the functionality of the guidance and control system and experimentally validate the system's path-following control robustness in adverse weather conditions. The safe operational condition can be regarded as a key supplement to the existing control system structure that can notably improve a USV's safety in an ocean survey mission.

1.5 The Scope of the Thesis

Chapter 1

Background information about the research has been presented in this chapter. Our research motivation was introduced, based on which, literature review was conducted about the recent development of the Unmanned Surface Vehicle (USV) technology, Guidance, Navigation and Control (GNC) System, dynamics modeling methods and safety analysis technique. The research platform was described and its system structure, functions and applications were reviewed. Towards the end of this chapter, the main contributions of this thesis are summarized.

Chapter 2

A systematic procedure for derivation of the USV's planar motion model from the 6 DOF rigid-body motion equations has been introduced. Using this model, a hybrid model parameter identification method that combines tow tank and on-board sensor-based identification technique is followed. The identified dynamic motion model approximates

the real-world planar motion data reasonably well, and a Matlab/Simulink model has been constructed for further guidance and control algorithm development.

Chapter 3

Three well-accepted geometric path-following control methods, namely Vector Field Method (VF), Carrot Chasing Method (CC) and Line-of-Sight Method (LOS), have been comprehensively studied in this chapter. We provide the complete parameter space exploration of each algorithm, based on which we show their mathematical origins and reveal their intrinsic connection. Our search of the parameter space is demonstrated by performing extensive simulation and real-world field experiments. Through comparison of these test results, we can evaluate their varied straight-line, circular and waypoint path-following performances. Our path-following control algorithms are evaluated in adverse weather conditions, and thus these results will provide a valuable reference for USV practitioners for their future work when they have to decide on an appropriate strategy for completion of a specific ocean survey mission.

Chapter 4

The USV's oscillatory motion in heave, roll and pitch is not very well researched in the USV community, but they are closely related to a USV's operational safety while running a mission in dynamic ocean environments. In this chapter, we introduce well-accepted decoupled linear and nonlinear oscillatory motion models. Through performing the convenient and cost-effective tank tests, the model parameters are successfully identified. The primary contribution for the vehicle's oscillatory movements comes from ocean waves, and thus we introduce the formulation of the wave excitation forces and moments for the corresponding degree of freedom. The results from this chapter serves as the basis for a USV's safety analysis.

Chapter 5

In this chapter, three methods including Analytical Method, Melnikov's Method and

Erosion Basin Method have been introduced to analyze a USV's nonlinear roll and pitch motion dynamics. Based on the discussion, the USV's safe operational condition has been established and expressed in 2D polar coordinates. Our analysis provides a helpful reference for USV practitioners to determine on a USV's operational safety considering the unexpected environmental influences. Further, the safe operational condition can be integrated into USV's on-board path-planning system to improve the vehicle's safety during a survey mission.

Chapter 6

In this chapter, we present a concise summary of the significant results. Based on the author's research experience as summarized in this thesis as well as through designing, developing and experimenting with the USV SeaCat, an outlook for the future USV researchers towards safe and reliable USV operation in harsh ocean environments is provided.

Chapter 2

Planar Motion Dynamics Modeling and Parameter Identification

In this chapter, we introduce a systematic procedure for Unmanned Surface Vehicle (USV) planar motion modeling and parameter identification. Our objective is to build a dynamic motion model that is convenient for model parameter identification and accurate enough for efficient control algorithm development. The investigated USV model is simplified from the 6 DOF rigid-body motion equations considering the vehicle's hydrodynamics and other external forces and moments [20]. Using this motion model, a hybrid method, which combines the tow tank identification routine with the popular on-board sensor-based identification technique, has been implemented for model parameter identification.

2.1   6 DOF Nonlinear Motion Model

In this section, we provide an overview of the derivation of the mathematical model for describing a marine vehicle's 6 DOF motion dynamics. By convention, the 6 motion components are divided into two groups: the translational motion in surge, sway and

heave, and the rotational motion in roll, pitch and yaw. We follow the SNAME (1950) standard to define the motion variables, and they have been summarized in Table 2.1.

Table 2.1: SNAME (1950) notation used for marine vehicles

Degrees of freedom	Positions and Euler angles	Linear and angular velocity	Forces and moments
Surge	x	u	X
Sway	y	v	Y
Heave	z	w	Z
Roll	ϕ	p	K
Pitch	θ	q	M
Yaw	ψ	r	N

To analyse the dynamic motion of a marine vehicle, two reference frames are considered, i.e. the inertial and body frames. As shown in Fig. 2.1, in this research the North-East-Down (NED) frame is chosen as the inertial frame $\{I\}$, and its origin O_I is fixed to the earth. The body frame $\{B\}$ is a moving frame, and its origin O_B is fixed to the research platform. The body frame axes are defined as:

- $O_B x_B$ is directed from aft to fore along the longitudinal direction of the vehicle

- $O_B y_B$ is directed to starboard along the transverse direction of the vehicle

- $O_B z_B$ is directed from top to bottom along the normal direction of the vehicle

It is important to note that the position $[x, y, z]^T$ and orientation $[\phi, \theta, \psi]^T$ of the vehicle are normally expressed in the inertial frame $\{I\}$, while the linear velocity $[u, v, w]^T$, angular velocity $[p, q, r]^T$, forces $[X, Y, Z]^T$ and moments $[K, M, N]^T$ are expressed in the body frame $\{B\}$. To formulate the motion equations for a marine vehicle in the following

discussion, we define the vectors as below

$$\eta = [x, y, z, \phi, \theta, \psi]^T$$

$$\nu = [u, v, w, p, q, r]^T \tag{2.1}$$

$$\tau = [X, Y, Z, K, M, N]^T.$$
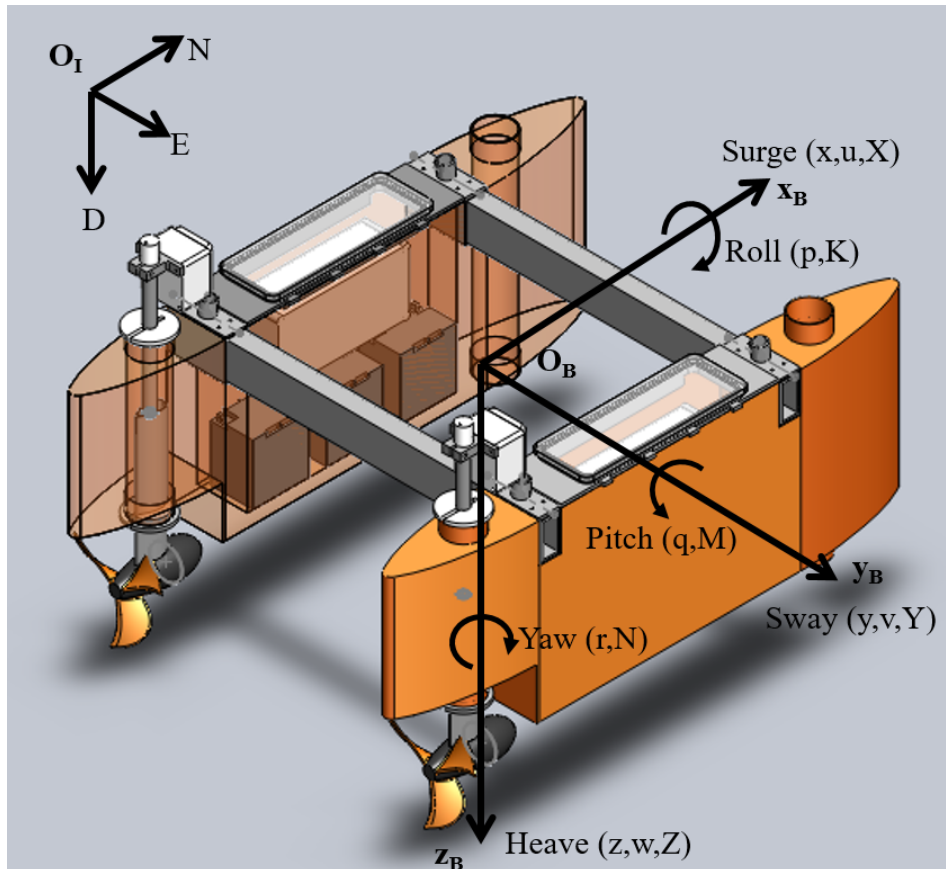
Figure 2.1: The standard notation for describing a marine vehicle's 6 DOF motion (SNAME, 1950). The inertial frame $\{I\}$ is an earth-fixed frame, while the body frame $\{B\}$ is attached to the vehicle.

The kinematics deals with the geometric part of the motion, and it can be formulated as [20]

$$\dot{\eta} = J(\eta)\nu \tag{2.2}$$

where $J(\eta)$ is a transformation matrix that depends on the Euler angles, and it transforms the linear and angular velocity of a marine vehicle from $\{B\}$ to $\{I\}$. The transformation matrix can be written as

$$J(\eta) = \begin{bmatrix} J_1 & 0_{3\times 3} \\ 0_{3\times 3} & J_2 \end{bmatrix}$$

where

$$J_1 = \begin{bmatrix} c(\psi)c(\theta) & -s(\psi)c(\phi) + c(\psi)s(\theta)s(\phi) & s(\psi)s(\phi) + c(\psi)c(\phi)s(\theta) \\ s(\psi)c(\theta) & c(\psi)c(\phi) + s(\psi)s(\theta)s(\phi) & -c(\psi)s(\phi) + s(\psi)c(\phi)s(\theta) \\ -s(\theta) & s(\phi)c(\theta) & c(\theta)c(\phi) \end{bmatrix}$$

and

$$J_2 = \begin{bmatrix} 1 & s(\phi)t(\theta) & c(\phi)t(\theta) \\ 0 & c(\phi) & -s(\phi) \\ 0 & s(\phi)/c(\theta) & c(\phi)/c(\theta) \end{bmatrix}.$$

Note that we define $s() \triangleq \sin()$, $c() \triangleq \cos()$ and $t() \triangleq \tan()$.

The kinetics, on the other hand, focuses on the forces and moments and their influences on a vehicle's motion. We consider the marine vehicle as a rigid body, using Newtonian and Lagrangian formalism, the 6 DOF rigid-body motion equations can be formulated as [20]

$$M_{RB}\dot{\nu} = \tau - C_{RB}(\nu)\nu. \tag{2.3}$$

M_{RB} is the rigid-body inertia matrix that is given as

$$
M_{RB} = \begin{bmatrix}
m & 0 & 0 & 0 & mz_G & -my_G \\
0 & m & 0 & -mz_G & 0 & mx_G \\
0 & 0 & m & my_G & -mx_G & 0 \\
0 & -mz_G & my_G & I_{xx} & -I_{xy} & -I_{xz} \\
mz_G & 0 & -mx_G & -I_{yx} & I_{yy} & -I_{yz} \\
-my_G & mx_G & 0 & -I_{zx} & -I_{zy} & I_{zz}
\end{bmatrix}
$$

where m is the total mass of the vehicle, $\vec{r}_G = [x_G, y_G, z_G]^T$ is the vector that defines the location of the center of gravity in $\{B\}$ and

$$
I = \begin{bmatrix}
I_{xx} & -I_{xy} & -I_{xz} \\
-I_{yx} & I_{yy} & -I_{yz} \\
-I_{zx} & -I_{zy} & I_{zz}
\end{bmatrix}
$$

represents the inertia tensor where the off-diagonal terms arise from the asymmetry with respect to the body frame axes. In Eq. 2.3, $C_{RB}(\nu)\nu$ denotes the Coriolis and centripetal

forces and moments and $C_{RB}(\nu)$ can be written as

$$C_{RB}(\nu) = \begin{bmatrix} 0 & 0 & 0 \\ 0 & 0 & 0 \\ 0 & 0 & 0 \\ -m(y_G q + z_G r) & m(y_G p + w) & m(z_G p - v) \\ m(x_G q - w) & -m(z_G r + x_G p) & m(z_G q + u) \\ m(x_G r + v) & m(y_G r - u) & -m(x_G p + y_G q) \end{bmatrix}$$

$$\begin{matrix} m(y_G q + z_G r) & -m(x_G q - w) & -m(x_G r + v) \\ -m(y_G p + w) & m(z_G r + x_G p) & -m(y_G r - u) \\ -m(z_G p - v) & -m(z_G q + u) & m(x_G p + y_G q) \\ 0 & -I_{yz}q - I_{xz}p + I_{zz}r & I_{yz}r + I_{xy}p - I_{yy}q \\ I_{yz}q + I_{xz}p - I_{zz}r & 0 & -I_{xz}r - I_{xy}q + I_{xx}p \\ -I_{yz}r - I_{xy}p + I_{yy}q & I_{xz}r + I_{xy}q - I_{xx}p & 0 \end{matrix} .$$

The last term τ in Eq. 2.3 stands for the vector of generalized forces and moments that potentially includes the hydrodynamic forces and moments τ_h, the forces and moments from the propulsion system τ_p, the control surfaces τ_c, such as from the rudder and fins, and the environmental disturbances τ_e. Therefore, τ can be formulated as

$$\tau = \tau_h + \tau_p + \tau_c + \tau_e.$$

According to [20], the hydrodynamic forces and moments can be formulated as

$$\tau_h = -M_A \dot{\nu} - C_A(\nu)\nu - D(\nu)\nu - g(\eta). \tag{2.4}$$

In Eq. 2.4, M_A is the added inertia matrix and it is given as

$$M_A = - \begin{bmatrix} X_{\dot{u}} & X_{\dot{v}} & X_{\dot{w}} & X_{\dot{p}} & X_{\dot{q}} & X_{\dot{r}} \\ Y_{\dot{u}} & Y_{\dot{v}} & Y_{\dot{w}} & Y_{\dot{p}} & Y_{\dot{q}} & Y_{\dot{r}} \\ Z_{\dot{u}} & Z_{\dot{v}} & Z_{\dot{w}} & Z_{\dot{p}} & Z_{\dot{q}} & Z_{\dot{r}} \\ K_{\dot{u}} & K_{\dot{v}} & K_{\dot{w}} & K_{\dot{p}} & K_{\dot{q}} & K_{\dot{r}} \\ M_{\dot{u}} & M_{\dot{v}} & M_{\dot{w}} & M_{\dot{p}} & M_{\dot{q}} & M_{\dot{r}} \\ N_{\dot{u}} & N_{\dot{v}} & N_{\dot{w}} & N_{\dot{p}} & N_{\dot{q}} & N_{\dot{r}} \end{bmatrix}$$

where each term can be employed for calculation of the added mass forces or moments. For example,

$$X_{\dot{u}} \triangleq \frac{\partial X}{\partial \dot{u}}$$

and $X_{\dot{u}}\dot{u}$ can be used for calculating the added mass force along surge direction with a contribution from the surge acceleration or deceleration. The added mass Coriolis and centripetal forces and moments are represented by $C_A(\nu)\nu$ and

$$C_A(\nu) = \begin{bmatrix} 0 & 0 & 0 & 0 & -c_{A3} & c_{A2} \\ 0 & 0 & 0 & c_{A3} & 0 & -c_{A1} \\ 0 & 0 & 0 & -c_{A2} & c_{A1} & 0 \\ 0 & -c_{A3} & c_{A2} & 0 & -c_{A6} & c_{A5} \\ c_{A3} & 0 & -c_{A1} & c_{A6} & 0 & -c_{A4} \\ -c_{A2} & c_{A1} & 0 & -c_{A5} & c_{A4} & 0 \end{bmatrix}$$

where

$$c_{A1} = X_{\dot{u}}u + X_{\dot{v}}v + X_{\dot{w}}w + X_{\dot{p}}p + X_{\dot{q}}q + X_{\dot{r}}r$$

$$c_{A2} = X_{\dot{v}}u + Y_{\dot{v}}v + Y_{\dot{w}}w + Y_{\dot{p}}p + Y_{\dot{q}}q + Y_{\dot{r}}r$$

$$c_{A3} = X_{\dot{w}}u + Y_{\dot{w}}v + Z_{\dot{w}}w + Z_{\dot{p}}p + Z_{\dot{q}}q + Z_{\dot{r}}r$$

$$c_{A4} = X_{\dot{p}}u + Y_{\dot{p}}v + Z_{\dot{p}}w + K_{\dot{p}}p + K_{\dot{q}}q + K_{\dot{r}}r$$

$$c_{A5} = X_{\dot{q}}u + Y_{\dot{q}}v + Z_{\dot{q}}w + K_{\dot{q}}p + M_{\dot{q}}q + M_{\dot{r}}r$$

$$c_{A6} = X_{\dot{r}}u + Y_{\dot{r}}v + Z_{\dot{r}}w + K_{\dot{r}}p + M_{\dot{r}}q + N_{\dot{r}}r$$

It is important to note that both M_A and $C_A(\nu)$ are due to the inertia of the surrounding fluid.

The damping forces and moments of $D(\nu)\nu$ include those from the pressure drag, skin friction and damping due to the vortex shedding and wave making. To achieve a tractable model, we assume that $D(\nu)$ only consists of the linear laminar friction

$$D_l(\nu) = - \begin{bmatrix} X_u & X_v & X_w & X_p & X_q & X_r \\ Y_u & Y_v & Y_w & Y_p & Y_q & Y_r \\ Z_u & Z_v & Z_w & Z_p & Z_q & Z_r \\ K_u & K_v & K_w & K_p & K_q & K_r \\ M_u & M_v & M_w & M_p & M_q & M_r \\ N_u & N_v & N_w & N_p & N_q & N_r \end{bmatrix}$$

and the quadratic pressure drag

$$
D_q(\nu) = - \begin{bmatrix}
X_{u|u|}|u| & X_{v|v|}|v| & X_{w|w|}|w| & X_{p|p|}|p| & X_{q|q|}|q| & X_{r|r|}|r| \\
Y_{u|u|}|u| & Y_{v|v|}|v| & Y_{w|w|}|w| & Y_{p|p|}|p| & Y_{q|q|}|q| & Y_{r|r|}|r| \\
Z_{u|u|}|u| & Z_{v|v|}|v| & Z_{w|w|}|w| & Z_{p|p|}|p| & Z_{q|q|}|q| & Z_{r|r|}|r| \\
K_{u|u|}|u| & K_{v|v|}|v| & K_{w|w|}|w| & K_{p|p|}|p| & K_{q|q|}|q| & K_{r|r|}|r| \\
M_{u|u|}|u| & M_{v|v|}|v| & M_{w|w|}|w| & M_{p|p|}|p| & M_{q|q|}|q| & M_{r|r|}|r| \\
N_{u|u|}|u| & N_{v|v|}|v| & N_{w|w|}|w| & N_{p|p|}|p| & N_{q|q|}|q| & N_{r|r|}|r|
\end{bmatrix},
$$

and thus,

$$
D(\nu) = D_l(\nu) + D_q(\nu).
$$

The last term $g(\eta)$ in Eq. 2.4 stands for the restoring forces and moments that arise from the gravitational and buoyant forces and it can be formulated as

$$
g(\eta) = \begin{bmatrix}
-\rho g \int_0^z A_{wp}(h)dh \sin(\theta) \\
\rho g \int_0^z A_{wp}(h)dh \cos(\theta)\sin(\phi) \\
\rho g \int_0^z A_{wp}(h)dh \cos(\theta)\cos(\phi) \\
\rho g \nabla \overline{GM}_T \cos(\theta)\sin(\phi)\cos(\phi) \\
\rho g \nabla \overline{GM}_L \sin(\theta)\cos(\theta)\cos(\phi) \\
\rho g \nabla (\overline{GM}_T - \overline{GM}_L \cos(\theta))\sin(\theta)\sin(\phi)
\end{bmatrix} \tag{2.5}
$$

where ρ is the water density, g is the gravitational acceleration, ∇ is the displaced water volume, $A_{wp}(h)$ is the water plane area with respect to the heave position, and the integration $\int_0^z A_{wp}(h)dh$ denotes the variation of the displaced water volume due to the heave motion. Additionally, the transversal and longitudinal metacentric height are represented as $\overline{GM}_T$ and $\overline{GM}_L$, respectively, and they are an indication of the initial roll and pitch stability of a marine vehicle. To give an example, the transversal metacentric height has

been depicted in Fig. 2.2, and it is measured as the distance between the center of gravity CG and the metacentre. When the vehicle has a roll angle of ϕ, the center of buoyancy CB moves to a new position, and the metacentre is denoted as the intersection point of the new and original vertical lines that pass through CB. Similarly, the metacentric height along the longitudinal direction can also be defined.
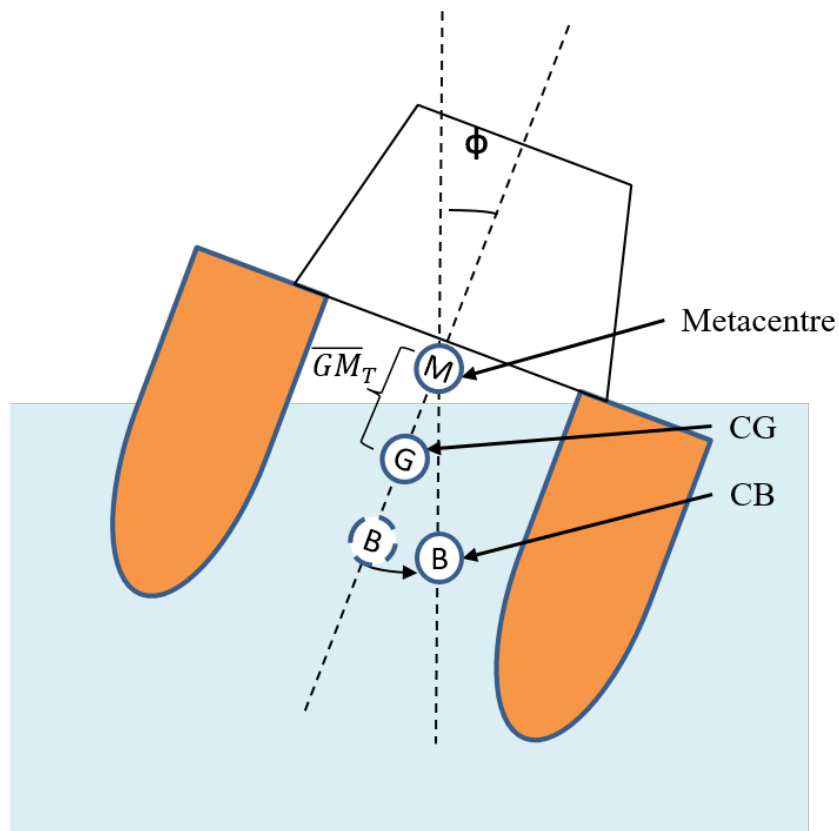
Figure 2.2: The transversal metacentric height $\overline{GM}_T$ on a marine vehicle.

As a summary, a lumped form representation of the 6 DOF nonlinear motion model for a marine vehicle operating in the ocean can be written as

$$(M_{RB} + M_A)\dot{\nu} + (C(\nu) + C_A(\nu))\nu + D(\nu)\nu + g(\eta) = \tau_p + \tau_c + \tau_e \qquad (2.6)$$

2.2 Planar Motion Model

The 6 DOF motion model can describe the complete movement of the vehicle in the seaway, but it is highly nonlinear and the motion components are coupled. In this section, we will derive a simplified planar motion model from the 6 DOF dynamic motion equations. We will later show that this model has a relatively good fidelity in representing the vehicle's actual planar motion, and further, it can be conveniently employed for model parameter identification and guidance and control algorithm development.

The planar movement of a marine vessel includes three motion components, i.e. surge, sway and yaw, and to get to this model we need to assume the vehicle's motion in the other three degrees of freedom, i.e. heave, roll and pitch, to be small and negligible. Note that in most cases the oscillatory motions are relatively small compared to the planar ones, and it will also be an appropriate assumption if we only consider about developing path-following control algorithms for a surface vehicle in the horizontal plane [18, 19]. To be consistent with the previous section, the same inertial and body frames as depicted in Fig. 2.1 are chosen, and we also employ the same SNAME variable definitions. Therefore, the position-orientation, linear-angular velocity and force-moment vectors in surge, sway and yaw are given as

$$\eta = [x, y, \psi]^T$$

$$\nu = [u, v, r]^T$$

$$\tau = [X, Y, N]^T.$$

By substituting $\phi = \theta = 0$ into Eq. 2.2 and neglecting the rows and columns for heave, roll and pitch, we can achieve the planar motion kinematics and the new transformation

matrix as

$$J(\eta) = \begin{bmatrix} \cos(\psi) & -\sin(\psi) & 0 \\ \sin(\psi) & \cos(\psi) & 0 \\ 0 & 0 & 1 \end{bmatrix}.$$

The planar motion kinetics keep the same form as Eq. 2.3, but in this section the inertia matrix is simplified as

$$M_{RB} = \begin{bmatrix} m & 0 & -my_G \\ 0 & m & mx_G \\ -my_G & mx_G & I_{zz} \end{bmatrix}$$

and the simplified Coriolis and centripetal forces and moments matrix is given as

$$C_{RB}(\nu) = \begin{bmatrix} 0 & 0 & -m(x_G r + v) \\ 0 & 0 & -m(y_G r - u) \\ m(x_G r + v) & m(y_G r - u) & 0 \end{bmatrix}$$

The total forces and moments along surge, sway and yaw include those from the vehicle hydrodynamics, propulsion system, control surfaces and the surrounding environmental influences. In this research though, since the studied USV features no rudders or fins, we can neglect τ_c, and thus

$$\tau = \tau_h + \tau_p + \tau_e$$

where τ_h can be expanded as Eq. 2.4.

By convention, the surge motion can be decoupled from the steering dynamics due to

the xz-plane symmetry, so the added inertia of the vehicle can be simplified as [11, 20]

$$M_A = - \begin{bmatrix} X_{\dot{u}} & 0 & 0 \\ 0 & Y_{\dot{v}} & Y_{\dot{r}} \\ 0 & N_{\dot{v}} & N_{\dot{r}} \end{bmatrix}, \tag{2.7}$$

and similarly the added mass Coriolis and centripetal forces and moments matrix is simplified as

$$C_A(\nu) = \begin{bmatrix} 0 & 0 & Y_{\dot{v}}v + Y_{\dot{r}}r \\ 0 & 0 & -X_{\dot{u}}u - Y_{\dot{v}}v \\ -Y_{\dot{v}}v - Y_{\dot{r}}r & X_{\dot{u}}u + Y_{\dot{v}}v & 0 \end{bmatrix}.$$

The damping forces and moments can be calculated as the summation of the linear laminar friction and the quadratic pressure drag. For simplicity, we assume that the damping matrix is diagonal, and thus it is written as

$$D(\nu) = - \begin{bmatrix} X_u + X_{u|u|}|u| & 0 & 0 \\ 0 & Y_v + Y_{v|v|}|v| & 0 \\ 0 & 0 & N_r + N_{r|r|}|r| \end{bmatrix}.$$

It will be shown in the later section that the simplified damping model can approximate the real experimental data reasonably well.

According to Eq. 2.5, when considering that the vehicle's roll and pitch motion is small, the restoring forces and moments for surge, sway and yaw are close to zero, so

$$g(\eta) = \begin{bmatrix} 0 \\ 0 \\ 0 \end{bmatrix}.$$

Now, we can write down the compact form nonlinear planar motion model as

$$(M_{RB} + M_A)\dot{\nu} + (C(\nu) + C_A(\nu))\nu + D(\nu)\nu = \tau_p + \tau_e \qquad (2.8)$$

where $\tau_p = [X_p, Y_p, N_p]^T$ and $\tau_e = [X_e, Y_e, N_e]^T$. Substituting the vectors and matrices into Eq. 2.8 yields the expanded form motion equations as below

$$
\begin{aligned}
(m - X_{\dot{u}})\dot{u} - my_G\dot{r} + (Y_{\dot{r}} - mx_G)r^2 + (Y_{\dot{v}} - m)vr - X_u u - X_{u|u|}u|u| &= X_p + X_e \\
(m - Y_{\dot{v}})\dot{v} + (mx_G - Y_{\dot{r}})\dot{r} - my_G r^2 + (m - X_{\dot{u}})ur - Y_v v - Y_{v|v|}v|v| &= Y_p + Y_e \\
-my_G\dot{u} + (mx_G - N_{\dot{v}})\dot{v} + (I_{zz} - N_{\dot{r}})\dot{r} + (mx_G - Y_{\dot{r}})ur + (X_{\dot{u}} - Y_{\dot{v}})uv & \\
+my_G vr - N_r r - N_{r|r|}r|r| &= N_p + N_e
\end{aligned} \qquad (2.9)
$$

By choosing O_B to coincide with the center of gravity, we get $\vec{r}_G = [x_G, y_G, z_G]^T = [0,0,0]^T$, and Eq. 2.9 can be simplified to

$$
\begin{aligned}
(m - X_{\dot{u}})\dot{u} + Y_{\dot{r}}r^2 + (Y_{\dot{v}} - m)vr - X_u u - X_{u|u|}u|u| &= X_p + X_e \\
(m - Y_{\dot{v}})\dot{v} - Y_{\dot{r}}\dot{r} + (m - X_{\dot{u}})ur - Y_v v - Y_{v|v|}v|v| &= Y_p + Y_e \\
-N_{\dot{v}}\dot{v} + (I_{zz} - N_{\dot{r}})\dot{r} - Y_{\dot{r}}ur + (X_{\dot{u}} - Y_{\dot{v}})uv - N_r r - N_{r|r|}r|r| &= N_p + N_e
\end{aligned} \qquad (2.10)
$$

Note that for a reasonably balanced vehicle, the values of $Y_{\dot{r}}$ and $N_{\dot{v}}$ will be much smaller than the diagonal terms in the added inertia matrix of Eq. 2.7. Therefore, the planar motion equations can be further simplified as

$$
\begin{aligned}
(m - X_{\dot{u}})\dot{u} &= X_{u|u|}u|u| + X_u u + (m - Y_{\dot{v}})vr + X_p + X_e \\
(m - Y_{\dot{v}})\dot{v} &= Y_{v|v|}v|v| + Y_v v - (m - X_{\dot{u}})ur + Y_p + Y_e \\
(I_z - N_{\dot{r}})\dot{r} &= N_{r|r|}r|r| + N_r r + (Y_{\dot{v}} - X_{\dot{u}})uv + N_p + N_e
\end{aligned} \qquad (2.11)
$$

Our indoor and outdoor identification experiments are performed in an ideal condition with minimum environmental disturbances, so the forces and moments as the result from different environmental factors can be neglected. Further, the studied USV SeaCat employs two independently controlled thrusters for its steering control, and there is no direct control input for the sway movement, i.e. $Y_p = 0$. This propulsion system configuration makes the planar motion control problem as underactuated [40], i.e. the number of available control inputs is lower than the vehicle's degrees of freedom. Finally, the planar motion model for the research platform can be formulated as

$$
\begin{aligned}
(m - X_{\dot{u}})\dot{u} &= X_{u|u|}u|u| + X_u u + (m - Y_{\dot{v}})vr + X_p \\
(m - Y_{\dot{v}})\dot{v} &= Y_{v|v|}v|v| + Y_v v - (m - X_{\dot{u}})ur \\
(I_z - N_{\dot{r}})\dot{r} &= N_{r|r|}r|r| + N_r r + (Y_{\dot{v}} - X_{\dot{u}})uv + N_p
\end{aligned}
\qquad . \qquad (2.12)
$$

2.2.1 Surge Motion Modeling

The surge motion is dominant, and by convention it can be regarded as decoupled from sway and yaw. Thus, we neglect the second-order term involving vr in Eq. 2.12 and the further simplified decoupled surge model is given as

$$
(m - X_{\dot{u}})\dot{u} = X_{u|u|}u|u| + X_u u + X_p. \qquad (2.13)
$$

2.2.2 Steering Motion Modeling

The USV SeaCat's designed maximum surge speed is $1\ m/s$ and its sway motion is always small, so the multiplication uv will be relatively small. Meanwhile, we know that $Y_{\dot{v}}$ and $X_{\dot{u}}$ are of a comparable order and the studied platform has a similar dimension in terms of its length and width. Hence, without loss of generality, we neglect the term of $(Y_{\dot{v}} - X_{\dot{u}})uv$

for the yaw motion model in Eq. 2.12 [20], and the steering dynamics is given as

$$(m - Y_{\dot{v}})\dot{v} = Y_{v|v|}v|v| + Y_v v - (m - X_{\dot{u}})ur$$
$$(I_z - N_{\dot{r}})\dot{r} = N_{r|r|}r|r| + N_r r + N_p$$
$$\tag{2.14}$$

In the steering motion model of Eq. 2.14, the coupling term of $(m - X_{\dot{u}})ur$ acts as the control inputs for sway dynamics. The proposed simplification of the yaw motion model decouples yaw dynamics from surge and sway, and this turns out to be a reasonable assumption because a direct relationship between the applied steering moment N_p and the turning rate is conventionally employed. For instance, in the well-known Nomoto's model for describing a marine vessel's steering dynamics, a linear or second-order relationship between the rudder angle (steering moment) and the turn rate is established [9].

2.2.3 Thruster Dynamics Modeling

The two thrusters of the USV SeaCat are installed at the stern of two hulls, and thus the water flow speed u_f through the propellers will be affected by the surge motion of the hulls. This effect can be modeled with the wake fraction coefficient w_f as

$$u_f = (1 - w_f)u. \tag{2.15}$$

The available thrust from one thruster is also influenced by the hull-propeller interaction [18] and it can be modeled as

$$T_a = (1 - t_d)T \tag{2.16}$$

where t_d is the thrust deduction factor with a typical value of 0.05 to 0.2, T_a represents the available thrust and T is the propulsive force from one thruster. Using the bilinear

thruster model [20], the available propulsive force exerted by one thruster is given by

$$T_a = (1 - t_d)(k_1^* \Omega^2 + k_2^*(1 - w_f)u\Omega) \tag{2.17}$$

where k_1^* and k_2^* are the model coefficients and Ω is the propeller's revolution rate. A lumped-form representation for the port- and starboard-side thrust force T_p and T_s is given as

$$\begin{aligned} T_p &= k_1\Omega_p^2 + k_2 u\Omega_p \\ T_s &= k_1\Omega_s^2 + k_2 u\Omega_s \end{aligned} \tag{2.18}$$

where

$$\begin{aligned} k_1 &= (1 - t_d)k_1^* \\ k_2 &= (1 - t_d)(1 - w_f)k_2^* \end{aligned}$$

are the lumped model coefficients for the bilinear thruster model, and Ω_p and Ω_s denote the revolution rate of port- and starboard-side propellers. Based on Eq. 2.18, the surge forces and steering moments from the propulsion system are formulated as:

$$\begin{aligned} X_p &= T_p + T_s \\ N_p &= (T_p - T_s) \cdot l \end{aligned} \tag{2.19}$$

where l=0.41 m and it represents the perpendicular distance from one propeller's axle to the USV's centerplane.

2.3   Model Parameter Identification

This section introduces the detailed procedures we employ for planar motion model parameter identification. First, we carry out the standardized tests in the tow tank for characterising the surge damping coefficients and identifying the bilinear thruster model. Second, the on-board sensor-based identification routine has been followed, and extensive field experiments are performed in open water conditions. Finally, the fidelity of the identified model is demonstrated using the field test data.

2.3.1   Tow Tank Tests

Taking advantage of the small size of the studied platform, full-scale tow tank tests can be performed. The tow tank is located at the Engineering Building of Memorial University of Newfoundland, and it is 70 m long and 4 m wide. We follow the ITTC Recommended Procedure 7.5-02-02-01 to setup the platform in the tank as shown in Fig. 2.3. In this experimental setup, the superstructure has been removed and the measuring head of the towing dynamometer from the tow carriage is fixed on an aluminum bar that is installed across the two cross beams. The aluminum bar is in the centreplane of SeaCat, and the measuring head is attached right above the longitudinal centre of buoyancy to prevent artificial trim effects. This configuration prevents SeaCat from yawing and rolling, but allows the vehicle to pitch and heave freely. The draft and trim of SeaCat have been adjusted by adding more weights on the aluminum bar, so that we can keep the same operational condition as the case with the superstructure. The towing force, vehicle speed through water, trim and sinkage are measured during the tests. Before performing the experiments, all devices have been calibrated, and all sensor data are recorded in the same computer with a sampling rate of 1.6 KHz. In the following, we will introduce the procedures for performing the resistance and self-propulsion tests for identification of the

surge damping coefficients $X_{u|u|}$ and X_u as well as the bilinear thruster model coefficients k_1 and k_2.
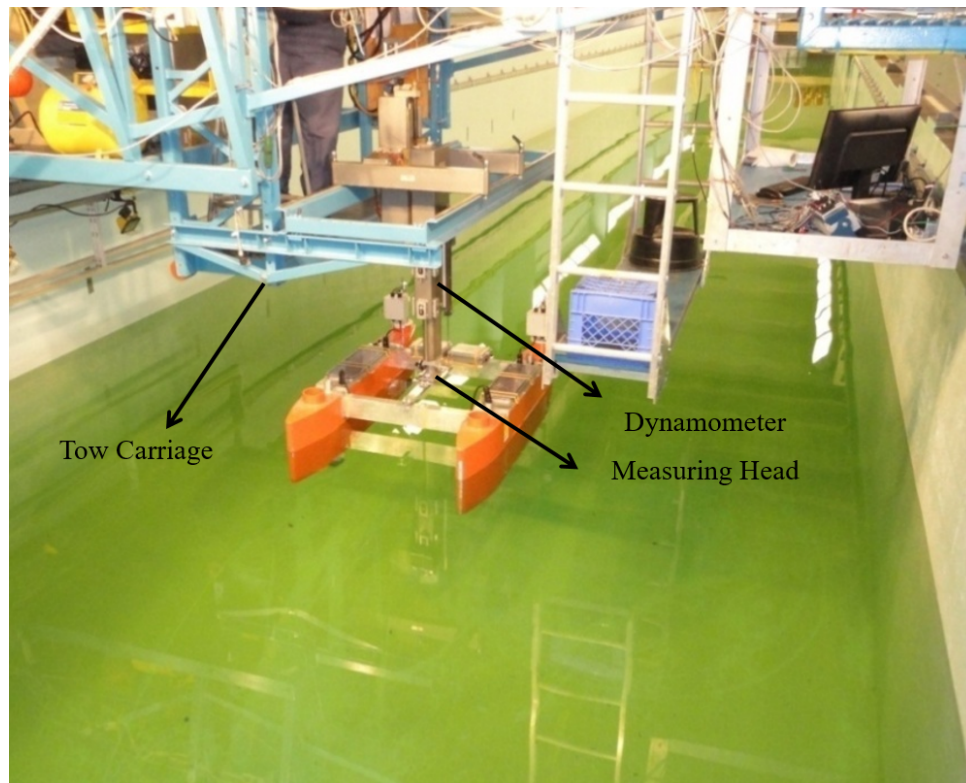
Figure 2.3: Experimental setup of SeaCat in the tow tank. The measuring head is connected to an aluminum bar that is installed across the two cross beams, and the vehicle is positioned in the centreline of the tank parallel to the carriage rails.

2.3.1.1 Resistance Tests

According to ITTC Recommended Procedure 7.5-02-02-01, the test speed range is determined by calculating the Froude number as

$$F_r = \frac{u}{\sqrt{gL}}$$

where F_r is the Froude number that should be less than 0.45, g is the local acceleration of gravity and L is the waterline length. Through calculation, u needs to be less than 1.73

m/s so that the vehicle is in displacement mode. Since the designed operational speed of SeaCat is around 1.0 m/s, we determine that the test speed range is from 0.2 m/s to 1.2 m/s with a step of 0.2 m/s.

Prior to each run, the zero readings for all sensors are recorded for around 10 s to provide a representative mean offset value. Then, the vehicle is towed from rest to the designated speed by the tow carriage. The steady-state moving condition is normally maintained for around 20 to 30 s for required data logging. After that, the tow carriage decelerates to a stop and moves back to the initial position for the next run. Note that sufficient time is needed between the consecutive runs to keep the same testing conditions. The resistance of the vehicle is calculated by subtraction of the zero offsets from the measured average steady-state tow force. To reduce the propeller-induced drag, both propellers are replaced by the same profile nose cones. The resistance test results are depicted in Fig. 2.4, where the damping force is plotted with the standard deviation error bars. It can be seen that a fast increment of the drag force occurs when the vehicle speed exceeds 1.0 m/s, and this is caused by the heavy running trim making the bow head into the water. Note that the tow point on the SeaCat is relatively high, and this will lead to the bow-down pitch during high speeds. In the test runs where the vehicle speed is below 0.8 m/s though, the vehicle pitch angle is small and it has been used for compensation of the calculated cross-sectional area. Therefore, when fitting the surge damping model, only the data points between 0.2 m/s to 0.8 m/s are employed. According to Eq. 2.13, when the vehicle is towed with constant speed through the water, the surge motion equation is given as

$$0 = X_{u|u|}u|u| + X_u u + X_t$$

where X_t denotes the external tow force along the surge direction. The damping coefficients have been identified as $X_{u|u|}$=-13.21 kg/m and X_u=-1.31 kg/s, and the fitted curve is plotted as dashed line in Fig. 2.4. A simpler damping model with only the quadratic

term can also be used to represent the resistance characteristics of the vehicle. In this case, we identify $X_{u|u|}$=-14.98 kg/m and the fitted curve is depicted as dot line in Fig. 2.4. It clearly shows that the two fitted curves are close to each other in the experimental speed range.
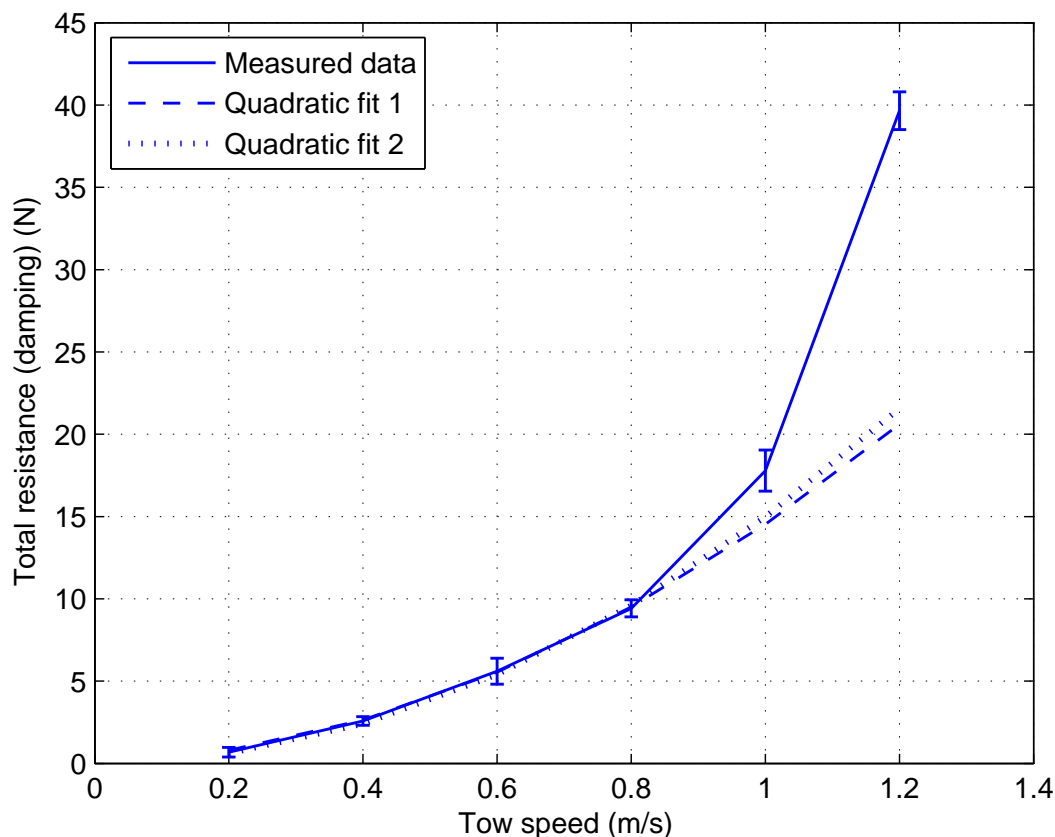
Figure 2.4: Resistance test results. Each data point is calculated as an average of the steady-state towing force subtracted by the zero offset, and it is plotted with standard deviation error bars. The dashed line shows the data fitting result using both quadratic $X_{u|u|}$ and linear X_u damping coefficients, while the dotted line shows the fitted model with only the quadratic damping coefficient $X_{u|u|}$. Note that only the measurements up to 0.8 m/s are employed for model coefficients identification and the others are shown for completeness.

2.3.1.2 Self-propulsion Tests

According to ITTC Recommended Procedure 7.5-02-03-01.1, the measurements of the thrust, torque, revolution rate, vehicle speed through the water and external tow force are required in the self-propulsion experiments. However, since our main goal is to use the collected data from resistance and self-propulsion tests to identify the lumped coefficients of k_1 and k_2 in Eq. 2.18, it is not necessary to determine the thrust deduction factor t_d and the wake fraction w_f. Therefore, the propeller open water tests are not performed and the propeller thrust and torque measurements are not performed. Moreover, the propeller's revolution rate is controlled by the thruster's inner closed-loop controller, so no additional measurement sensor is needed. Finally, we only need to measure the vehicle's moving speed and the external tow force, which is the same configuration as the resistance tests. This series of simplification can help us to save time and cost while carrying out the tow tank experiments.

Prior to performing the self-propulsion tests, the propellers are re-installed on the vehicle. The whole system is ballasted to maintain the same weight and trim as in the resistance tests, and the measuring head is connected to the vehicle at the same location on the aluminum bar. We follow the Load Varying Method (ITTC Recommended Procedure 7.5-02-03-01.1) to run the tests. The tow speed and propeller loading are determined in advance according to the resistance test results and an estimation of the thrust. During the tests, two propellers are commanded to run at the same rate of revolution, and then the tow carriage accelerates from the rest to the designated moving speed. The steady-state moving condition is maintained for 20 to 30 s for all required data logging. Sufficient time is given between the consecutive runs, and we repeat the runs at the same vehicle speed with three different propeller loadings. The self-propulsion test speed range is determined to be from 0.4 m/s to 1.0 m/s with a step of 0.2 m/s. Our experimental results are depicted in Fig. 2.5, and it shows that in all experiments the self-propulsion

condition, i.e. zero external tow force condition, has been included by changing the propeller loadings. The self-propulsion points have been summarized in Table 2.2, based on which, a proportional relationship between one propeller's revolution rate and the vehicle's steady-state moving speed can be established as

$$u_{ss} = 0.0043\Omega_c - 0.016$$
$$\approx 0.0043\Omega_c \tag{2.20}$$

where Ω_c is the commanded revolution rate for both port- and starboard-side propellers, and u_{ss} is the achieved steady-state surge velocity. This simple relationship will be validated by carrying out the field trials.

Table 2.2: A summary of the self-propulsion points

Surge velocity (m/s)	Propeller revolution rate $\Omega_p = \Omega_s = \Omega_c$ (rpm)
0.4	98
0.6	140
0.8	187
1.0	236

2.3.1.3 Bilinear Thruster Model

In the self-propulsion tests, when the vehicle is towed with a constant speed the measured external tow force can be formulated as

$$X_t = -(T_p + T_s + X_{u|u|}u|u| + X_u u)$$
$$= -k_1(\Omega_p^2 + \Omega_s^2) - k_2 u(\Omega_p + \Omega_s) - X_{u|u|}u|u| - X_u u \tag{2.21}$$
$$= \underbrace{-2k_1\Omega_c^2 - 2k_2 u\Omega_c}_{\text{Total thrust force}} \underbrace{- X_{u|u|}u|u| - X_u u}_{\text{Damping}}.$$
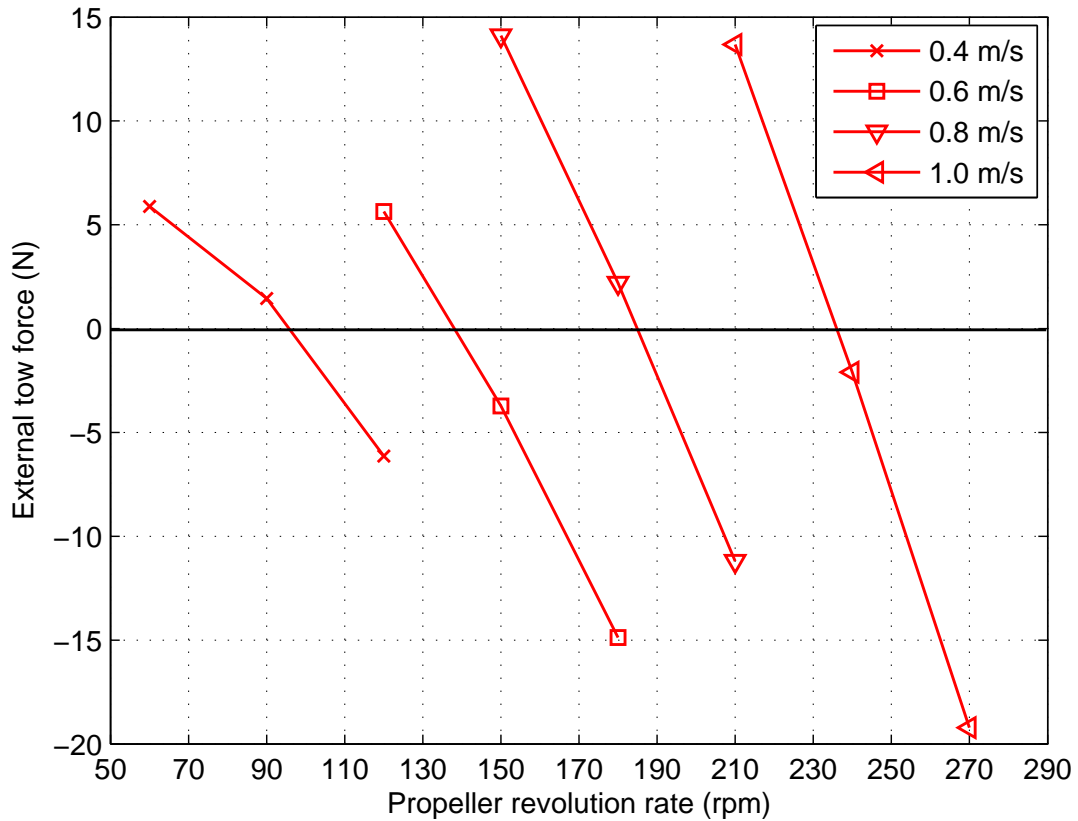
Figure 2.5: Self-propulsion test results. Each data point represents the measured external tow force under the corresponding steady moving speed and propeller loading condition. The test speed range is from 0.4 m/s to 1.0 m/s, and tests performed at the same speed include three different propeller loadings to cover the self-propulsion condition.

In Eq. 2.21, the tow force is directly measured by the dynamometer, the damping force have already been attained from the resistance tests, both propellers' revolution rate is commanded as Ω_c, and tow carriage speed u is recorded. Therefore, the only unknown part is the lumped model coefficients k_1 and k_2. The identification of k_1 and k_2 employs all the self-propulsion experimental data with corresponding resistance test data, and the surface fitting results are shown in Fig. 2.6. The root mean square error (RMSE) has been calculated as 1.78 N, and the identified value of the coefficients are k_1=0.000968 N/rpm^2 and k_2=-0.19425 $kg/(s \cdot rpm)$.
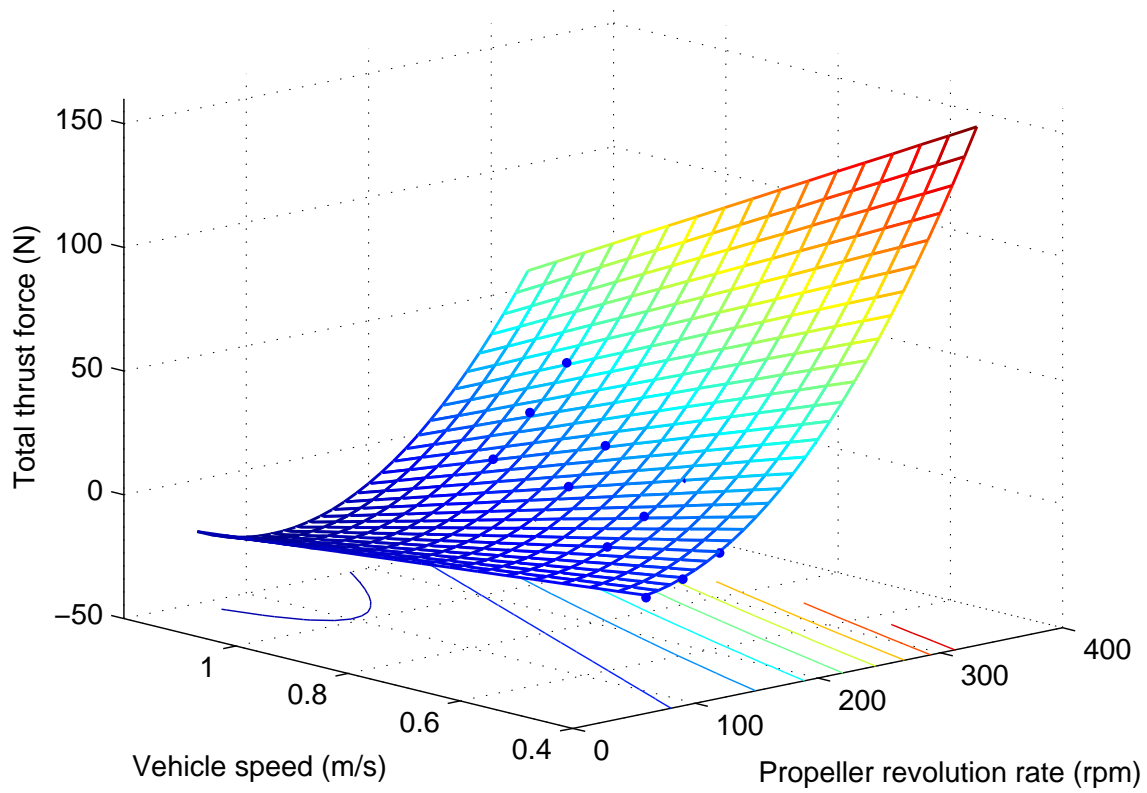
Figure 2.6: Surface fitting results of the total thrust force versus vehicle speed and propeller rate of revolution. The total thrust force from the two propellers are calculated as a subtraction of the measured external tow force and the damping force. The data points corresponds to those from the self-propulsion tests shown in Fig. 2.5.

2.3.2 Field Tests

The field experiments have been performed at Montreal's Pointe Claire Yacht Club during the NSERC Canadian Field Robotics Network (NCFRN) coordinated field trial. To accurately identify the unknown planar motion model parameters, it is required to perform the tests in an ideal weather condition, preferably with no current, waves and wind effect [18]. We managed to complete the required experiments in some calm days with relatively low disturbances. However, it is noteworthy that our tests are still inevitably influenced by the water current, the travelling vessels and the wind gusts, which will cause the

uncertainty of some identified parameter values.

The USV SeaCat's dynamic motion in surge, sway and yaw is measured by its on-board sensors, and these data are post-processed for model parameter identification. The equipped GPS receiver provides the measurements of the vehicle position, course angle to true north and the total velocity at 1 Hz update rate, with the accuracy of 2.5 m[1], 0.5° and 0.1 m/s, respectively. The high-performance AHRS integrates the triaxial accelerometer, gyro and magnetometer to accurately calculate the vehicle's orientation in roll, pitch and yaw in the inertial frame. For the purpose of this research though, only the yaw rate and magnetic heading angle are employed for parameter identification.

The sway motion is not directly measured by the available sensors but can be calculated based on the sideslip angle when the vehicle is steering. For example, when a USV turns at low speed as indicated in Fig. 2.7, the direction of the total velocity $V = \sqrt{u^2 + v^2}$ will differ from that of the surge velocity u. This angle difference is defined as the sideslip angle β, and since the total velocity can be measured by the GPS receiver, the surge and sway speed can be calculated as [9]

$$
\begin{aligned}
u &= V \cos(\beta) \\
v &= V \sin(\beta)
\end{aligned}
\tag{2.22}
$$

where β is given as

$$
\beta = \chi - \psi.
\tag{2.23}
$$

Note that in Eq. 2.23, χ and ψ define the vehicle's course and yaw angle, respectively, and these angles are measured with respect to true north. The course angle is readily available from the GPS measurement, and the yaw angle can be calculated as

$$
\psi = \psi_M + \psi_D
$$

[1]The position accuracy is evaluated using circular error probable (CEP), 50%.

where ψ_M is the magnetic heading angle measured by the AHRS and ψ_D defines the local magnetic declination angle and has been determined as -14.524°.
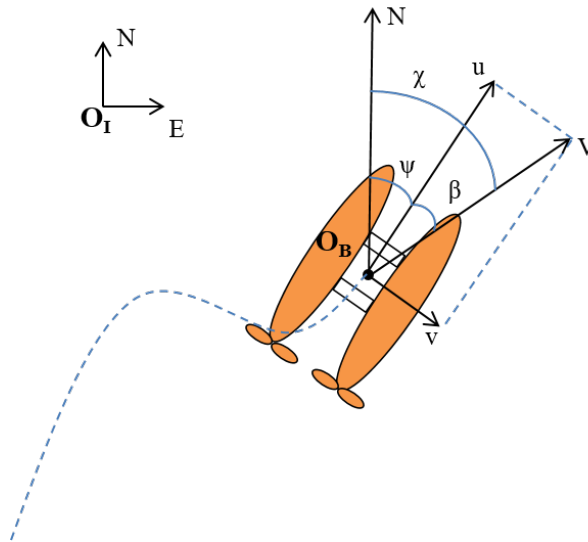
Figure 2.7: The definition of the sideslip angle when the vehicle performs a turning at low speeds. Note that O_I and O_B denote the origin of the inertial and body frame, respectively.

Preliminary experiments have demonstrated the slow dynamics of the studied USV in its surge, sway and yaw motion, and we find out that it normally takes above 10 *s* for the vehicle to accelerate to a specific steady-state condition. Thus, the installed sensor configuration and its sampling rate is sufficient for identifying the model parameters. Further, considering the investigated surge and steering motion models in Eq. 2.13 and Eq. 2.14 are of first-order type, to identify the model parameters we can simply apply the step inputs while performing the straight-line and turning circle tests. There are many techniques available for parameter identification, and here we will implement the benchmark least-squares (LS) method. In the following, we will first provide a general overview of the LS method, and then detailed procedures for performing the field tests are introduced. Although our experiments are frequently interrupted by the traffic in the docking area in the yacht club, we are able to perform some zigzag tests. The fidelity of

the identified planar motion model is validated using the collected zigzag data.

2.3.2.1 Least-Squares Method

The least-squares method (LS) has been widely used for parameter identification in the field of marine robotics [9, 23, 18, 24, 41], and it provides a benchmark for evaluation of other identification techniques, such as adaptive identification [27]. In this research, the surge and steering motion model in Eq. 2.13 and Eq. 2.14 can be rewritten as

$$\dot{u} = A_{11}u|u| + A_{12}u + A_{13}X_p$$
$$\dot{v} = A_{21}v|v| + A_{22}v + A_{23}ur \tag{2.24}$$
$$\dot{r} = A_{31}r|r| + A_{32}r + A_{33}N_p$$

where the coefficients of A_{11} to A_{33} are unknown lumped model parameters, which are written as

$$
\begin{aligned}
A_{11} &= \frac{X_{u|u|}}{m - X_{\dot{u}}} & A_{12} &= \frac{X_u}{m - X_{\dot{u}}} & A_{13} &= \frac{1}{m - X_{\dot{u}}} \\
A_{21} &= \frac{Y_{v|v|}}{m - Y_{\dot{v}}} & A_{22} &= \frac{Y_v}{m - Y_{\dot{v}}} & A_{23} &= -\frac{m - X_{\dot{u}}}{m - Y_{\dot{v}}} \\
A_{31} &= \frac{N_{r|r|}}{I_{zz} - N_{\dot{r}}} & A_{32} &= \frac{N_r}{I_{zz} - N_{\dot{r}}} & A_{33} &= \frac{1}{I_{zz} - N_{\dot{r}}}
\end{aligned}
\tag{2.25}
$$

Note that in order to get the lumped model of Eq. 2.24, $m - X_{\dot{u}}$, $m - Y_{\dot{v}}$ and $I_z - N_{\dot{r}} \neq 0$, which is valid since the mass and moment of inertia of the vehicle is positive and the added mass terms $X_{\dot{u}}$, $Y_{\dot{v}}$ and $N_{\dot{r}} < 0$. As shown in Eq. 2.24, the motion model in each degree of freedom is of similar form, and thus a generalized model structure can be achieved as

$$\dot{x}_i = A_{j1}f(x_i) + A_{j2}x_i + A_{j3}u_i \ (j = 1, 2, 3) \tag{2.26}$$

where $x_i \in \Re^{1,1}$ and $\dot{x}_i \in \Re^{1,1}$ represent the state variable of surge, sway and yaw and their time derivative measured at time $t = i$, $f() \in \Re^{1,1}$ is a nonlinear function and

$u_i \in \Re^{1,1}$ is the control input. We can write down the unknown model parameters in the vector form of $\Phi=[A_{j1} \ A_{j2} \ A_{j3}] \in \Re^{1,3}$, which needs to be identified. Assuming that the investigated model is linear and time-invariant in terms of its model parameters, a least-squares fitting can be carried out. Sufficient data of the state variables and control inputs can be measured during the experiments, and they are summarized in vector and matrix form as

$$X_v = [x_i \ x_{i+1} \ ... \ x_{i+n}]$$

and

$$F(X_v) = \begin{bmatrix} f(x_i) & f(x_{i+1}) & ... & f(x_{i+n}) \\ x_i & x_{i+1} & ... & x_{i+n} \\ u_i & u_{i+1} & ... & u_{i+n} \end{bmatrix}.$$

Therefore, a lumped form representation of Eq. 2.26 including all sensor measurements and control input history is given as

$$\dot{X}_v = \Phi F(X_v).$$

If $F(X_v)$ is full rank, an estimation of the unknown parameters are calculated by

$$\hat{\Phi} = \dot{X}_v F(X_v)^T (F(X_v)F(X_v)^T)^{-1}.$$

The implemented LS method requires the value of the state derivatives $\dot{X}_v$, which is not directly measured during the field trials. Hence, a Savitsky-Golay filter [9] [42] is employed for smoothing the data before the differentiation of the measured data to get $\dot{X}_v$. The percentile parameter error $100(\hat{\sigma}_\Phi/|\hat{\Phi}|)$ [23] can be calculated to evaluate the quality of the identified parameters. Note that $\hat{\sigma}_\Phi$ denotes the standard deviation of $\hat{\Phi}$

and it can be calculated as

$$\hat{\sigma}_\Phi = \sqrt{diag((\Phi^T\Phi)^{-1}\sigma_\epsilon^2)}$$

where σ_ϵ^2 denotes the variance of measurement noise that can be estimated by

$$\hat{\sigma}_\epsilon^2 = \frac{(\dot{X}_v - \hat{\Phi}F(X_v))(\dot{X}_v - \hat{\Phi}F(X_v))^T}{dim(\dot{X}_v) - dim(\hat{\Phi})}.$$

2.3.2.2 Straight-line Tests

We refer to the self-propulsion points in Table 2.2 as well as the identified proportional relationship in Eq. 2.20 to determine the propeller setting profiles in the straight-line tests. The experimental speed range is from 0.4 m/s to 1.0 m/s with a step of 0.1 m/s, and the propeller revolution rate $\Omega_p = \Omega_s = \Omega_c$ is commanded from the list $\underline{\Omega_{ls}} = [98, 122, 140, 166, 187, 216, 236]$ rpm. In the preliminary tests, it is found that the open loop step input can not drive the vehicle along the straight line owing to environmental disturbances and the asymmetry of manufactured hulls. Therefore, a PI heading controller has been developed and integrated to introduce the differential rotational speed $\Delta\Omega$ for the two propellers as

$$\begin{aligned} \Omega_p &= \Omega_c + \Delta\Omega \\ \Omega_s &= \Omega_c - \Delta\Omega \end{aligned} \tag{2.27}$$

Note that in Eq. 2.27, $\Delta\Omega$ can be either positive or negative depending on the required steering direction, and it is the output from the PI heading controller. When there is a large difference between the actual and reference heading angle, $\Delta\Omega$ can be potentially a large value. To eliminate this aggressive steering control, we artificially apply a limit to guarantee that $\Delta\Omega \in [-25, 25]$ rpm. The introduction of $\Delta\Omega$ will vary the total thrust force from the propellers and we examine this according to Eq. 2.18 and Eq. 2.19, and

the difference of the applied thruster forces can be calculated as

$$\Delta X_p = X_p|_{\Omega_p = \Omega_s = \Omega_c} - X_p|_{\Omega_p = \Omega_c + \Delta\Omega, \, \Omega_s = \Omega_c - \Delta\Omega}$$

$$= 2k_1 \Delta\Omega^2$$

where k_1=0.000968 N/rpm^2, so $\Delta X_p <= 1.21$ N. It can be concluded that with the differential setting the propulsion system will provide less thrust force. However, since this force difference is relatively small and will only occur during the vehicle's steering motion, its effect can be neglected in the identification process. Further, it is validated that during each test the sway speed and turn rate is small, and thus we can perform the parameter identification using the decoupled surge motion model in Eq. 2.13.

The straight-line tests are performed in a calm day with relatively low environmental disturbances. We choose the value of Ω_c from $\underline{\Omega}_{ls}$ and carry out the tests one after another. Since the vehicle moves along the straight path, the measured speed from the GPS can be regarded as the surge velocity, using which the surge acceleration can also be calculated in the post-processing.

The least-squares method from section 2.3.2.1 has been employed for identification of the surge model parameters, and the identification results are summarized in Table 2.3. It is noteworthy that our initial identification is based on the quadratic plus linear damping model, but the results show an inconsistent identification of the value for $A_{12} = \frac{X_u}{m - X_{\dot{u}}}$. This phenomenon is due to the small linear damping coefficient X_u, which has been analytically determined in the resistance tests of section 2.3.1.1 with a value of around 10% of $X_{u|u|}$. For identification consistency, only the quadratic drag is included and identified. This is a viable solution, because as shown in Fig. 2.4 the simulation of the damping models with and without the linear laminar drag actually shows a close performance.

In Table 2.3, the steady-state velocity is calculated as the average of the tabulated

Table 2.3: A summary of the identified surge model parameters for different acceleration processes

Steady-state velocity (m/s)	$\hat{A}_{11}$ (m^{-1})	$\hat{A}_{13}$ (kg^{-1})	$100\frac{\hat{\sigma}_{A_{11}}}{|\hat{A}_{11}|}$	$100\frac{\hat{\sigma}_{A_{13}}}{|\hat{A}_{13}|}$	RMSE (m/s)	$X_{u|u|} \approx \frac{\hat{A}_{11}}{\hat{A}_{13}}$ (kg/m)
0.40	-0.1035	0.0047	5.39	4.34	0.007	-22.02
0.51	-0.0704	0.0035	5.23	3.55	0.007	-20.11
0.60	-0.0453	0.0026	4.74	2.88	0.009	-17.42
0.71	-0.0553	0.0034	2.64	1.91	0.010	-16.26
0.80	-0.0568	0.0036	3.36	2.30	0.019	-15.78
0.92	-0.0564	0.0035	2.34	1.79	0.017	-16.11
1.00	-0.0440	0.0026	2.86	2.02	0.021	-16.92

velocity after 15 s in each acceleration process, and these measurements validate the accuracy of the achieved self-propulsion points from the tow tank tests. In addition, the percentile error of the estimated parameters $\hat{A}_{11}$ and $\hat{A}_{13}$ shows a good consistency and accuracy. The root mean square error (RMSE) has been calculated to measure the difference between the surge model and the actual observed values, and the small values indicate the fidelity of the identified model. It is evident that except for the first two rows, the estimated value of $X_{u|u|}$ from the open water tests is very close to that of the tow tank tests in section 2.3.1.1 considering the sensor measurement errors and unexpected environmental influences. As for the first two rows, a probable reason for the notable difference is that while the vehicle moves with low speeds it is easily influenced by the steering motion from the PI controller and environmental disturbances. We have shown the simulation results of four identified models in Fig. 2.8, and through comparison to the measured speed, it can be concluded that our identified motion models can approximate the observed surge motion reasonably well.

Using the identified parameter values from Table 2.3, a speed-scheduled motion model is normally established [9]. However, in this research, based on our experimental results, we are able to generate a generic surge motion model that is more convenient to be used for

simulation study and guidance and control algorithm development. As shown in the table, the independently identified parameter values are quite close to each other, especially for the steady speed range from 0.7 m/s to 0.9 m/s. Since the operation speed of the USV SeaCat is normally above 0.5 m/s, we determine to use an average of the identified values of $\hat{A}_{11}$ and $\hat{A}_{13}$ in this speed range, i.e. $\overline{\hat{A}_{11}} = -0.0562 \; m^{-1}$ and $\overline{\hat{A}_{13}} = 0.0035 \; kg^{-1}$, for the generic surge model. The performance of the generic model has been investigated, and the simulation results are depicted in Fig. 2.9. It shows that the generic model has a relatively good fidelity with regards to the sampled surge speed data when the vehicle's steady-state speed is above 0.5 m/s as expected.
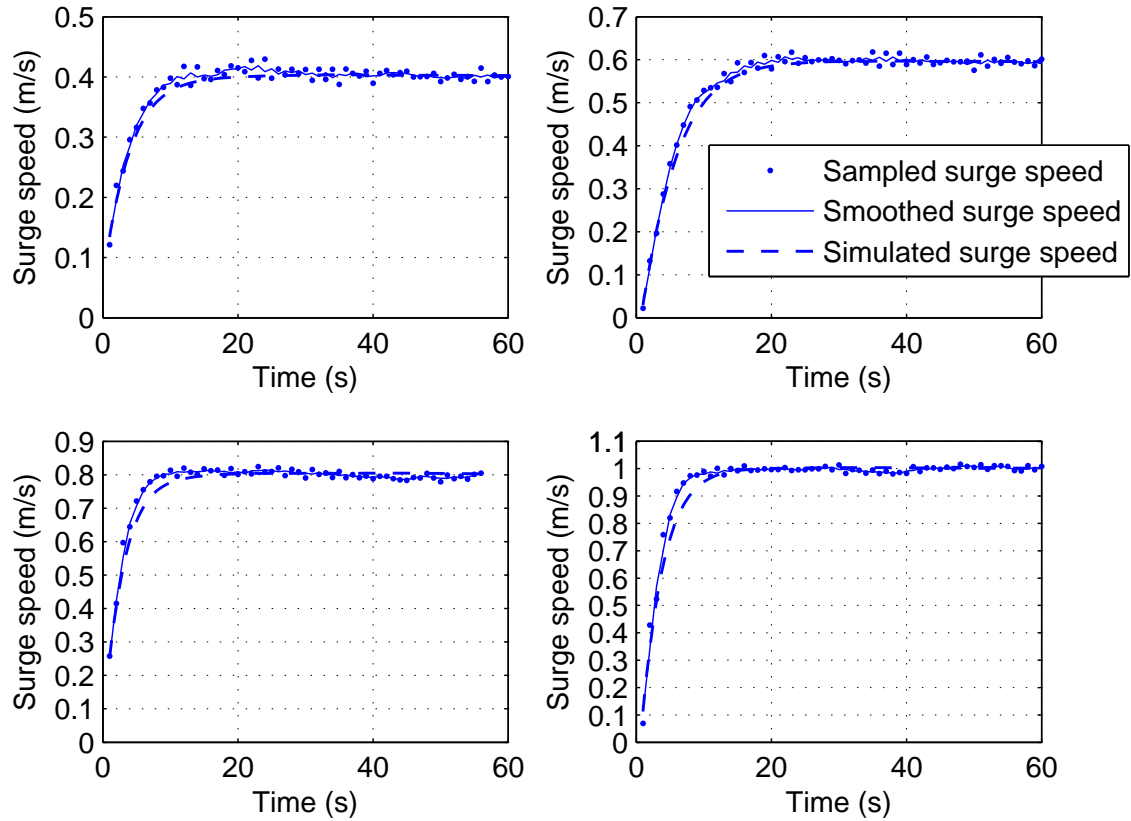
Figure 2.8: The evaluation of the identified surge motion models for the acceleration processes to 0.4 m/s, 0.6 m/s, 0.8 m/s and 1.0 m/s. The performed simulation employs different model parameter values as indicated in the corresponding row of Table 2.3.
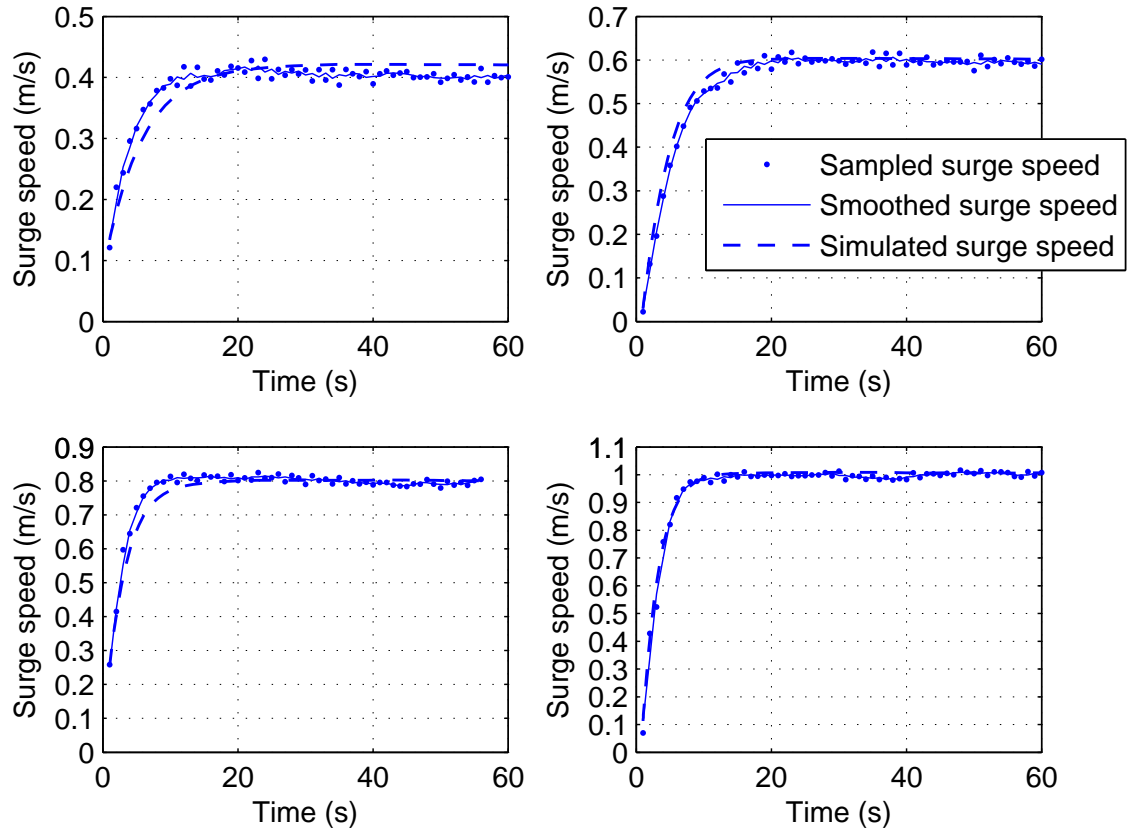
Figure 2.9: The evaluation of the generic surge model for the acceleration processes to 0.4 m/s, 0.6 m/s, 0.8 m/s and 1.0 m/s. Every simulation employs the same model parameter values with $\widehat{A}_{11} = -0.0562\ m^{-1}$ and $\widehat{A}_{13} = 0.0035\ kg^{-1}$.

2.3.2.3   Turning Circle Tests

Through the initial tests, it is found that the vehicle has an evident difference between its port- and starboard-side turning dynamics. This may be a result of the asymmetry of the manufactured hulls, the non-ideal ballast condition and the minor difference of the two thrusters. Therefore, in order to build a complete steering motion model, we need to perform both clockwise (starboard-side) and counter-clockwise (port-side) turning circle tests with step inputs. The identified port- and starboard-side steering model can be combined together for simulation and control algorithm design purposes.

The turning circle tests are performed without incorporating any speed or heading control algorithms. The two propellers are just set at a constant revolution rate following Eq. 2.27, and we wait for the vehicle to accelerate and turn until it completes a couple of full circles. The differential propeller setting is maintained the same as $|\Delta\Omega|$=50 *rpm* through all the tests, and Ω_c is chosen from the list $\underline{\Omega_{lc}}$=[100 142 186 238] *rpm*. During the tests, sufficient sensor data including total velocity, course angle, magnetic heading angle and turn rate are recorded.

To identify the steering motion model parameters in Eq. 2.24, we need to postprocess the collected data. We employ Eq. 2.22 and Eq. 2.23 to get the surge and sway speed during the vehicle's turning. Using the calculated sway speed and measured yaw rate, their time derivative can be computed. The steering torque N_p is calculated following Eq. 2.19. Now, the least-squares fitting technique can be carried out to identify the unknown parameters from A_{21} to A_{33}, and these results are summarized in Table 2.4 and Table 2.5, respectively. Again, for identification consistency, only the quadratic damping related terms of A_{21} and A_{31} are kept in the sway and yaw motion model.

We analyse the sway model parameter identification results in Table 2.4. According to Eq. 2.27, since Ω_c is positive, when $2\Delta\Omega \cdot \Omega_c$>0 the USV undergoes a starboard-side turning, otherwise it is turning to the port-side. The two columns of the computed percentile error represent a relatively high uncertainty of the identified parameters. A probable reason is that the sway motion of the vehicle is quite small, and it is potentially influenced by environmental disturbances. The calculated RMSE is small, but it is due to the small sway velocity. The last column of the identified quadratic damping coefficient $X_{v|v|}$ clearly indicates that the studied USV has quite different damping characteristics between its port- and starboard-side turning. Four models from Table 2.4 (two clockwise and two counter-clockwise) have been chosen and their simulation results are depicted in Fig. 2.10. Through checking the actual measured sway speed, we can determine that the

vehicle is affected by the constant environmental disturbances, and this is the reason that the sway speed oscillates around a roughly constant value. Although there are adverse factors that reduce the identification accuracy, through comparison of the actual and simulated sway motion in the figure, we can conclude that our identified models still provide a reasonably good representation of the sway motion dynamics. In particular, if we only refer to the port-side (or starboard-side) turning case, the identified damping values $X_{v|v|}$ are close through different turning scenarios. However, owing to the different identified parameter values of $\hat{A}_{21}$ and $\hat{A}_{23}$, we have to implement a speed-scheduled sway motion model to perform simulation studies in the later discussion.

Table 2.4: A summary of the identified sway model parameters for different turning circle tests

$2\Delta\Omega \cdot \Omega_c$ (rpm^2)	$\hat{A}_{21}$ (m^{-1})	$\hat{A}_{23}$ (rad^{-1})	$100\frac{\hat{\sigma}_{A_{21}}}{|\hat{A}_{21}|}$	$100\frac{\hat{\sigma}_{A_{23}}}{|\hat{A}_{23}|}$	RMSE (m/s)	$X_{v|v|} \approx \frac{\hat{A}_{21}}{\hat{A}_{23}}$ (kg/m)
10000	-0.5472	-0.4654	15.39	14.95	0.026	1.18
14200	-0.2680	-0.2881	27.11	27.08	0.038	0.93
18600	-0.6025	-0.4784	12.57	12.36	0.019	1.26
23800	-0.7038	-0.4373	12.44	12.49	0.025	1.61
-10000	-0.9415	-0.2343	23.35	22.87	0.018	16.11
-14200	-0.7854	-0.1113	28.32	28.70	0.019	16.92
-18600	-1.5176	-0.2940	19.59	20.84	0.025	16.26
-23800	-1.0886	-0.0704	26.61	49.49	0.038	15.78

According to Table 2.5, we can discuss about the yaw motion model identification results. Based on the percentile errors, we can summarize that the performed identification is reliable and accurate. The calculated RMSE through the evaluation tests has really low values, and it represents the accuracy of the identified models. Again, the last column, where the yaw quadratic damping coefficient $X_{r|r|}$ is computed, suggests the different yaw dynamics for the port- and starboard-side turning. It is also noteworthy that for the maximum propeller settings in clockwise and counter-clockwise cases, i.e. the rows of $\pm 23800\ rpm^2$, the calculated $X_{r|r|}$ stands out from the others. This phenomenon
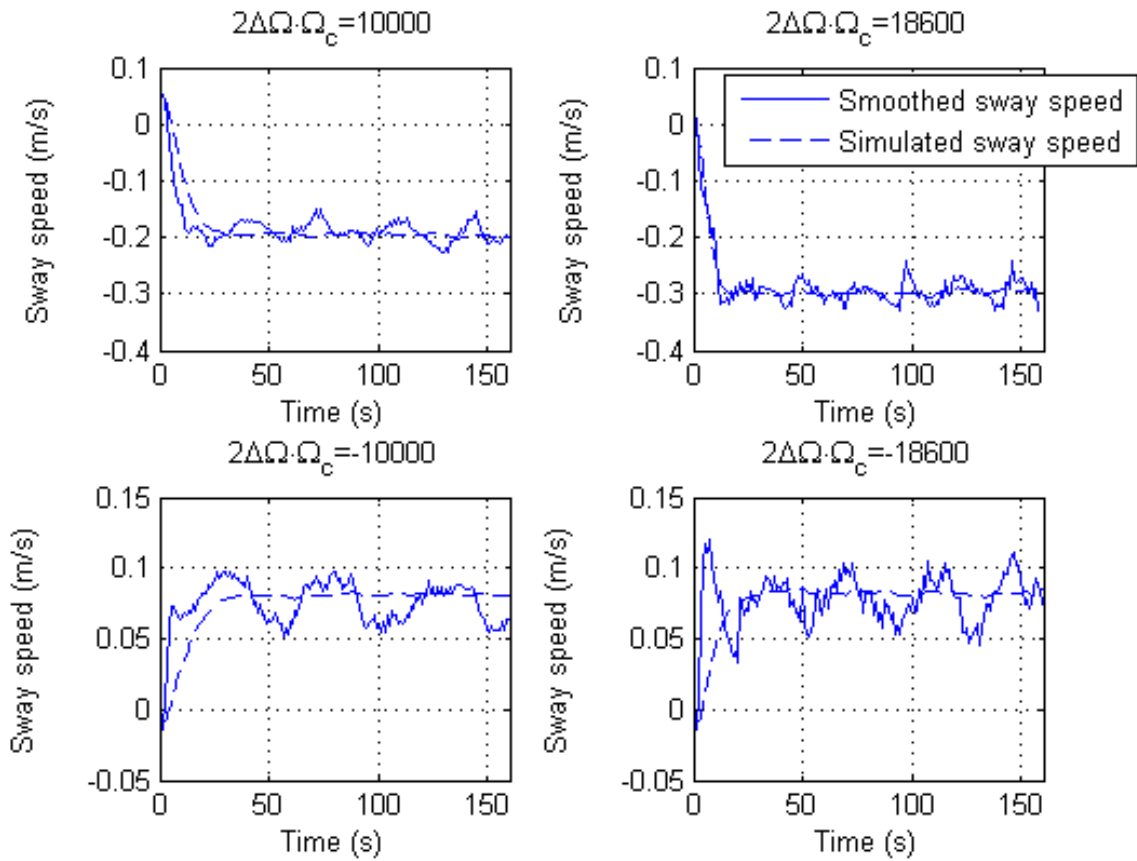
Figure 2.10: The evaluation of the identified sway motion models for clockwise and counter-clockwise turning scenarios, i.e. $2\Delta\Omega\cdot\Omega_c$=10000, 18600, -10000 and -18600 rpm^2. The depicted simulation results employ the model parameter values in the corresponding row of Table 2.4.

has actually been observed for large marine vessels [20], and it may indicate that the yaw motion dynamics enter the nonlinear area with the increment of the steering torque. Four evaluation results (two clockwise and two counter-clockwise) are picked and shown in Fig. 2.11. Although our collected data are potentially influenced by environmental disturbances, the identified yaw motion model performs reasonably well in representing the yaw dynamics.

A generic yaw motion model can be achieved based on our identification results in Table 2.5. For clockwise turning, we propose to use the average of the first three rows to

calculate the average of $\overline{\hat{A}_{31,cw}} = -1.387\ rad^{-1}$ and $\overline{\hat{A}_{33,cw}} = 0.003\ rad \cdot kg^{-1} \cdot m^{-2}$. In terms of the counter-clockwise turning, the fifth, sixth and seventh rows are used, and thus $\overline{\hat{A}_{31,ccw}} = -2.5959\ rad^{-1}$ and $\overline{\hat{A}_{33,ccw}} = 0.0021\ rad \cdot kg^{-1} \cdot m^{-2}$. The evaluation of the generic model is performed and the results are shown in Fig. 2.12. It turns out that the two generic models work well when $|2\Delta\Omega \cdot \Omega_c| <= 18600\ rpm^2$.

Table 2.5: A summary of the identified yaw model parameters for different turning circle tests

$2\Delta\Omega \cdot \Omega_c$ (rpm^2)	$\hat{A}_{31}$ (rad^{-1})	$\hat{A}_{33}$ $(rad \cdot kg^{-1} \cdot m^{-2})$	$100\frac{\hat{\sigma}_{A_{31}}}{|\hat{A}_{31}|}$	$100\frac{\hat{\sigma}_{A_{33}}}{|\hat{A}_{33}|}$	RMSE (rad/s)	$X_{r|r|} \approx \frac{\hat{A}_{31}}{\hat{A}_{33}}$ $(kg \cdot m^2 \cdot rad^{-2})$
10000	-2.0729	0.0044	6.36	6.23	0.0042	-476.04
14200	-1.1277	0.0025	9.30	9.08	0.0063	-449.17
18600	-0.9604	0.0021	11.27	11.12	0.0052	-462.97
23800	-1.2715	0.0020	7.42	7.31	0.0070	-634.01
-10000	-2.8859	0.0024	12.88	12.82	0.0046	-1221.1
-14200	-2.5340	0.0021	9.04	8.92	0.0055	-1225.1
-18600	-2.3677	0.0018	10.76	10.63	0.0051	-1314.4
-23800	-2.6540	0.0010	12.74	12.75	0.0071	-2631.8

The surge dynamics during the USV's steering can be different from the straight-line moving case, and thus we need to re-examine if the originally determined surge model is still applicable. Through investigation, we find that our identified generic surge motion model from section 2.3.2.2 works well while the vehicle undergoes a clockwise turning, but for the counter-clockwise turning, the surge dynamics is quite different. Therefore, we need to identify the surge motion model parameters to take into account the counter-clockwise situation. Following the procedures in section 2.3.2.2, the generic surge motion model parameters in clockwise turning is the same as $\overline{\hat{A}_{11,cw}} = -0.0562$ m^{-1} and $\overline{\hat{A}_{13,cw}} = 0.0035\ kg^{-1}$, while for the counter-clockwise case they are given as $\overline{\hat{A}_{11,ccw}} = -0.0657\ m^{-1}$ and $\overline{\hat{A}_{13,ccw}} = 0.00255\ kg^{-1}$.
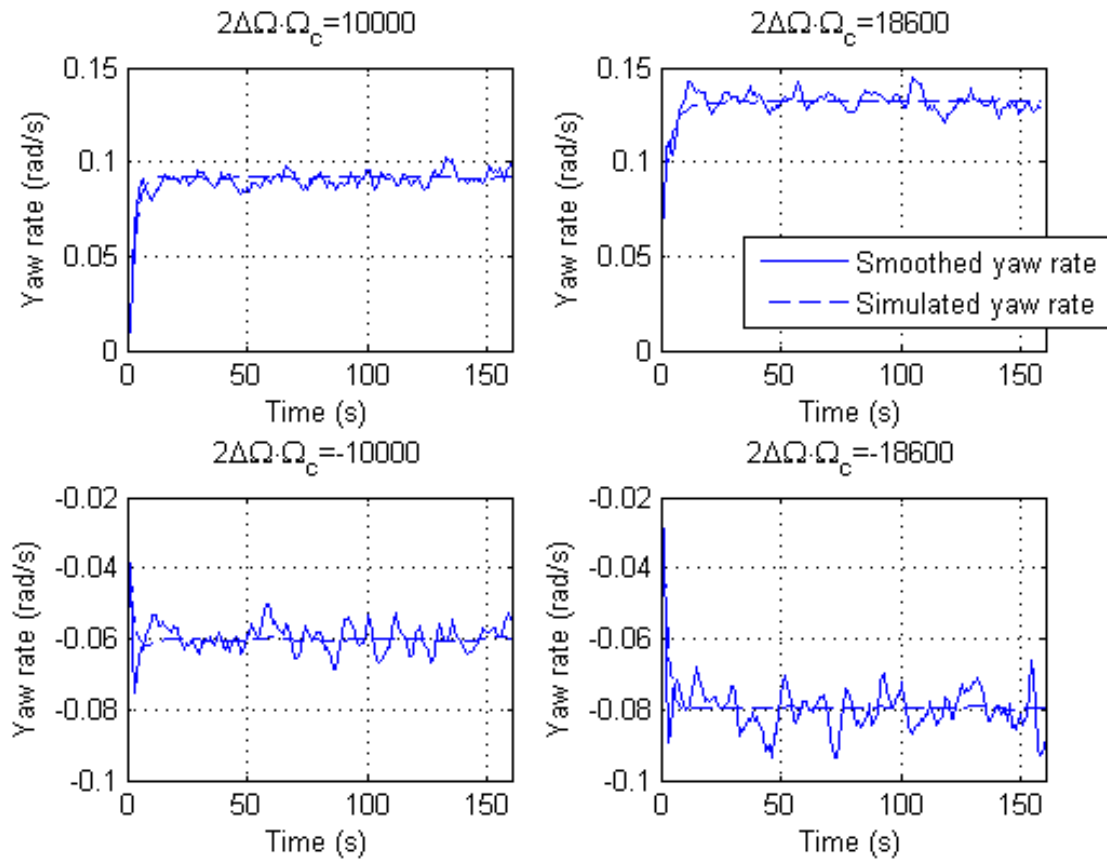
Figure 2.11: The evaluation of the identified yaw motion models for clockwise and counter-clockwise turning, i.e. $2\Delta\Omega \cdot \Omega_c$=10000, 18600, -10000 and -18600 rpm^2. The depicted simulation results employ the model parameter values as indicated in the corresponding row of Table 2.5.

2.3.2.4   Zigzag Evaluation Experiments

Based on the parameter identification results, we can construct the USV SeaCat's planar motion model in the simulation environments of Matlab/Simulink for evaluation tests and further guidance and control algorithms development. A summary of the identified parameter values in surge, sway and yaw depending on the vehicle moving conditions has been summarized in Table 2.6. Note that for surge and yaw motion, we have the option to use the generic model parameter values without much sacrifice of the model's performance, and this will bring considerable convenience when we build the Simulink
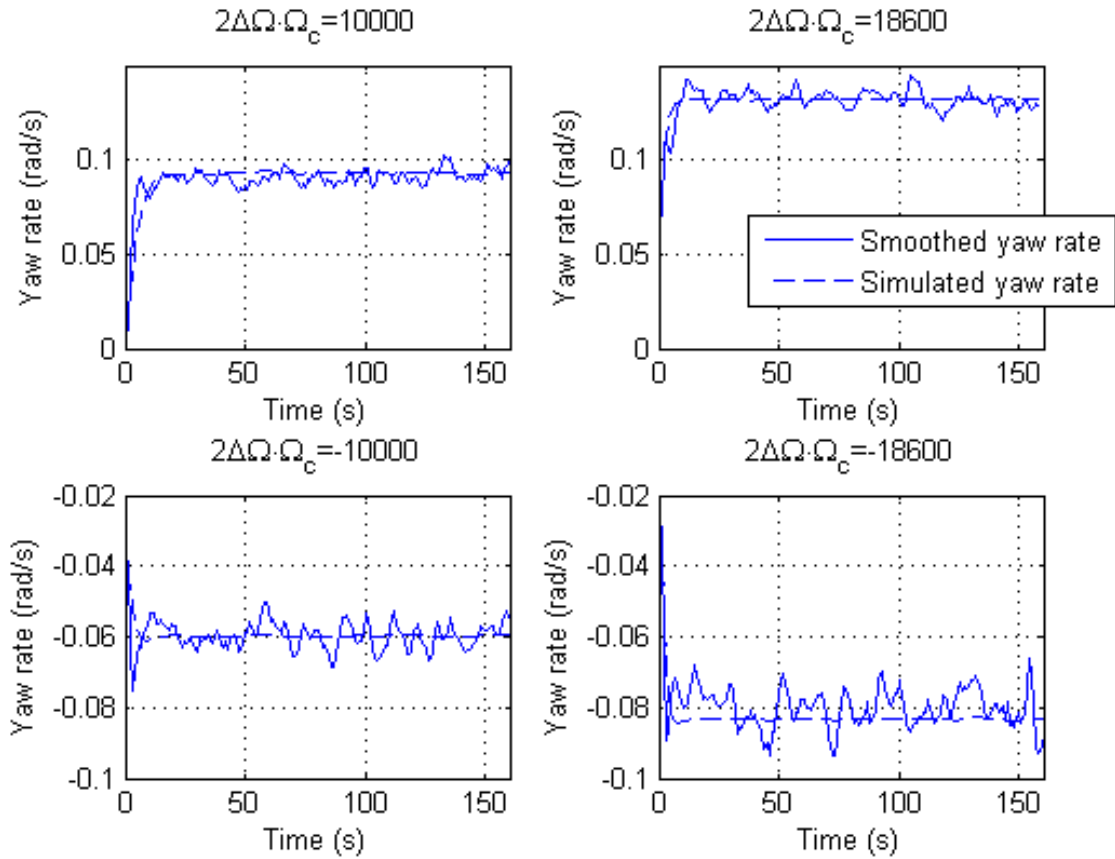
Figure 2.12: The evaluation of the generic yaw motion model for clockwise and counter-clockwise turning, i.e. $2\Delta\Omega \cdot \Omega_c$=10000, 18600, -10000 and -18600 rpm^2. The two clockwise turning simulations employ the same parameter values of $\overline{\hat{A}_{31,cw}} = -1.387\ rad^{-1}$ and $\overline{\hat{A}_{33,cw}} = 0.003\ rad \cdot kg^{-1} \cdot m^{-2}$, and the two counter-clockwise turning simulations use the same parameter values of $\overline{\hat{A}_{31,ccw}} = -2.5959\ rad^{-1}$ and $\overline{\hat{A}_{33,ccw}} = 0.0021\ rad \cdot kg^{-1} \cdot m^{-2}$.

model and develop the control algorithm. In terms of the sway motion, however, we need to construct a speed-scheduled model. In the following chapters, we will demonstrate how we can tune the low-level controllers and carry out different path-following control algorithm tests using the constructed Simulink planar motion model, and we will show its close performance to the real-world trails.

Finally, the zigzag experiments are performed and the collected data are used for evaluation of the identified planar motion model as a whole. A conventional zigzag test is

Table 2.6: A summary of the planar motion model parameter values

Motion	Straight-line	Clockwise turning	Counter-clockwise turning
Surge	$\overline{\hat{A}_{11}} = -0.0562 \ m^{-1}$ $\overline{\hat{A}_{13}} = 0.0035 \ kg^{-1}$ or Table 2.3	$\overline{\hat{A}_{11,cw}} = -0.0562 \ m^{-1}$ $\overline{\hat{A}_{13,cw}} = 0.0035 \ kg^{-1}$	$\overline{\hat{A}_{11,ccw}} = -0.0657 \ m^{-1}$ $\overline{\hat{A}_{13,ccw}} = 0.00255 \ kg^{-1}$
Sway	$\overline{\hat{A}_{21}} = \overline{\hat{A}_{23}} = 0$	Table 2.4	Table 2.4
Yaw	$\overline{\hat{A}_{31}} = \overline{\hat{A}_{33}} = 0$	$\overline{\hat{A}_{31,cw}} = -1.387 \ rad^{-1}$ $\overline{\hat{A}_{33,cw}} = 0.003 \ rad\cdot$ $kg^{-1} \cdot m^{-2}$ or Table 2.5	$\overline{\hat{A}_{31,ccw}} = -2.5959 \ rad^{-1}$ $\overline{\hat{A}_{33,ccw}} = 0.0021 \ rad\cdot$ $kg^{-1} \cdot m^{-2}$ or Table 2.5

carried out for large marine vessels to examine their manoeuvrability, and in a traditional setting the rudder deflection angles will be changed between positive and negative values so that the vehicle will have this zigzag motion. In this study, however, we steer the USV SeaCat by applying differential thrust from the two stern propellers. During the tests, we set $\Delta\Omega$ to vary between $\pm 50 \ rpm$, and Ω_c is kept as a constant value of 142 rpm. Using Eq. 2.27, Ω_p and Ω_s can be calculated and their time history has been shown in the first plot of Fig. 2.13. The zigzag tests involve the vehicle's motion dynamics in surge, sway and yaw, and thus it serves as a good candidate for evaluation of the identified planar motion model. The evaluation is based on our constructed Simulink model (Table 2.6), where the generic models for surge and yaw motion are used and the sway motion model implements the tabulated parameter values from Table 2.4.

As shown in the second and fourth graph of Fig. 2.13, the identified generic surge and yaw motion model has a reasonably good fit to the actual observed motion data. Due to the imperfection of the manufactured hulls and the small difference of the thrusters, the surge speed value will vary between the clockwise and counter-clockwise turning as shown in the second graph. However, the implemented surge model can fully capture this difference with really small errors. The yaw motion model, on the other hand, shows a

promising performance for the steady-state conditions considering the different damping characteristics during clockwise and counter-clockwise steering motion. Nevertheless, the simulated yaw model lags the actual measured sensor data. This phenomenon is owing to the usage of a simplified decoupled yaw motion model that only includes the quadratic damping term. In order to improve the performance, a higher-order coupled yaw motion model structure can be implemented, but the increased complexity will make it difficult for model parameter identification and the further investigation of different control algorithms. Therefore, considering the benefits of a simple model and its relatively good performance for matching the steady yaw rate, this generic yaw model will be employed for further discussion.

The evaluation of the sway motion has been depicted in the third graph of Fig. 2.13, and it indicates that the identified model is considerably lagging the observed sway velocity, and this will result in a relatively large mismatch during the transition period. If we consider the simplified sway motion model structure, the small sway movement compared to unexpected environmental disturbances and the high uncertainty of the identified parameter values, the simulation results are understandable. Although there is an evident defect of the identified sway motion model, it will not affect our further investigation of different guidance and control algorithms. It is important to note that the studied USV SeaCat is underactuated, and there is no direct control inputs for the sway motion according to Eq. 2.24. Therefore, our low-level controllers will be designed around the surge and yaw motion, and the sway movement of the vehicle can be taken into account by the proper guidance strategy. Meanwhile, although not very accurate, the integrated Simulink sway motion model is a necessary part for the vehicle's planar motion dynamics and it is of great importance for determination of the vehicle's location in the inertial frame. Without the sway model, it is not able for us to examine the performance of the developed guidance and control strategy. We also want to point out that the environ-

mental factors of wind, wave and water current can play an important role in varying the sway motion of the vehicle because it is not controllable, so a sway model with relatively high uncertainty can potentially represent these adverse conditions.
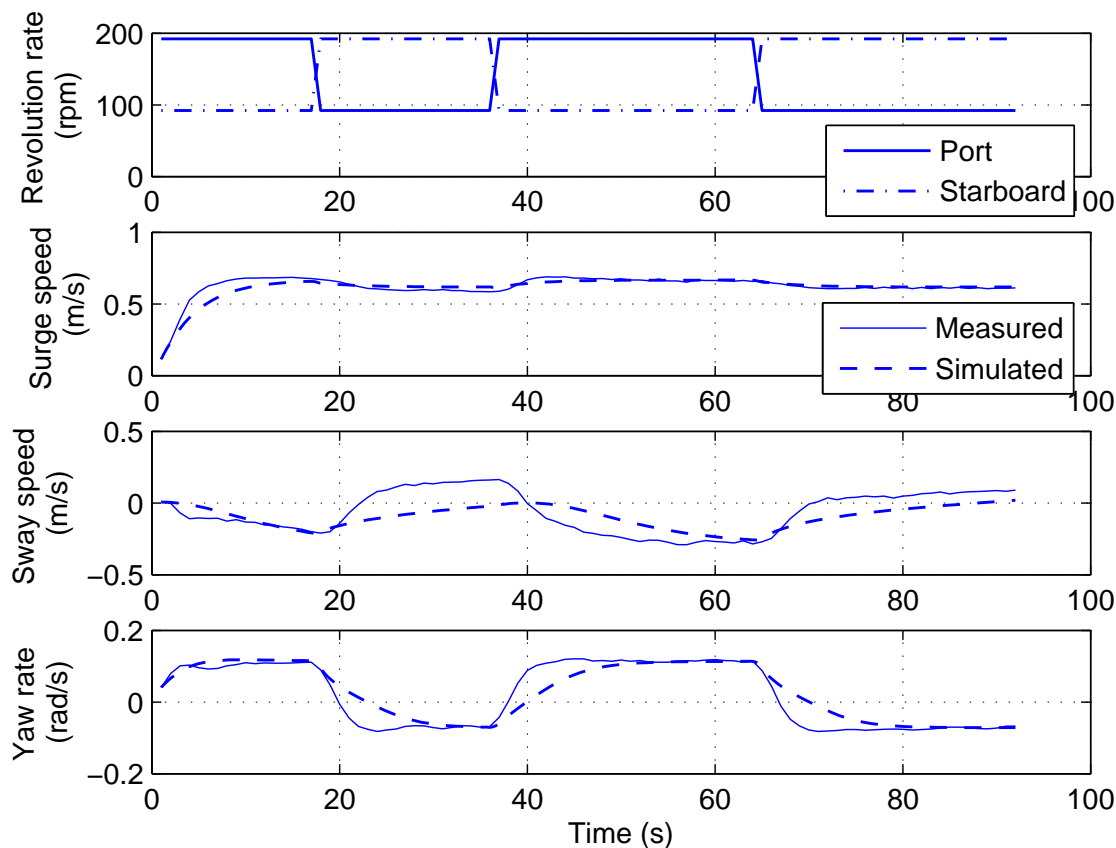
Figure 2.13: Zig-zag experimental data collected from the field trials are used for evaluation of the identified planar motion model as a whole.

2.4 General Chapter Summary

In this chapter, a planar motion model of the USV SeaCat was derived from the general 6 DOF rigid-body motion equations. The achieved model was in a concise form, and it could be conveniently employed for parameter identification. To identify the model parameters,

a hybrid method that combined the standardized tow tank tests and the onboard sensor-based identification routine had been implemented. Based on the tank tests, we had successfully identified the surge damping coefficients and a precise bilinear thruster model. Extensive field experiments were carried out to collect the motion data for identification of the remaining unknown model parameters. We employed the step inputs for straight-line and turning circle tests (clockwise and counter-clockwise), and using the gathered data the surge, sway and yaw motion model parameters were successfully determined. The control-related planar motion models showed a really promising performance in the evaluation tests, considering their simplicity and fidelity to the observed vehicle motion. In the next chapter, we will demonstrate how we can employ the constructed dynamic motion model to develop and test different guidance and control algorithms.

Chapter 3

Path-Following Control

Many ocean survey missions require an Unmanned Surface Vehicle (USV) to accurately follow predefined paths, and thus, an efficient and robust path-following control algorithm is essential for many applications [4]. This chapter introduces and compares three extensively employed geometric path-following control strategies, namely Vector Field Method (VF), Carrot Chasing Method (CC) and Line-of-Sight Method (LOS). We provide a comprehensive study of each individual method, which includes investigating their mathematical origins, performing simulation evaluations and carrying out field experiments in adverse weather conditions.

3.1   Problem Statement

Preplanned and re-planned paths are usually defined by a list of waypoints, which are specified by the operator considering weather conditions, obstacles and so forth. According to the well-known results from Dubins [43], for a USV moving with constant forward speed in the 2D plane, the shortest path between two configurations (waypoint positions and vehicle heading), can be constructed by straight lines and circular arcs. To provide a complete analysis, we investigate each path-following control method in both straight-line

and circular path-following scenarios. In a later section, we will also discuss how linear and circular paths can be joined together so that the vehicle can transit smoothly between adjacent waypoints to complete a specific mission.

The two path-following control problems have been illustrated in Fig. 3.1. Again, the North-East-Down (NED) frame is chosen as the inertial frame, and a position in this coordinate is defined as $p_r = (n_r, e_r)^T$, where n_r and e_r denote the translational position along north and east direction, respectively. Therefore, the straight-line path can be explicitly defined based on the location of the two adjacent waypoints, i.e. $wp_i = (n_i, e_i)^T$ and $wp_{i+1} = (n_{i+1}, e_{i+1})^T$. The circular path, on the other hand, can be specified by the position of the circle's origin $p_c = (n_c, e_c)^T$ and circle radius R. If we define the generalized followed path as $P \in \Re^2$ in the 2D plane and the time-varying USV position as $p(t) = (n(t), e(t))^T$, the goal is to develop the path-following control law that can guide a USV to adjust its speed and heading to minimize the cross track error $d(t)$, i.e. d_s or d_c in Fig. 3.1, which can be written as

$$\lim_{t \to \infty} ||d(t)|| = \lim_{t \to \infty} ||p(t) - P|| = 0. \tag{3.1}$$

Referring to Fig. 3.1, the kinematic model of the vehicle can be formulated as

$$\begin{aligned} \dot{n} &= V \cos(\chi) \\ \dot{e} &= V \sin(\chi) \end{aligned} \tag{3.2}$$

where $\dot{n}$ and $\dot{e}$ denote the USV's speed along $O_I N$ and $O_I E$ axes, V is the total velocity and χ represents the course angle with respect to true north. It is important to note that in this chapter we employ $(n, e)^T$ to represent the vehicle's location instead of $(x, y)^T$ from chapter 2. The reason is that this definition can be intuitively related to inertial NED frame, which will bring great convenience while formulating different path-following
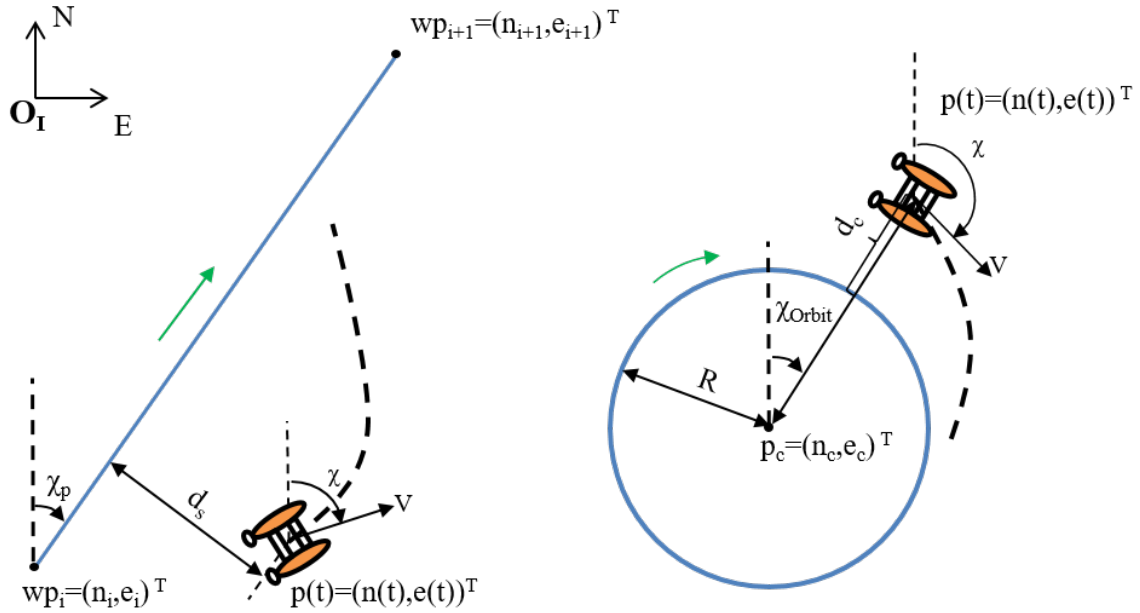
Figure 3.1: An illustration of the USV path-following control problems. The left figure shows that a straight-line path-following control algorithm needs to be implemented to steer the USV towards the path from wp_i to wp_{i+1}. On the right, a USV is controlled to follow the circular path in the clockwise direction by employing the circular path-following control methods.

control algorithms. In Eq. 3.2, the total velocity is measured by a USV's onboard GPS, and it may be considered as the summation of the platform's own moving speed, the water current speed and the contribution from other environmental disturbances. The course angle χ measures the direction of the total velocity, and it needs to be distinguished from a USV's heading. We have already shown an example where χ and ψ differs from each other during a USV's steering motion in Fig. 2.7. In fact, for a USV working in an environment with constant water current influences, the course and heading angles are always different except for the case where a USV drives towards or follows the current direction. In this framework, considering the dynamic ocean environments with varying current, wind and wave disturbances, we can argue that the two angles are hardly the same.

The following introduced path-following control laws are developed by adjusting the

course angle instead of the heading angle of the vehicle. This is a practical choice be-
cause the course angle is directly measured by a USV's onboard GPS receiver, and more
importantly, employing χ in the closed-loop path-following control system can increase
the path tracking robustness and accuracy. For instance, as shown in Fig. 3.2, a USV is
assumed to be readily positioned on the followed straight-line path and it just needs to
follow the path direction χ_p until it reaches the next waypoint. The left figure depicts
the case where the vehicle's heading direction is controlled. It can be seen that due to
the constant water current influences, the USV's total velocity diverges from the path
direction, and the vehicle will move away from the followed path. The path-following
control algorithm works to bring the USV back, but whenever the vehicle's heading angle
is aligned with χ_p, it will, again, leave the followed path. On the contrary, if the course
angle is chosen for path-following control, shown on the right graph of Fig. 3.2, the USV
can precisely follow the desired path. Note that when there is current influences, the
vehicle's heading will differ from χ_p, but the direction of χ can always be controlled to
align with the path direction. Hence, employing the course angle in the control law can
improve the path-following accuracy and robustness, especially when considering the con-
stant current influences. It is important to note that the purpose of the path-following
control algorithm is to minimize the cross track error as indicated in Eq. 3.1. Therefore,
with regard to other potential environmental disturbances that push the USV away from
the followed path, the implemented path-following control law will be able to bring the
USV back to the followed path regardless of the scenarios of controlling either the heading
or course angle.

A couple of terms will be repeatedly used in the following discussion, and thus they
are introduced in detail in this section. The straight-line path direction with respect to
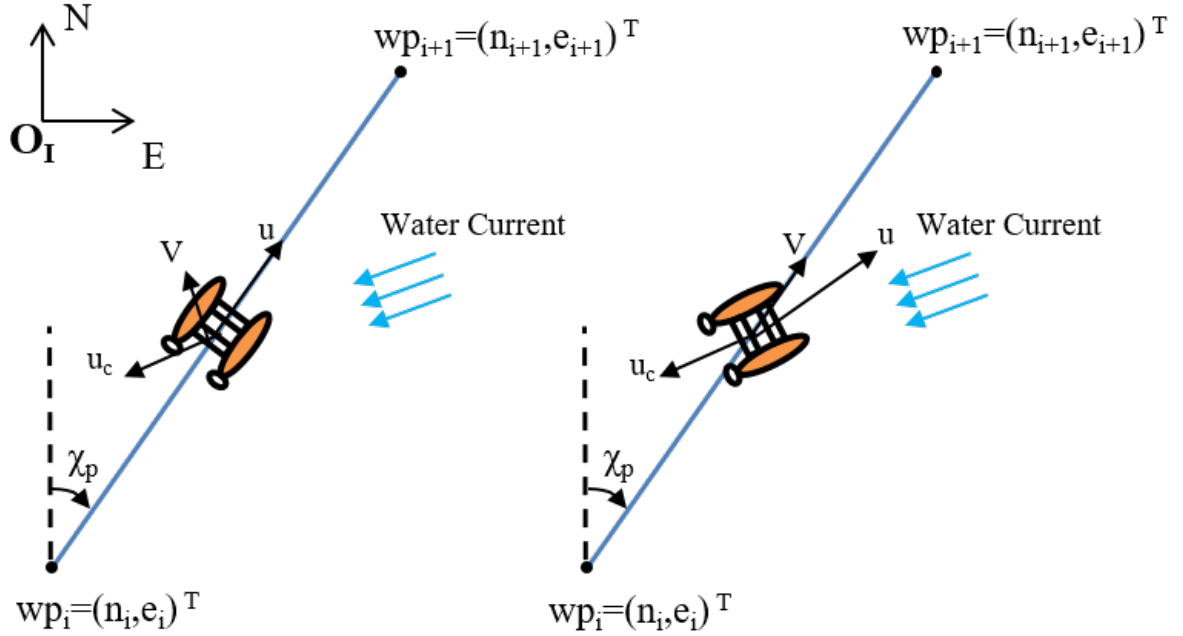
Figure 3.2: A USV's straight path-following control with constant water current influences. On the left, the vehicle's heading angle is employed in the closed-loop path-following control algorithm, while the figure on the right shows that the course angle is used and adjusted to follow the desired path.

true north is defined as χ_p and it can be calculated as

$$\chi_p = \text{arctan2}(e_{i+1} - e_i, n_{i+1} - n_i) \tag{3.3}$$

where arctan2 is the four-quadrant inverse tangent function, so $\chi_p \in (-\pi, \pi]$. For the circular path in Fig. 3.1, the direction of the vector $\overrightarrow{p_c p}$ with respect to true north is defined as χ_{Orbit} and it is computed as

$$\chi_{Orbit} = \text{arctan2}(e(t) - e_c, n(t) - n_c). \tag{3.4}$$

The distance between the USV location and the circle origin is given as

$$||\overrightarrow{p_c p}|| = \sqrt{(e(t) - e_c)^2 + (n(t) - n_c)^2}.$$

As shown in Fig. 3.1, the cross track error $d(t)$ denotes the difference between the USV location and the desired followed path. For the straight path case, it is the perpendicular distance that is given as

$$d_s = -(n(t) - n_i)\sin(\chi_p) + (e(t) - e_i)\cos(\chi_p), \tag{3.5}$$

while for the circular path

$$d_c = ||\overrightarrow{p_c p}|| - R. \tag{3.6}$$

Note that the cross track error can be either positive or negative. In Eq. 3.5, when $d_s > 0$ it indicates that the USV is located on the starboard-side of the straight-line path, while if $d_s < 0$ the USV is on the port-side. Similarly, Eq. 3.6 suggests that when $d_c > 0$ the USV is located outside of the circle, while $d_c < 0$ means the USV is inside the circle.

3.2 Guidance and Control System Architecture

Before we move on to discuss about different path-following control algorithms, we need to introduce the guidance and control system architecture of the research platform. The block diagram of the implemented guidance and control system has been depicted in Fig. 3.3. In the figure, the rounded rectangular area with the dash dot boundary line defines the USV's guidance module, where the reference speed V_d and desired course angle χ_d are generated for the low-level controllers. In a survey mission, we normally command a USV to operate at a constant moving speed so that the payload sensor data can be collected with equally travelled distance. The list of waypoint positions are calculated from path planning algorithms or from user settings, and they are normally defined following the geographic coordinate using latitude and longitude. Note that in Fig. 3.3, the blocks of coordinate conversion are used to transform the waypoint positions and measured USV
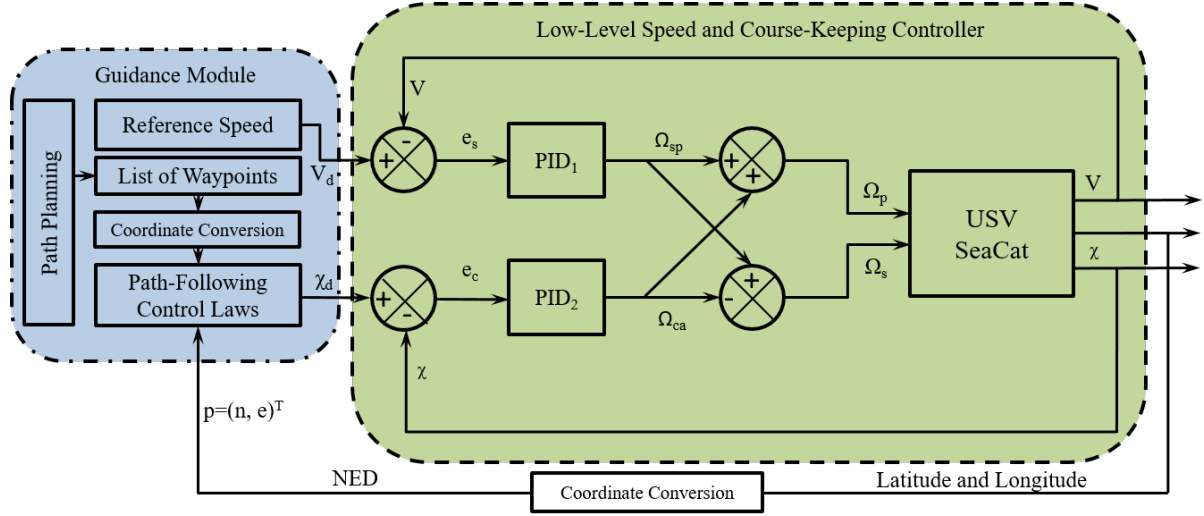
Figure 3.3: The USV SeaCat's guidance and control system block diagram.

positions into the local NED frame in meters. Through implementation of a specific path-following control method, the desired course angle is calculated to direct the USV to the followed path.

In Fig. 3.3, the structure of the low-level speed and course-keeping controller is shown in the rounded rectangular area with the dash boundary line. The speed controller needs to be designed so that the USV can maintain a specific cruising speed or speed profile, and the course-keeping controller is responsible for adjusting the vehicle's course direction according to the desired course angle. In this study, we employ the well-accepted proportional-integral-derivative (PID) controller for the speed and course-keeping control system development. The input signal for the speed controller PID_1 is the speed error

$$e_s = V_d - V$$

where V_d and V represent the reference and current moving speed of the USV, respectively. Hence, this PID controller can be formulated as

$$\Omega_{sp} = K_{p1}e_s + K_{i1} \int_0^t e_s dt + K_{d1}\frac{de_s}{dt}$$

where K_{p1}, K_{i1} and $K_{d1} > 0$ and Ω_{sp} defines the output signal from PID$_1$. The input signal for the course-keeping controller PID$_2$ comes from the error term

$$e_c = \chi_d - \chi$$

where χ_d and χ define the desired and current course angle of a USV. Similarly, the control law for PID$_2$ is written as

$$\Omega_{ca} = K_{p2}e_c + K_{i2} \int_0^t e_c dt + K_{d2}\frac{de_c}{dt}$$

where K_{p2}, K_{i2} and $K_{d2} > 0$ and Ω_{ca} defines the output signal from PID$_2$. In this multi-variable control system, to provide the correct control command for port- and starboard-side propellers, i.e. Ω_p and Ω_s, we formulate the output signals from the two PID controllers as

$$\Omega_{sp} \triangleq \frac{\Omega_p + \Omega_s}{2}$$

and

$$\Omega_{ca} \triangleq \frac{\Omega_p - \Omega_s}{2}.$$

Therefore, the function of the two low-level PID controllers can be summarized as follows: PID$_1$ will act to increase or reduce both propellers' rotational speed to manipulate the vehicle's velocity, while PID$_2$ will vary the differential speed between the two thrusters in order to change the USV's course angle. This interpretation serves as the basis for us to tune the PID control parameters in the following discussion.

3.3 Path-Following Control Algorithms

In this section, three extensively employed path-following control algorithms, i.e. Vector Field Method (VF), Carrot Chasing Method (CC) and the well-known Line-of-Sight (LOS) Method, are investigated [44]. We will provide detailed procedures for derivation of all algorithms, based on which, their mathematical origins, connections and distinctions are revealed. We explore the parameter space of each algorithm, and through this process we examine different control parameters and their influences on the controller performance. The in-depth analysis in this section provides rationale for the following simulation studies and field experiments.

3.3.1 Vector Field Method

The vector field method was introduced in [45] for path-following control of small Unmanned Aerial Vehicles (UAVs), and in this research we will examine the applicability of this algorithm for USVs. The idea is to construct the vector fields around the followed path so that the vector direction serves as the reference angle for the vehicle to follow. For example, the vector fields formed around the straight-line and circular paths are depicted in Fig. 3.4. While implementing this algorithm, the vector at a specific location in the NED frame denotes the desired USV course angle direction. Through following a series of vectors, a USV will finally converge to the followed path.

The constructed vector fields need to meet two conditions. If a USV is far away from the followed path, the vector direction needs to guide the vehicle back to the path at the maximum approaching angle. If, however, the USV is close to the path, the vector field should align the vehicle with the straight path direction or the tangential direction of the circular path. Therefore, the desired course angle for the straight-line and circular path
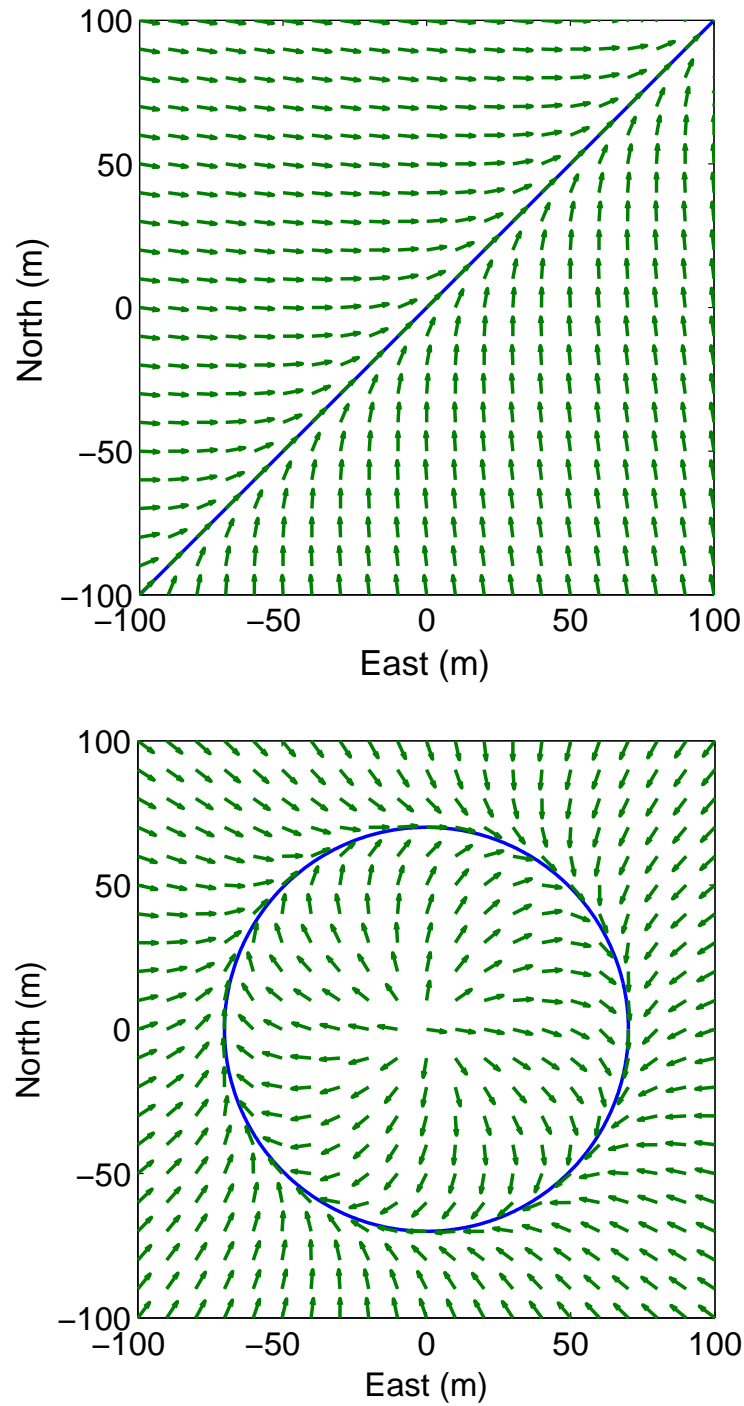
Figure 3.4: An example of the vector fields constructed around the straight-line and circular paths. The vectors in both figures indicate the reference course angle for a USV to follow.

can be formulated as

$$\chi_d = \chi_p - \frac{2}{\pi}(\chi_{Ms}) \arctan(k_s d_s) \tag{3.7}$$

and

$$\chi_d = \chi_{Orbit} + \rho_d \left[\frac{\pi}{2} + \frac{2}{\pi}(\chi_{Mc}) \arctan(k_c d_c) \right], \tag{3.8}$$

respectively.

In Eq. 3.7 and Eq. 3.8, k_s and k_c are control parameters (positive real number) for the vector field convergence rate, and a larger value indicates a group of faster converging vectors. The maximum approaching angles are defined as χ_{Ms} and χ_{Mc}, and they are user selectable within the value range of $(0, \pi/2]$. A USV may be required to follow the circular path in a clockwise or counter-clockwise direction and ρ_d denotes this direction with a corresponding value of 1 or -1. For completeness, we summarize the vector field path-following control methods in Algorithm 1 and Algorithm 2.

Algorithm 1 Vector field path-following control law (straight-line path).

1: Initialize: $p(t) = (n(t), e(t))^T, wp_i = (n_i, e_i)^T, wp_{i+1} = (n_{i+1}, e_{i+1})^T, \chi_{Ms}, k_s$
2: $\chi_p = \arctan2(e_{i+1} - e_i, n_{i+1} - n_i)$
3: $d_s = -(n(t) - n_i)\sin(\chi_p) + (e(t) - e_i)\cos(\chi_p)$
4: $\chi_d = \chi_p - \frac{2}{\pi}(\chi_{Ms})\arctan(k_s d_s)$

Algorithm 2 Vector field path-following control law (circular path).

1: Initialize: $p(t) = (n(t), e(t))^T, p_c = (n_c, e_c)^T, R, \chi_{Mc}, k_c, \rho_d$
2: $\chi_{Orbit} = \arctan2(e(t) - e_c, n(t) - n_c)$
3: $||\overrightarrow{p_c p}|| = \sqrt{(e(t) - e_c)^2 + (n(t) - n_c)^2}$
4: $d_c = ||\overrightarrow{p_c p}|| - R$
5: $\chi_d = \chi_{Orbit} + \rho_d \left[\frac{\pi}{2} + \frac{2}{\pi}(\chi_{Mc})\arctan(k_c d_c) \right]$

Our parameter space exploration is based on Eq. 3.7 and Eq. 3.8, using which we can examine how the desired course angle is generated depending on the cross track error and different control parameter configurations. For the straight-line path case, without loss

of generality, we assign the desired path direction as $\chi_p = 0°$, and the exploration of the parameter space of Eq. 3.7 is depicted in Fig. 3.5. The solid curves are simulated with the same maximum approaching angle of $\chi_{Ms} = 90°$ or $\pi/2$, and they can be compared to examine how the control parameter k_s will influence the changing tendency of the desired course angle χ_d. It can be seen that when $k_s = 0$, $\chi_d = \chi_p = 0°$ regardless of the cross track errors, and this case defines the vector fields where all vectors point to the same direction as the followed path χ_p. When $k_s \neq 0$, the curves follow the shape of the inverse tangent function, and their asymptotic lines are given as $\chi_d = \pm\chi_{Ms} = \pm90°$. If the vehicle is far away from the desired path, i.e. $|d_s|$ is large, it will be directed by a course angle close to $\pm\chi_{Ms}$, while if it is in close proximity of the path, χ_d will quickly converge to χ_p. It is evident that with larger values for k_s, χ_d will have a faster convergence rate. In Fig. 3.5, a group of green curves have been generated to check how χ_d is influenced by χ_{Ms}. We can see that χ_{Ms} controls the maximum approaching angles or the asymptotic lines.

In terms of exploring the parameter space for circular path following, it is assumed that $\chi_{Orbit} = 0°$ and that the maximum approaching angle is $\chi_{Mc} = 90°$ or $\pi/2$, the circle radius is 50 m and the desired circular path-following direction is clockwise, i.e. $\rho_d = 1$. The exploration of parameter space is shown in Fig. 3.6. Again, when $k_c = 0$, $\chi_d = 90°$ regardless of the cross track error d_c and it corresponds to the tangential direction of the circle. By following this direction, however, a vehicle can not converge to the desired circular path. If $k_c \neq 0$, the desired course angle follows the tendency of the inverse tangent function curves like the straight-line path case. When $d_c > 0$, $\chi_d \in (90°, 180°]$, it represents that the USV is directed towards the followed path from outside of the circle. On the contrary, if $d_c < 0$ and $\chi_d \in [0°, 90°)$, the USV approaches the path from inside of the circle. As depicted in Fig. 3.6, we can observe that the control parameter k_c determines the convergence rate of χ_d, and the maximum approaching angle when the
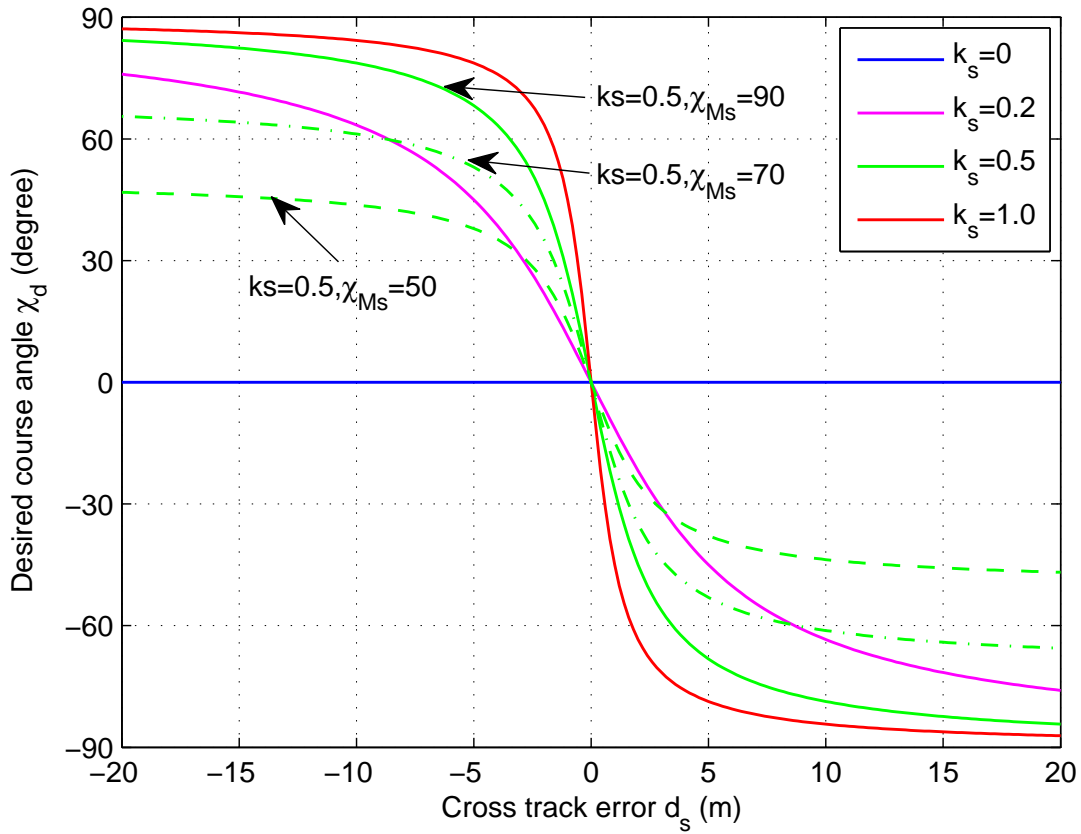
Figure 3.5: The exploration of the parameter space for Eq. 3.7 to determine the relationship between desired course angle χ_d and the cross track error d_s with varied settings of k_s and χ_{Ms}. The performed search of the parameter space is based on the vector field method for straight-line path-following control.

vehicle is far from the circle is decided by the value of χ_{Mc}.

3.3.2 Carrot Chasing Method

The Carrot Chasing Method (CC) is extensively used in missile guidance systems [46], but in this research we will try to implement this algorithm for a USV's path-following control. While implementing CC, a virtual target point (VTP) is always defined on the followed path that is right ahead of the vehicle. Through chasing VTP, the vehicle will be directed towards and eventually converge on the path.
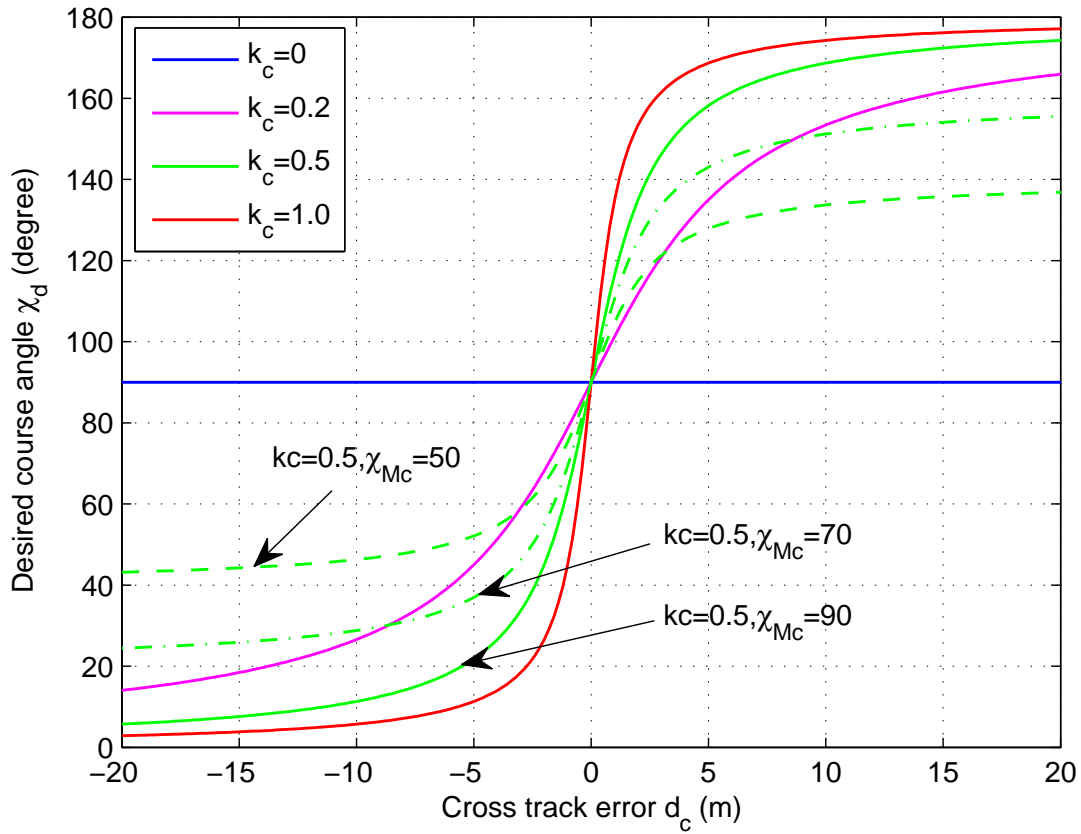
Figure 3.6: The exploration of the parameter space for Eq. 3.8 to determine the relationship between desired course angle χ_d and the cross track error d_c with varied settings of k_c and χ_{Mc}. The performed search of parameter space is based on the vector field method for circular path-following control.

3.3.2.1 Conventional Carrot Chasing Method

An intuitive representation of the CC path-following control method is depicted in Fig. 3.7. On the left, the USV's current location $p(t) = (n(t), e(t))^T$ is projected on the followed straight-line path as $p(t)' = (n(t)', e(t)')^T$. If the look-ahead distance is given as a constant number Δ_s, the VTP_1 position can be determined on the followed path. The VTP_1 position will be updated when the USV's projected location changes. Since the VTP_1 is always ahead of the vehicle, through chasing VTP_1 the USV will eventually converge to the followed path. We follow the conventional procedures to calculate the target point

position [46]. The distance between wp_i and the USV location can be calculated as

$$||\overrightarrow{L}|| = ||p(t) - wp_i|| = \sqrt{(e(t) - e_i)^2 + (n(t) - n_i)^2},$$

where the direction of $\overrightarrow{L}$ with respect to true north is given as

$$\chi_{\overrightarrow{L}} = \arctan2(e(t) - e_i, n(t) - n_i).$$

Hence,

$$\chi_\beta = \chi_{\overrightarrow{L}} - \chi_p.$$

Using the look-ahead distance Δ_s, the VTP_1 position p_{v1} can be computed as

$$p_{v1} = \begin{bmatrix} n_{v1} \\ e_{v1} \end{bmatrix} = \begin{bmatrix} (||\overrightarrow{L}|| \cos(\chi_\beta) + \Delta_s) \cos(\chi_p) + n_i \\ (||\overrightarrow{L}|| \cos(\chi_\beta) + \Delta_s) \sin(\chi_p) + e_i \end{bmatrix}.$$

Note that when $\cos(\chi_\beta) < 0$, the vehicle's projected location $p(t)'$ is on the extended line of the followed path through the end point wp_i, otherwise $p(t)'$ is located between wp_i and wp_{i+1}, which is the case drawn in Fig. 3.7. Therefore, the desired course angle can be calculated as

$$\chi_d = \arctan2(e_{v1} - e(t), n_{v1} - n(t)). \tag{3.9}$$

The right plot of Fig. 3.7 indicates the carrot chasing method implemented on the circular path-following problem. The look-ahead angle is defined as a constant number Δ_c and the virtual target point on the circle is defined as VTP_2. Note that Δ_c can be either a positive or negative angle, and they represent the clockwise and counter-clockwise path-following scenarios, respectively. We follow the same definition from section 3.1, and thus the circle origin is $p_c = (n_c, e_c)^T$, the radius is R and $\overrightarrow{p_c p}$ defines the vector pointed
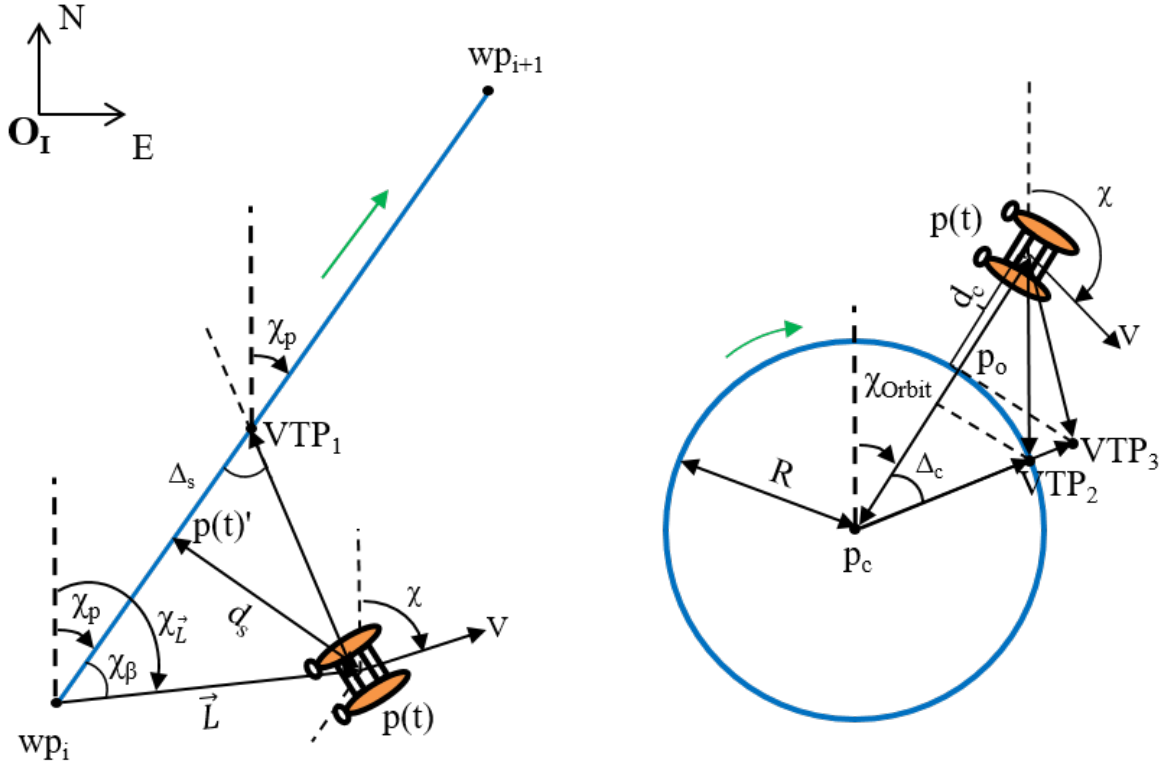
Figure 3.7: The demonstration of the Carrot Chasing path-following control for straight-line and circular paths.

to the vehicle position from the circle origin. We can compute the unit vector of $\overrightarrow{p_c p}$ as

$$\overrightarrow{q}_{\overrightarrow{p_c p}} = \frac{\overrightarrow{p_c p}}{||\overrightarrow{p_c p}||} = \frac{(n(t) - n_c, e(t) - e_c)^T}{\sqrt{(n(t) - n_c)^2 + (e(t) - e_c)^2}}.$$

If the VTP_2 position is defined as $p_{v2} = (n_{v2}, e_{v2})^T$, the unit vector along $\overrightarrow{p_c p_{v2}}$ can be calculated using the rotation matrix

$$J_{\Delta_c} = \begin{bmatrix} \cos(\Delta_c) & \sin(\Delta_c) \\ -\sin(\Delta_c) & \cos(\Delta_c) \end{bmatrix}$$

as

$$\overrightarrow{q}_{\overrightarrow{p_c p_{v2}}} = J_{\Delta_c} \overrightarrow{q}_{\overrightarrow{p_c p}}.$$

Hence, the VTP_2 position can be formulated as

$$p_{v2} = p_c + Rq_{\overrightarrow{p_c p_{v2}}}.$$

and the desired course angle can be calculated as

$$\chi_d = \arctan2(e_{v2} - e(t), n_{v2} - n(t)). \tag{3.10}$$

Based on the previous analysis, we summarize the carrot chasing algorithms for straight-line and circular path-following cases in Algorithm 3 and Algorithm 4.

Algorithm 3 Carrot chasing path-following control law (straight-line path).

1: Initialize: $p(t) = (n(t), e(t))^T, wp_i = (n_i, e_i)^T, wp_{i+1} = (n_{i+1}, e_{i+1})^T, \Delta_s$
2: $\chi_p = \arctan2(e_{i+1} - e_i, n_{i+1} - n_i)$
3: $||\overrightarrow{L}|| = \sqrt{(e(t) - e_i)^2 + (n(t) - n_i)^2}$
4: $\chi_{\overrightarrow{L}} = \arctan2(e(t) - e_i, n(t) - n_i)$
5: $\chi_\beta = \chi_{\overrightarrow{L}} - \chi_p$
6: $n_{v1} = (||\overrightarrow{L}|| \cos(\chi_\beta) + \Delta_s) \cos(\chi_p) + n_i$
7: $e_{v1} = (||\overrightarrow{L}|| \cos(\chi_\beta) + \Delta_s) \sin(\chi_p) + e_i$
8: $\chi_d = \arctan2(e_{v1} - e(t), n_{v1} - n(t))$

Algorithm 4 Carrot chasing path-following control law (circular path).

1: Initialize: $p(t) = (n(t), e(t))^T, p_c = (n_c, e_c)^T, R, \Delta_c$
2: $\chi_{Orbit} = \arctan2(e(t) - e_c, n(t) - n_c)$
3: $\overrightarrow{q}_{\overrightarrow{p_c p}} = \frac{(n(t) - n_c, e(t) - e_c)^T}{\sqrt{(n(t) - n_c)^2 + (e(t) - e_c)^2}} = (q_n, q_e)^T$
4: $n_{v2} = R(q_n \cos(\Delta_c) + q_e \sin(\Delta_c)) + n_c$
5: $e_{v2} = R(-q_n \sin(\Delta_c) + q_e \cos(\Delta_c)) + e_c$
6: $\chi_d = \arctan2(e_{v2} - e(t), n_{v2} - n(t))$

Similar to section 3.3.1, we carry out the exploration of the parameter space to examine the relationship between the desired course angle and the cross track errors with different control parameter settings using the conventional CC algorithm. For the straight-line path case, we still assume the path direction $\chi_p = 0°$, and since the VTP_1 position is

determined, the cross track error can be calculated as

$$d_s = \pm\sqrt{(e_{v1} - e(t))^2 + (n_{v1} - n(t))^2 - \Delta_s^2}$$

where $d_s > 0$ or $d_s < 0$ represent that the vehicle is on the starboard- or port-side of the followed path. The parameter space exploration results with the look-ahead distance Δ_s changing from 0 to 5 m have been depicted in Fig. 3.8. It can be seen that a smaller value of Δ_s corresponds to the curve that has a faster changing rate. When $\Delta_s = 0$ m, the virtual target point is the projected position of the vehicle on the straight-line path and this features the steepest tendency of the desired course angle for a vehicle to follow. It is interesting when we compare these results with those in Fig. 3.5, because both vector field and carrot chasing algorithms construct similar shaped reference course angle. Through comparing Algorithm 1 and Algorithm 3, we can conclude that both algorithms implement the inverse tangent function to formulate the desired course angle. In the following section, we will implement a different methodology to derive CC, based on which the intrinsic connection between the two methods can be revealed.

We keep the same testing condition as section 3.3.1 to explore the CC circular path-following algorithm parameter space. The results with look-ahead angle Δ_c varying from $0°$ to $10°$ have been shown in Fig. 3.9. Again, the curves follow the shape of the inverse tangent function that are close to those constructed in Fig. 3.6 using the vector field method, and a small Δ_c is related to the curve with a faster convergence rate. However, it is important to note that the CC algorithm might not be feasible for accurate circular path tracking control. For instance, as depicted in the enlarged graph of Fig. 3.9, when the USV is on the circular path, i.e. $d_c = 0$, the desired course angle $\chi_d > 90°$ for the cases where $\Delta_c > 0$. In cases where the look-ahead angle is nonzero, the vehicle's desired course angle is not aligned with the tangential direction of the circular path. This control

Figure 3.8: The exploration of the parameter space for Algorithm 3 to determine the relationship between desired course angle χ_d and the cross track error d_s with varied settings of Δ_s. The performed search of parameter space is based on the carrot chasing method for straight-line path-following control.

configuration violates our goal of precise path tracking, and its deficiency will potentially prevent this method from being employed for precise circular path-following control.

3.3.2.2 Connection Between Carrot Chasing Method and Vector Field Method

In this section, we will provide a novel insight into the theoretical origin of the carrot chasing algorithm. An alternative method for derivation of the CC path-following control algorithm will be introduced, based on which the connection to the vector field algorithm can be revealed.

Figure 3.9: The exploration of the parameter space for Algorithm 4 to determine the relationship between desired course angle χ_d and the cross track error d_c with varied settings of Δ_c. The performed search of parameter space is based on the carrot chasing method for circular path-following control.

A conventional carrot chasing method, as presented in section 3.3.2.1, requires us to compute the position of the virtual target point and then calculate the desired course angle χ_d for a USV to follow. However, as shown in Fig. 3.7, there is another more compact way to formulate χ_d using just the path direction χ_p, cross track error d_s and the look-ahead distance Δ_s, and it is given as

$$\chi_d = \chi_p - \arctan\left(\frac{d_s}{\Delta_s}\right). \tag{3.11}$$

Interestingly, although the carrot chasing and vector field methods are derived from different perspectives, through comparing Eq. 3.11 and Eq. 3.7, we can see that the theoretical origin of both methods are intrinsically the same. The control parameter k_s is equivalent to the inverse of the look-ahead distance Δ_s, i.e. $k_s = 1/\Delta_s$. Note that we denote the maximum approaching angle $\chi_{Ms} = \pi/2$ in Eq. 3.7 for the comparison.

In a similar way, as for the circular path in Fig. 3.7, the desired course angle is given as

$$\chi_d = \chi_{Orbit} + \rho_d \left[\frac{\pi}{2} + \arctan \left(\frac{||\overrightarrow{p_c p}|| - R\cos(\Delta_c)}{R\sin(\Delta_c)} \right) \right]. \tag{3.12}$$

Although Eq. 3.12 and Eq. 3.8 have similar form, CC is not efficient in following the circular path accurately. We have already demonstrated this deficiency in section 3.3.2.1 through performing the parameter space exploration, but here we can provide an alternative view through analysing the formula directly. Concretely, when the vehicle is positioned on the circle and it follows in the clockwise direction, if the look-ahead angle $\Delta_c > 0$, Eq. 3.12 can be written as

$$\chi_d = \chi_{Orbit} + \left[\frac{\pi}{2} + \arctan \left(\frac{R - R\cos(\Delta_c)}{R\sin(\Delta_c)} \right) \right]$$
$$\neq \chi_{Orbit} + \frac{\pi}{2},$$

which indicates that the desired course angle is not following the tangential direction of the circle. If Δ_c is close to zero, though, we can apply L'Hopital's rule as

$$\lim_{\Delta_c \to 0} \chi_d = \lim_{\Delta_c \to 0} \left[\chi_{Orbit} + \frac{\pi}{2} + \arctan \left(\frac{R - R\cos(\Delta_c)}{R\sin(\Delta_c)} \right) \right]$$
$$= \lim_{\Delta_c \to 0} \left[\chi_{Orbit} + \frac{\pi}{2} + \arctan \left(\frac{\sin(\Delta_c)}{\cos(\Delta_c)} \right) \right]$$
$$= \chi_{Orbit} + \frac{\pi}{2},$$

and it shows that only when the look-ahead angle is close to zero will the vehicle be

directed to follow the circle's tangential direction. Nevertheless, a really small look-ahead angle Δ_c corresponds to a fast converging reference course angle as shown in Fig. 3.9, and it may not be viable for a USV to track.

Inspired by Eq. 3.8, we can make a small modification of Eq. 3.12 to solve its problem. As shown in Fig. 3.7, we denote p_o as the intersection point of vector $\overrightarrow{p_c p}$ and the circle, and a new virtual target point VTP_3 is defined on the extended line of $p_c VTP_2$ such that $p_o VTP_3$ is tangent to the circle. The USV can track VTP_3 instead of VTP_2, and thus, the new desired course angle can be computed as

$$\chi_d = \chi_{Orbit} + \rho_d \left[\frac{\pi}{2} + \arctan\left(\frac{||\overrightarrow{p_c p}|| - R}{R \tan(\Delta_c)} \right) \right]. \tag{3.13}$$

Now in cases where the vehicle is positioned on the followed circle, the desired course direction will be the same as the tangential direction of the circular path. It is important to note that, if in Eq. 3.8 the maximum approaching angle is assumed as $\chi_{Mc} = \pi/2$, we can compare it with the modified carrot chasing method in Eq. 3.13. It clearly shows that the two methods have exactly the same form, and the control parameter k_c in Eq. 3.8 is actually equivalent to inverse of $R \tan(\Delta_c)$ in Eq. 3.13, i.e. $k_c = 1/(R \tan(\Delta_c))$.

3.3.2.3 Integral Gain for the Carrot Chasing Method

In the carrot chasing method, the control parameters of $1/\Delta_s$ (Eq. 3.11) and $1/(R \tan(\Delta_c))$ (Eq. 3.13) act like the proportional gain of a conventional PID controller [11]. For example, according to the simulation results in Fig. 3.8 and Fig. 3.9, we can conclude that a larger proportional gain, i.e. smaller value of Δ_s and Δ_c, will lead to a more aggressive reference course angle curve for the vehicle to follow. Based on this analysis, we artificially

add the integral gain into the original carrot chasing algorithms, which are given as

$$\chi_d = \chi_p - \arctan\left(K_{ps}d_s(t) + K_{is}\int d_s(t)dt\right) \tag{3.14}$$

and

$$\chi_d = \chi_{Orbit} + \rho_d\left[\frac{\pi}{2} + \arctan\left(K_{pc}d_c(t) + K_{ic}\int d_c(t)dt\right)\right]. \tag{3.15}$$

In Eq. 3.14, $K_{ps} = 1/\Delta_s$ and it denotes the proportional gain, and K_{is} is the integral gain for the straight-line path-following control case. Similarly, in Eq. 3.15, we have $K_{pc} = 1/(R\tan(\Delta_c))$ as the proportional gain and K_{ic} as the integral gain for the circular path tracking control case. Note that Eq. 3.15 is generated based on the modified version of the CC method in Eq. 3.13.

Although the introduction of the integral gain can notably increase the path-following control robustness to the unexpected environmental disturbances, this algorithm may introduce aggressive path tracking overshoot depending on the initial position of the vehicle relative to the followed path. We will illustrate this phenomenon in the following sections.

3.3.3 Line-of-Sight Method

The Line-of-Sight (LOS) path-following control algorithm is very popular in the USV research community, and there are many variants [1, 11, 40, 46]. In this research, we will employ the conventional LOS concept as shown in Fig. 3.10. We define a circle with a time-varying center that coincides with the USV's body frame origin at $p(t) = (n(t), e(t))^T$, and the radius of this vehicle circle is defined as a constant number R_p. When the USV is close enough to the followed path, the circle R_p will intersect the path at two points and the one that is closer to the next waypoint is chosen as the line-of-sight position. For example, in Fig. 3.10, p_{t1} and p_{t2} are the target line-of-sight positions that

the vehicle is directed to. When the vehicle is moving, the intersection point will change to a new location, and through following this target position the USV will follow the desired path.
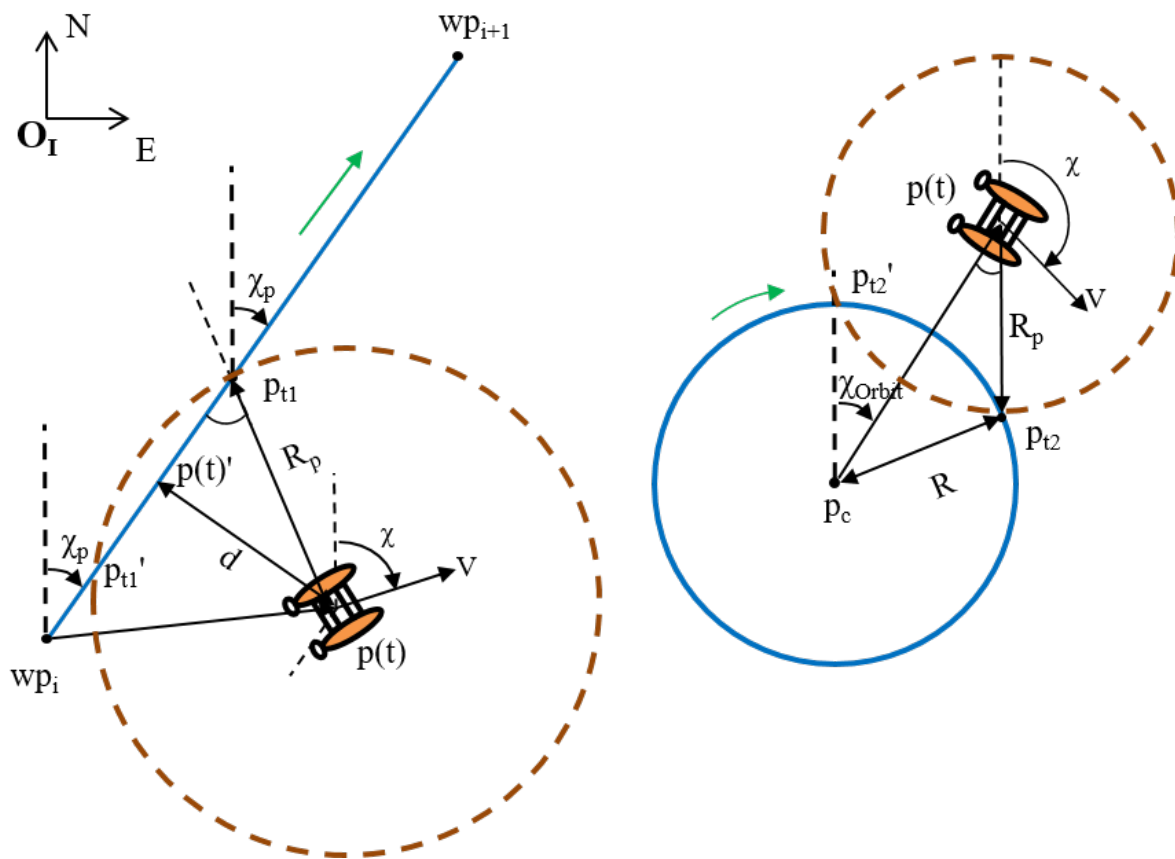
Figure 3.10: The demonstration of the Line-of-Sight path-following control for straight-line and circular paths.

The size of the circle surrounding the USV determines the path-following control performance, and in practice, it is difficult to assign a large enough circle to guarantee the intersection of the circle with the followed path at all time. A practical way is to formulate the desired course angle based on whether the intersection points exist. If there are no intersection points, the USV can be steered to the followed path at the maximum approaching angle $\pi/2$. After the USV moves closer and the intersection points exist, the vehicle can choose the right line-of-sight point to track. The LOS algorithms are

summarized in Algorithm 5 and Algorithm 6.

Algorithm 5 Line-of-sight path-following control law (straight-line path).

1: Initialize: $p(t) = (n(t), e(t))^T, wp_i = (n_i, e_i)^T, wp_{i+1} = (n_{i+1}, e_{i+1})^T, R_p$
2: $\chi_p = \arctan2(e_{i+1} - e_i, n_{i+1} - n_i)$
3: $d_s = -(n(t) - n_i)\sin(\chi_p) + (e(t) - e_i)\cos(\chi_p)$
4: **if** $d_s > R_p$ **then**
5:    $\chi_d = \chi_p - \frac{\pi}{2}$
6: **else if** $d_s < -R_p$ **then**
7:    $\chi_d = \chi_p + \frac{\pi}{2}$
8: **else**
9:    $\chi_d = \chi_p - \arcsin\left(\frac{d_s}{R_p}\right)$
10: **end if**

Algorithm 6 Line-of-sight path-following control law (circular path).

1: Initialize: $p(t) = (n(t), e(t))^T, p_c = (n_c, e_c)^T, \rho_d, R, R_p(R_p < R)$
2: $\chi_{Orbit} = \arctan2(e(t) - e_c, n(t) - n_c)$
3: $||\overrightarrow{p_c p}|| = \sqrt{(e(t) - e_c)^2 + (n(t) - n_c)^2}$
4: **if** $||\overrightarrow{p_c p}|| > R + R_p$ **then**
5:    $\chi_d = \chi_{Orbit} + \pi$
6: **else if** $||\overrightarrow{p_c p}|| < R - R_p$ **then**
7:    $\chi_d = \chi_{Orbit}$
8: **else**
9:    $\chi_d = \chi_{Orbit} + \rho_d \left(\frac{\pi}{2} + \arcsin\left(\frac{||\overrightarrow{p_c p}||^2 + R_p^2 - R^2}{2||\overrightarrow{p_c p}||R_p}\right)\right)$
10: **end if**

Using the formulated line-of-sight path-following control algorithms, we can investigate the relationship between the desired course angle and the cross track errors with varied circle radius R_p. We still keep the same testing conditions as in section 3.3.1 and 3.3.2. For the straight-line path case, the parameter space exploration results are depicted in Fig. 3.11. In the figure, the flat parts when $\chi_d = \pm 90°$ indicate that the USV is directed to the followed path by the maximum approaching angle, and when the intersection happens, the desired course angle χ_d changes according to the inverse sinusoidal function as summarized in Algorithm 5. When the cross track error $d_s = 0$, the USV's desired course angle will be equal to the followed path direction $\chi_p = 0°$. It can be seen that a

larger value of R_p will generate a smoother transition to χ_p. However, it is important to note that χ_d is not changing smoothly. According to the figure, at the point where the circle-path intersection occurs, χ_d will quickly drop from 90° to a much smaller angle. This abrupt change of the desired course angle might be adverse for the path-following control of a USV, especially for those with slow motion dynamics. Note that the low-level controller can maneuver SeaCat to keep up with the desired course angle, but due to its slow motion dynamics, there will be a time delay. We will demonstrate this phenomenon in the following PID controller tuning section.
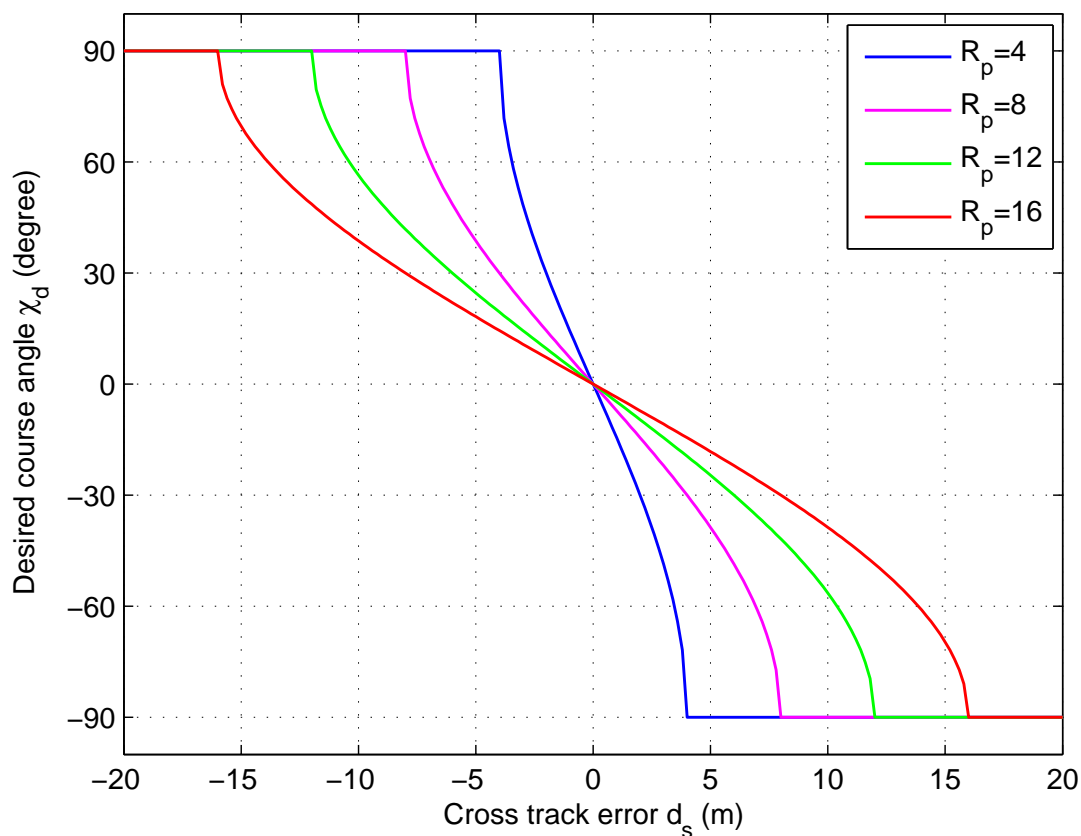
Figure 3.11: The exploration of the parameter space for Algorithm 5 to determine the relationship between desired course angle χ_d and the cross track error d_s with varied R_p. The performed search of parameter space is based on the line-of-sight method for straight-line path-following control.

In terms of the circular path, the results are depicted in Fig. 3.12 with a similar changing pattern of χ_d as in the straight-line case. Again, the abrupt change of the desired course angle exists, and it is adverse for a USV's motion control. When the vehicle is on the followed circular path, i.e. $||\overrightarrow{p_c p}|| = R$, we can calculate χ_d as

$$\chi_d = \chi_{Orbit} + \frac{\pi}{2} + \arcsin(\frac{R_p}{2R}). \tag{3.16}$$

According to Eq. 3.16, only when $R_p = 0$ could the desired course angle be the tangential direction of the circular path, i.e. $\chi_d = \chi_{Orbit} + \pi/2$. This characteristic has been clearly shown in the enlarged graph of Fig. 3.12, in which we can see when $d_c = 0$, $\chi_d \neq 90°$ that indicates the desired course direction is not along the tangential direction.

3.3.4 Summary of Path-Following Control Methods

A summary of the investigated Vector Field Method (VF), Carrot Chasing Method (CC), Carrot Chasing Method with integral gain (CCI), and Line-of-Sight Method (LOS) has been shown in Table 3.1.

Table 3.1: A summary of path-following control algorithms

Straight-line path	Circular Path
VF (Eq. 3.7) / CC (Eq. 3.9 or Eq. 3.11)	VF (Eq. 3.8) / Modified CC (Eq.3.13)
CCI (Eq. 3.14)	CCI (Eq. 3.15)
LOS (Algorithm 5)	LOS (Algorithm 6)

It is important to note that since VF and CC have the same mathematical origin, they will show the same path-following control performance. This is the reason that they are listed in the same row. In the following, we will evaluate all the algorithms listed in Table 3.1 by performing simulations and real-world field experiments.
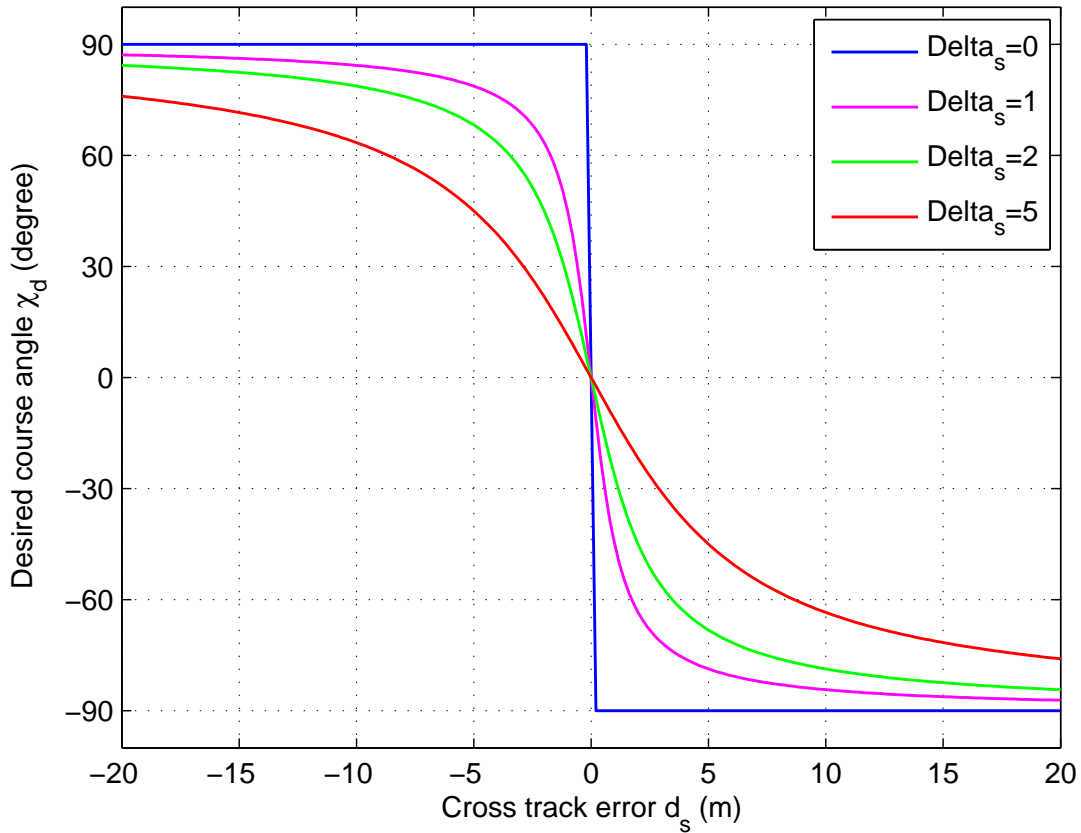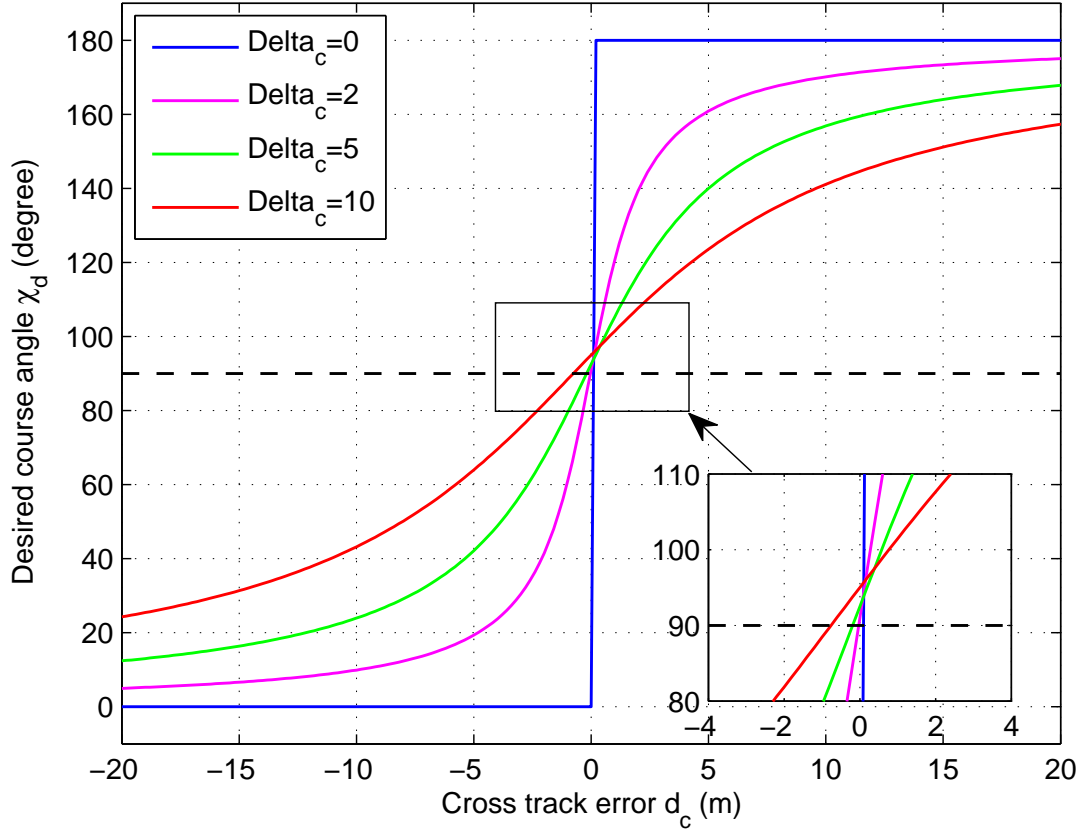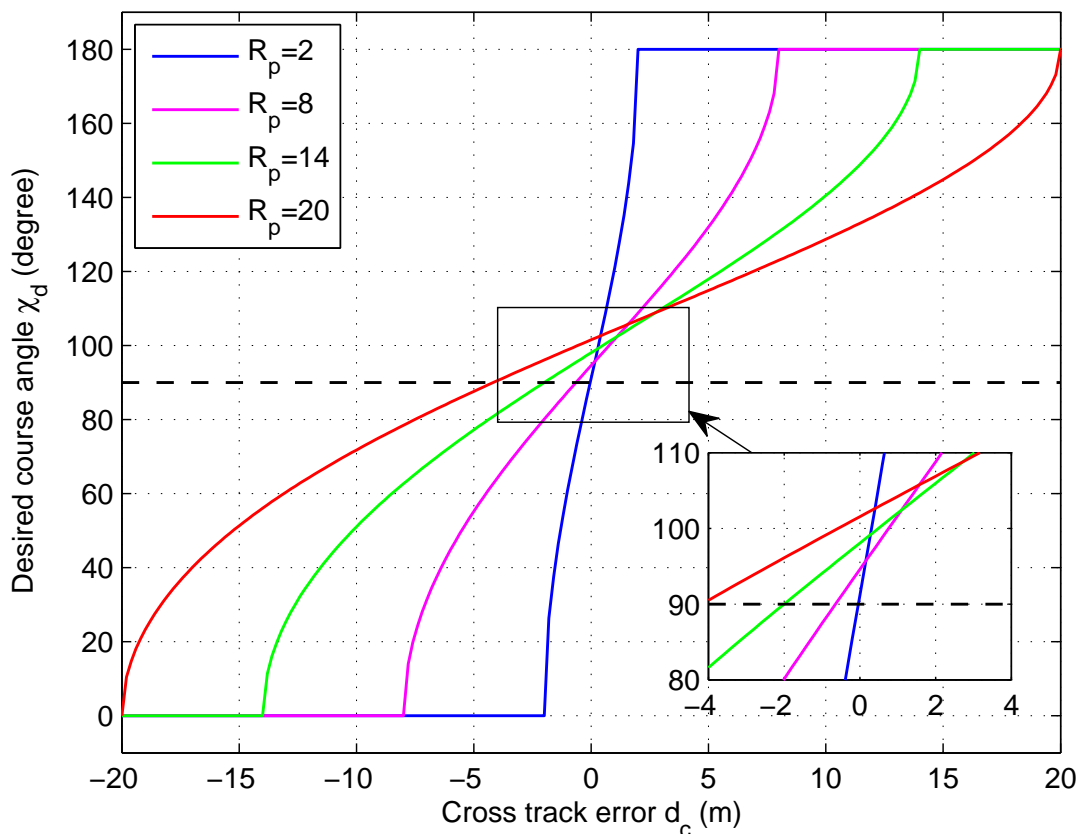
Figure 3.12: The exploration of the parameter space for Algorithm 6 to determine the relationship between desired course angle χ_d and the cross track error d_c with varied R_p. The performed search of parameter space is based on the line-of-sight method for circular path-following control.

3.4 Simulation Experiments

In chapter 2, the USV SeaCat's planar dynamic motion model in surge, sway and yaw has been constructed and the model parameters are successfully identified by performing tow tank tests and extensive field experiments. Taking advantage of this realistic motion model, a Matlab/Simulink simulator with the guidance and control system structure as shown in Fig. 3.3 has been built so that we can perform different path-following control experiments. For example, according to the flow chart in Fig. 3.13, we build the Simulink model for testing the vector field method. In Fig. 3.13, the initialization or the

preparation stage reads in the waypoint locations and perform the required coordinate conversion. The vector field path-following control stage decides whether we need to follow the straight-line or circular path, and depending on the relative position of the vehicle and the followed path, the desired course angle can be determined. The low-level control stage implements the PID controllers and continuously adjusts the two propellers' speed in order to track the desired speed and course direction. The flow chart in Fig. 3.13 displays an advantageous modular structure, based on which some advanced features can be conveniently incorporated. The initialization stage can integrate different path-planning features (e.g. obstacle avoidance) so that the waypoint list can be autonomously generated online instead of being defined by users. The path-following control stage is swappable, and the other two presented path-following control methods can be included without changing the rest of the whole structure.

The simulator is of great importance at the preliminary testing stage, because it can be conveniently employed for tuning and improving the guidance and control programs. In this section, we first introduce procedures to determine the PID parameter values for the two low-level motion controllers. Then, the metrics for evaluation of the performances of different algorithms are defined. Finally, a series of straight-line and circular path-following control tests are carried out to further illustrate the results we achieved from the parameter space exploration in section 3.3.

It is important to note that simulation experiments in this section are quite different from the previous parameter space exploration. Through exploring each algorithm's parameter space, we can only theoretically study the desired course angle with respect to different cross track errors. However, in the following discussion, when incorporating a USV's motion dynamics, we can investigate whether a platform can track the generated desired course angle successfully. This will be a valuable experience for us to choose appropriate path-following control parameters before we do any further field experiments.

Initialization

Vector Field
Path-Following Control

Low-level Speed and
Course Angle Control

Start

Load
Waypoint List

Coordinate
Conversion

Straight or
Circular Path ?

Straight

Circular

V_d=constant

$\chi_d = \chi_p - \dfrac{2}{\pi}(\chi_{Ms})\mathrm{atan}(k_s d_s)$

V_d=constant

$\chi_d = \chi_{Orbit} + \rho\left[\dfrac{\pi}{2} + \dfrac{2}{\pi}(\chi_{Mc})\mathrm{atan}(k_c d_c)\right]$

Reference V_d and χ_d

V_d

χ_d

$p=(n, e)^T$

V

$e_s = 0$?

$e_c = 0$?

χ

$p=(n, e)^T$

N

N

PID_1

PID_2

Ω_{sp}

Ω_{ca}

$\Omega_p = \Omega_{sp} + \Omega_{ca}$
$\Omega_s = \Omega_{sp} - \Omega_{ca}$

Ω_p

Ω_s

USV

Coordinate
Conversion
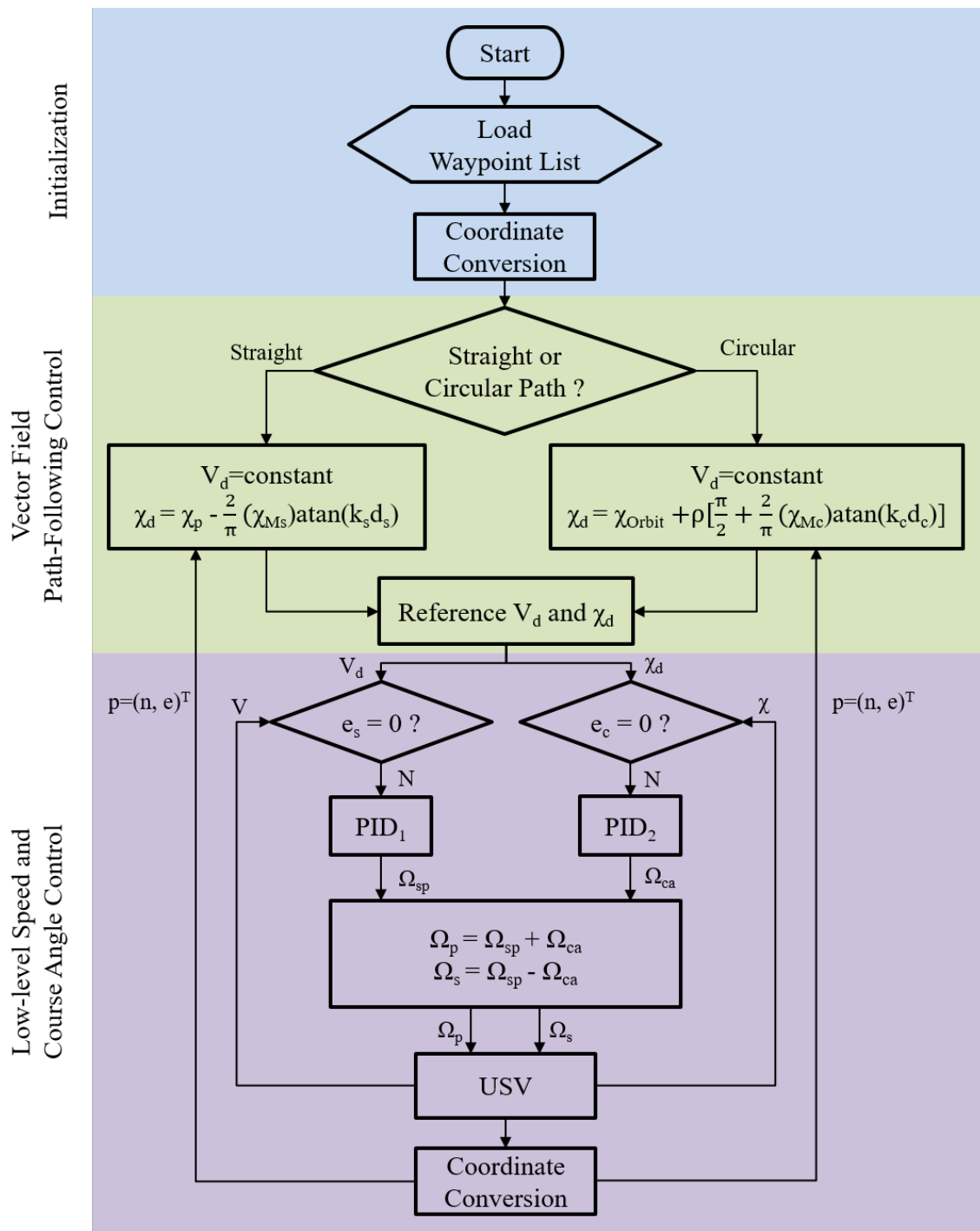
Figure 3.13: The USV SeaCat's guidance and control strategy flow chart. The guidance system implements the vector field method and the low-level controllers are responsible for speed and course-keeping control.

3.4.1 PID Controller Parameter Tuning

The low-level motion control system in Fig. 3.3 is Multiple-Input-Multiple-Output (MIMO) type, where the vehicle speed and course angle need to be controlled by the two thrusters. Our strategy is to first tune the PID control parameters for the speed controller to gain the best performance, and then we keep the settings and try to find the appropriate control parameter values for the course keeping controller.

The speed controller needs to quickly respond to the reference speed setting and minimize the steady-state speed error. Following this principle, we manually tune the speed controller parameters using the constructed simulator. It is assumed that the reference speed is 0.8 m/s, and some simulation results during the tuning process have been chosen and depicted in Fig. 3.14. In the figure, it can be seen that the incorporation of the integral gain K_{i1} will notably reduce the steady-state errors, and with larger values for K_{i1} the system response speed is increased until the overshoot happens when $K_{i1} = 100$. It has been found that using the derivative gain will not effectively vary the system response speed, and thus we use a constant value of $K_{d1} = 20$ in the last three tests in Fig. 3.14. If we use a higher proportional gain of $K_{p1} > 250$, we can further reduce the response time. However, a large value of K_{p1} corresponds to a large control signal for the two thrusters in the real-world tests, which may make them wear fast as time goes on. Additionally, when the USV is accelerated from zero speed, an instant large propeller setting will introduce large pitch motion, which is adverse for on-board sensor data collection and system stability. Therefore, we finally determine to use the parameter values of $K_{p1} = 250$, $K_{i1} = 80$ and $K_{d1} = 20$ for the following path-following control simulation experiments.

Based on the determined speed controller, we can start tuning the course-keeping controller parameters by implementing the heuristic Ziegler-Nichols method [47]. We assume that the reference speed is still 0.8 m/s, the vehicle's initial course angle is $0°$
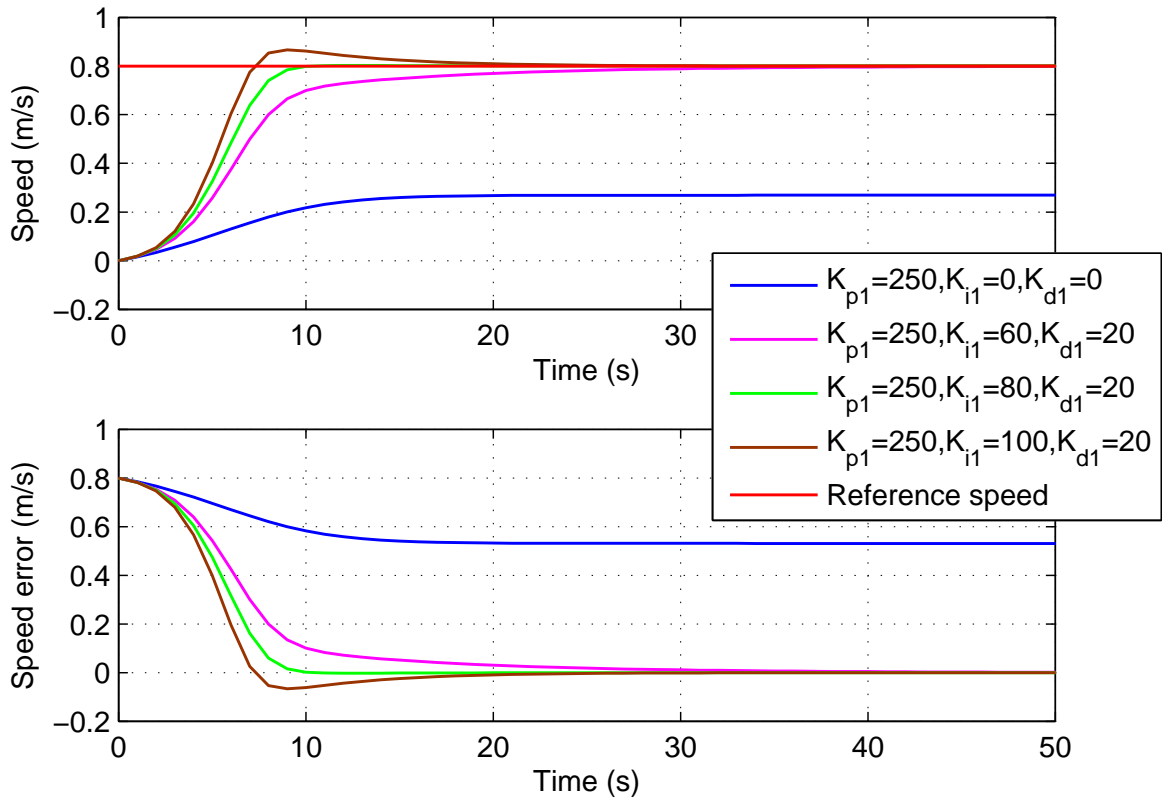
Figure 3.14: Demonstration of the speed controller with different control parameter settings. In this set of simulations, the reference speed is 0.8 m/s.

and the desired course angle is $40°$. The parameter tuning results are shown in Fig. 3.15. In the figure, the blue line represents when the proportional gain is increased to a large value when the vehicle's controlled course angle oscillates around the desired course angle. In this scenario, the proportional gain value and the oscillation period are determined and recorded as $K_u = 4$ and $T_u = 40\ s$. Following the Ziegler-Nichols method, we can compute the PID parameter values as $K_{p2} = 0.6K_u = 2.4$, $K_{i2} = 1.2K_u/T_u = 0.12$ and $K_{d2} = 3K_uT_u/40 = 12$. However, it turns out that when we implement the Ziegler-Nichols suggested controller, there is a large course angle overshoot. Through performing extensive tests as depicted in Fig. 3.15, we find out that by reducing the integral gain of K_{i2} the overshoot reduces.

To compare the performances with different PID parameter value settings, we employ the standard performance measure that includes rise time, settling time, steady-state error and percent of overshoot. A summary of the performance measure is given in Table 3.2. We can conclude that a larger integral gain K_{i2} will lead to a shorter rise time, but the percent of overshoot and settling time are much longer. Ultimately, to gain the best performance, we choose to implement the PD controller as our course-keeping controller, i.e. $K_{p2} = 2.4$, $K_{i2} = 0$ and $K_{d2} = 12$.

Table 3.2: Performance measure of the PID course-keeping controller

Integral gain K_{i2}	Rise time (s)	Settling time (s)	Steady-state error (°)	Percent of overshoot
0.12 (PID)	14	55	0	72.9%
0.06 (PID)	15	100	0	45.7%
0 (PD)	17	31	0	17.8%

3.4.2   Evaluation Metrics

In this section, we introduce the employed metrics for evaluation of the performance of different path-following control algorithms. In either simulation or field experiments, the USV SeaCat will be commanded to start from a remote location with respect to the followed path. Through implementation of a specific path-following control law, the platform will converge to and finally track the path. We define the time it takes from the initial position to when the vehicle enters the $\pm 2\ m$ band around the followed path as the convergence time T_c. Therefore, we can name the time range before T_c, i.e. $t \in [0, T_c]$, as the vehicle's transition period, while the time range of $t \in [T_c, +\infty)$ as the steady-state path-following period.

Two groups of metrics are developed corresponding to each time period. The first group focuses on the controller's performance during the transition period, and under
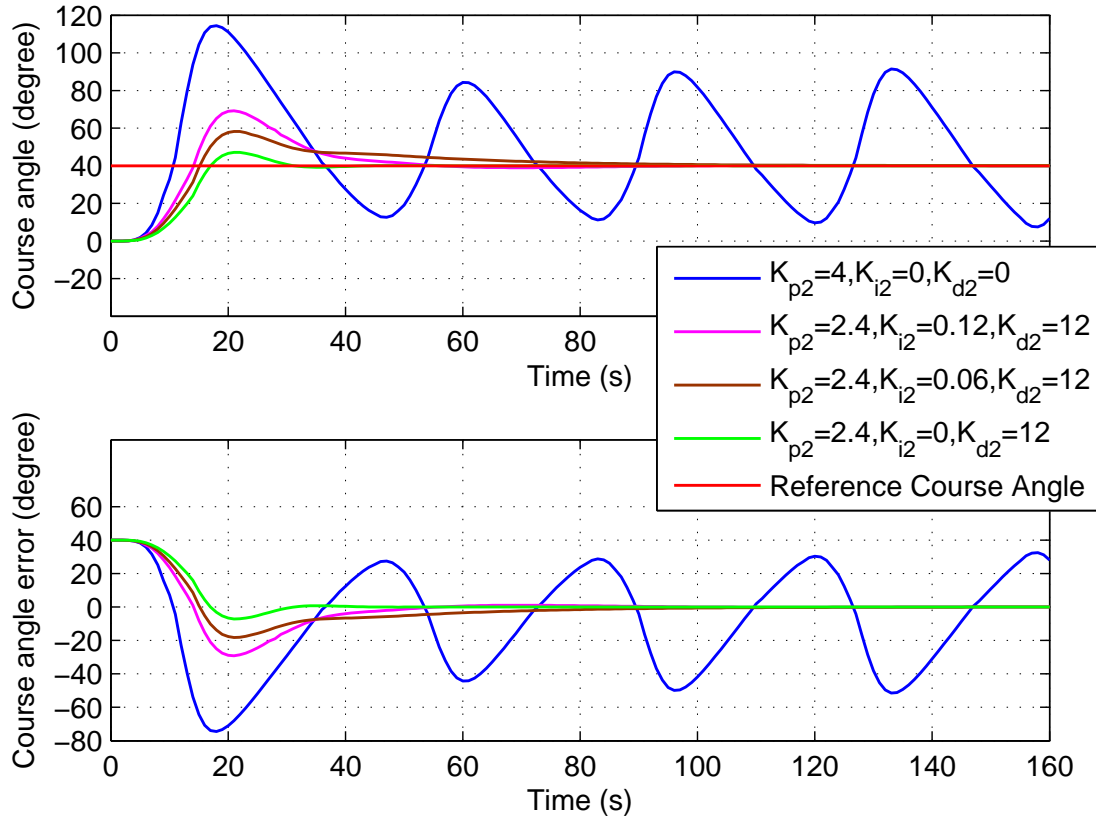
Figure 3.15: Demonstration of the course-keeping controller with different control parameter settings. In this set of simulations, the reference speed and course angle are 0.8 m/s and 40°, respectively.

this category we define the total control energy as

$$U_1 = \sum_{t=0}^{t=T_c} (\Omega_s(t) + \Omega_p(t))^2,$$

the total steering energy as

$$U_2 = \sum_{t=0}^{t=T_c} (\Omega_s(t) - \Omega_p(t))^2,$$

and the total path tracking error for the transition period as

$$E = \sum_{t=0}^{t=T_c} |d(t)|$$

where $d(t)$ represents the cross track error for either straight-line or circular path tracking case. The metrics of U_1 and U_2 provide a direct measure of the energy it takes for a USV to follow the desired path using the specific algorithm. A large number will indicate that this algorithm's control demand is high. For example, a large value of U_2 may indicate that the vehicle undergoes multiple turns to follow the straight-line path, which is not desirable.

The second group is used for evaluating the steady-state path tracking performance, and we choose to compute the average and standard deviation of the cross track errors as

$$E_{AV} = \frac{1}{N_t} \sum_{t=T_c}^{t=T_f} |d(t)|$$

and

$$E_{SD} = \sqrt{\frac{1}{N_t} \sum_{t=T_c}^{t=T_f} (d(t) - E_{AV})^2}.$$

Note that for these two metrics, the calculation time range is selected as $t \in [T_c, T_f]$, and since the sampling rate is 1 Hz, $N_t = T_f - T_c$ is the number of samples of the cross track error in this time range.

Although we have introduced five different metrics for evaluation of a path-following controller's performance, it is necessary to point out that some metrics may be more significant than others depending on the specific application. For example, if we need to operate a USV for an enduring mission, the total control energy and steering energy will be more important. We will need to find an algorithm that is most energy efficient, while the path tracking accuracy may not be a big concern. On the contrary, there may be

cases where a USV can only operate safely following a specific path in the seaway, under this circumstance, the safe path tracking accuracy will be much more important than the controller's consumed energy.

3.4.3 Straight-line Path-Following Control

In this section, we test the vehicle's straight-line path-following control performance by implementing the vector field, carrot chasing with integral gain and line-of-sight methods. Without loss of generality, in the simulation experiments, the straight-line path to be followed by a USV is defined in the NED frame with the northern path direction $\chi_p = 0°$. The two waypoints (endpoints) of the path are defined as $wp_i = (n_i, e_i)^T = (0,0)^T$ and $wp_{i+1} = (n_{i+1}, e_{i+1})^T = (250,0)^T$, and the initial USV location is assumed to be on the starboard side of the path, which is given as $p(0) = (n(0), e(0))^T = (0, 40)^T$. The vehicle's initial and desired moving speed is determined to be 0.8 m/s, and from the starting location the vehicle's initial course angle $\chi_i = 0°$. In addition, χ is the vehicle's actual course angle, and χ_d is the desired course angle computed from a specific path-following control algorithm.

3.4.3.1 Vector Field Method

In this section, we will examine how the control parameter k_s and the maximum approaching angle χ_{Ms} in Eq. 3.7 influence the vector field (VF) path-following control performance. By changing k_s and χ_{Ms}, the desired course angle curve varies, and we can investigate if a USV can track the generated reference angles successfully.

The simulation results with varied k_s have been depicted in Fig. 3.16. The left graph of Fig. 3.16a shows the vehicle trajectory while tracking the straight-line path. As expected, with larger values for k_s, the vehicle can be controlled to converge to the followed path at a faster rate. Nevertheless, if k_s is too large the vehicle will oscillate around the path.

Referring to the right graph in Fig. 3.16a, we can conclude that d_s will converge to zero with appropriate k_s values, but when k_s is too large d_s will oscillate around 0 m that indicates a bad path tracking performance. It is interesting to note that in the figure the path tracking error is not symmetric about $d_s = 0$, and this is due to the difference of the vehicle's starboard- and port-side turning dynamics as introduced in chapter 2. The graph in Fig. 3.16b compares the actual course angle χ with the desired course angle χ_d. Note that the curves of χ_d are related to the inverse tangent curves as shown in the parameter space exploration part in Fig. 3.5. Through this set of simulations, we can see when χ_d changes slowly, such as the case when $k_s = 0.03$, χ can be controlled to follow χ_d with a small mismatch. Whereas, when $k_s = 0.1$, due to the slow dynamics of the vehicle, it will take the vehicle some time before χ_d can be tracked. When the changing rate of χ_d is too fast, i.e. $k_s = 0.3$, χ will not converge to χ_d but oscillates around it.

Similarly, we can illustrate the influence of the maximum approaching angle χ_{Ms}. In section 3.3.1, we have already shown that the value of χ_{Ms} is related to the asymptotic lines of χ_d, and a larger value of χ_{Ms} corresponds to the χ_d curve with a faster changing rate. In this set of simulations, we keep a constant value of $k_s = 0.1$ and change three different settings of χ_{Ms} to check the path-following performance. The simulation results with varied χ_{Ms} are depicted in Fig. 3.17. Again, the left graph of Fig. 3.17a shows three different USV trajectories while tracking the path, and it clearly demonstrates that with a larger χ_{Ms} the vehicle will be controlled to converge faster. To the right of Fig. 3.17a, we can see the cross track error d_s converges to zero in all scenarios at different convergence rates. The plots in Fig. 3.17b further show that a larger value of χ_{Ms} will make the desired course angle χ_d converge at a faster rate, which makes it difficult for a USV to track. For example, when $\chi_{Ms} = 90°$, there is a large mismatch between χ and χ_d. It can also be visualized in Fig. 3.17b that a small oscillation occurs near (0,0) before χ finally converges to χ_d or χ_p.
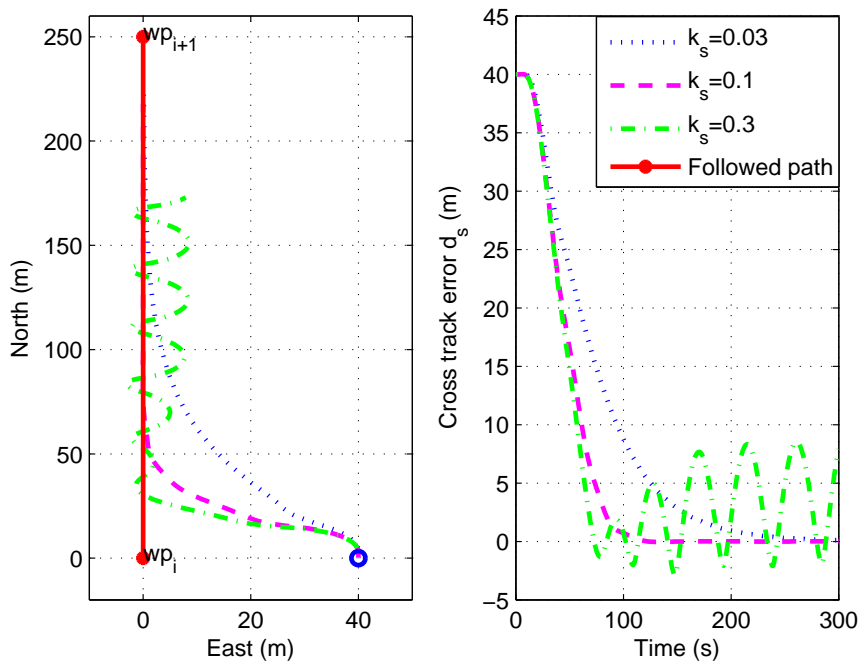
(a) USV trajectories (left) and cross track error plots (right)
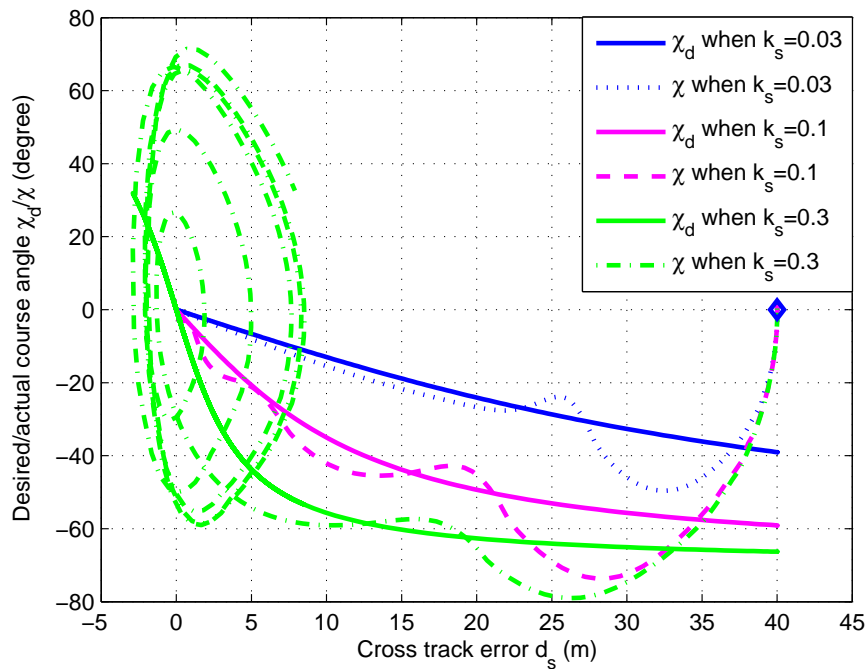
(b) Desired and actual course angle versus the cross track error

Figure 3.16: Simulation results using the vector field method with varied control parameter values of k_s. In the left graph of Fig. (a), the vehicle's initial location is marked with a circle, and it corresponds to the initial condition of $(d_s, \chi) = (40, 0)$ in Fig. (b), which has been marked with a diamond.
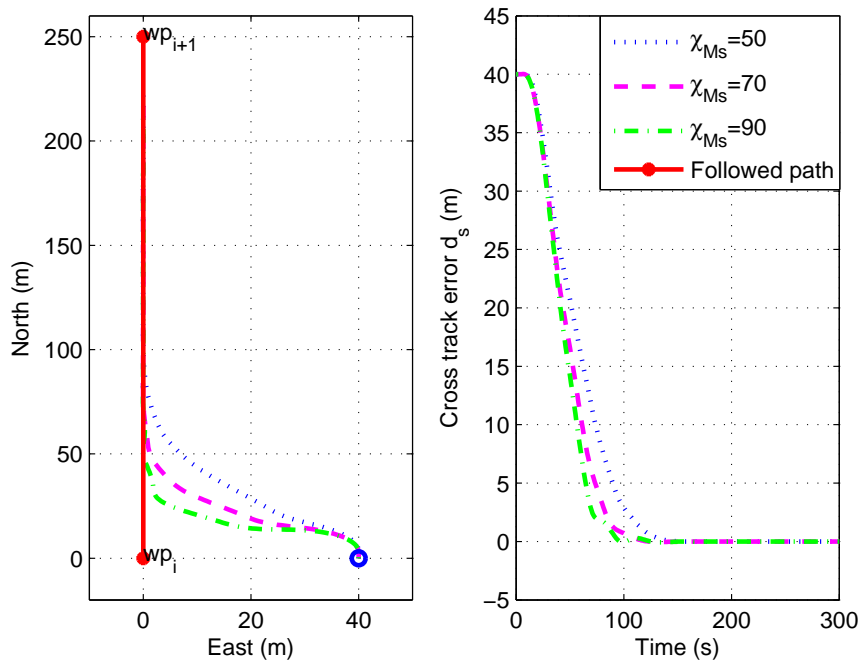
(a) USV trajectories (left) and cross track error plots (right)

(b) Desired and actual course angle versus the cross track error

Figure 3.17: Simulation results using the vector field method with varied maximum approaching angles of χ_{Ms}. In the left graph of Fig. (a), the vehicle's initial location is marked with a circle, and it corresponds to the initial condition of $(d_s, \chi) = (40, 0)$ in Fig. (b), which has been marked with a diamond.

Using the introduced metrics from section 3.4.2, we can numerically compare the path-following control performances with varied parameter settings of k_s and χ_{Ms}, and these results have been summarized in Table 3.3. The term k_s controls the vehicle's path-following convergence rate, and the column of T_c clearly shows that with larger values for k_s the convergence time T_c decreases. The transition period can be evaluated by U_1, U_2 and E, and we can see that with a shorter transition time, the computed U_1 and E values are also smaller. However, in order to quickly converge, the steering control energy will increase as indicated by U_2. During the steady-state path-following period, the best performance is achieved when $k_s = 0.1$. Comparing the simulation results in Fig. 3.16 to the last two columns in Table 3.3, we can see that when $k_s = 0.3$ the vehicle will oscillate around the desired path that will lead to large values of E_{AV} and E_{SD}.

The term χ_{Ms} defines the maximum approaching angle, and it will also affect the vehicle's convergence rate to the desired path. In Table 3.3, we can see that with larger values for χ_{Ms}, the vehicle can be controlled to converge faster, which corresponds to lower control energy U_1 and path tracking error E, and a higher energy demand for the steering control U_2. Whereas, the increment of χ_{Ms} will not increase the steady-state path tracking performance. Actually, in the case when $\chi_{Ms} = 90°$, the vehicle will undergo the oscillation before it finally track the desired path, and this phenomenon leads to larger computed values of E_{AV} and E_{SD}. Through comparison, we can determine that both k_s and χ_{Ms} should not be set to a very large value, or the USV will not be able to track the desired path successfully with acceptable performance.

3.4.3.2 Carrot Chasing Method with Integral Gain

We employ the same testing conditions as in section 3.4.3.1, i.e. the initial position $p(0) = (n(0), e(0))^T = (0, 40)^T$, $\chi_i = 0°$ and the desired speed is 0.8 m/s. In terms of the control parameters, the proportional gain is set as $K_{ps} = 0.1$ and the integral gain

Table 3.3: Performance evaluation of the vector field straight-line path-following method

Parameter	Value	T_c (s)	U_1 $(\times 10^7$ rpm$^2)$	U_2 $(\times 10^5$ rpm$^2)$	E $(\times 10^3$ $m)$	E_{AV} (m)	E_{SD} (m)
k_s (Fig. 3.16)	0.03	166	2.109	1.327	2.762	0.641	0.531
	0.1	85	0.940	2.446	1.862	0.128	0.362
	0.3	69	0.744	2.696	1.721	3.463	3.355
χ_{Ms} (Fig. 3.17)	50°	108	1.275	1.485	2.199	0.143	0.392
	70°	85	0.940	2.446	1.862	0.128	0.362
	90°	75	0.810	3.367	1.725	0.142	0.411

K_{is} is varied to achieve different path-following control performances. The simulation results have been depicted in Fig. 3.18. The left graph of Fig. 3.18a compares different vehicle trajectories, and it clearly shows that with larger values for K_{is}, the path tracking overshoot becomes larger. For instance, when $K_{is} = 0.01$, the overshoot is so large and the USV system turns unstable. The cross track error shown to the right of Fig. 3.18a indicates that the integral gain can cause a significant overshoot for d_s if it is not properly chosen. If $K_{is} = 0.0001$, d_s will converge to zero at a really slow rate during the steady-state period, while if $K_{is} = 0.01$, d_s will oscillate with large amplitude around the followed path. When $0.0001 < K_{is} < 0.01$, there will be a path tracking overshoot before the vehicle starts to converge. It can also be seen that a larger K_{is} setting in this range will cause more significant overshoot but will also drive the vehicle back to the path faster. Basically, we can summarize that we have to choose K_{is} carefully for the USV SeaCat, because the path-following performance is very sensitive to the value of this integral gain. In Fig. 3.18b, a comparison of the desired and actual course angle is depicted. Note that we only include the cases when the path-following control system is controllable. If $K_{is} = 0.0001$, the integral action is very small and there is no overshoot, and we can see that the existence of K_{is} introduces an offset, i.e. when $\chi_d = 0°$, $d_s \neq 0$. We can explain this situation by referring to Eq. 3.14. Because the vehicle approaches the path from one side, the integration $K_{is} \int d_s(t) dt$ will be a positive number that is added to $K_{ps} d_s(t)$ and

it acts as an offset. In the other two cases, the existence of integral gain will stretch the curve of χ_d to the negative plane first, and then the curve converges back to the origin. This effect corresponds to the occurrence of the overshoot in Fig. 3.18a.

To reduce the path tracking overshoot, one solution is to start the tests with small initial cross track error. In order to validate this, we perform the following supplementary simulation. All other testing conditions are maintained except that the vehicle's initial position is changed to $p(0) = (0, 20)^T$. The simulation results shown in Fig. 3.19 demonstrate our predictions. The trajectories and cross track errors depicted in Fig. 3.19a indicate that in all simulated scenarios the overshoot is reduced significantly compared to the results of Fig. 3.18a. However, when $K_{is} = 0.0001$, the path tracking offset still exists.

We evaluate the controller performance by using the metrics from section 3.4.2. Owing to the large overshoot for some tests, we need to make small modifications for the calculation of the convergence time T_c. If the overshoot occurs, T_c will be measured until the second time the vehicle enters the ± 2 m narrow band around the path. The other five metrics will be kept the same. The numerical evaluation results for experiments shown in Fig. 3.18 have been summarized in Table 3.4. Note that the case when the system is unstable is not included. With larger values for the integral gain K_{is}, T_c reduces and the total control energy U_1 also decreases since shorter time is needed for the vehicle's transition stage. As K_{is} increases, U_2 drops a little bit and then increases to a large number, and the reduced transition time T_c is believed to be the reason for the initial reduction of the value U_2. When $K_{is} = 0.003$, the overshoot is so large and it requires much more steering energy than the other two cases. The overshoot has adverse effects for the transition period path-following accuracy and this can be directly seen from the column of E. According to the computed E_{AV} and E_{SD}, we can conclude that a larger integral gain is better for the steady-state path tracking performances.
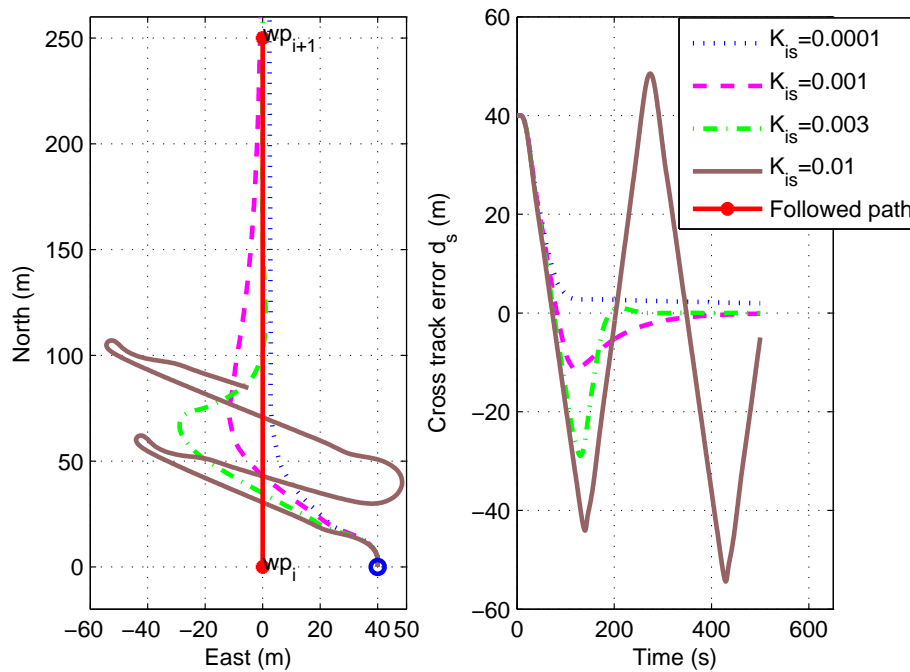
(a) USV trajectories (left) and cross track error plots (right)
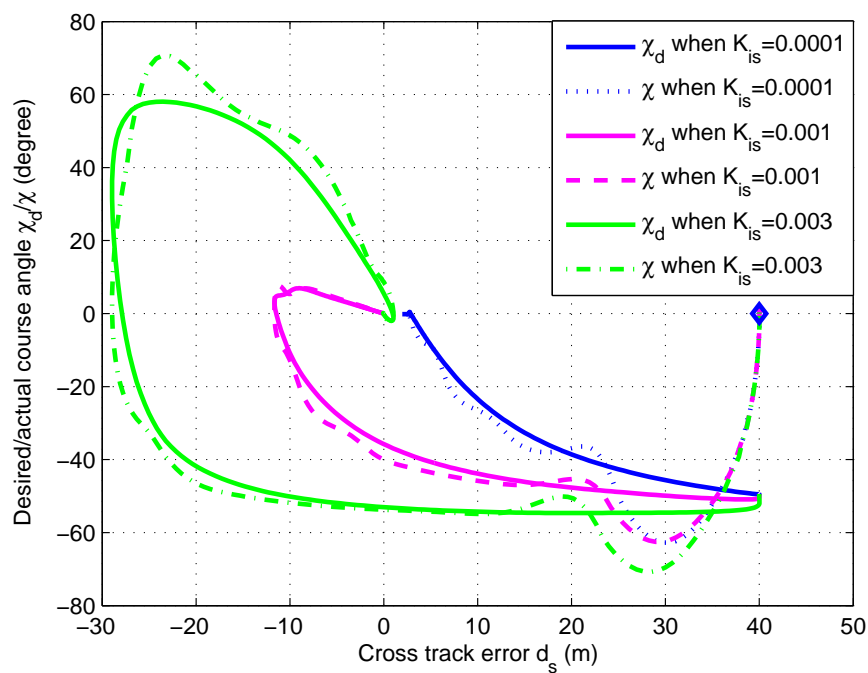
(b) Desired and actual course angle versus the cross track error

Figure 3.18: Simulation results using the carrot chasing method with different integral gain settings K_{is}. In the left graph of Fig. (a), the vehicle's initial location is marked with a circle, and it corresponds to the initial condition of $(d_s, \chi) = (40, 0)$ in Fig. (b), which has been marked with a diamond.
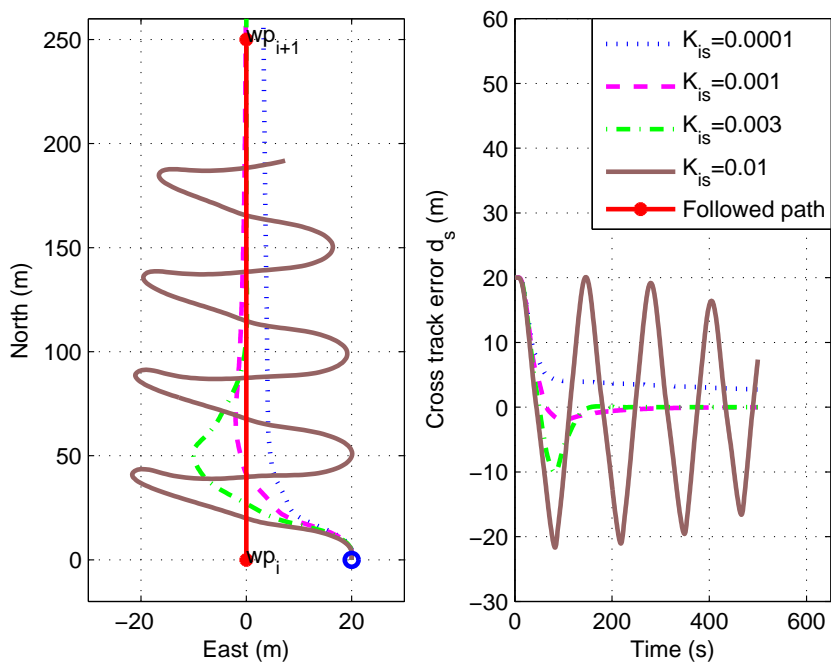
(a) USV trajectories (left) and cross track error plots (right)
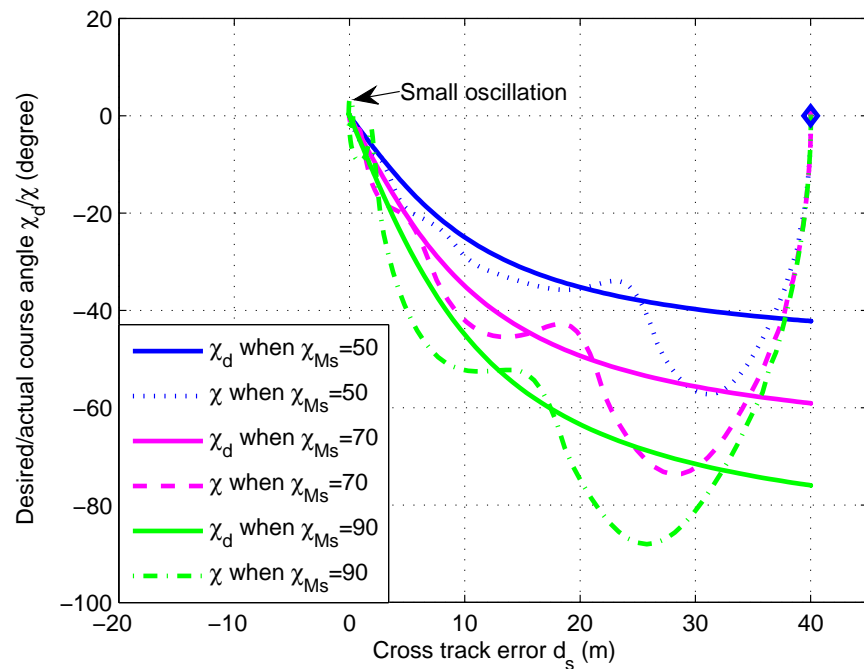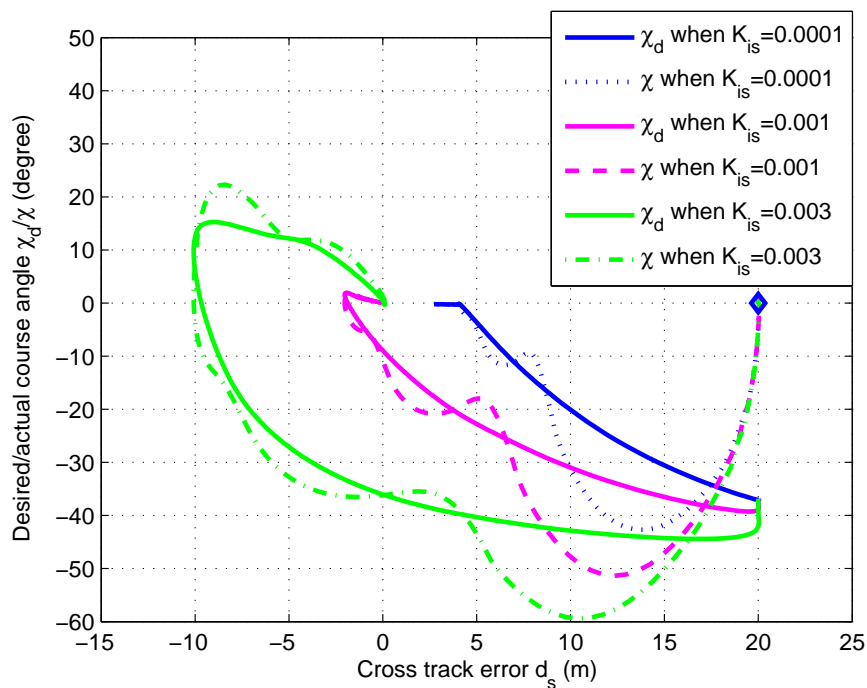

(b) Desired and actual course angle versus the cross track error

Figure 3.19: Simulation results using the carrot chasing method with different integral gain settings K_{is}. In the left graph of Fig. (a), the vehicle's initial location is marked with a circle, and it corresponds to the initial condition of $(d_s, \chi) = (20, 0)$ in Fig. (b), which has been marked with a diamond.

In summary, the integral gain needs to be chosen carefully, or there will be offset and large overshoot that are not favorable for the path tracking control of the vehicle. The path tracking performance is also closely related to the initial position of the vehicle with respect to the desired path, and a closer initial position will lead to smaller overshoot. Although the integral gain is disadvantageous during the vehicle's transition period, it shows a promising performance if only the steady-state path tracking stage is considered. Intrinsically, the integral gain will be the most effective if there are constant environmental influences that push the vehicle away from the followed path. The reason is the constant cross track errors will be accumulated to a large value, and thus the computed desired course angle χ_d in Eq. 3.14 will be further increased or decreased so that the vehicle can be guided back to the desired path.

Table 3.4: Performance evaluation of the carrot chasing straight-line path-following method with integral gain

Parameter	Value	T_c (s)	U_1 $(\times 10^7$ rpm$^2)$	U_2 $(\times 10^5$ rpm$^2)$	E $(\times 10^3$ $m)$	E_{AV} (m)	E_{SD} (m)
K_{is} (Fig. 3.18)	0.0001	481	6.396	1.831	3.030	1.981	0.0316
	0.001	282	3.638	1.770	3.145	0.705	0.515
	0.003	182	2.244	3.163	3.491	0.166	0.371

3.4.3.3 Line-of-Sight Method

In this part, we evaluate the Line-of-Sight (LOS) path-following control method. There is only one control parameter that can be changed to vary the controller's performance and it is the circle radius R_p around the vehicle. In section 3.3.3, we have demonstrated that when the circle-path intersection happens, an abrupt change of χ_d might make it difficult for a USV with slow dynamics to track. In this series of simulations, the vehicle motion dynamics are considered, and we can determine if LOS can be successfully employed for straight-line path tracking.

We keep the same simulation test conditions, and the results are depicted in Fig. 3.20. The left graph of Fig. 3.20a shows that during the initial transition period, i.e. $t \in [20, 40]$, the three trajectories coincide. If we refer to Fig. 3.20b, we can determine that the reason is when the vehicle is too far away from the path the desired course angle is $-90°$ in all three testing conditions. In Fig. 3.20a, the vehicle trajectories become different after the circle-path intersection occurs, and it shows that when $R_p = 8$ the system tends to be unstable and the vehicle will oscillate around the followed path. The cross track error shown to the right of Fig. 3.20a suggests that small R_p will quickly drive d_s to zero but will generate the d_s oscillation. In Fig. 3.20b, χ_d will be orthogonal to the followed path direction $\chi_p = 0°$ until the path and circle intersects. It can be seen that when R_p varies, the intersection points are different, which has been indicated by the three arrows. The abrupt change of χ_d also happens at these positions, where a large mismatch between χ and χ_d occurs. If $R_p = 8$, χ_d converges at a fast rate which makes it even impossible for the USV with slow dynamics to track successfully, and this will cause path tracking oscillation during the steady-state period. As for the other two cases, the vehicle will undergo small oscillations before χ_d finally converges to the followed path direction.

The numerical evaluation using the introduced metrics is summarized in Table 3.5. The small R_p corresponds to a fast converging χ_d as the reference, and it will lead to a short converging time. For the other two cases, T_c is larger and their values are close with each other. The column of U_1 is mainly influenced by T_c, and a longer time requires higher energy. The steering energy U_2 shows much larger values compared to Table 3.3 and Table 3.4, and this is because at the initial stage the vehicle is directed by the maximum approaching angle of $\chi_d = -90°$. The transition path tracking error E is the smallest when $R_p = 8$. Whereas, during the steady-state path tracking period, $R_p = 8$ will control the vehicle to oscillate around the path with large and choppy path tracking
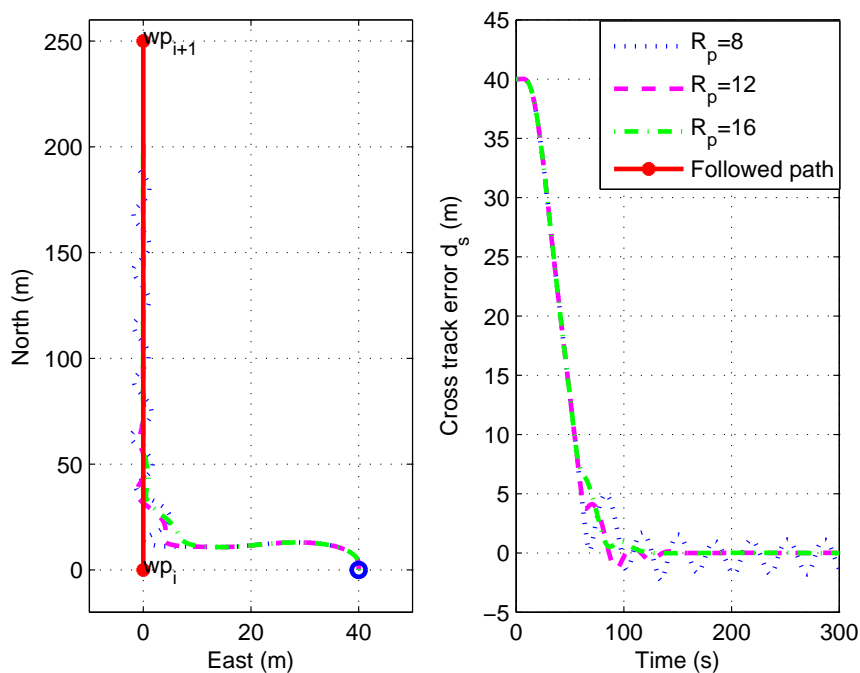
(a) USV trajectories (left) and cross track error plots (right)
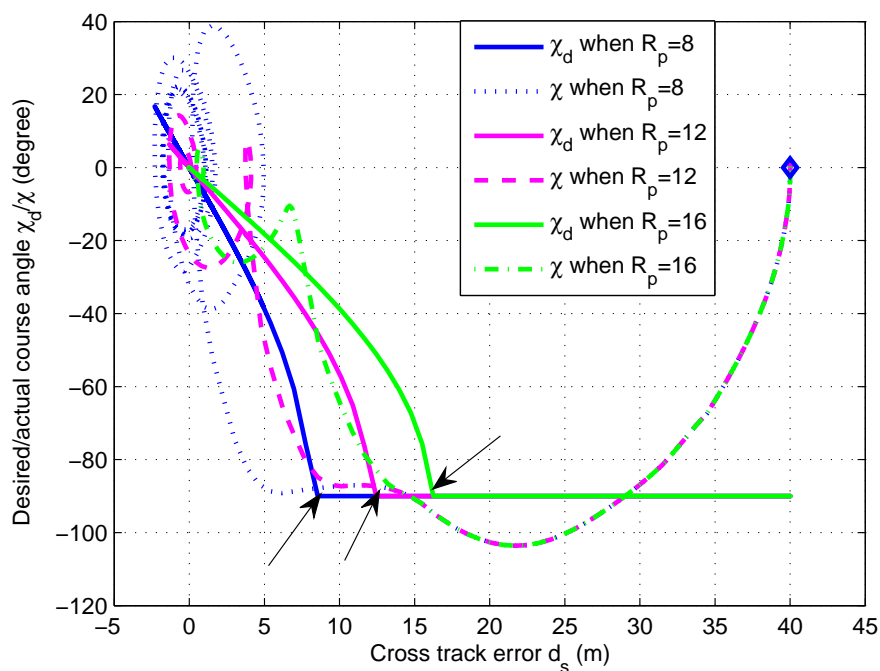
(b) Desired and actual course angle versus the cross track error

Figure 3.20: Simulation results using the line-of-sight method with different settings R_p. In the left graph of Fig. (a), the vehicle's initial location is marked with a circle, and it corresponds to the initial condition of $(d_s, \chi) = (40, 0)$ in Fig. (b), which has been marked with a diamond.

errors indicated by E_{AV} and E_{SD}. As for the other two cases, we can summarize that the path can be accurately tracked with really small cross track errors.

Table 3.5: Performance evaluation of the line-of-sight straight-line path-following method

Parameter	Value	T_c (s)	U_1 ($\times 10^7$ rpm^2)	U_2 ($\times 10^5$ rpm^2)	E ($\times 10^3$ m)	E_{AV} (m)	E_{SD} (m)
R_p (Fig. 3.20)	8	65	0.722	4.993	1.661	1.228	1.576
	12	81	0.929	5.954	1.722	0.153	0.378
	16	79	0.882	4.981	1.740	0.139	0.344

3.4.3.4 Comparison of Straight-line Path-Following Control Methods

The best parameter setting for each path-following control algorithm has been chosen for comparison, and the results are summarized in Table 3.6. The CCI method has a relatively bad performance for the transition period, and the reason is the occurrence of large overshoot. Through comparison of the other two algorithms, we can find LOS will make the vehicle converge at a faster rate, but at the same time it requires a higher steering energy U_2. Additionally, a smaller T_c will correspond to a smaller control energy U_1 and transition tracking error E. Although LOS provides a better transition performance, we have to be aware that it is at the cost of supplying twice the energy that is needed for VF. According to the last two columns, we can see the steady-state path tracking stage features a close performances across the three methods. However, it is noteworthy that CCI will be more robust to the environmental disturbances, and potentially, it will have a better performance in the real tests.

3.4.4 Circular Path-Following Control

In this part, we will evaluate the circular path-following performance using the introduced algorithms from Table 3.1. Similar to the straight-line path tests, we employ the USV

Table 3.6: Comparison between the three straight-line path-following control methods

Method	Value	T_c (s)	U_1 ($\times 10^7$ rpm^2)	U_2 ($\times 10^5$ rpm^2)	E ($\times 10^3$ m)	E_{AV} (m)	E_{SD} (m)
VF	k_s=0.1	85	0.940	2.446	1.862	0.128	0.362
CCI	K_{is}=0.003	182	2.244	3.163	3.491	0.166	0.371
LOS	R_p=16	79	0.882	4.981	1.740	0.139	0.344

SeaCat's dynamic motion model from chapter 2 and the guidance and control system structure in Fig. 3.3. Without loss of generality, in the simulation the circular path origin is defined as the local origin, i.e. $p_c = (n_c, e_c)^T = (0,0)^T$, and the USV position is defined in NED frame in meters. We assume that the USV's starting position is located at $p(0) = (n(0), e(0))^T = (0, 60)^T$, its initial and desired moving speed is 0.8 m/s, and the initial course angle $\chi_i = 0°$.

3.4.4.1 Vector Field Method

We start by examining the followed circle radius R and its influence on the path-following control performance. We assume that $k_c = 0.1$, the maximum approaching angle $\chi_{Mc} = 70°$ and R has values of 20 m, 50 m and 100 m. The simulation results are depicted in Fig. 3.21. In Fig. 3.21a, the desired circular paths are represented by solid lines. Through comparison, we can conclude that in all simulated cases the desired paths can be tracked successfully. However, referring to the top graph of Fig. 3.21b, we can determine that the steady-state cross track errors d_c for different sized circles are non-zero. Actually, it turns out that when the followed circle is larger, the steady-state value of d_c gets smaller with less oscillation. This phenomenon is owed to the slow yaw dynamics of the USV SeaCat. In section 3.4.1, we have investigated the tuning of the course-keeping PID controller parameters. As shown in Fig. 3.15, even with the well-tuned parameters, it will still take around 30 s to reach the reference desired course angle χ_d. While tracking the circle, χ_d is always changing and the low-level controller is not able to keep up with it as shown to

the top of Fig. 3.21b, and this will result in the constant offset d_c during the steady state. A smaller circle corresponds to χ_d that changes at a much faster rate, which will make it more difficult for a USV to keep up with. The bottom graph compares the desired and actual course angle of the vehicle. To clearly show the results, both χ_d and χ are unwrapped so that the angles are not restricted within (-180°,180°]. We can summarize that in all testing conditions, χ will be successfully controlled to converge to χ_d. When $R = 20$, the steady-state χ_d will oscillate around a constant offset d_c, while in the other two cases, the offset and oscillation are smaller.

We have already shown the similar control effects when adjusting k_s and χ_{Ms} in section 3.4.3.1, and for simplicity, in this part we will only examine control parameter k_c and its influence on following the circular path. We assume that $R = 20$ m and $\chi_{Mc} = 70°$. The results have been shown in Fig. 3.22. In Fig. 3.22a, we can see with larger values for k_c, the vehicle converges much faster. Whereas, if k_c is too large, the system will start to oscillate around the desired path. The graph to the top of Fig. 3.22b depicts the converging tendency for d_c, and it clearly shows that in the first two cases, the increased value of k_c will lead to a smaller steady-state value of d_c, as can also be visualized in Fig. 3.22a. However, for the last case, the system tends to be unstable and d_c will oscillate around zero. The bottom graph of Fig. 3.22b shows that if k_c is small the desired course angle χ_d changes slowly and it is easy for the vehicle to follow with small oscillation.

We can numerically evaluate the controller performance using the metrics introduced in section 3.4.2, and these results are summarized in Table 3.7. When evaluating the controller performance with varied circle radius R, the initial relative positions of the vehicle are quite different with respect to the followed circle as shown in Fig. 3.21. Hence, we can only compare the steady-state cross track errors using E_{AV} and E_{SD}. It is evident that a larger circle will be tracked with better accuracy. The remaining computed metrics can be used for comparison with other path-following algorithms in our later discussion.
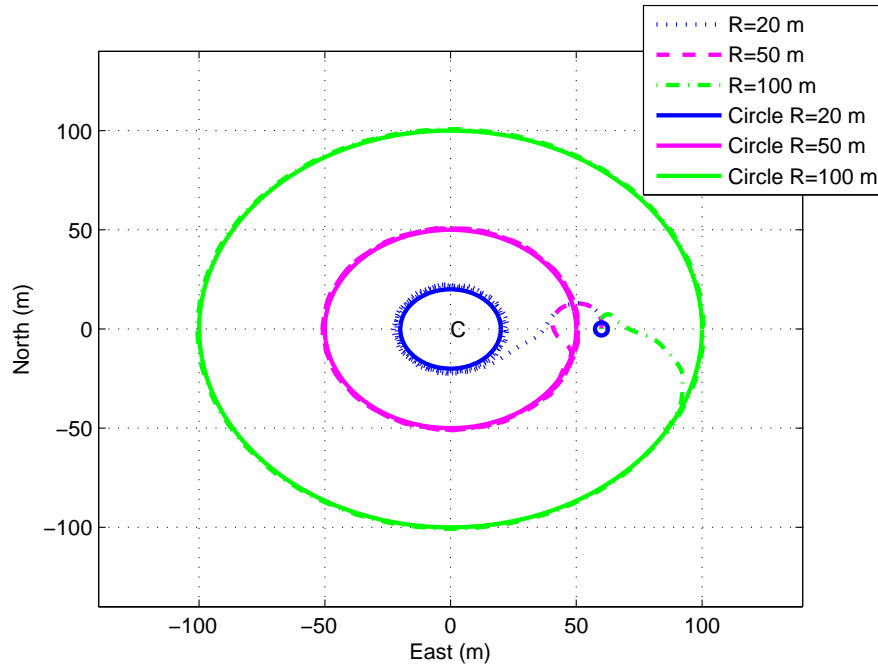
(a) USV trajectories
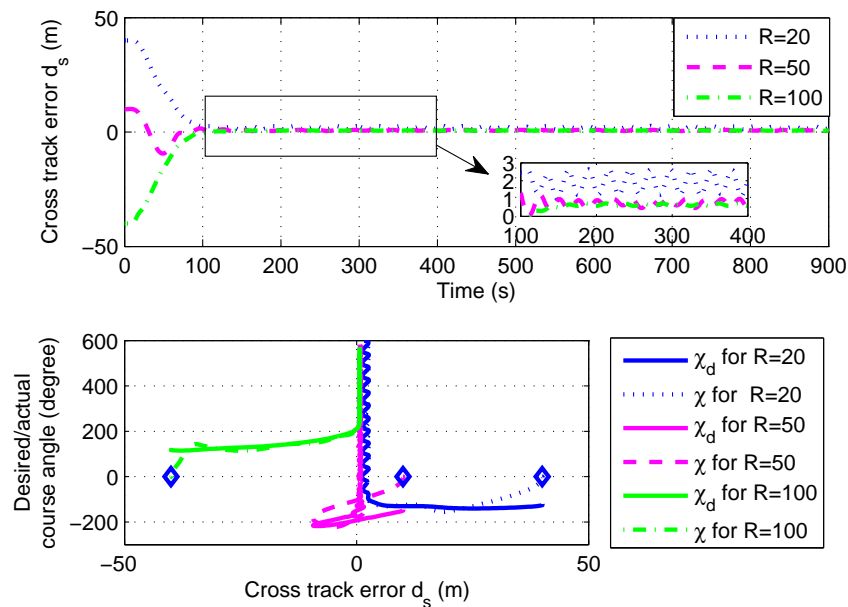
(b) Path-following performance

Figure 3.21: Circular path-following simulation results using the vector field method with different followed circle radius R. In Fig. (a), the vehicle's initial position is marked with a circle, and it corresponds to three different initial conditions for the three circular path tracking cases, i.e. $(d_s, \chi) = (40, 0)$, $(10, 0)$ and $(-40, 0)$, which have been marked with diamonds to the bottom of Fig. (b). Note that Fig. (a) shows circles that appear non-circular due to the aspect ratio of the plot.

(a) USV trajectories

(b) Path-following performance
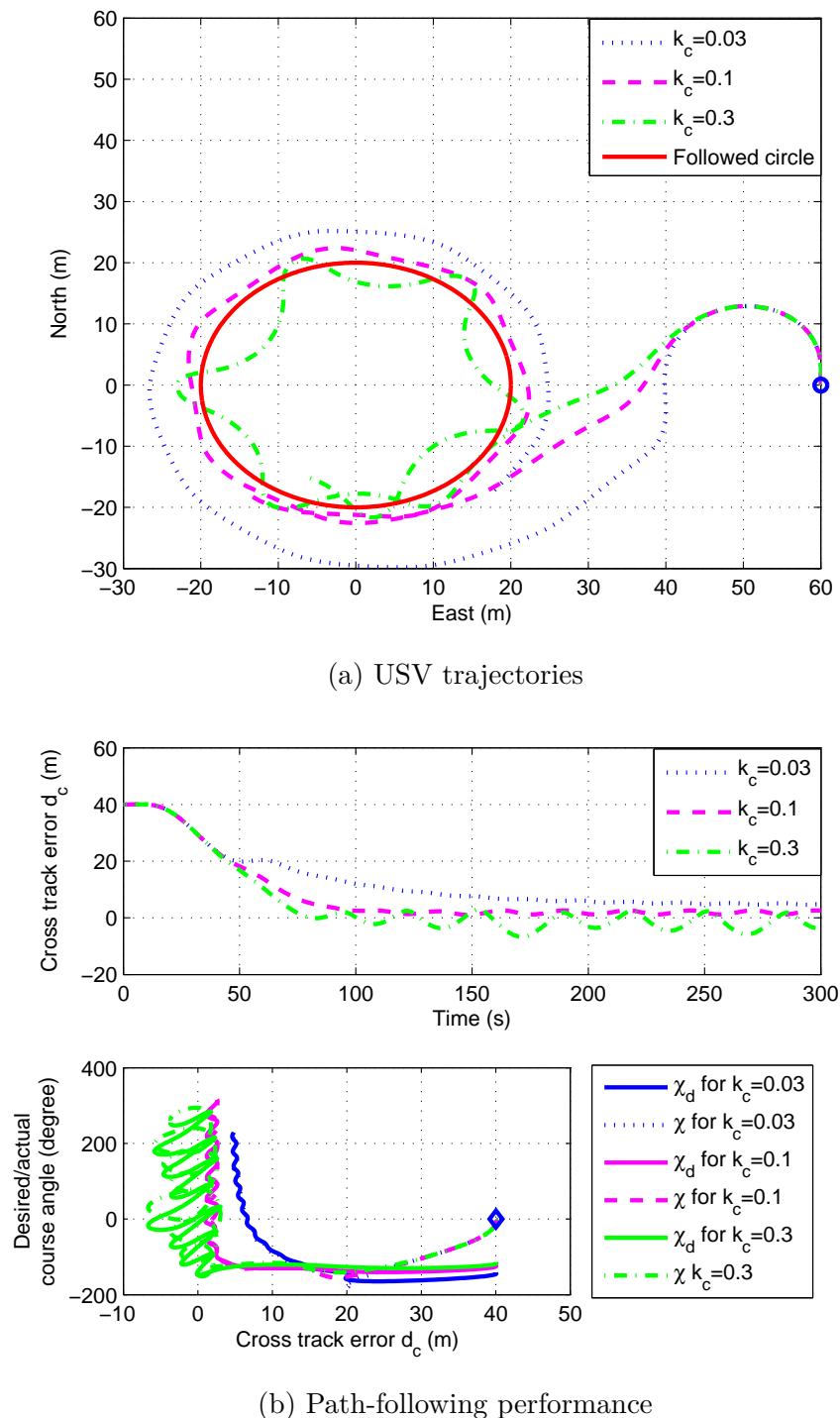
Figure 3.22: Circular path-following simulation results using the vector field method with different control parameter k_c settings. In Fig. (a), the vehicle's initial position is marked with a circle, and it corresponds to the initial condition $(d_s, \chi) = (40, 0)$ that has been marked with a diamond to the bottom of Fig. (b). Note that Fig. (a) shows circles that appear non-circular due to the aspect ratio of the plot.

The term k_c controls the convergence rate, and the column of T_c clearly shows that with larger values for k_c the convergence time reduces. During the transition period, when T_c is smaller, the required total and steering energy, i.e. U_1 and U_2, will get lower. Meanwhile, a smaller tracking error E will be achieved. During the steady-state path-following period, when k_c is too small, there will be a large constant cross track error d_c with small variance. If, however, k_c is too large, the vehicle will follow the desired path with large oscillations. The best performance is achieved when $k_c = 0.1$ but with a small constant error. Through analysis, we can determine that due to the slow dynamics of the studied platform, it is easier to track larger circles with better performance. Further, the control parameter k_c needs to be chosen with an appropriate value or the system will have a large circular path tracking error and the system may turn unstable.

Table 3.7: Performance evaluation of the vector field circular path-following method

Parameter	Value	T_c (s)	U_1 ($\times 10^7$ rpm^2)	U_2 ($\times 10^5$ rpm^2)	E ($\times 10^3$ m)	E_{AV} (m)	E_{SD} (m)
R (Fig. 3.21)	20	116	1.333	6.302	2.084	1.878	0.477
	50	66	0.760	10.836	0.454	0.756	0.314
	100	85	0.923	4.164	1.820	0.639	0.274
k_c (Fig. 3.22)	0.03	247	2.924	8.535	3.520	4.924	0.194
	0.1	116	1.333	6.302	2.084	1.870	0.496
	0.3	75	0.850	5.537	1.849	2.279	2.525

3.4.4.2 Carrot Chasing Method with Integral Gain

To the best of the author's knowledge, there is no equivalent study of implementation of the carrot chasing method with integral gain (CCI) for the circular path-following control. However, it is important to research this method since the incorporation of the integral gain can potentially increase the path-following robustness to environmental disturbances.

We examine the controller performance on different sized circles, and the results are shown in Fig. 3.23. It is assumed that $K_{pc} = 0.1$ and $K_{ic} = 0.0001$. As shown in Fig.

3.23a, started from the same location the USV can be successfully controlled to follow each desired circle. Referring to the top graph of Fig. 3.23b, we can determine that incorporation of the integral gain will make the vehicle slowly converge to the followed path so that d_c tends to zero. The enlarged plots show that when $R = 100$, d_c converges slowly with less oscillation. While, if $R = 20$ or $R = 50$, d_c will converge faster to zero but there are more oscillations around the path. The bottom graph of Fig. 3.23b shows that while tracking a larger circle the oscillation around the path becomes smaller. When $R = 100$, d_c will have an overshoot before the vehicle is slowly directed back to the desired path. This phenomenon has also been revealed in section 3.4.3.2 for the straight-line path case.

Now, we can examine the integral gain K_{ic} and its influence on the vehicle performance. The followed circle radius is assumed as 20 m, and $K_{pc} = 0.1$ is kept as constant. The simulation results have been depicted in Fig. 3.24. In Fig. 3.24a, we can see with larger values for K_{ic} the vehicle can be controlled to converge more quickly, but the control effort also becomes more aggressive. For instance, when $K_{ic} = 0.001$, the vehicle is controlled to move inside the followed circle and then converges to the path. We can refer to the top graph of Fig. 3.24b to compare the system performance. Apparently, large K_{ic} introduces large overshoot of d_c, but if time is long enough, in all simulated conditions the cross track error will converge to zero. A similar finding can also be visualized in the bottom graph of Fig. 3.24b, where for the cases of $K_{ic} = 0.0003$ and $K_{ic} = 0.001$, χ_d stretches to the negative plane and then converges back to the line of $d_c = 0$. A very large gain setting may introduce significant overshoot with respect to the followed circle. Therefore, we can conclude that the integral gain needs to be chosen carefully to achieve the best path tracking performance. For the long run, K_{ic} can drive the cross track error to zero and this is a better characteristic than the vector field method in section 3.4.4.1 where a constant tracking error exists.
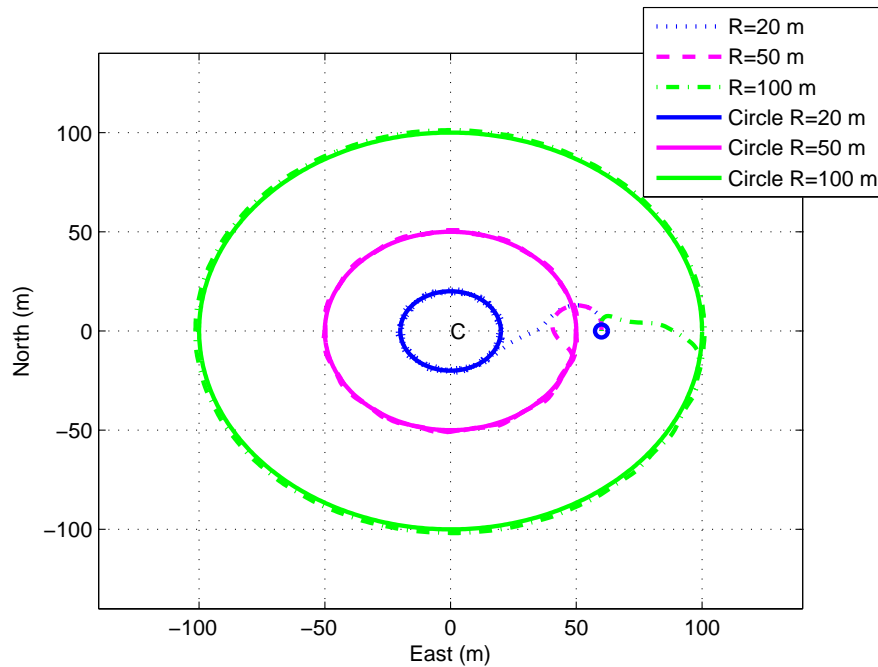
(a) USV trajectories
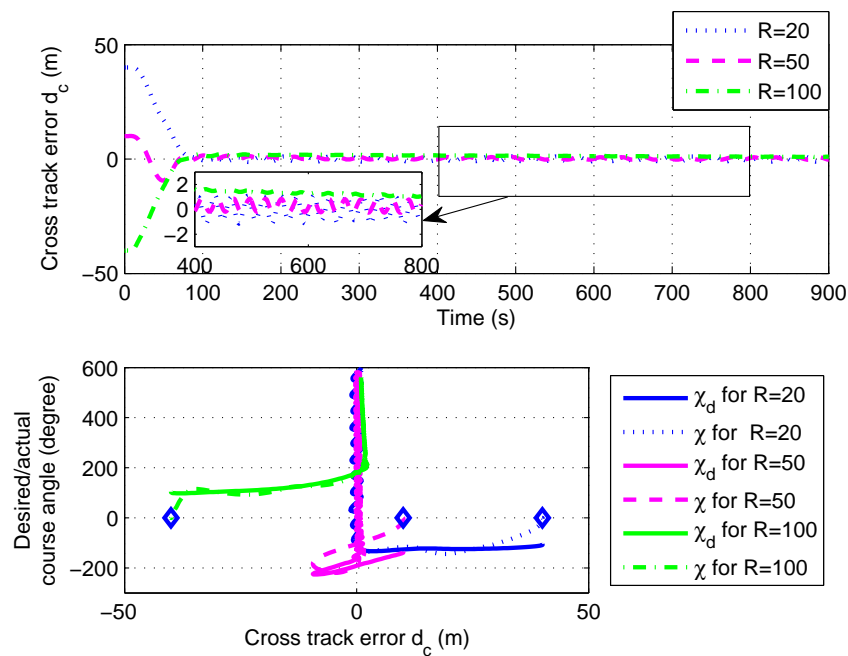
(b) Path-following performance

Figure 3.23: Circular path-following simulation results using the carrot chasing method with integral gain. In Fig. (a), the vehicle's initial position is marked with a circle, and it corresponds to three different initial conditions for the three circular path tracking cases, i.e. $(d_c, \chi) = (40, 0)$, $(10, 0)$ and $(-40, 0)$, which have been marked with diamonds to the bottom of Fig. (b). Note that Fig. (a) shows circles that appear non-circular due to the aspect ratio of the plot.

(a) USV trajectories
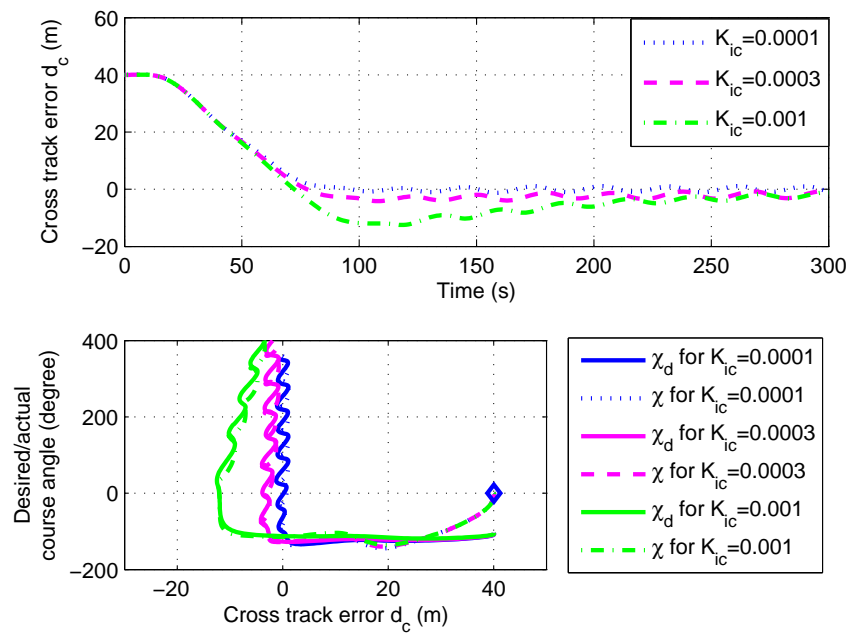
(b) Path-following performance

Figure 3.24: Circular path-following simulation results using the carrot chasing method with different integral gain settings K_{ic}. In Fig. (a), the vehicle's initial position is marked with a circle, and it corresponds to the initial condition $(d_c, \chi) = (40, 0)$ that has been marked with a diamond to the bottom of Fig. (b). Note that Fig. (a) shows circles that appear non-circular due to the aspect ratio of the plot.

The numerical evaluation is based on the defined metrics from section 3.4.2, and the results are summarized in Table 3.8. Again, we only compare E_{AV} and E_{SD} for varied sized circles, and the remaining calculated metrics will be used for later discussion. Based on the last two columns, we can conclude that the best performance is achieved when tracking the 50 m circle, and when the tracked circle is 20 m, there will be relatively large oscillations as suggested by E_{SD}. Combining the table with Fig. 3.23, we can see when $R = 100$ the vehicle needs time to converge to the path, and this is the reason E_{AV} has a large value.

The integral gain K_{ic} will introduce significant path tracking overshoot, and it will elongate the convergence time as indicated by the column of T_c. It can be seen that a larger T_c corresponds to a higher value of U_1, U_2 and E. In terms of the steady-state path tracking stage, we can see when $K_{ic} = 0.0001$ the mean tracking error E_{AV} is the smallest. Still, our evaluation time is limited and for the cases where overshoot is large it needs long time to converge. This is the reason the computed E_{AV} for the other two scenarios has relatively large values.

The incorporation of the integral gain will lead to overshoots with respect to the followed circle in the transition stage. However, for the long run, the integral gain can potentially reduce the path tracking error and behave more robust when considering the environmental disturbances in the real tests.

Table 3.8: Performance evaluation of the carrot chasing circular path-following control algorithm with integral gain

Parameter	Value	T_c (s)	U_1 ($\times 10^7$ rpm^2)	U_2 ($\times 10^5$ rpm^2)	E ($\times 10^3$ m)	E_{AV} (m)	E_{SD} (m)
R (Fig. 3.23)	20	78	0.881	5.297	1.867	0.656	0.737
	50	66	0.761	10.991	0.453	0.421	0.439
	100	67	0.689	3.939	1.592	1.409	0.420
K_{ic} (Fig. 3.24)	0.0001	78	0.881	5.297	1.867	0.643	0.738
	0.0003	149	1.734	6.313	2.045	2.201	0.895
	0.001	268	3.151	10.678	3.152	2.157	0.677

3.4.4.3 Line-of-Sight Method

The exploration of the parameter space in section 3.3.3 reveals that the Line-of-Sight (LOS) method may not be feasible for the accurate circular path tracking. In this part, we employ the dynamic motion model to evaluate LOS's performance.

The LOS method applied on varied sized circles is firstly evaluated, and the results are depicted in Fig. 3.25. In this set of simulation, $R_p = 8$ and the followed circle is changed from 20 m to 100 m. In Fig. 3.25a, started from the same position, the USV can be successfully controlled to follow each desired path. The top graph of Fig. 3.25b indicates that in all cases the steady-state cross track error converges to zero, and the enlarged plots also show that d_c will oscillate around zero. The bottom graph provides another perspective for evaluation of d_c and it can be seen that in all cases d_c will eventually converge and oscillate around zero. From this plot, we can also notice that the abrupt change of χ_d, highlighted by the arrows, will make it difficult for a USV with slow dynamics to track and it is where large mismatch occurs.

We evaluate the path tracking performance with different control parameter values of R_p, and the results are shown in Fig. 3.26. Note that the followed circle radius is assumed as $R = 20$ m. In Fig. 3.26a, an interesting phenomenon can be visualized where with larger values for R_p the vehicle turns out to operate inside the followed circle with a close to constant cross track error. This feature is owed to the fact that when implementing LOS, the target point position is towards the inside of the circle instead of the circle's tangential direction, which has already been discussed in section 3.3.3. It also shows that with the larger setting of R_p the path-following convergence rate decreases. The graph to the top of Fig. 3.26b displays that the best performance is achieved by setting $R_p = 8$, and in the other two cases, there will be constant negative cross track errors. The graph on the bottom shows that with larger values for R_p, the actual course angle χ will diverge from the line $d_c = 0$, which suggests a bad path-following performance. However, when
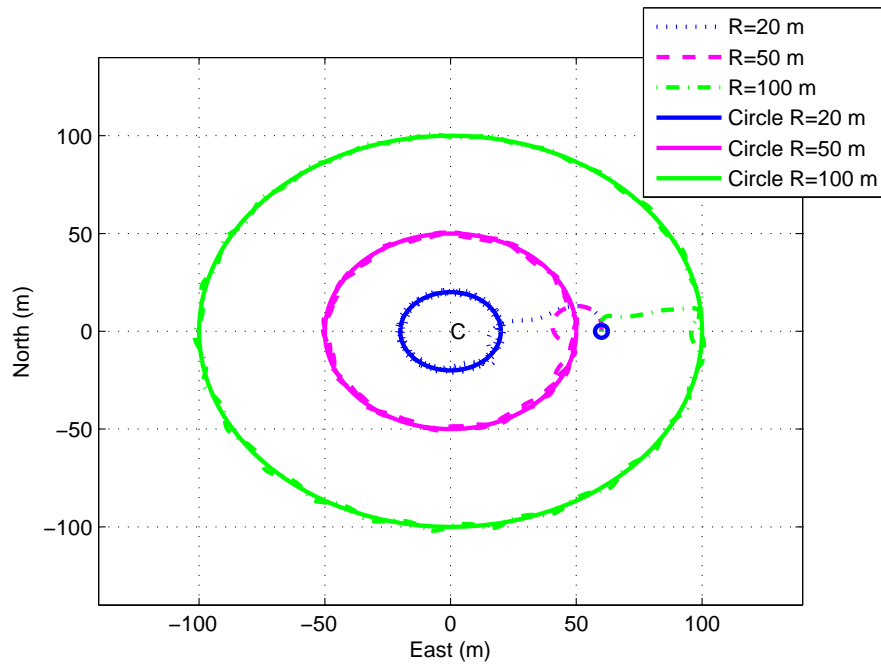
(a) USV trajectories
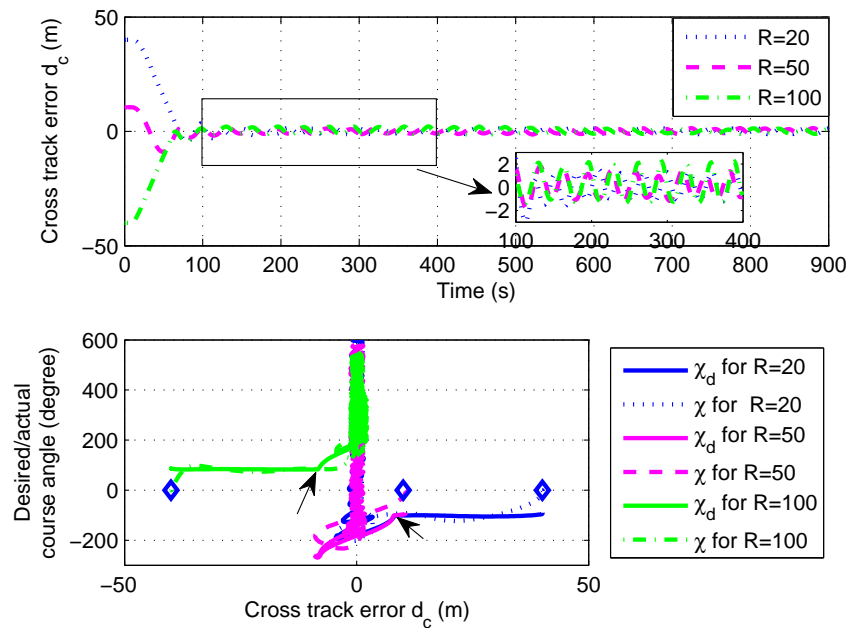
(b) Path-following performance

Figure 3.25: Circular path-following simulation results using the line-of-sight method with different followed circle radius R. In Fig. (a), the vehicle's initial position is marked with a circle, and it corresponds to three different initial conditions for the three circular path tracking cases, i.e. $(d_c, \chi) = (40, 0)$, $(10, 0)$ and $(-40, 0)$, which have been marked with diamonds. Note that Fig. (a) shows circles that appear non-circular due to the aspect ratio of the plot.

$R_p = 8$ the desired path can be followed with acceptable accuracy, but there are also oscillations around the path.

We numerically analyse the LOS path-following controller and the results are summarized in Table 3.9. For different circles, we can see the mean cross track errors E_{AV} are all within 1 m, but there are also relatively large oscillations around the path as indicated by E_{SD}. With larger values for the control parameter R_p, the converging time T_c increases, but it also shows that T_c is not varied very much. Similarly, U_1, U_2 and E are computed with close values. The column of E_{AV} shows that the best performance is achieved when $R_p = 8$ with the steady-state cross track error of around 1 m. According to E_{SD} though, the smallest oscillation while tracking the path is achieved when $R_p = 12$.

Table 3.9: Performance evaluation of the line-of-sight circular path-following control algorithm

Parameter	Value	T_c (s)	U_1 ($\times 10^7$ rpm^2)	U_2 ($\times 10^5$ rpm^2)	E ($\times 10^3$ m)	E_{AV} (m)	E_{SD} (m)
R (Fig. 3.26)	20	67	0.733	5.787	1.758	0.883	1.077
	50	64	0.750	12.551	0.447	0.773	0.892
	100	62	0.655	4.852	1.534	0.921	1.124
R_p (Fig. 3.25)	8	67	0.733	5.787	1.758	1.153	1.470
	12	68	0.747	6.070	1.760	1.509	0.820
	16	69	0.759	5.623	1.765	3.654	1.712

3.4.4.4 Comparison of Circular Path-Following Control Methods

The computed evaluation metrics data while tracking three different sized circles have been collected from the previous sections and summarized in Table 3.10. Through comparison, it can be seen that LOS will drive the vehicle to the desired path with the minimum time T_c in all cases. It requires the smallest total energy U_1, relatively large steering energy U_2, and the transition path tracking error E is the smallest. During the steady-state path-following stage, the CCI algorithm provides the best performance owing to
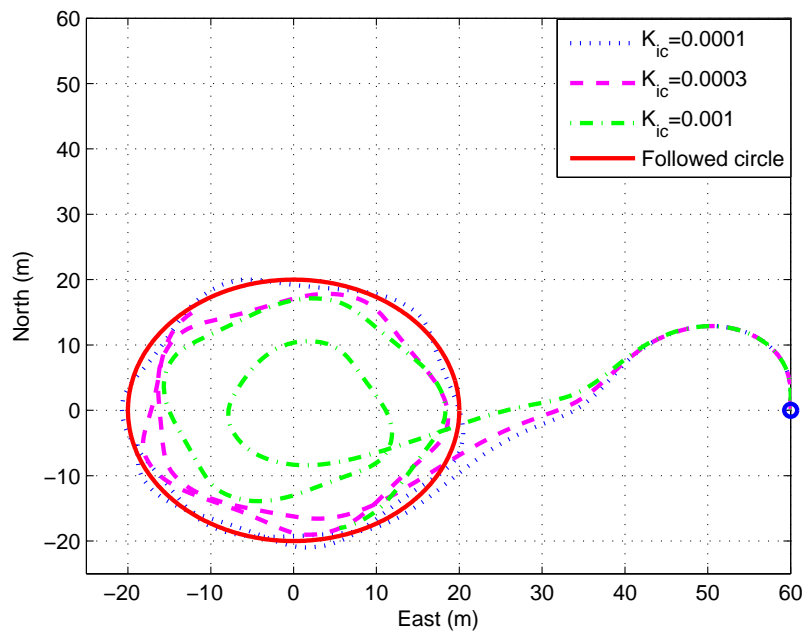
(a) USV trajectories

(b) Path-following performance
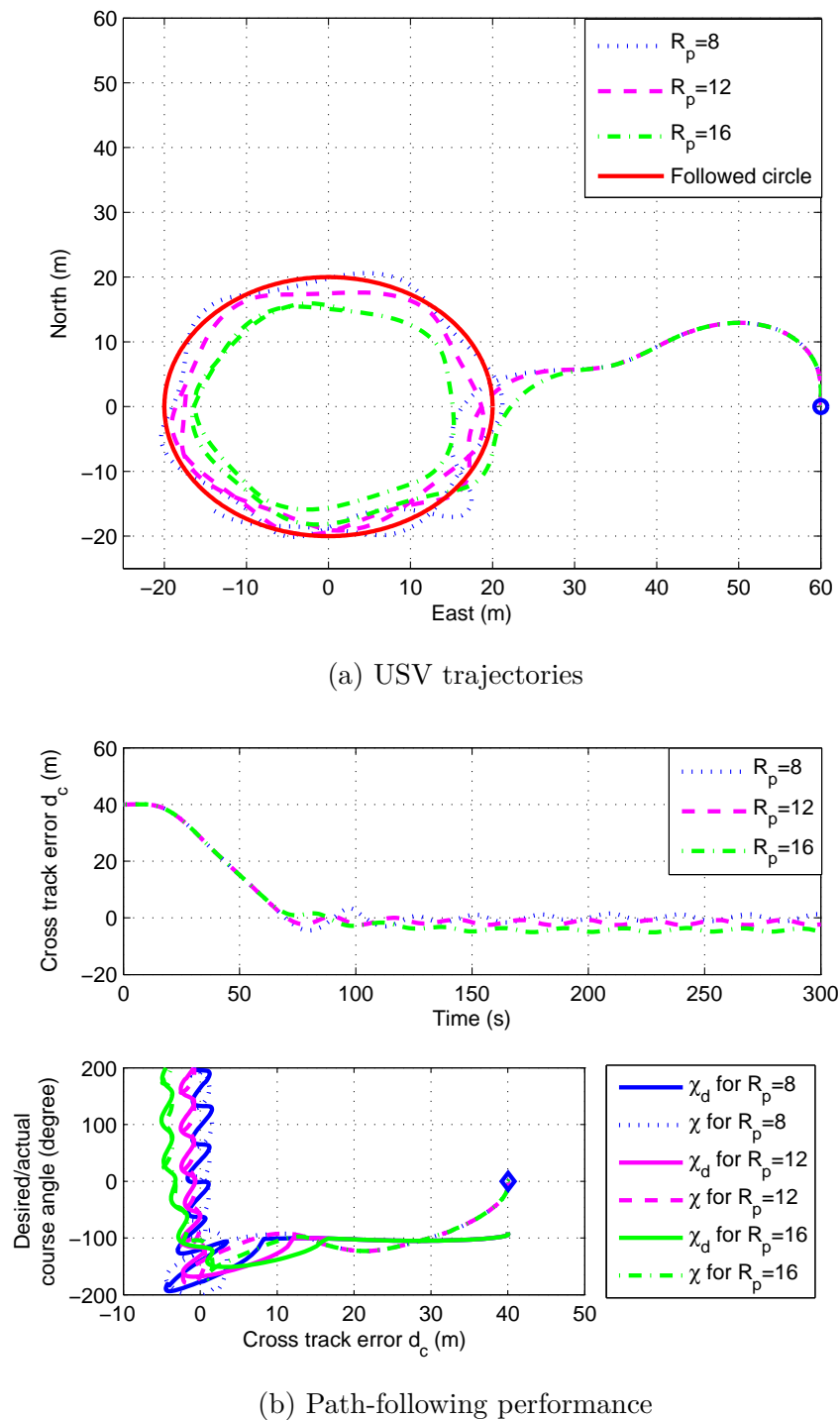
Figure 3.26: Circular path-following simulation results using the line-of-sight method with different control settings R_p. In Fig. (a), the vehicle's initial position is marked with a circle, and it corresponds to the initial condition $(d_c, \chi) = (40, 0)$ that has been marked with a diamond. Note that Fig. (a) shows circles that appear non-circular due to the aspect ratio of the plot.

the integral gain. It is important to note that when $R = 100$, the computed E_{AV} of CCI is larger than VF and LOS, but that is because the evaluation time is not long enough. We can also expect CCI performs better than the other two methods considering about the unexpected environmental disturbances in the real experiments. Although when implementing VF there is constant cross track errors during the steady-state stage, the path-following oscillation is the smallest among all experimented algorithms. Additionaly, the same algorithm may have different performance for different followed circles. For instance, CCI has the best performance for $R = 50$, and that is because this method is sensitive to the initial relative position with respect to the circle. VF will behave much better if the followed circle is large. LOS is very consistent through all testing scenarios, but note that the abrupt change of the desired course angle χ_d will make it difficult for a USV with slow dynamics to follow during the transition period.

Table 3.10: Comparison of the three circular path-following control methods

Method	Radius (m)	T_c (s)	U_1 ($\times 10^7$ rpm^2)	U_2 ($\times 10^5$ rpm^2)	E ($\times 10^3$ m)	E_{AV} (m)	E_{SD} (m)
VF		116	1.333	6.302	2.084	1.878	0.477
CCI	20	78	0.881	5.297	1.867	0.656	0.737
LOS		67	0.733	5.787	1.758	0.883	1.077
VF		66	0.760	10.836	0.454	0.756	0.314
CCI	50	66	0.761	10.991	0.453	0.421	0.439
LOS		64	0.750	12.551	0.447	0.773	0.892
VF		85	0.923	4.164	1.820	0.639	0.274
CCI	100	67	0.689	3.939	1.592	1.409	0.420
LOS		62	0.655	4.852	1.534	0.921	1.124

3.4.5 Waypoint Path-Following Control

In this part, we examine the three path-following control methods and their performances on a specific survey mission. If the waypoints are determined, the paths that link the waypoints can be constructed based on the straight lines and circular arcs. An illustrative

example is given in Fig. 3.27. For instance, if we would like the vehicle to follow the path from wp_i to wp_{i+2}, the circular arc will be planned for wp_{i+1} and it will intersect the two adjacent paths at p_c and p_n. The lines of $\overline{o_{i+1}p_c}$ and $\overline{o_{i+1}p_n}$ can divide the followed path into three different regions, i.e. region R_1 where the vehicle has to follow the straight-line path before reaching the line of $\overline{o_{i+1}p_c}$, region R_2 where the vehicle needs to track the circular path, and region R_3 where the vehicle passes the line of $\overline{o_{i+1}p_n}$ and switches back to the straight-line path-following mode.
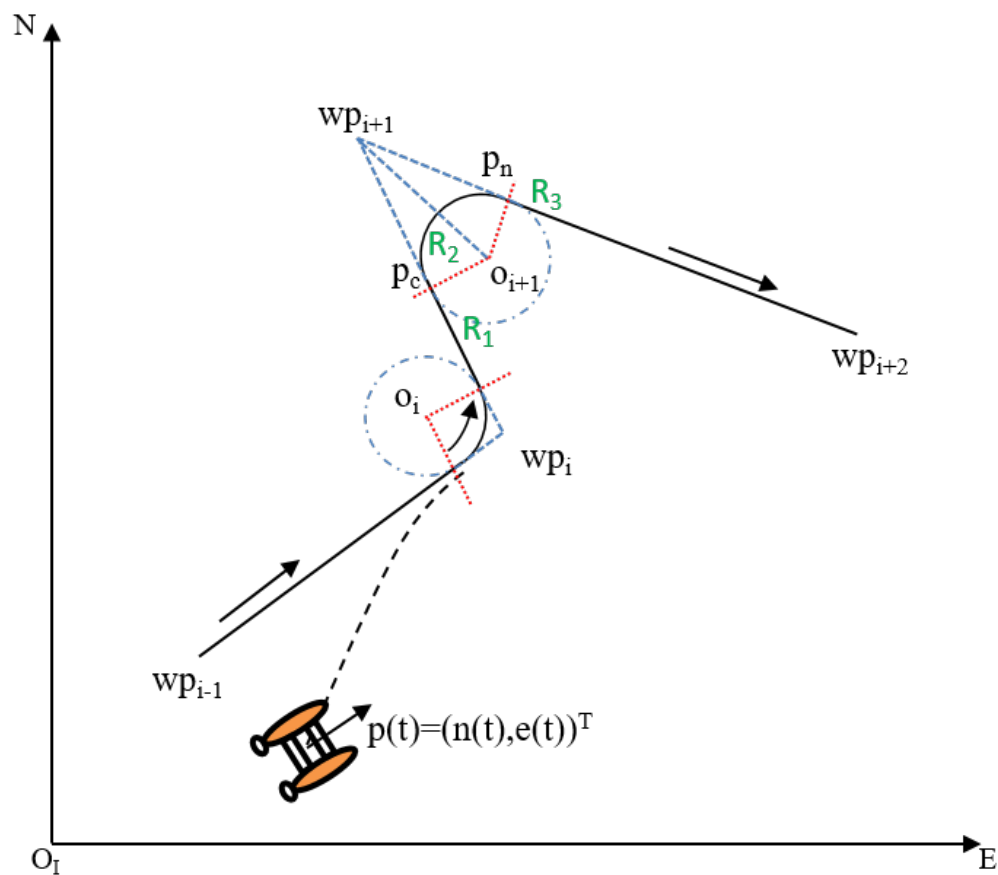
Figure 3.27: Illustration of the construction of waypoint paths.

The flow chart showing the combination of waypoint path generation and path-following control algorithms has been depicted in Fig. 3.28. During the initialization stage, the waypoint position and circle radius are achieved from the end users. Based on these

settings, the position of the circle origin and the tangential points of the circle can be computed. The USV position $p(t)$ is measured by the GPS receiver, and it can be compared with the boundary line $\overline{o_{i+1}p_c}$ and $\overline{o_{i+1}p_n}$ to determine if the vehicle has moved into a new region. The path-following control algorithm is switched depending on whether the desired path is straight or circular.
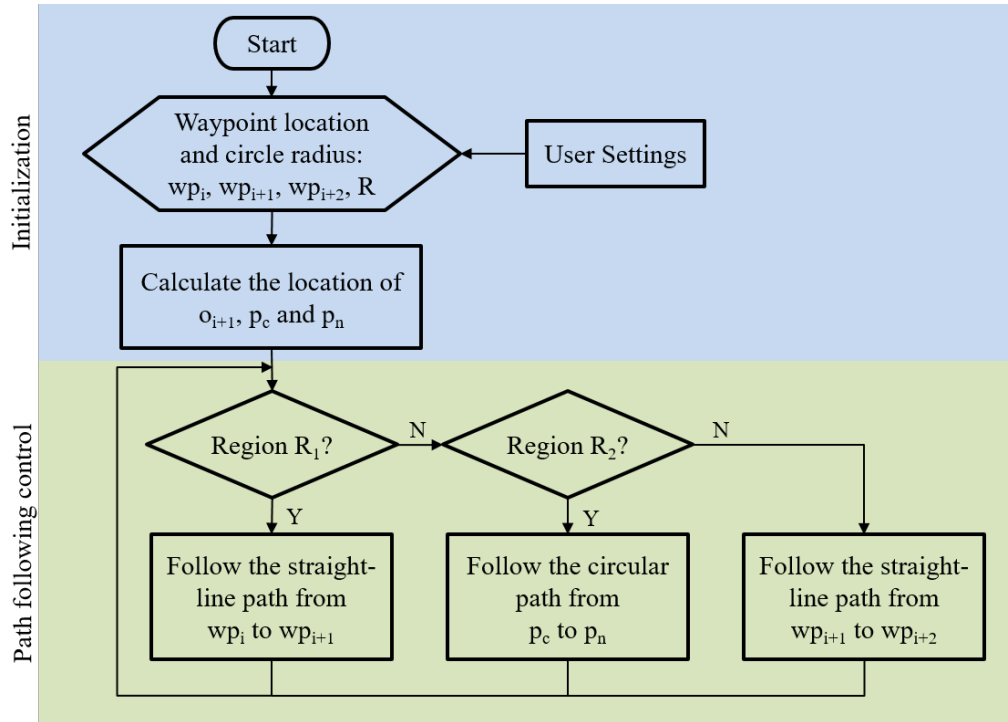
Figure 3.28: The flowchart indicating the generation of the waypoint paths and the switching between straight-line and circular path-following control.

In the simulated survey mission, we determine to use four waypoints defined using the geographic coordinates of latitude and longitude as

$$
\begin{aligned}
wp_1 &= (47.5773°, -52.7341°)\\
wp_2 &= (47.5776°, -52.7349°)\\
wp_3 &= (47.5784°, -52.7341°)\\
wp_4 &= (47.5779°, -52.7331°).
\end{aligned}
\tag{3.17}
$$

Note that these waypoints were chosen within the testing area using Google Earth, and they will be used in the real-world field trials in our later discussion. To make it convenient to implement the formulated path-following control algorithms, we convert the designated waypoints into the local NED frame with respect to the origin wp_1. Therefore, the waypoint positions in NED frame using the unit of meters are computed as

$$wp_1 = (0,0)^T$$
$$wp_2 = (-59.4144, 34.6847)^T$$
$$wp_3 = (2.7321, 122.2464)^T$$
$$wp_4 = (76.6891, 64.9991)^T.$$

To gain the best performance for each investigated method, we employ the control parameter values as listed in Table 3.11 to perform the waypoint path-following simulation tests. It is assumed that the vehicle's initial position is $p(0) = (n(0), e(0))^T = (0, -20)^T$, its initial and desired moving speed is 0.8 m/s, the initial course angle $\chi_i = 0°$ and the connection circle radius is chosen as $R = 20\ m$. The waypiont path tracking results using VF, CCI and LOS are depicted in Fig. 3.29, Fig. 3.30 and Fig. 3.31.

In Fig. 3.29a, the simulated vehicle trajectory is plotted using the dash line. We can see that a reasonably good path tracking performance is achieved, especially for the straight-line paths. We have demonstrated that VF is not good at tracking the circular path in section 3.4.4.1, and this phenomenon can also be visualized in the figure. The top graph of Fig. 3.29b shows the time history of the cross track error $d(t)$. Started from the initial position, $d(t)$ converges to zero smoothly. The vibration of $d(t)$ mainly happens around the circular path-following part, and a maximum error is around 2 m. A comparison of the desired and actual course angle has been shown to the bottom graph of Fig. 3.29b, and to clearly illustrate the results the path direction has also been drawn

on the figure. Apparently, owing to the slow yaw dynamics, the vehicle can not track the changing desired course angle during the circular path tracking stage very well. However, when it starts to track the straight-line path, the vehicle works quite well.

As shown in Fig. 3.30a, while implementing the CCI algorithm, the vehicle's trajectory is choppy after the circular path-following stage. Compared to Fig. 3.29a, we can see the vehicle's circular path tracking performance is improved a little. However, the oscillation around the desired path is unfavorable. It also shows that when tracking the first straight-line path $\overline{wp_1 wp_2}$, there is a large cross track error. If we refer to the top graph of Fig. 3.30b, we can determine that the value of $d(t)$ for the first followed path is around 2 m, and it converges quite slowly due to the small integral gain K_{is}. As the vehicle starts to track the path of $\overline{wp_2 wp_3}$, due to the accumulation of the error $d(t)$ and the effect of integral gain, the straight-line path tracking performance is improved with small $d(t)$. The bottom graph of Fig. 3.30b compares the desired and actual course angle, and it can be seen that the big mismatch occurs around the circular path-following stage.

The LOS waypoint path-following control simulation results are shown in Fig. 3.31. As depicted in Fig. 3.31a, the vehicle trajectory is quite choppy, but it shows that the circular path-following performance is the best among the three methods. As shown, it takes some time before the vehicle can settle down to follow the straight-line path. Referring to the top graph of Fig. 3.31b, the maximum cross track error $d(t)$ is around 4 m. It also demonstrates that $d(t)$ oscillates around zero through the whole waypoint path tracking process. The bottom graph of Fig. 3.31b shows that the actual course angle can follow the desired one relatively well.

A numerical comparison of the three methods are performed, and the results are summarized in Table 3.11. Note that since the vehicle is commanded to track multiple line segments, we employ the evaluation time T_e instead of the convergence time T_c. The term T_e measures the time it takes from start to the end of a survey. In the performed
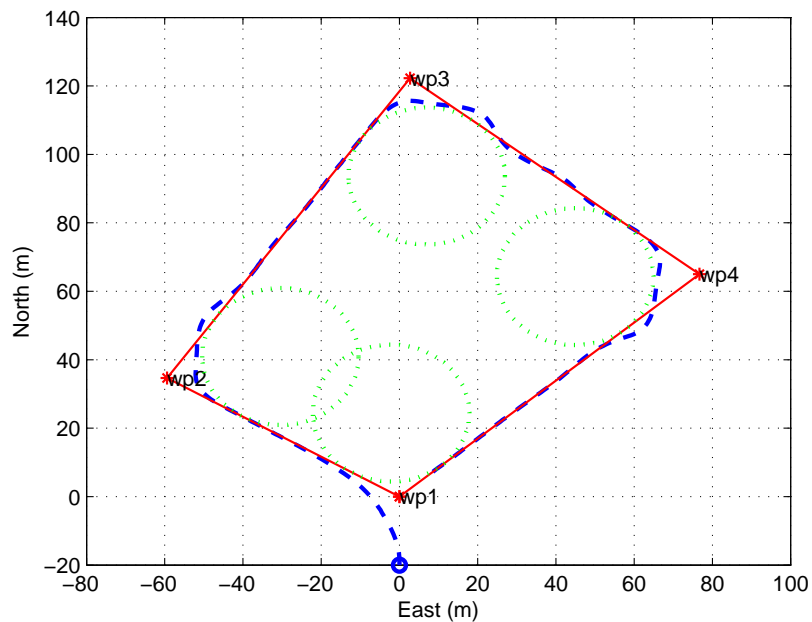
(a) USV trajectories in NED frame
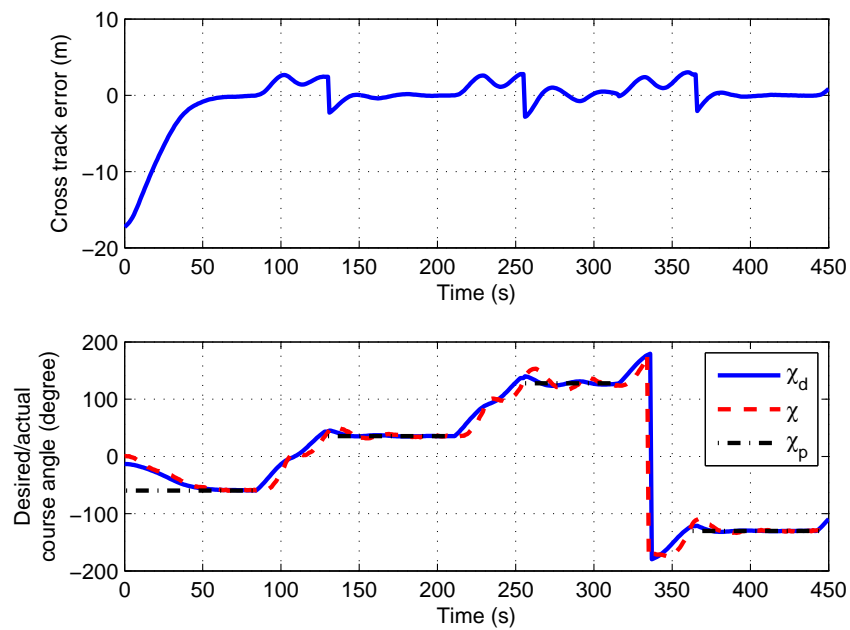
(b) Path-following control performance

Figure 3.29: Waypoint path-following control simulation tests using the vector field method. In Fig. (a), we show the actual USV trajectories compared to the desired path. The desired circular path is indicated by the dot line. In Fig. (b), we show the time history of cross track error, desired course angle, actual vehicle course angle and the path direction.
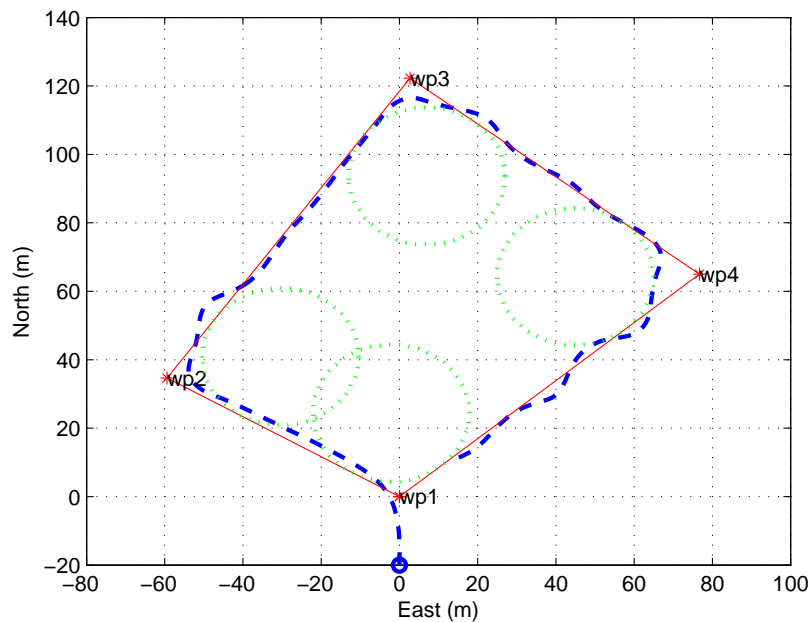
(a) USV trajectories in NED frame
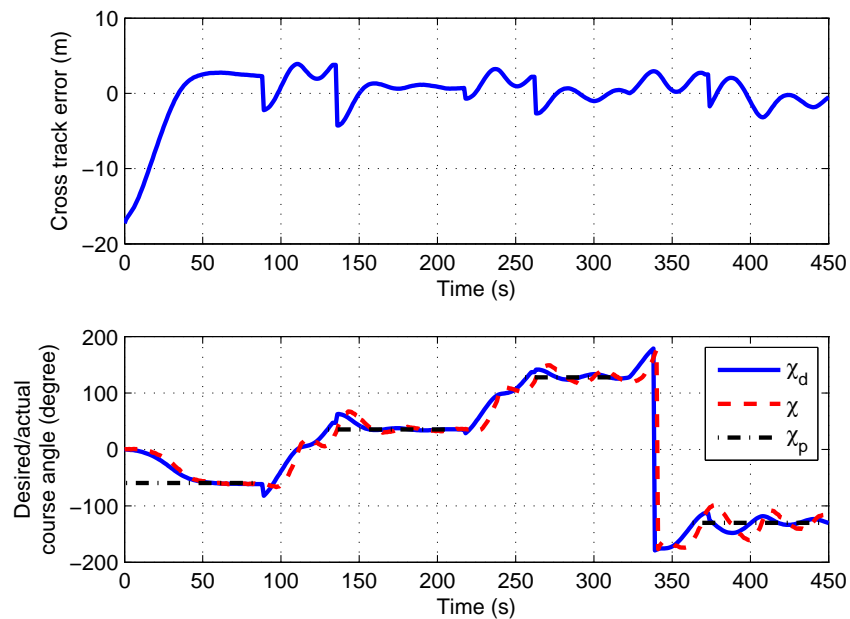
(b) Path-following control performance

Figure 3.30: Waypoint path-following control simulation tests using the carrot chasing method with integral gain. In Fig. (a), we show the actual USV trajectories compared to the desired path. The desired circular path is indicated by the dot line. In Fig. (b), we show the time history of cross track error and desired course angle, actual vehicle course angle and the path direction.
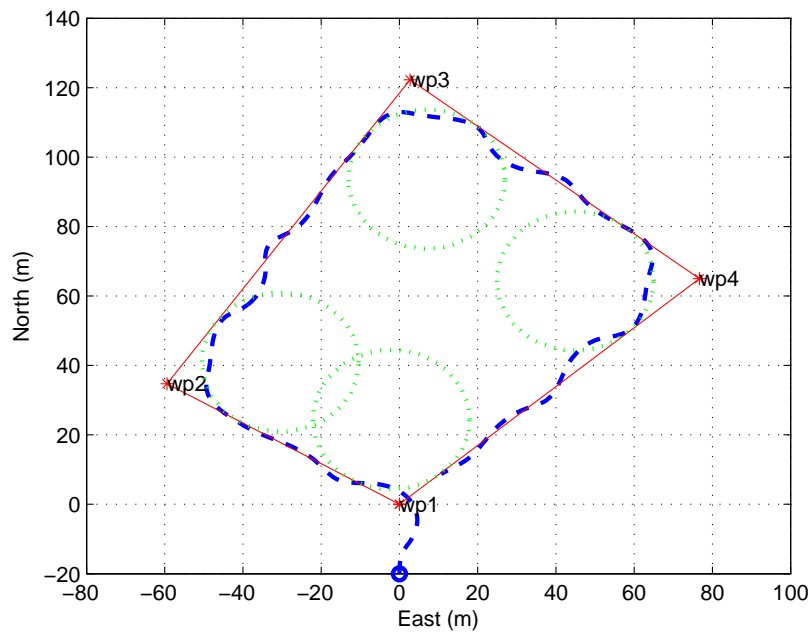
(a) USV trajectories in NED frame
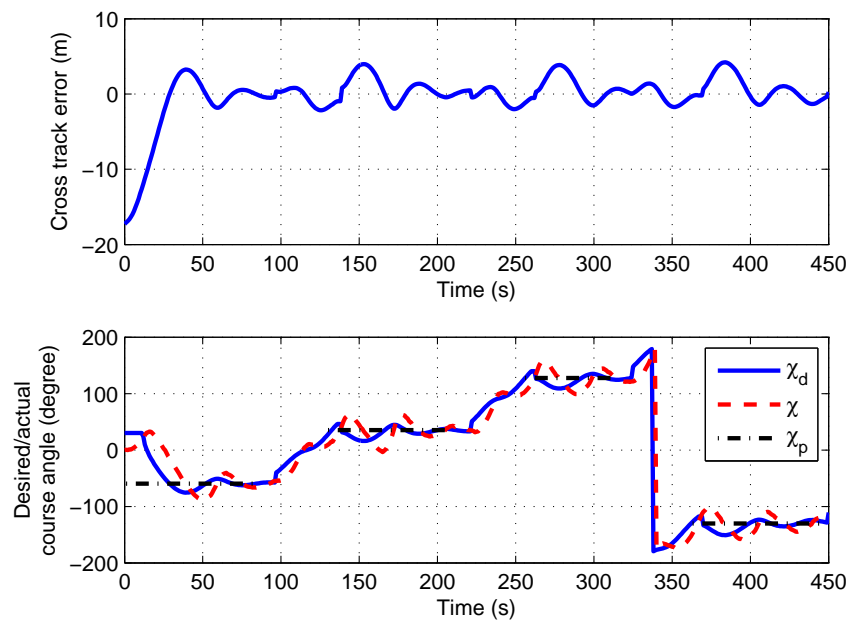
(b) path-following control performance

Figure 3.31: Waypoint path-following control simulation tests using the line-of-sight method. In Fig. (a), we show the actual USV trajectories compared to the desired path. The desired circular path is indicated by the dot line. In Fig. (b), we show the time history of cross track error, desired course angle, actual vehicle course angle and the path direction.

Table 3.11: Comparison of the waypoint path-following control simulation experiments

Method	Value	T_e (s)	U_1 ($\times 10^7$ rpm^2)	U_2 ($\times 10^6$ rpm^2)	E ($\times 10^2$ m)	E_{AV} (m)	E_{SD} (m)
VF	$k_s=k_c=0.1$ $\chi_{Ms}=\chi_{Mc}=70°$	437	5.521	0.574	7.218	0.872	1.172
CCI	$K_{ps}=K_{pc}=0.1$ $K_{is}=K_{ic}=0.001$	447	5.594	1.079	9.540	1.546	1.701
LOS	$R_p=12$	443	5.451	1.850	8.031	1.247	1.586

simulations, the ending condition is when the vehicle is within 20 m of wp_1. While computing U_1, U_2 and E, we use T_e. Hence, U_1 and U_2 represent the total control energy and steering energy, and E is the summation of the absolute cross track error through the whole waypoint path tracking event. The values of E_{AV} and E_{SD} are calculated using the time range started from when the vehicle first enters the ± 2 m band of the followed path. Through comparison, we find that VF provides the best waypoint path-following results. To complete the same mission, VF requires the lowest time and steering energy. The path-following cross track error is also the smallest among the three methods. Although CCI does not show as good performance as VF in terms of control energy and path tracking accuracy, it can be expected that CCI will have an improved performance in the real-world tests since it has more robustness to environmental disturbances. The LOS method requires the lowest total control energy U_1, but since the vehicle trajectory is quite choppy, the consumed steering energy is the highest. The path tracking accuracy is average among the three methods.

3.5 Field Trial Experiments

The field trial experiments were carried out at Long Pond near Memorial University of Newfoundland providing the opportunity to evaluate different path-following control algo-

rithms and check their actual performances under unknown environmental disturbances, such as gusting winds and a strong localized current running through the lake. We chose to perform some typical straight-line and circular path-following tests to illustrate and compare with the simulation tests. Based on the successful results, we imitate an ocean survey mission where a USV is required to follow the paths defined by a list of waypoints.

It is important to note that the employed dynamic motion model in the simulation tests was identified based on the original USV SeaCat's system configuration. However, due to the requirements of other experiments, a new type of superstructure was installed and a sonar head had been integrated into the port-side hull. Therefore, our field experiments had to be performed based on the new heavier system settings, whose motion dynamics were altered from the simulated motion model. We tuned the PID controllers for the real platform in the field based on our experience in section 3.4.1, and the parameters were selected as $K_{p1} = 200$, $K_{i1} = 90$ and $K_{d1} = 20$ for the speed controller, and $K_{p2} = 3$ and $K_{d2} = 12$ for the course keeping controller. The actual implemented PID controllers varied a little from the simulated ones in section 3.4.1, and again it is owed to the different system dynamics. The difference between the simulated model and the real platform will also influence our tuned parameters for different path-following controllers. We will provide more details in the following discussion.

3.5.1   Straight-line Path-following Control

The straight-line path-following field experiment results using Vector Field Method (VF), Carrot Chasing with Integral Gain (CCI) Method and Line-of-Sight Method (LOS) are depicted in Fig. 3.32, Fig. 3.33 and Fig. 3.34. In each test, the USV SeaCat's initial speed is close to zero, the desired moving speed is 0.8 m/s and the vehicle is commanded to follow the straight-line path defined from wp_4 to wp_2 in Eq. 3.17. Due to the changing weather conditions, it is difficult to make the vehicle start from exactly the same location

in the field trail, and thus we tried to maintain the initial position of the vehicle within a small region. The same initial course angle χ_i is also difficult to be achieved among different experiments. However, through performing the simulation we find that χ_i will not play an important role in varying the vehicle's path tracking performance. Again, to clearly show the results the waypoint positions and collected GPS data are converted to the local NED coordinates in meters. As for the local origin, we still use wp_1 from Eq. 3.17.

The onboard weather station and sonar head P66 can be employed to measure environmental conditions while performing the straight-line path-following experiments. The list of variables that can be measured include the average apparent wind speed V_{aw}, maximum apparent wind speed V_{maw}, dominant wind direction χ_{aw} with respect to magnetic north, air temperature T_a, barometric pressure B_p and the water temperature T_w. A summary of the measured variable values is shown in Table 3.12.

As for the water current condition, it is not measured but is estimated by performing a drifting test. In this test, the USV SeaCat's propellers are turned off, and the vehicle will drift with the water current. The onboard GPS can measure the moving speed and course direction, and they can be regarded as an indication of the current velocity and direction. Hence, mean current speed and direction are determined as 0.1 m/s and 180° with respect to true north.

Table 3.12: Environmental conditions for straight-line path-following experiments

Method	V_{aw} (m/s)	V_{maw} (m/s)	χ_{aw} (°)	T_a (°C)	B_p (kPa)	T_w (°C)
VF	2.291	3.133	-8.782	12.103	100.676	15.500
CCI	2.329	4.500	7.036	12.186	100.760	14.688
LOS	2.858	4.623	-9.034	12.045	100.701	15.500

Our field trial results demonstrate the fidelity of the performed simulations and the robustness of each straight-line path-following control algorithm. We can compare the
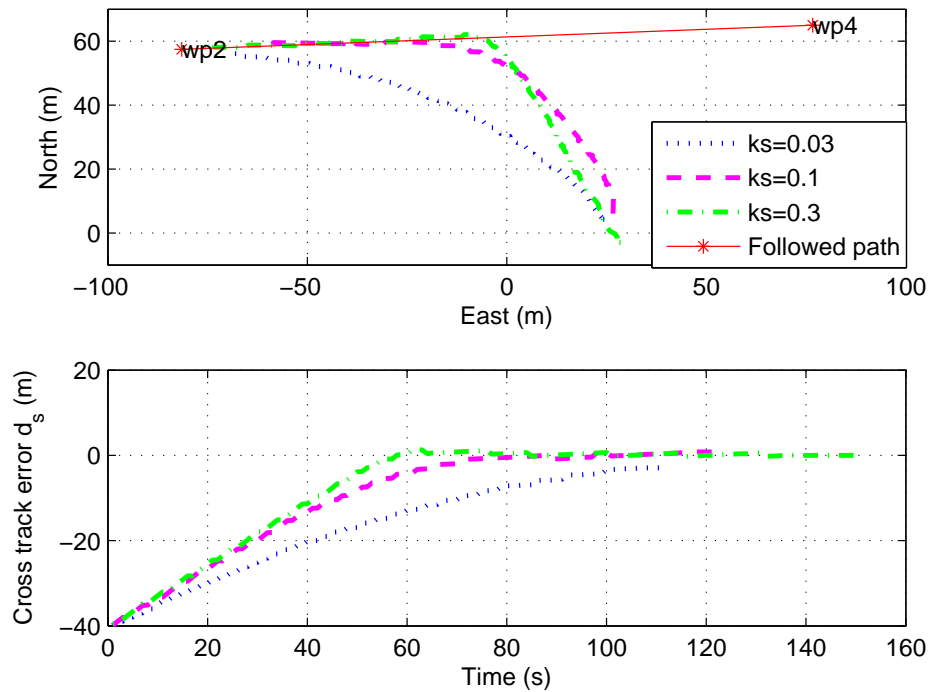
Figure 3.32: The straight-line path-following field trial results based on the vector field method with varied value of k_s. The maximum approaching angle $\chi_{Ms} = 70°$. Note that the USV is controlled to follow the path from wp_4 to wp_2.

trajectories of the vehicle from Fig. 3.32 with those of Fig. 3.16, and it can be seen that the increment of the control parameter k_s from 0.03 to 0.1 can reduce the vehicle's response time to follow the desired path. Due to the different initial positions, we choose to start evaluating the cross track error d_s when the vehicle enters within 40 m of the path, and the results are depicted to the bottom of Fig. 3.32. This is a reasonable choice because the vehicle will have enough time to accelerate to the desired moving velocity from its starting position, and it will also make it convenient for us to compare the evaluation results with those in Fig. 3.16. Through comparison, we can determine that in the field experiments, $k_s = 0.3$ will not lead to the vehicle's oscillation around the followed path, and this is a result of varied dynamics of the studied platform and the added drag in the real-world experiments. Other than that, the actual and simulated vehicle motion are
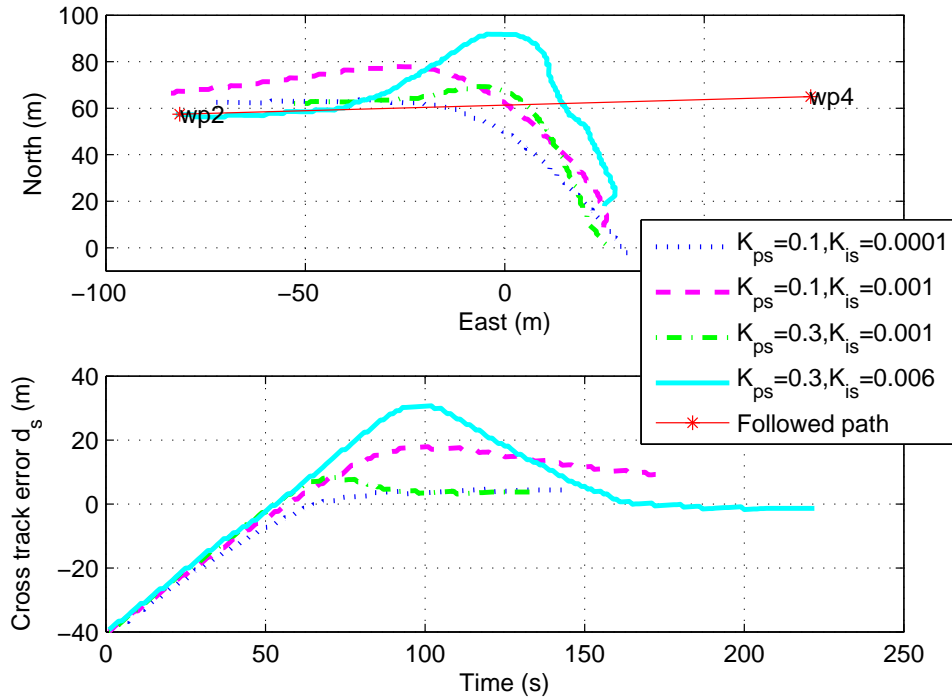
Figure 3.33: The straight-line path-following field trial results based on the carrot chasing method with integral gain. The experiments are performed with different values of K_{ps} and K_{is}. Note that the USV is controlled to follow the path from wp_4 to wp_2.

very close, and in both cases d_s converges to zero.

In section 3.4.3.2, we have demonstrated that the integral gain for the conventional carrot chasing method will introduce significant overshoot for the vehicle while tracking the path. This phenomenon has been further demonstrated in the real tests of Fig. 3.33. The results comply well with the simulation tests. However, since the vehicle dynamics is different, we have to tune the parameters again to find the best settings. We find that when $K_{ps} = 0.3$ and $K_{is} = 0.006$, the vehicle will be brought back to the followed path within a reasonable time. The bottom graph of Fig. 3.33 shows that when K_{is} is small, for example when $K_{is} = 0.0001$, the cross track error converges to the path slowly, which is similar to the simulated cases. The large overshoots occur when the value of K_{ps} is large, and it can be dealt with if the vehicle's initial position is closer to the tracked
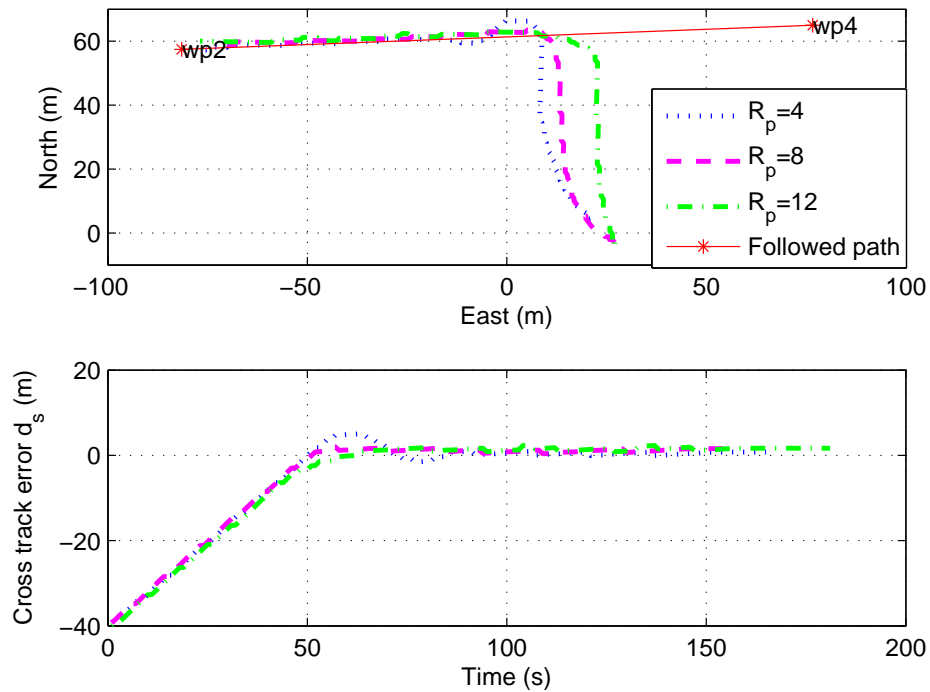
Figure 3.34: The straight-line path-following field trial results based on the line-of-sight method with varied value of R_p. Note that the USV is controlled to follow the path from wp_4 to wp_2.

path. This characteristic has also been shown in section 3.4.3.2. Note that CCI is robust to environmental disturbances, and we will show this feature in the section of waypoint path-following control tests.

The LOS straight-line path tracking results are depicted in Fig. 3.34. In the real case scenario, the value of R_p can be chosen as small as 4 m and the system will still be operating correctly without large oscillation around the followed path. Again, this is due to the varied dynamics of the studied platform and additional damping in the field trial. The graph of the cross track error to the bottom of Fig. 3.34 shows that when R_p gets smaller, the converging speed of d_s increases a little. When $R_p = 4$, there will be a small path tracking overshoot before the vehicle converges back to the followed path. The transition process of the vehicle in the real tests suggests a good consistency with respect

Table 3.13: Evaluation of different straight-line path-following control algorithms in the field trials

Method	Value	T_c (s)	U_1 $(\times 10^7$ rpm$^2)$	U_2 $(\times 10^5$ rpm$^2)$	E $(\times 10^3$ $m)$	E_{AV} (m)	E_{SD} (m)
VF	k_s=0.3 χ_{Ms}=70°	54	1.396	2.366	1.124	0.581	0.604
CCI	K_{ps}=0.3 K_{is}=0.001	51	1.312	5.253	1.302	5.207	2.472
LOS	R_p=4	48	1.347	7.530	1.092	1.803	2.124

to the simulations in Fig. 3.20. In all field tests scenarios, d_s will finally converge to zero.

We evaluate the path-following control performance based on our field trial experimental data. To be consistent, we still implement the defined six metrics from section 3.4.2. Owing to the different initial vehicle positions, we make a small adjustment for measuring the convergence time T_c, and it is calculated starting from when the vehicle enters the 40 m range of the followed path. The evaluation results have been summarized in Table 3.13. Note that only the path-following controllers with the best performance are included. Due to the restriction of the testing area, we can not collect enough data for the CCI tests until the vehicle converges and that is the reason the calculated values of E_{AV} and E_{SD} are large. Whereas, we can notice that the CCI algorithm performs well in the real experiment during the transition stage, and that is due to the fine tuning of the controller settings.

Through comparing VF and LOS, we can see LOS has a faster convergence rate. During the transition stage, LOS consumes smaller total control energy U_1 but much larger steering energy U_2. The path tracking accuracy E is close between the two methods, but LOS has a little bit better performance. These results comply well with those in Table 3.6. During the steady-state path-following period, VF has a better average cross track error E_{AV} and standard deviation E_{SD}, which also follows our previous analysis from the simulation section.

3.5.2   Circular Path-Following Control

In this part, we evaluate the real-world performance of different circular path-following control algorithms. Due to the limitation of the testing area, we decided to perform the experiments with the circle radius of 5 *m*, 10 *m*, 20 *m* and 40 *m*. When evaluating VF and LOS methods, we manually change the reference circle radius in one trial such that the vehicle can follow the circle from small to large in one path-following mission. In terms of CCI, we have to carry out separate experiments for each followed circle, because the cross track error keeps accumulating and a bad path tracking result from one circle will influence another. Among all experiments, the circle origin is chosen as p_c=(47.5779°, -52.7341°), which provides us with the largest space for doing the tests. Similar to the straight-line path tests, the recorded vehicle position data are converted from the geographic coordinate of latitude and longitude to the NED local coordinate frame in meters with respect to the chosen origin.

The environmental conditions while performing the circular path-following control tests have been summarized in Table 3.14, and we predict the mean water current speed as 0.1 *m/s* from 225° south-west. In Table 3.14, CCI and LOS were performed on a rainy day that is different from when the VF experiments were carried out.

Table 3.14: Environmental conditions for circular path-following experiments

Method	V_{aw} (m/s)	V_{maw} (m/s)	χ_{aw} (°)	T_a (°C)	B_p (kPa)	T_w (°C)
VF	2.702	5.785	8.363	11.826	100.682	15.870
CCI	3.783	7.030	-4.623	7.634	99.300	14.000
LOS	3.643	7.150	9.321	7.322	99.300	13.900

The field experimental results converted to the local NED frame based on VF, LOS and CCI circular path-following methods are depicted in Fig. 3.35, Fig. 3.36 and Fig. 3.38, and their cross track error evaluation results are depicted in Fig. 3.37 and Fig. 3.39. In Fig. 3.35, we can see when the followed circle is 5 *m* or 10 *m*, there is a large

constant path tracking error d_c. With larger circle radius, the path-following performance improves. Through comparison of Fig. 3.35a and Fig. 3.35b, we can determine that by increasing the control gain of k_c, the vehicle can still track the circle without any oscillation. Further, the increment of k_c can also improve the small circle's path-following performance. An evaluation of the cross track error for the performed two experiments are depicted in Fig. 3.37a. It shows that large spikes occur when the vehicle switches from one to another followed circular trajectory. On one hand, it proves our previous discussion that VF is more suitable for tracking large circles than small ones, on the other hand, the actual vehicle dynamics allow us to implement a higher control gain $k_c = 0.3$, which provides a better circular path-following performance. By comparing the results in this section with those in section 3.4.4.1, we find that the actual VF's circular path-following characteristics comply well with our simulation study.

The LOS field experimental results are depicted in Fig. 3.36. When $R_p = 4$ and the followed circle is 5 m or 10 m, we can see the vehicle can partially track the desired circle, and the portion with large mismatch may be due to the environmental influences and the vehicle's slow dynamics limit. LOS definitely has a better performance than VF when considering about tracking small circular paths. At the same time, when $R_p = 4$, there will be a large overshoot when the vehicle transits from one to another followed path as shown in Fig. 3.36a. The analysis can be further proved by the evaluation results shown in the top graph of Fig. 3.37b. It can be seen the transition stage involves multiple oscillation before the vehicle can be successfully controlled to track the desired paths. With a larger setting, i.e. $R_p = 8$, the vehicle can follow the path without any oscillation as shown in Fig. 3.36b. However, we can see the vehicle trajectory is inside the followed circle with a constant value of d_c. Again, this scenario agrees with the LOS simulation study in section 3.4.4.3. Note that to implement LOS, we need to guarantee that $R_p < R$ (Algorithm 6), and this is the reason we did not perform the tests to track the 5 m circle

when $R_p = 8$.

The field trail results for the CCI algorithm have been depicted in Fig. 3.38. While tracking the small circle with radius of 5 m or 10 m, CCI will drive the vehicle inside the followed circle, and this phenomenon can be regarded as the vehicle is over-controlled. Comparing Fig. 3.38a and Fig. 3.38b, we can see by only increasing the value of K_{ps}, the small circle's tracking performance is improved. However, the vehicle's yaw dynamics is slow, even the integral gain is included we still can not effectively control the vehicle to quickly converge to the desired small circular paths. To follow the larger circles with radius of 20 m or 40 m, we can achieve better results. However, as discussed in section 3.4.4.3, the small integral gain may introduce the path tracking overshoot, and the vehicle will converge to the path slowly, and we can see these characteristics in both figures. The evaluation of the cross track error is depicted in Fig. 3.39, and it clearly shows the cross track error overshoot and the slow converging process for each path-following control process.

We compute the metrics values for numerical evaluation of different circular path-following controllers. Note that for comparison we only include the best controller from each algorithm for tracking the circle with radius of 20 m and 40 m, and these results are summarized in Table 3.15. Owing to different initial positions and experimental conditions of the vehicle, the convergence time T_c is calculated differently for the 20 m and 40 m circle cases. For the 20 m circle, T_c is computed from when the vehicle first enters the 8 m range of the circle to the 2 m narrow band around the followed path. As for the 40 m circle, the measured time is between 18 m and 2 m around the path. The large overshoot of LOS will influence the vehicle's transition stage performance, and thus its T_c is measured until the vehicle enters the 2 m narrow band around the circular path for the second time. Due to the large overshoot of the LOS method, T_c is much larger than the other two methods as shown in Table 3.15, and our analysis of the transition stage of
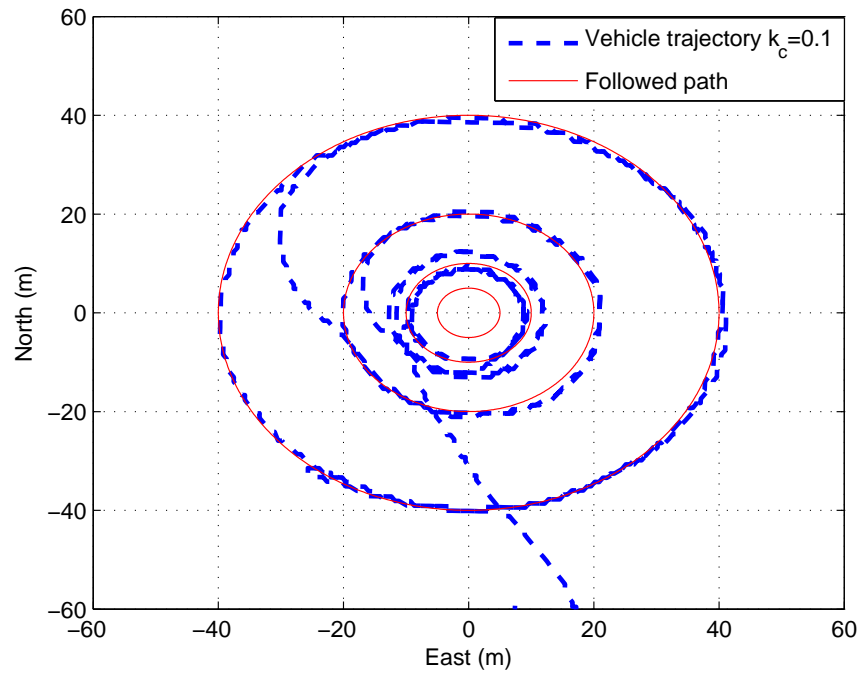
(a) USV trajectories in NED frame with $k_s = 0.1$
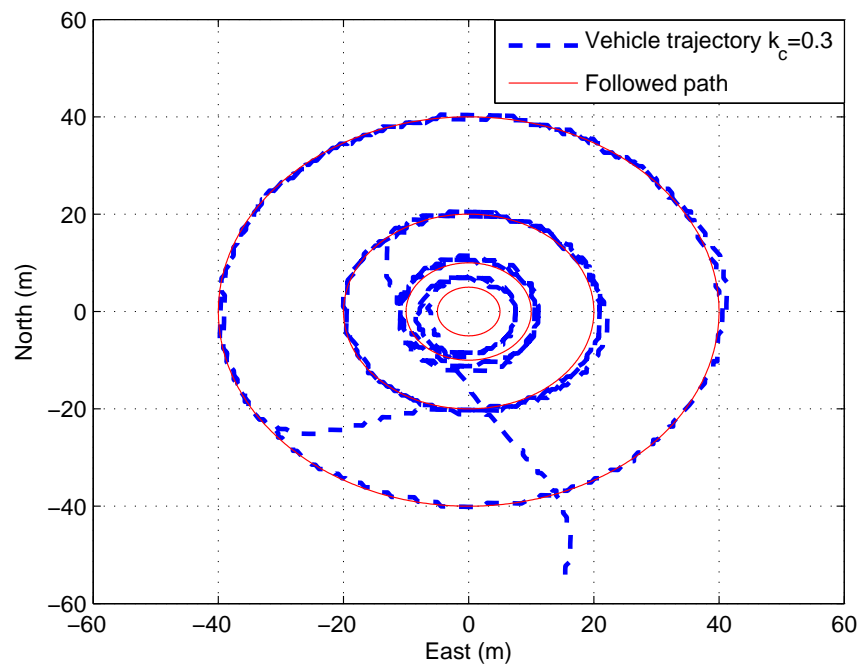
(b) USV trajectories in NED frame with $k_s = 0.3$

Figure 3.35: Circular path-following field experiments using the vector field method.
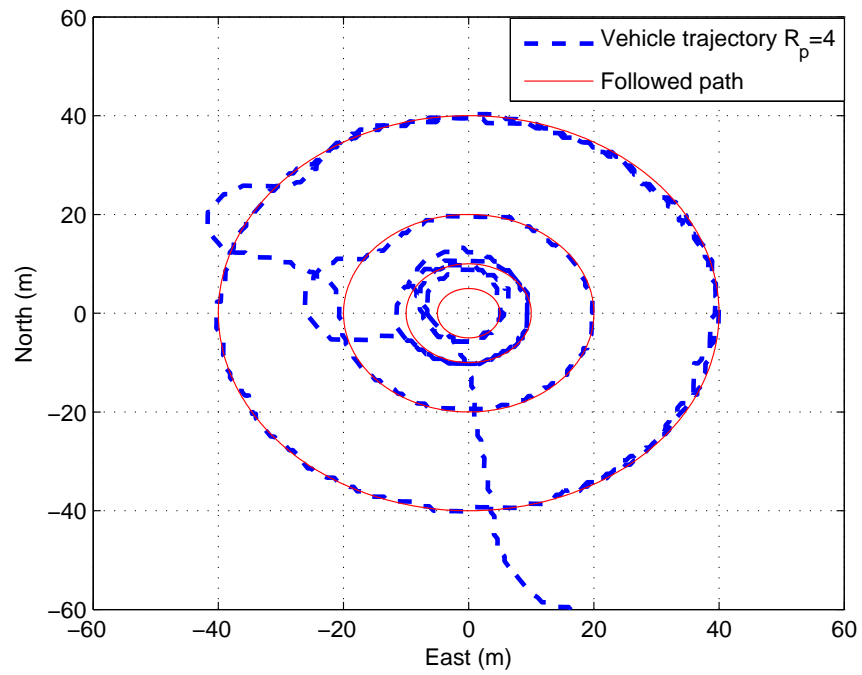
(a) USV trajectories in NED frame with $R_p = 4\ m$
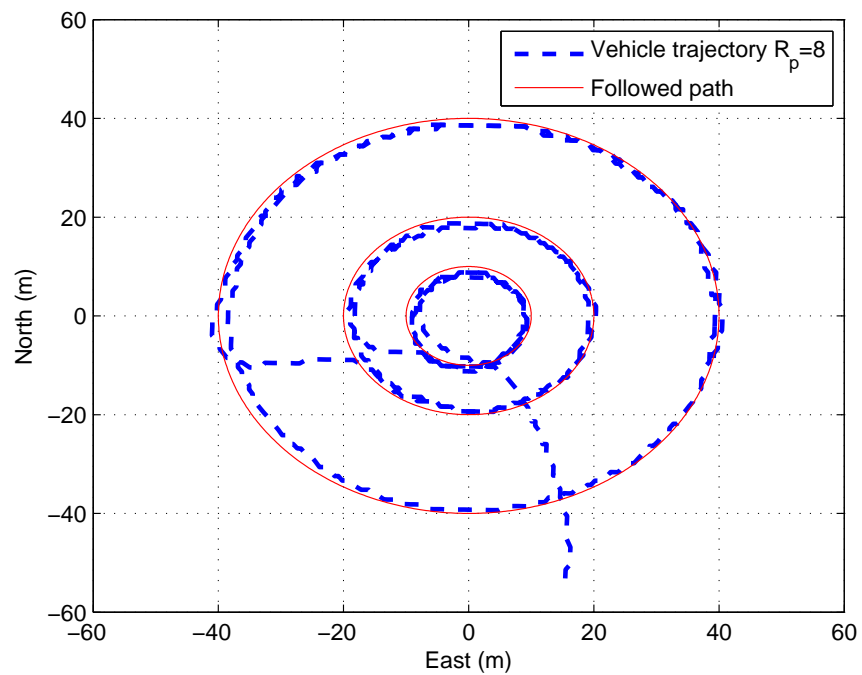
(b) USV trajectories in NED frame with $R_p = 8\ m$

Figure 3.36: Circular path-following field experiments using the line-of-sight method.
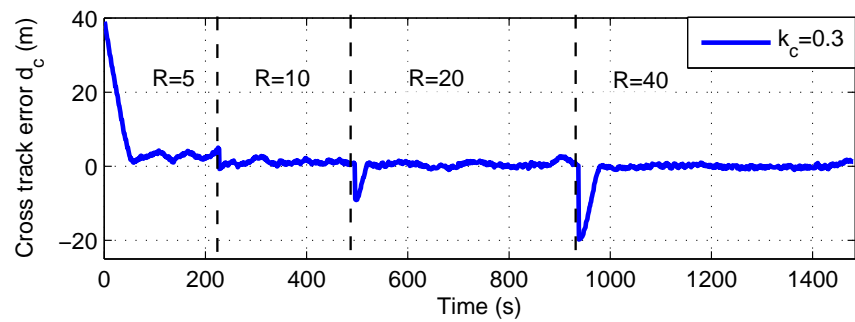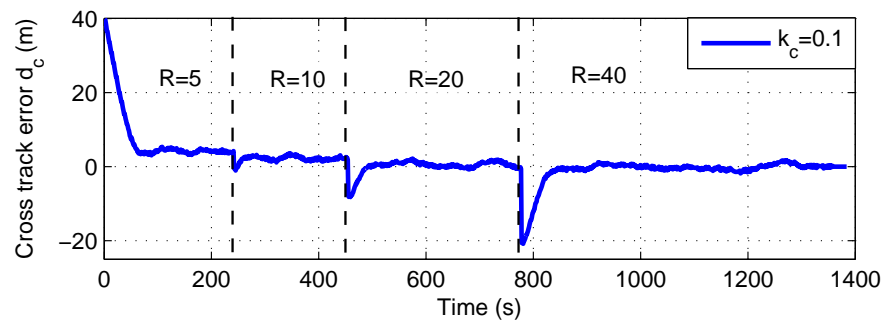
(a) VF
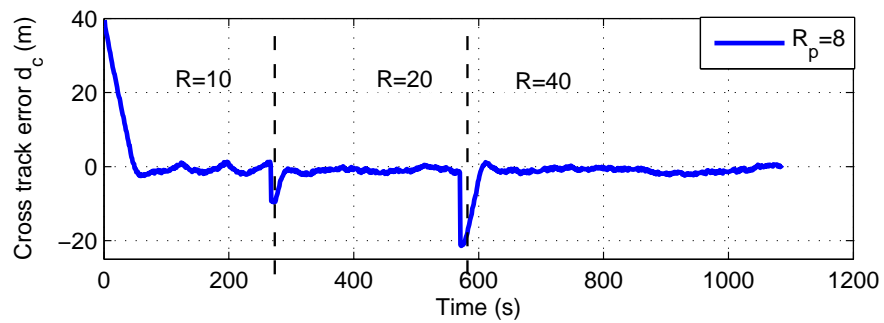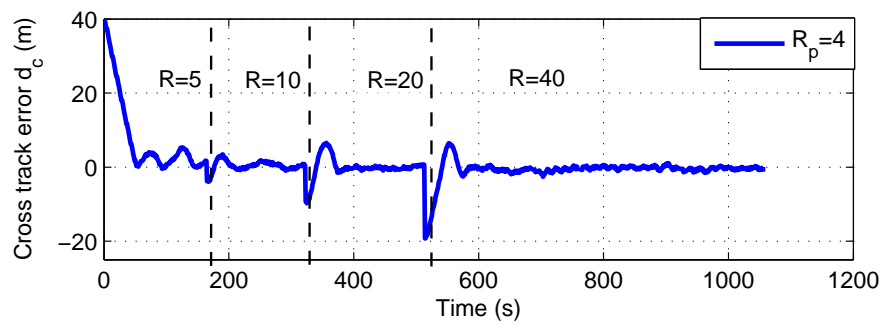
(b) LOS

Figure 3.37: Cross track error time history for VF (Fig. 3.35) and LOS (Fig. 3.36) methods.
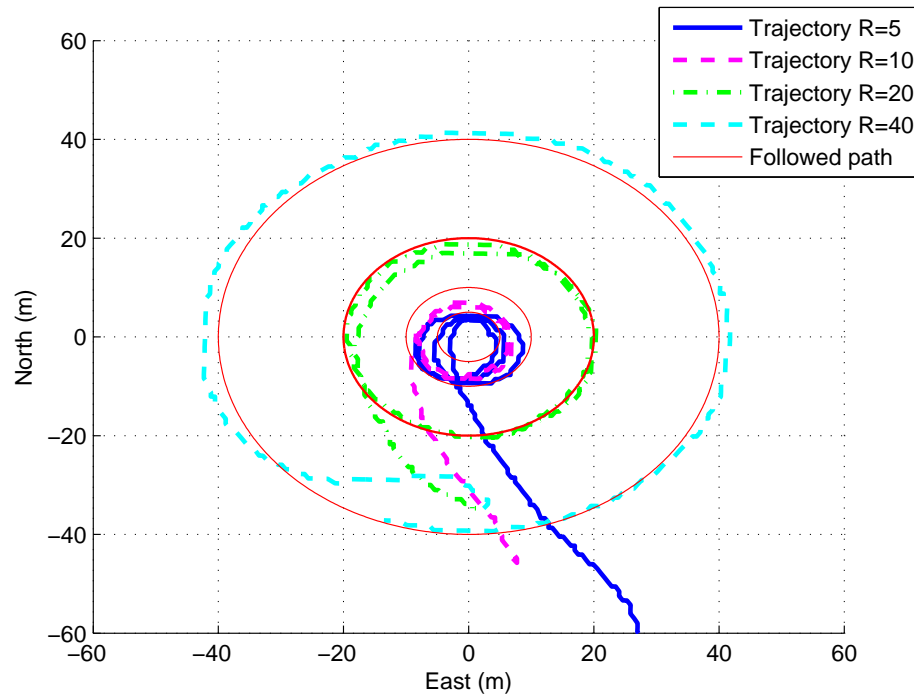
(a) USV trajectories in NED frame with $K_{ps} = 0.1$ and $K_{is} = 0.001$
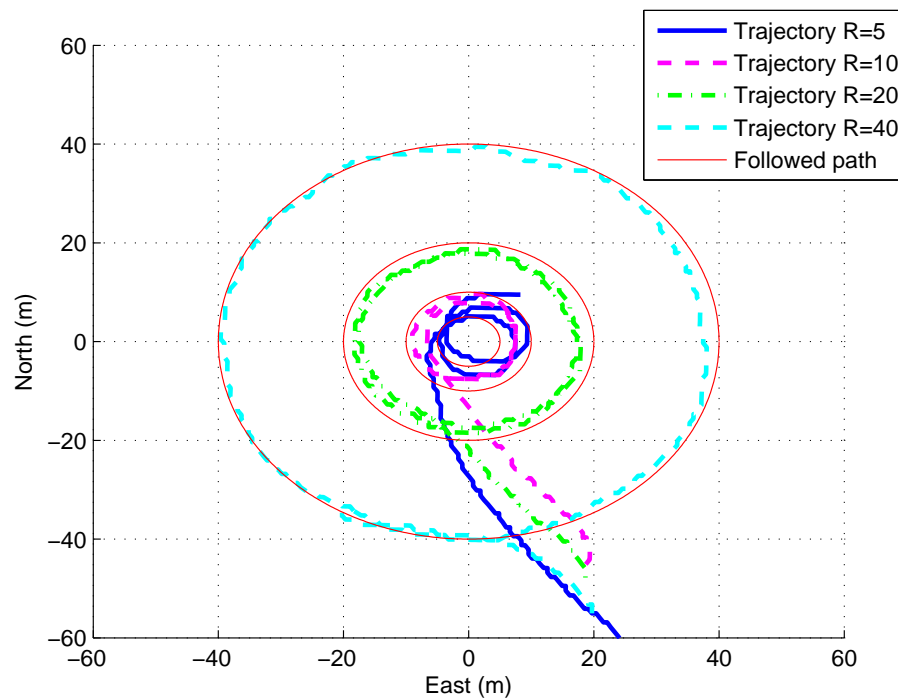
(b) USV trajectories in NED frame with $K_{ps} = 0.3$ and $K_{is} = 0.001$

Figure 3.38: Circular path-following field experiments using the carrot chasing method with the integral gain.
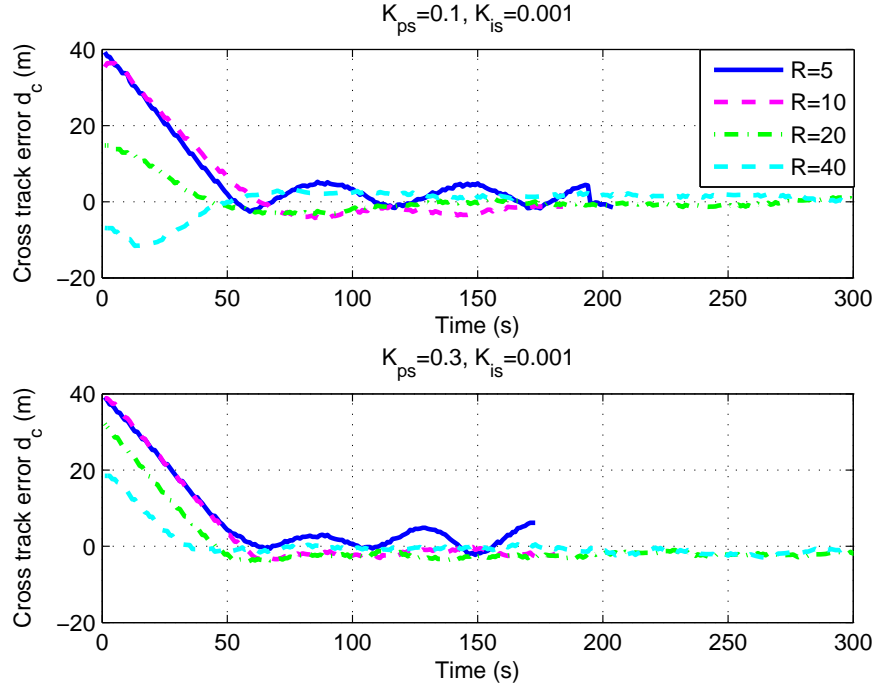
Figure 3.39: Cross track error time history for CCI (Fig. 3.38) method.

LOS may be different from our simulation studies in section 3.4.4.3.

From Table 3.15, we can see that the 20 m circle can be tracked well by the LOS algorithm. Through comparison with the other two methods, we can determine that LOS has a better steady-state path tracking performance. However, due to the path tracking overshoot, LOS requires larger T_c, U_1 and U_2 than the other two algorithms, and its transition error is also the largest. The CCI algorithm provides the best transition control performance, but its steady state is not showing promising results because our evaluation time is not long enough for the vehicle to converge. The VF method shows a balanced performance, where the steady-state path-following performance is close to LOS and the energy cost and path tracking error in the transition stage is relatively small. As for the 40 m circle, interestingly, the VF algorithm has the best performance. Note that VF and the other two methods were experimented on two different days, and thus the environmental disturbances on the vehicle are different. The LOS still needs the largest

Table 3.15: Evaluation of different circular path-following control algorithms

Method	Radius (m)	T_c (s)	U_1 ($\times 10^7$ rpm^2)	U_2 ($\times 10^5$ rpm^2)	E ($\times 10^3$ m)	E_{AV} (m)	E_{SD} (m)
VF		12	0.164	0.225	0.0616	0.540	0.585
CCI	20	9	0.161	0.0119	0.0507	2.428	0.879
LOS		38	0.507	7.006	0.173	0.418	0.466
VF		27	0.338	0.235	0.286	0.371	0.468
CCI	40	26	0.296	0.718	0.273	0.753	0.670
LOS		46	0.348	6.335	3.357	0.821	0.689

energy during the transition stage evaluated by U_1 and U_2, and since there is path tracking overshoot, the transition path tracking error is also the largest. The CCI algorithm has a close transition stage performance as VF, but it requires larger steering energy U_2. The CCI's 40 m circle tracking steady-state performance shows a better performance compared to the 20 m case, and their calculated values of E_{AV} and E_{SD} are close to the LOS case. As a summary, VF and CCI algorithms have a better performance in the transition stage, while both VF and LOS provide a reasonably good steady-state path tracking characteristics.

3.5.3 Waypoint Path-Following Control

In this section, we investigate the three path-following control methods and their actual performances for a survey mission with unexpected environmental disturbances. Again, we employ the waypoints defined in Eq. 3.17 from our previous simulation tests in section 3.4.5. To clearly show the vehicle trajectory, we convert the waypoint and measured GPS position data into the local NED frame with respect to the origin wp_1. In this specific mission, the USV SeaCat is commanded to continuously follow the paths defined by the four waypoints from wp_1 to wp_4. The generation of straight-line and circular paths that link the four waypoints have been discussed in the previous section. The USV is equipped with a sonar in the actual mission, and it can be used to measure the depth information

during the experiments. The connection circle radius is chosen as 10 m since we would like to push the turning dynamics limit of the vehicle, and the desired cruising speed is still selected as 0.8 m/s.

Note that the waypoint experiments were purposely performed in bad weather conditions with relatively large wind and water current influences, so we can examine each algorithm's path tracking robustness to the adverse environmental conditions. Due to the lack of required equipment, the wave condition is not numerically measured. However, by observing the water surface, we can determine there are small waves with frequent breaking crests. The measured environmental parameter values have been summarized in Table 3.16. Through performing the drifting tests, we can predict the mean water current speed as 0.1 m/s from 197° south-west.

Table 3.16: Environmental conditions for waypoint path-following experiments

Method	V_{aw} (m/s)	V_{maw} (m/s)	χ_{aw} $(°)$	T_a $(°C)$	B_p (kPa)	T_w $(°C)$
VF	3.895	9.360	5.029	8.979	100.813	11.400
CCI	3.701	8.330	18.830	10.249	100.900	11.460
LOS	4.746	9.610	4.669	9.327	100.899	11.437

The field trial results have been depicted in Fig. 3.40, Fig. 3.41 and Fig. 3.42. Through comparison of Fig. 3.40a, Fig. 3.41a and Fig. 3.42a, we can determine that all introduced algorithms provide a relatively good path tracking robustness considering the unexpected environmental disturbances. As shown to the top graph of Fig. 3.40b, when implementing VF, the transition from one to another straight-line path is smooth with small overshoot, and the cross track error remains a small value through the survey mission. In the bottom graph of Fig. 3.40b, we can see the vehicle's actual course angle χ can closely follow the desired course angle χ_d. Whereas, for the abrupt change of the reference angle χ_d from 180° to -180°, there will be a small lag due to the vehicle's slow motion dynamics. The CCI algorithm has a promising path tracking performance,

especially during the steady-state straight-line path-following stage as indicated in the top graph of Fig. 3.41b. However, as shown in the bottom graph of Fig. 3.41b, the downside of CCI is during the transition between the circular and straight-line path, where significant path tracking overshoot occurs. The incorporation of the integral gain makes the vehicle respond quickly to the abrupt change of χ_d from 180° to -180°. The LOS algorithm provides a reasonably good performance for following both circular and straight-line paths as indicated in Fig. 3.42b. Referring to the top graph, we can see in most cases the cross track error is within 2 m range of the followed paths. The bottom graph of Fig. 3.42b indicates that LOS can control the vehicle's course angle well to follow χ_d, and there is really small mismatch between χ and χ_d through the whole survey mission. Again, when χ_d changes abruptly from 180° to -180°, there will be a small lag.

Based on the collected data, we can numerically evaluate the USV SeaCat's waypoint path-following performance in completion of the same survey mission. Since we are more concerned about the vehicle's steady-state path tracking characteristics, we make small modifications of the existing metrics similar to section 3.4.5. The evaluation time T_e is defined to measure the time it takes from start to the end of a survey mission, and it has been used for calculating the values of U_1, U_2 and E instead of the convergence time T_c. To achieve the same initial condition through all performed experiments, T_e is calculated from when the vehicle starts tracking the path between wp_2 and wp_3 until it comes back to wp_1. In this way, we can guarantee that the vehicle has already converged to the path and starts from a close region.

The computed metrics values are summarized in Table 3.17. Owing to the constant changing environmental conditions, the actual experimental results may differ from our simulation studies. As can be seen, the VF method features the smallest control energy U_1 while it requires the largest steering energy U_2 during the survey mission. The CCI algorithm is more efficient in the steering motion and it provides a relatively good steady-
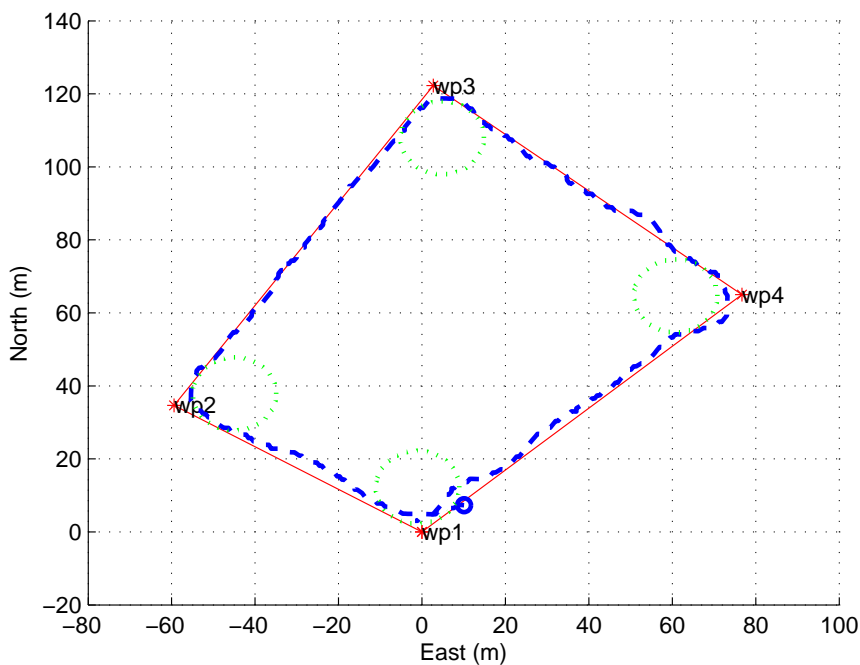
(a) USV trajectories in NED frame
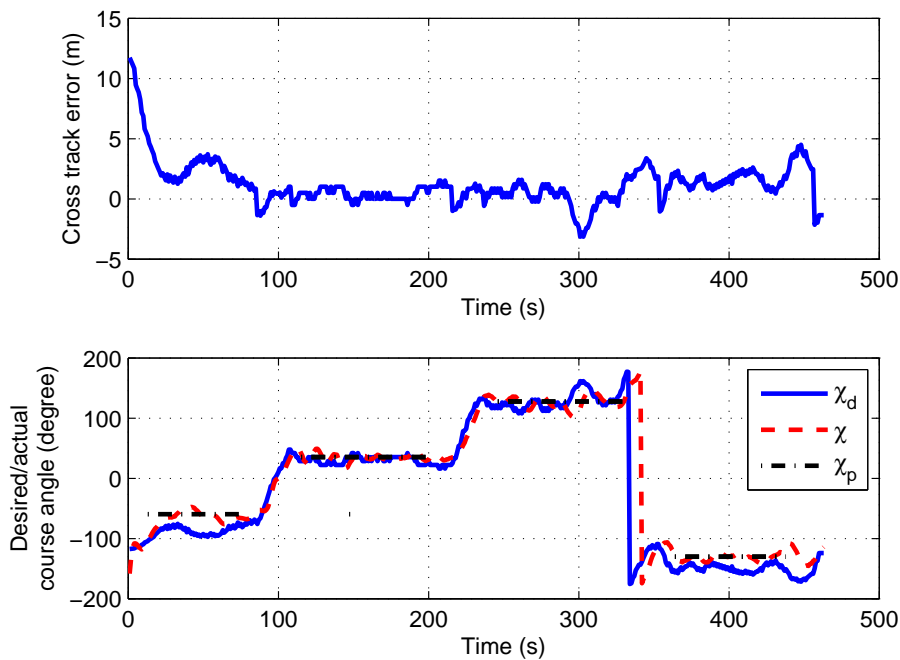
(b) Path-following control performance

Figure 3.40: Waypoint path-following field experiments using the vector field method. In Fig. (a), we show the actual USV trajectories compared to the desired path. The desired circular path is indicated by the dot line. In Fig. (b), we show the time history of cross track error, desired course angle, actual vehicle course angle and the path direction.
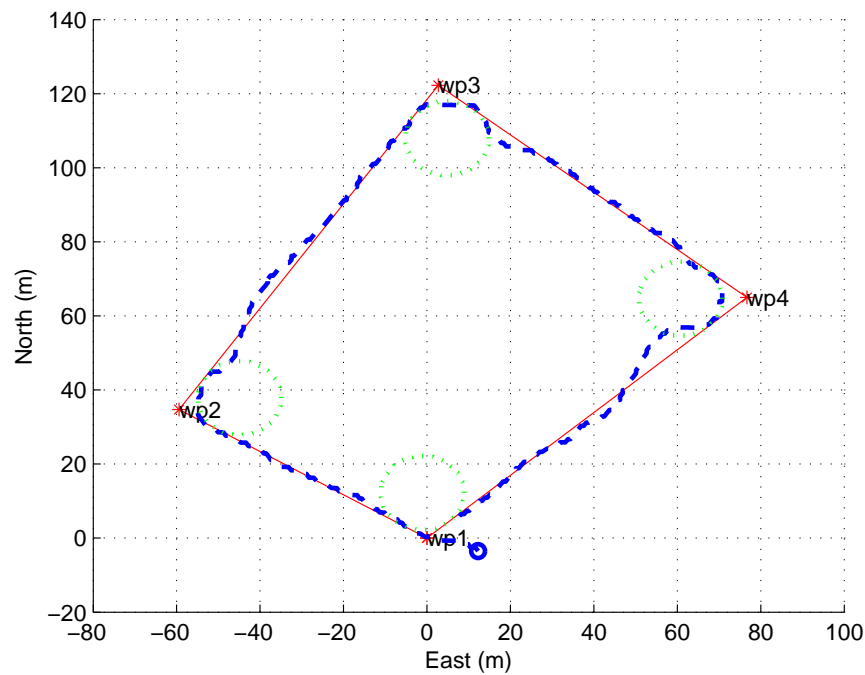
(a) USV trajectories in NED frame
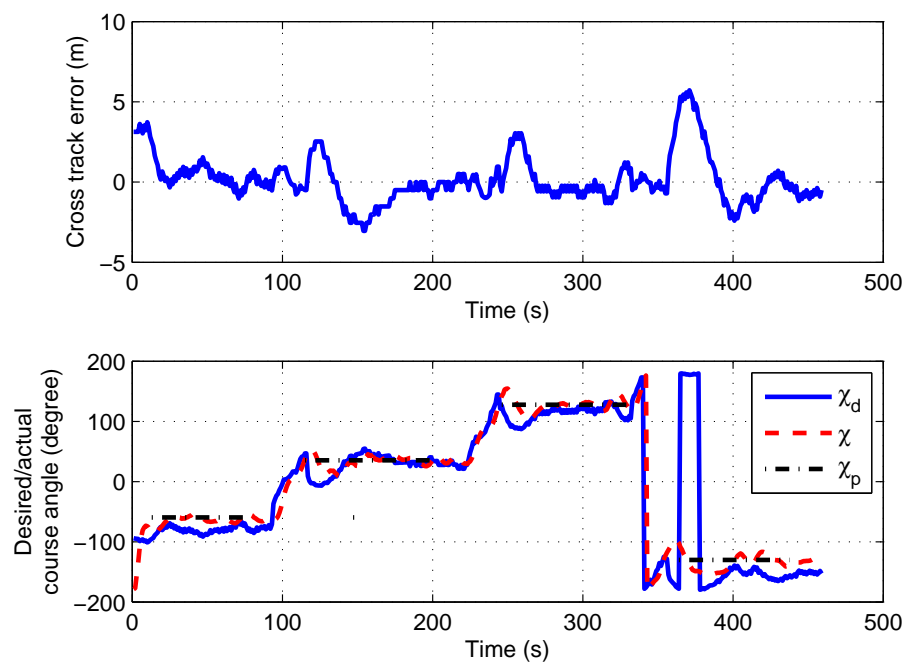
(b) Path-following control performance

Figure 3.41: Waypoint path-following field experiments using the carrot chasing method with integral gain. In Fig. (a), we show the actual USV trajectories compared to the desired path. The desired circular path is indicated by the dot line. In Fig. (b), we show the time history of cross track error, desired course angle, actual vehicle course angle and the path direction.
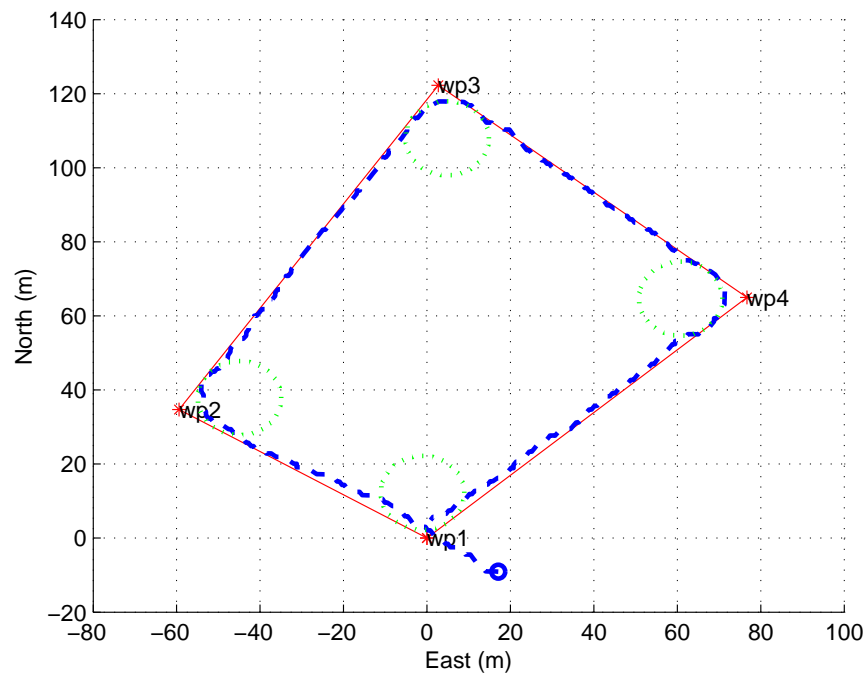
(a) USV trajectories in NED frame
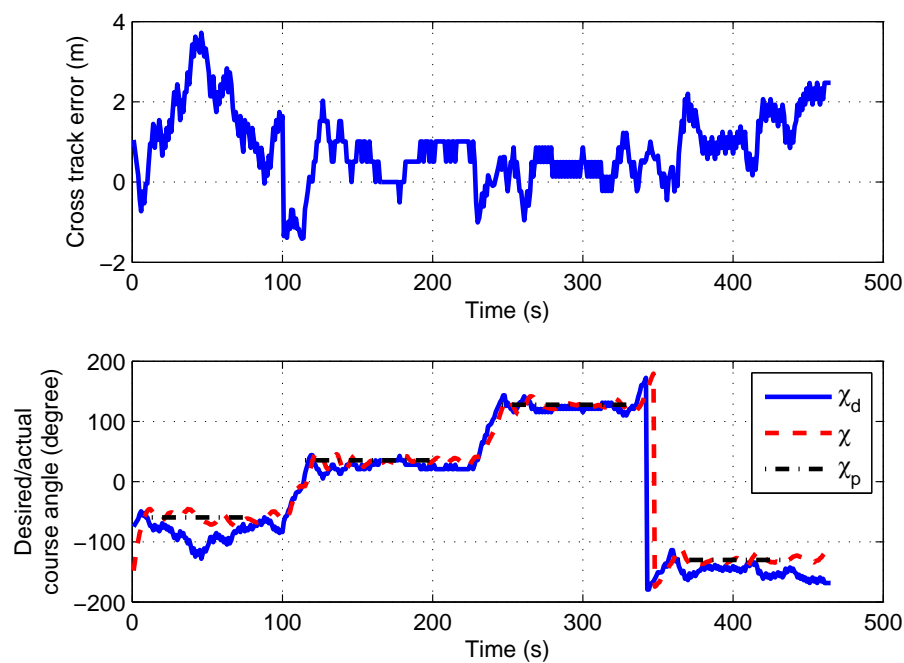
(b) Path-following control performance

Figure 3.42: Waypoint path-following field experiments using the line-of-sight method. In Fig. (a), we show the actual USV trajectories compared to the desired path. The desired circular path is indicated by the dot line. In Fig. (b), we show the time history of cross track error, desired course angle, actual vehicle course angle and the path direction.

Table 3.17: Comparison of the waypoint path-following field experiments

Method	Value	T_e (s)	U_1 ($\times 10^7$ rpm^2)	U_2 ($\times 10^6$ rpm^2)	E ($\times 10^2$ m)	E_{AV} (m)	E_{SD} (m)
VF	$k_s=k_c=0.3$ $\chi_{Ms}=\chi_{Mc}=70°$	367	4.682	2.966	3.870	1.054	1.080
CCI	$K_{ps}=K_{pc}=0.3$ $K_{is}=K_{ic}=0.001$	367	4.750	2.804	3.991	1.087	1.257
LOS	$R_p=4$	358	4.858	2.873	2.794	0.780	0.858

state path tracking performance. However, due to the oscillation motion when the vehicle switches between the followed circular and straight-line paths, E_{AV} and E_{SD} are calculated with large values. LOS consumes the maximum energy U_1, but it is the fastest method to complete one survey mission. When implementing LOS, the total and average path tracking error is the lowest across the three investigated algorithms.

In summary, by spending time tuning each individual control parameters, the evaluated algorithms, i.e. VF, CCI and LOS, provide reasonably good performance to complete the desired survey mission. The VF algorithm has a balanced performance without introducing large path tracking overshoot, but it is not good for following the circular path. The CCI algorithm has a better performance when performing the long-term mission, because the integral gain will have enough time to accumulate errors and influence the path tracking performance. However, as for the short followed path and the case where the vehicle has to switch between circular and straight-line paths frequently, it may not be a promising candidate. Interestingly, LOS provides the best path tracking results among the three methods. In the parameter space exploration section, we have investigated the potential problem of LOS for tracking the circular paths. Nevertheless, this deficiency becomes the advantage of LOS due to the vehicle's slow dynamics. The LOS can be regarded as providing an aggressive control for the vehicle to follow the straight-line and circular paths, and this will complement the slow motion dynamics of the vehicle.

3.6   General Chapter Summary

In this chapter, we investigated three well-accepted methods, i.e. Vector Field Method (VF), Carrot Chasing Method (CC) and Line-of-Sight Method (LOS), for path-following control of an Unmanned Surface Vehicle (USV). We provided a complete parameter space exploration and illustrated and evaluated these algorithms in simulations and real-world experiments. Our analysis and comparison of these methods are pioneering in the USV research community, and we hope our research can provide a good reference for the USV practitioners for their future work when they have to decide on an appropriate strategy for completion of a specific ocean survey mission. It is important to note that although there are minor differences between each controller, after well tuning of the control parameters, their path tracking performances in the field trial are close. Therefore, a self-tuning algorithm will be of great interest for future application of the introduced algorithms.

The successful field trial results had also proved the functionality of the guidance and control system architecture, and the path tracking accuracy demonstrated the robustness of the introduced algorithms. However, during the experiments we found out that the adverse weather conditions could sometimes cause the USV SeaCat to suffer significant unsafe rolling and pitching motion. Although we had already been able to control a USV to accurately track the desired paths in the horizontal plane, the uncontrollable oscillatory motion caused by the environmental factors can potentially lead to the capsizing at any moment. Therefore, in the next two chapters, we will investigate the oscillatory motion of a USV.

Chapter 4

Oscillatory Motion Modeling and Parameter Identification

We have already introduced the planar motion modeling, and based on that, three differ-
ent path-following control algorithms have been successfully developed, implemented and
tested on a USV. However, in reality, a USV experiences all six degrees of freedom motion
simultaneously in the seaway, and it is the oscillatory movement of heave, roll and pitch
that is closely related to a USV's operational safety. In this chapter, detailed procedures
for building the oscillatory motion model and performing model parameter identification
are introduced. To make the considered problem tractable, we follow the convention and
investigate the decoupled linear and nonlinear model in heave, roll and pitch. We assume
the primary disturbance for the oscillatory motion is from the ocean waves, and thus, we
also present the calculation method of the wave excitation forces and moments for the
corresponding degree of freedom. Using the presented model, we will carry out the safety
analysis of a USV in the next chapter.

4.1 Heave, Roll and Pitch Motion Modeling

In this section, we will introduce the decoupled linear and nonlinear model for a USV's heave, roll and pitch motion. As we know, a marine vessel's dynamic motion in the seaway is complicated, but for simplicity, we assume that each oscillatory motion can be decoupled from the other degrees of freedom. This assumption has actually been widely employed for analysing a ship's roll motion dynamics [29] in the naval architectural community, and it will also bring great convenience for the parameter identification process.

According to our defined 6 DOF motion variable vectors in Eq. 2.1, we can formulate the generic oscillatory motion model along heave, roll and pitch as

$$(M_i + M_{Ai})\ddot{\eta}_i + D_i(\dot{\eta}_i) + R_i(\eta_i) = \tau_i \ (i = 3, 4, 5) \tag{4.1}$$

where we define

$$[\eta_3, \eta_4, \eta_5]^T \triangleq [z, \phi, \theta]^T$$

$$[\tau_3, \tau_4, \tau_5]^T \triangleq [Z, K, M]^T$$

following the SNAME (1950) notation. In Eq. 4.1, M_i denotes the mass inertia or the moment of inertia, M_{Ai} is the added mass or the added moment of inertia, $D_i(\dot{\eta}_i)$ includes the damping terms and $R_i(\eta_i)$ stands for the restoring forces or moments. It is worth noting that the hydrodynamic coefficients in Eq. 4.1 are generally wave frequency dependent. In the scope of this study, however, the condition of regular wave excitation and small-amplitude response is assumed. Hence, the hydrodynamic coefficients can be treated as constant. In Eq. 4.1, τ_i stands for the excitation forces or moments, which may include the disturbances from wind, waves and ocean currents. The studied USV SeaCat has a relatively small portion above the water, so the wind effect is negligible.

The ocean current can be regarded as a constant or slowly changing vector in the vehicle's translational motion, and it can also be neglected from the oscillatory motion. Therefore, we can assume that the main contribution for τ_i is from the ocean waves.

The damping forces and moments are normally formulated as a linear, linear plus quadratic or higher order polynomial [48]. In this study, we will examine two common forms, i.e. linear and linear plus quadratic, which is given as

$$D_i(\dot{\eta}_i) = D_{i1}\dot{\eta}_i + D_{i2}\dot{\eta}_i|\dot{\eta}_i| \tag{4.2}$$

where D_{i1} and D_{i2} are the damping coefficients, and for the linear case $D_{i2} = 0$. The restoring forces and moments can be regarded as a linear function of η_i within the small range of the equilibrium position. However, when the displacement position and angle are large, this relationship is nonlinear and it is normally modeled as an odd polynomial form as [30]

$$R_i(\eta_i) = R_{i1} \cdot \eta_i + R_{i3} \cdot \eta_i^3 + R_{i5} \cdot \eta_i^5 + ...$$

In the following, we will introduce the linear model for heave, roll and pitch and the nonlinear model for roll and pitch. Note that we assume that the platform's heaving motion is not as critical as rolling and pitching, because the two latter movements can directly cause the capsizing.

If we assume that the vehicle's oscillatory motion is within a small range of the equilibrium position, the case for most USV's operations, the damping and restoring forces and moments can be regarded as linear. Therefore, the decoupled generic linear model can be written as

$$(M_i + M_{Ai})\ddot{\eta}_i + D_{i1}\dot{\eta}_i + R_{i1}\eta_i = \tau_i \ (i = 3, 4, 5) \tag{4.3}$$

A USV operating in the harsh ocean environments may encounter large oscillatory motions, and thus the linear model is not valid and we need to consider the nonlinearity in the damping and restoring forces and moments. A simplified generic decoupled nonlinear model for roll and pitch is given as

$$(M_i + M_{Ai})\ddot{\eta}_i + D_{i1}\dot{\eta}_i + D_{i2}\dot{\eta}_i|\dot{\eta}_i| + R_{i1}\eta_i + R_{i3}\eta_i^3 = \tau_i \ (i = 4, 5) \tag{4.4}$$

where we assume that the damping model includes the linear and quadratic terms, and the nonlinear restoring moment is modeled as a 3rd-order odd polynomial.

For convenience of the further discussion, we write down the vehicle's decoupled non-linear roll and pitch motion model as

$$I_r\ddot{\phi} + D_{41}\dot{\phi} + D_{42}\dot{\phi}|\dot{\phi}| + R_{41}\phi + R_{43}\phi^3 = K \tag{4.5}$$

and

$$I_p\ddot{\theta} + D_{51}\dot{\theta} + D_{52}\dot{\theta}|\dot{\theta}| + R_{51}\theta + R_{53}\theta^3 = M, \tag{4.6}$$

respectively. It is noteworthy that the virtual roll and pitch moment of inertia I_r and I_p include the added moment of inertia due to the surrounding water, and they can be calculated using the transverse and longitudinal metacentric height $\overline{GM}_T$ and $\overline{GM}_L$ as [49]

$$I_r = (\frac{T_{n4}}{2\pi})^2 \nabla g \overline{GM}_T \tag{4.7}$$

and

$$I_p = (\frac{T_{n5}}{2\pi})^2 \nabla g \overline{GM}_L \tag{4.8}$$

where T_{n4} and T_{n5} denote the natural roll and pitch period, ∇ defines the vehicle displacement and g is the gravitational acceleration.

4.2 Parameter Identification

Free decay tests in calm water conditions are carried out to collect the USV motion data for parameter identification. Note that to analyse a USV's safety, we need to find the worst case scenario considering the wide band wave influences in the dynamic ocean. Hence, the identified hydrodynamic parameter values at the natural frequency or resonance frequency, is helpful for us to determine the maximum motion response, i.e. the worst oscillatory motion.

During the tests, the USV SeaCat is put into a deep tank in engineering building of Memorial University. External forces are applied on the vehicle to introduce a static heave, roll or pitch displacement separately. When the external forces are removed, the vehicle will decay in the specific degree of freedom until the motion stabilizes around the equilibrium position. We employ the 3DM-GX1 Attitude and Heading Reference System (AHRS) to record the vehicle motion in heave, roll and pitch. The sensor has a sampling rate of 100 Hz, and its acceleration and angle measurement accuracy are 0.0015 m/s^2 and $\pm 0.5°$, respectively.

4.2.1 Linear Model Parameter Identification

In this section, we will introduce the parameter identification for linear heave, roll and pitch motion model. The results from this section will be used in Chapter 5 for dynamic response analysis.

When $\tau_i = 0$ in Eq. 4.3, the oscillation of heave, roll and pitch is known as damped oscillatory motion, and its solution in time domain is given as [32]

$$\eta_i = A_{mi} e^{-\upsilon_i t} \sin(\omega_{di} t + \delta_i) \tag{4.9}$$

where

$$v_i = \frac{D_{i1}}{2(M_i + M_{Ai})}$$

is the decaying constant, ω_{di} is the damped oscillation frequency which is given as

$$\omega_{di} = \sqrt{\omega_{ni}^2 - v_i^2}, \tag{4.10}$$

A_{mi} is the constant that can be determined from the initial condition, and δ_i is the initial phase angle. Note that ω_{ni} is the natural frequency of the undamped oscillatory motion when $D_{i1} = 0$, and it can be calculated as

$$\omega_{ni} = \sqrt{\frac{R_{i1}}{M_i + M_{Ai}}}.$$

In order to get the solution in Eq. 4.9, the following condition needs to stand

$$D_{i1} < \sqrt{4(M_i + M_{Ai})R_{i1}}.$$

The linear model coefficients of $\xi_i = [A_{mi}, v_i, \omega_{di}, \delta_i]^T$ in Eq. 4.9 can be identified by solving the problem of

$$\min_{\xi_i} ||f(\xi_i, t) - \eta_{im}||^2 = \min_{\xi_i} \sum_n (f(\xi_i, t) - \eta_{im})^2 \ (i = 3, 4, 5) \tag{4.11}$$

where $f(\xi_i, t) = \eta_i$ denotes the solution of the oscillatory motion, η_{im} represents the measurement of heave translation, roll angle and pitch angle from the decay experiments, and n represents the number of samples. Based on the sensor configuration, we have the direct measurement of the roll and pitch angle, and they can be directly used for parameter identification. As for the heave motion, we need to double integrate the acceleration data to get the translational distance. However, this integration process will not provide us

Table 4.1: Parameter identification results for the linear heave, roll and pitch model

Motion	A_{mi}	υ_i	ω_{di} (rad/s)	δ_i or $\delta_i - \varepsilon$ (rad)	ω_{ni} (rad/s)	T_{ni} (s)
Heave $(i = 3)$	0.0254	0.1619	4.6806	-1.7292	4.6833	1.3416
Roll $(i = 4)$	3.2981	0.0793	3.1189	8.1284	3.1199	2.0139
Pitch $(i = 5)$	-4.6440	0.0892	3.2992	1.5776	3.3004	1.9038

with accurate results due to sensor bias and noises. Therefore, instead we calculate the second-order derivative of Eq. 4.9 for heave motion as

$$
\begin{aligned}
\ddot{\eta}_3 &= A_{m3} e^{-\upsilon_3 t} [(\upsilon_3^2 - \omega_{d3}^2) \sin(\omega_{d3} t + \delta_3) - 2\upsilon_3 \omega_{d3} \cos(\omega_{d3} t + \delta_3)] \\
&= A_{m3} e^{-\upsilon_3 t} sin(\omega_{d3} t + \delta_3 - \varepsilon)
\end{aligned}
\tag{4.12}
$$

where

$$
\varepsilon = \tan^{-1}(\frac{2\upsilon_3 \omega_{d3}}{\upsilon_3^2 - \omega_{d3}^2}).
$$

Depending on this new form, we can directly use the measured acceleration data and identify the heave motion model parameters. The minimization problem for the heave motion is updated as

$$
\min_{\xi_3} ||f(\xi_3, t) - \ddot{\eta}_{3m}||^2 = \min_{\xi_3} \sum_n (f(\xi_3, t) - \ddot{\eta}_{3m})^2.
$$

A series of decay tests have been carried out with small initial displacement values from the equilibrium position for the heave, roll and pitch motion. It has been found that the identified parameter values of A_{mi} and δ_i $(\delta_i - \varepsilon)$ will vary depending on the specific initial condition, while as for the main characteristic parameters of ω_{di} and υ_i, the identified values are close. Therefore, only one set of data have been chosen and shown in Table 4.1. Note that according to Eq. 4.10, the natural frequency ω_{ni} and natural period T_{ni} are also computed and included in the table.

Employing the identified model parameter values from Table 4.1, we perform the simulation and compare it with the original experimental data. These results have been depicted in Fig. 4.1, Fig. 4.2 and Fig. 4.3. Through comparison, we can conclude that the identified linear models can closely approximate the studied platform's oscillatory movement within a small range of the equilibrium position.
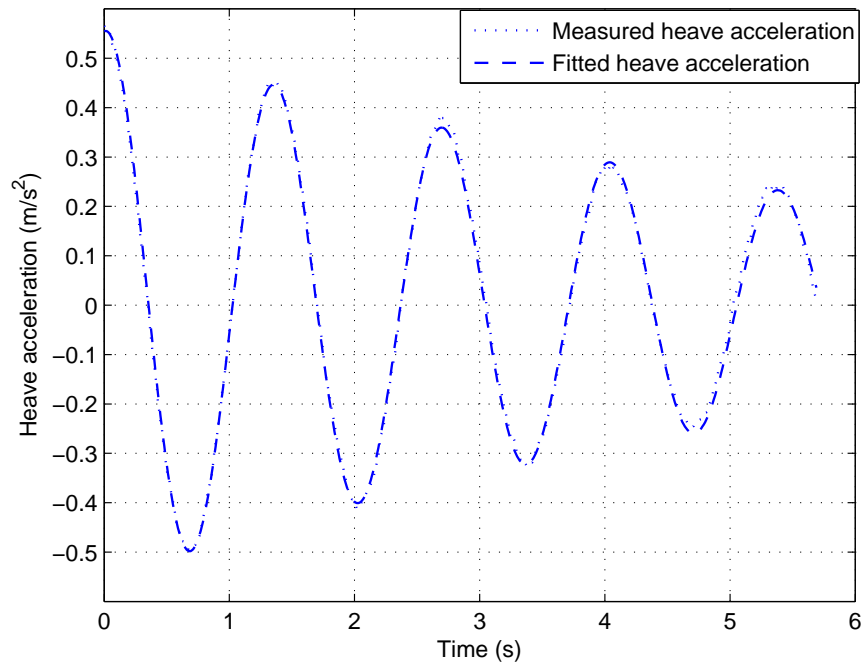
Figure 4.1: The comparison between the measured and simulated heave acceleration data using the linear heave motion model.

A set of independent data have been recorded to further prove the reliability of the identified roll and pitch linear motion model. In this experiment, we introduce an initial static roll and pitch angle at the same time, and then we let the vehicle have both roll and pitch decaying motion. In the simulation, we employ the identified parameter values of ω_{di} and υ_i from Table 4.1 and the newly identified values of A_{mi} and δ_i in the new test. The comparison results are depicted in Fig. 4.4, and we can see that our identified models have a reasonably good performance to approximate the vehicle's actual motion
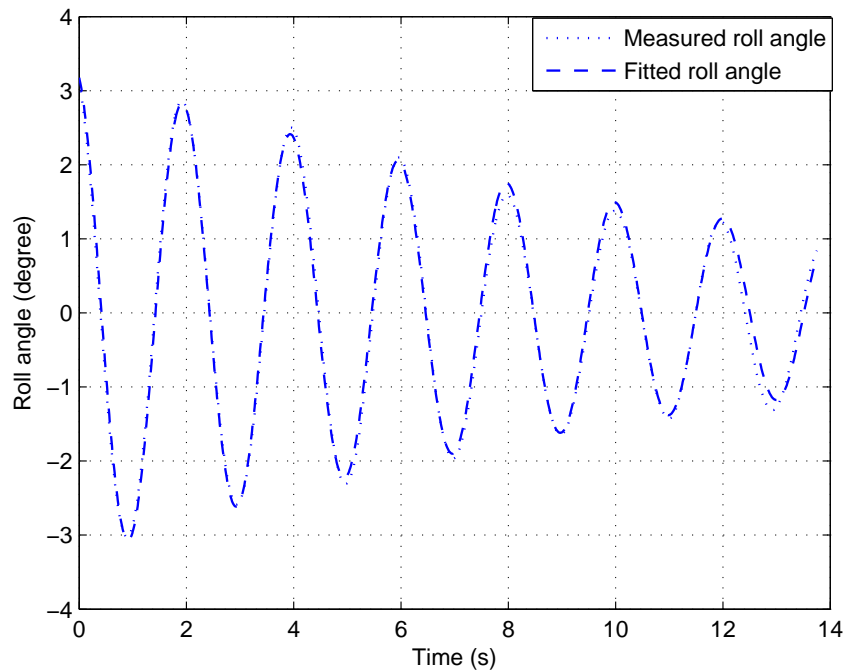
Figure 4.2: The comparison between the measured and simulated roll motion data using the linear roll motion model.

in roll and pitch.

Depending on our identification results, we can write down the generic linear state-space model for heave, roll and pitch as

$$\ddot{\eta}_i + 2\upsilon_i\dot{\eta}_i + \omega_{ni}^2\eta_i = 0 \ (i = 3, 4, 5)$$

where we assume that $\tau_i = 0$ and the value of $(M_i + M_{Ai}) \neq 0$ so we can divide it on both sides of Eq. 4.3.

4.2.2 Nonlinear Model Parameter Identification

In this section, we will follow the physical properties of rolling and pitching motion to identify the nonlinear model parameter values. Since the heave motion is not as critical
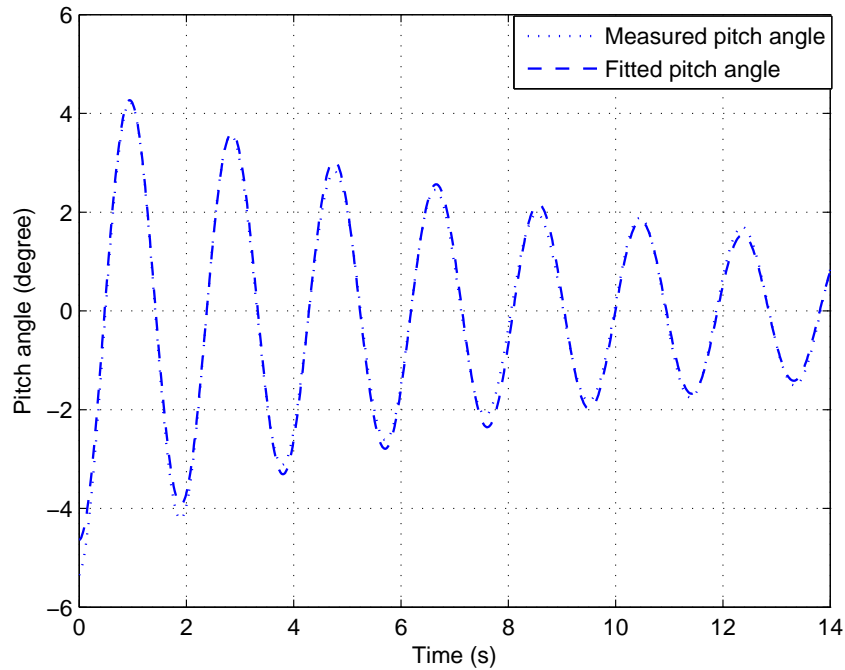
Figure 4.3: The comparison between the measured and simulated pitch motion data using the linear pitch motion model.

as roll and pitch in terms of the evaluation of a vehicle's safety, its nonlinear model is not included in our following discussion.

The virtual roll and pitch moment of inertia I_r and I_p can be computed based on Eq. 4.7 and Eq. 4.8. The required parameter values have been summarized in Table 4.2. Note that the natural period T_{n4} and T_{n5} have already been calculated in Table 4.1, so they are not included. In Table 4.2, ∇ denotes the vehicle displacement and g is the gravitational acceleration. The metacentric height $\overline{GM_T}$ and $\overline{GM_L}$ are experimentally determined by performing the inclining tests and these values are also validated using Rhinoceros 5 with Orca3D naval architecture toolbox [50]. Note that using Orca3D we will be able to compute intact hydrostatics for various type vessels. The produced report by Orca3D includes tabular data at the specified flotation condition as well as plots of calculated parameters. Finally, we calculate and validate I_r=48.7613 $kg \cdot m^2$ and I_p=32.2438 $kg \cdot m^2$.
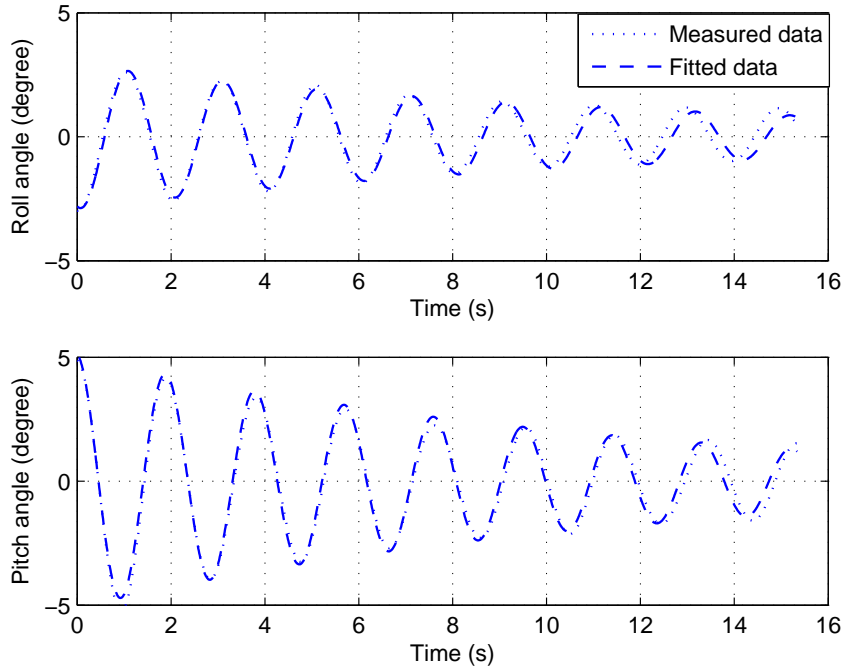
Figure 4.4: The comparison between the measured and simulated roll and pitch motion data. In this experiment, the vehicle has the roll and pitch decay motion simutaneously.

Table 4.2: Parameter values in Eq. 4.7 and Eq. 4.8

Parameters	∇ (kg)	g (m/s^2)	$\overline{GM_T}$ (m)	$\overline{GM_L}$ (m)
Values	163.4	9.81	0.2961	0.2191

We import the 3D model of the vehicle into the Rhinoceros 5 software and use its hydrostatics analysis package to generate the restoring moment curve. The critical roll angle is determined as around $45°$, above which the vehicle will capsize. Our nonlinear roll restoring moment model coefficients can be identified by fitting the polynomial equation to the collected data in the range of $\phi \in [-45°, 45°]$, and this fitting result is depicted in Fig. 4.5. As for the pitch restoring moment, we achieve its critical angle as $57.2°$, and by implementing the method from [32], we can calculate $R_{51} = \nabla g\overline{GM_L}$. The pitch restoring moment is a 3rd-order odd polynomial as shown in Eq. 4.6, and thus using
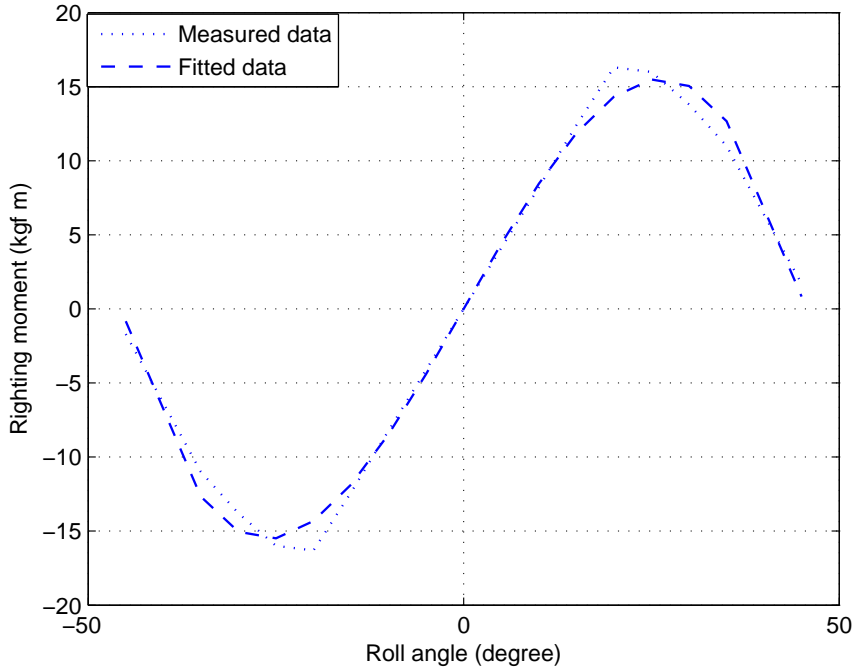
Figure 4.5: A comparison of the measured and fitted roll restoring moment curve, and the data fitting range is in $\phi \in [-45°, 45°]$.

the value of R_{51} and the critical angle, R_{53} can also be calculated. A summary of the identified restoring moment coefficients for roll and pitch motion has been provided in Table 4.3.

Table 4.3: Roll and pitch restoring moment model coefficients

Motion	R_{i1}	R_{i3}
Roll ($i = 4$)	499.1269	-792.4587
Pitch ($i = 5$)	351.2072	-352.3752

The energy method [51] has been used for identification of the nonlinear damping terms in Eq. 4.2. The nonlinear damping effect is evident with large roll motions, so we choose to use the experimental data set where we have a relatively large roll oscillations for the parameter identification. The decaying curve for vehicle's roll motion can be fitted

as an exponentially damped sinusoidal solution [52] with the form

$$\phi = A_{m4}e^{-\sum_{j=1}^{N}\beta_j t^j}cos(\omega_{d4}t + \delta_4) \tag{4.13}$$

where A_{m4} and δ_4 depend on the initial condition in the performed experiment. Compared to Eq. 4.9, we use $\sum_{j=1}^{N}\beta_j t^j$ as the exponent so that we can better represent the steeper nonlinear decaying envelope. The parameter values of β_j can be identified by using the maximum measured positive roll angle in each decay cycle, and the least-squares fitting results have been summarized in Table 4.4. Two fitted envelopes where one only uses the linear term β_1 and the other implements a 3rd-order polynomial of β_i have been depicted in Fig. 4.6. It clearly shows that the one with higher order decay terms can represent the decay envelope more accurately.

Table 4.4: Identified decay term values for Eq. 4.13

Order	A_{m4}	δ_4	β_1	β_2	β_3
1st	10.4341	0	0.1129	0	0
3rd	10.4341	0	0.1507	-0.0049	0.0001

In the roll decay process, the total energy at each time instant t_j can be formulated as

$$\begin{aligned} E(t_j) &= E_{kt_j} + E_{pt_j} \\ &= \frac{1}{2}I_r\dot{\phi}^2 + \int_0^{t_j}(R_{41}\phi + R_{43}\phi^3)\dot{\phi}dt \end{aligned}$$

where E_{kt_j} represents the kinetic energy and E_{pt_j} stands for the potential energy due to the rolling motion. The total energy will decrease due to the damping forces such as from skin friction effects. Therefore, the reduction of the total energy in a specific time range will be equal to the negative of the work that is done by the damping forces. This
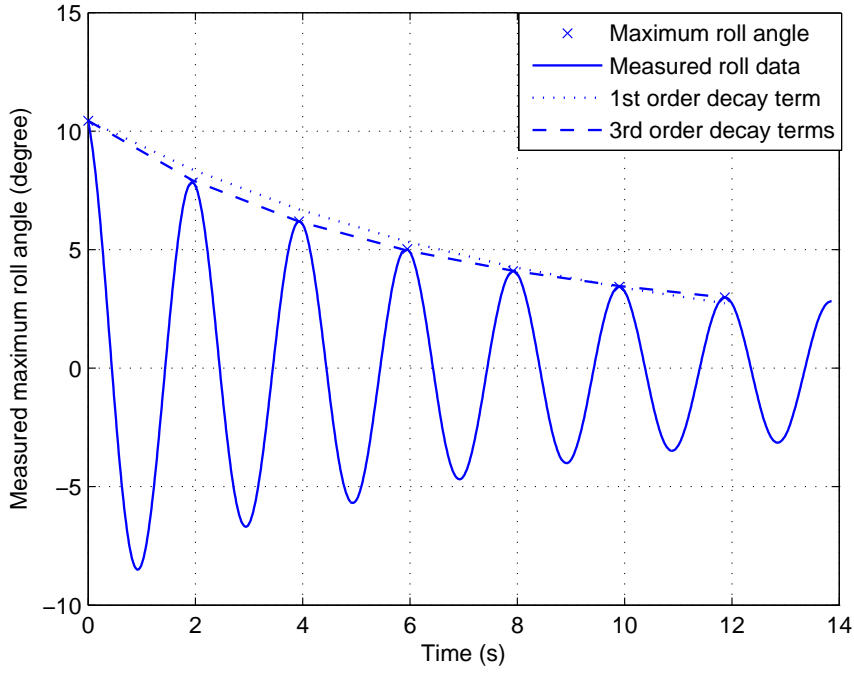
Figure 4.6: A comparison of the decay envelop with 1st-order decay term and 3rd-order decay terms. The 3rd-order one shows a better fitting to the experimental data.

relationship has been summarized in

$$
\begin{aligned}
E(t_{j+1}) - E(t_j) &= -\int_{t_j}^{t_{j+1}} (D_{41}\dot{\phi} + D_{42}\dot{\phi}|\dot{\phi}|)\dot{\phi}dt \\
&= -D_{41}\int_{t_j}^{t_{j+1}} \dot{\phi}^2 dt - D_{42}\int_{t_j}^{t_{j+1}} \dot{\phi}^2|\dot{\phi}|dt
\end{aligned}
\tag{4.14}
$$

In Eq. 4.14, $\dot{\phi}$ can be calculated based on Eq. 4.13, and the numerical integration is calculated using Euler Method. Therefore, the only unknown terms of D_{41} and D_{42} can be identified by performing the least-squares fitting, and the results have been summarized in Table 4.5. Note that for comparison, we also include the identification result where only the linear damping is considered.

We substitute all identified parameter values, including I_r, restoring moment and damping terms, into Eq. 4.5 to get the decoupled nonlinear roll motion model in state

Table 4.5: Identified damping parameter values for roll and pitch motion model

Damping model	D_{i1}	D_{i2}
Linear roll damping $(i = 4)$	12.8211	0
Linear pitch damping $(i = 5)$	6.7322	0
Nonlinear roll damping $(i = 4)$	6.8840	14.6273
Nonlinear pitch damping $(i = 5)$	4.5529	6.1423

space form. The simulation in time domain neglecting the wave exciting moments is performed, and the results are depicted in Fig. 4.7. It can be seen that the model with quadratic and linear damping terms shows a better agreement with the experimental data.
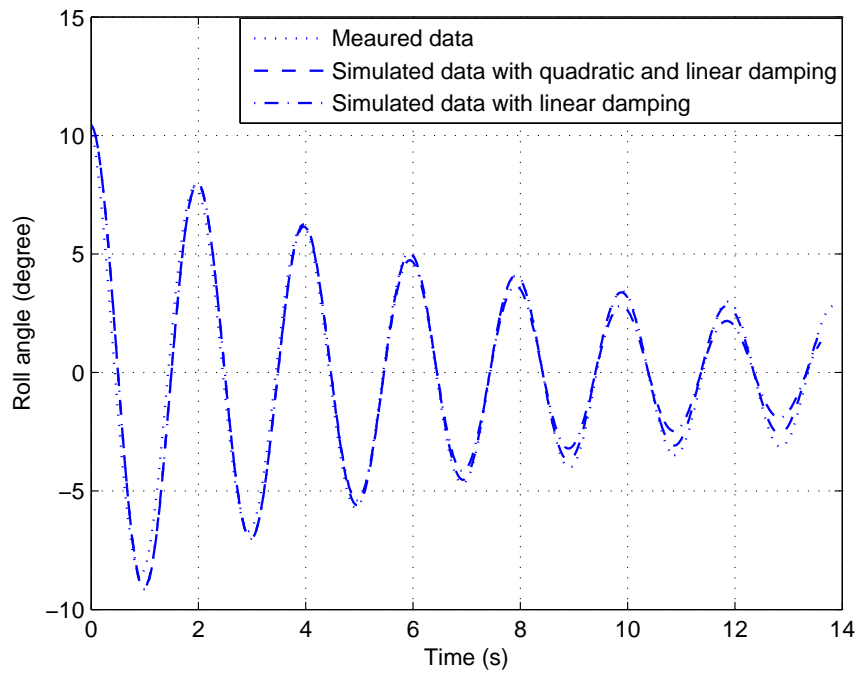
Figure 4.7: A comparison between the simulated and measured roll decay motion using the state space model in Eq. 4.5 without exciting moments. The dash line indicates the simulated data with the quadratic and linear damping terms, while the dash dot line represents the simulation with only the linear damping term.

For the pitch decay motion model, we follow a similar procedure as in the roll case to identify the damping terms. The identified parameter values of I_p and pitch restoring moment in Table 4.3 are used, and the damping terms have been determined as summa-

rized in Table 4.5 using the energy method. The simulation results of the nonlinear pitch model is shown in Fig. 4.8. Again, the model that takes into account the quadratic term provides a better fitting to the measured motion data.
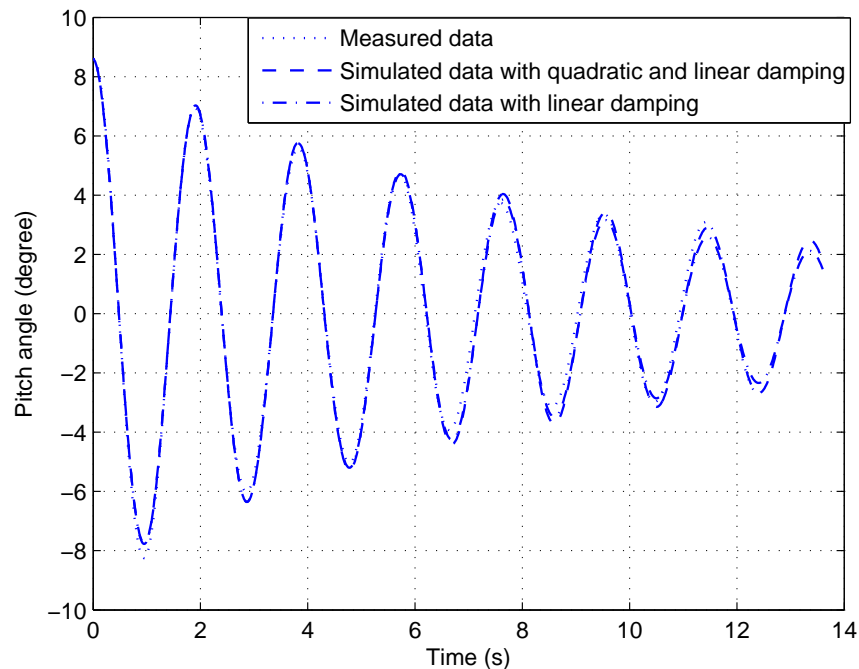
Figure 4.8: A comparison between the simulated and measured pitch decay motion using the state space model in Eq. 4.6 without exciting moments. The dash line indicates the simulated data with the quadratic and linear damping terms, while the dash dot line represents the simulation with only the linear damping term.

4.3 Wave Excitation Forces and Moments

In this section, we will introduce how we can formulate the wave-induced excitation forces and moments for the heave, roll and pitch motion. Some fundamental concepts of the waves are reviewed for convenience of the following discussion [32]. The equation of a sinusoidal wave travelling at a velocity of V_w in the positive x_s direction can be written

as

$$\begin{aligned}
\zeta &= \zeta_A \cos[k(x_s - V_w t)] \\
&= \zeta_A \cos(k x_s - \omega_w t).
\end{aligned}$$

(4.15)

In Eq. 4.15, ζ is the surface wave elevation, ζ_A is the wave amplitude, t is time in seconds, ω_w is the wave circular frequency and k is the wave number given as

$$k = \frac{2\pi}{L_w} = \frac{\omega_w^2}{g}$$

(4.16)

where L_w denotes the wave length. Assuming the deep water conditions, the wave velocity can be approximated as

$$V_w = \frac{gL_w}{2\pi},$$

which indicates that the wave velocity is proportional to wave length.

4.3.1 Heave Excitation Forces

To model the excitation force for heaving motion, we follow the method from [32]. The ocean waves may come from a specific direction χ_w with respect to a USV's heading angle, and thus the effective wave number can be computed as

$$k_e = \frac{2\pi}{L_{we}} = k \cos(\chi_w).$$

where L_{we} defines the effective wave length.

In the calculation of the heave exciting force, the wave is assumed to pass the USV gradually so that the platform remains stationary at any time instant. The excitation force can be calculated as the integration of the buoyancy force along the USV hulls. By assuming that at time t the wave crest is amidships, the buoyancy force can be computed

as the integration from the stern to the bow as

$$Z = \int_{-L/2}^{L/2} 2\rho g B(x_s)\zeta dx_s \qquad (4.17)$$

where we define $O_s x_s$ as an axis pointing to the positive surge direction with its origin O_s located amidships. In this equation, L is the total length of the USV, $B(x_s)$ is the beam width at a specific position along $O_s x_s$, ζ is the wave profile defined in Eq. 4.15, ρ is the fluid density and g is the gravitational acceleration. The multiplication of 2 into the equation is owing to that our studied USV platform is catamaran type. Through substitution of ζ from Eq. 4.15 into Eq. 4.17 and using the effective wave number k_e, the excitation force can be written as

$$Z = \rho g \zeta_A \int_{-L/2}^{L/2} 2B(x_s)\cos(k_e x_s - \omega_w t)dx_s.$$

The studied USV is roughly symmetric about the midship plane, so the excitation force can be simplified as

$$\begin{aligned} Z &= 2\rho g \zeta_A \int_{-L/2}^{L/2} B(x_s)\cos(k_e x_s)dx_s \cos(\omega_w t) \\ &= Z_0 \cos(\omega_w t) \end{aligned} \qquad (4.18)$$

where Z_0 is the amplitude of the heave excitation force, which is related to the wave amplitude ζ_A, wave number k and wave direction χ_w given as

$$Z_0 = 2\rho g \zeta_A \int_{-L/2}^{L/2} B(x_s)\cos(k x_s \cos(\chi_w))dx_s. \qquad (4.19)$$

We apply the well-known Simpson's Rules [32] for calculation of this integration. A summary of the beam width related with the station number is shown in Table 4.6.

Therefore, we can achieve

$$Z_0 = 2\rho g \zeta_A \frac{\Delta x_s}{3} [B_0 \cos(kx_{s0}\cos(\chi_w)) + 4B_1 \cos(kx_{s1}\cos(\chi_w)) + 2B_2 \cos(kx_{s2}\cos(\chi_w))$$

$$+ 4B_3 \cos(kx_{s3}\cos(\chi_w)) + 2B_4 \cos(kx_{s4}\cos(\chi_w))$$

$$+ 4B_5 \cos(kx_{s5}\cos(\chi_w)) + B_6 \cos(kx_{s6}\cos(\chi_w))]$$

where $\Delta x_s = 0.254\ m$.

Table 4.6: Station number, position and beam width for one hull

Station number j	0	1	2	3	4	5	6
$x_{sj}\ (m)$	-0.762	-0.508	-0.254	0	0.254	0.508	0.762
$B(x_{sj})$ or $B_j\ (m)$	0	0.155	0.171	0.171	0.171	0.155	0

We simulate the heave excitation force amplitude Z_0 with respect to the wave frequency (Eq. 4.16) and wave direction, and this result is shown in Fig. 4.9. Note that the polar coordinate system has been used and the radial distance represents the wave frequency value. In the simulation, the wave amplitude ζ_A is assumed as $0.2\ m$, and the wave frequency range is $\omega_w \in (0, 2\pi]\ rad$. As shown in the plot, under the beam sea conditions, the USV will encounter the maximum exciting force from the waves regardless of their frequencies. Actually, by substituting $\chi_w = 90°$ or $270°$ into Eq. 4.19, the maximum exciting force can be computed as

$$Z_{0max} = 2\rho g \zeta_A A_{WP}$$

where A_{WP} is the waterplane area for one of the hulls. In the heading sea ($\chi = 180°$) and following sea ($\chi = 0°$) conditions, a USV will suffer less wave-induced excitation force with the increment of the wave frequency.

If a USV operates with a surge velocity of u with respect to the mean water current in the horizontal plane, ω_w in the cosinusoidal term $\cos(\omega_w t)$ of Eq. 4.18 needs to be
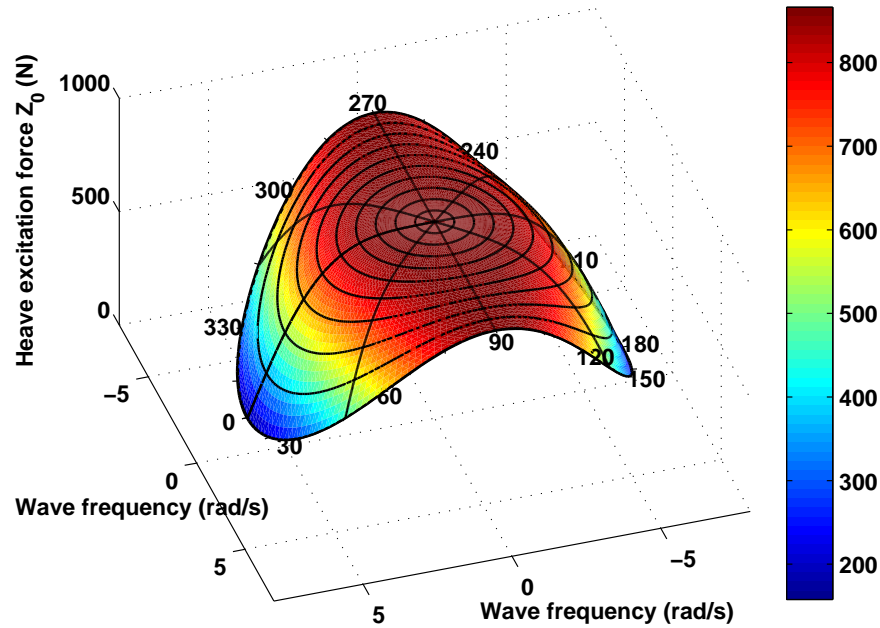
Figure 4.9: Heave exciting force amplitude Z_0 with respect to the wave frequency and wave direction represented in the polar coordinate systems. The maximum forces occur with beam sea conditions, while the minimum exciting force is when the USV heads towards or follows the sea waves direction.

substituted by the wave encounter frequency ω_e according to

$$\omega_e = \omega_w - \frac{\omega_w^2 u}{g} \cos(\chi_w). \tag{4.20}$$

Here we perform the simulation as shown in Fig. 4.10 to demonstrate the relationship between ω_w and ω_e with different wave directions χ_w. In Fig. 4.10, the thick line marks the beam wave conditions, and in this case $\omega_e = \omega_w$. Under the quartering sea conditions, i.e. $\chi_w \in (0°, 90°)$ or $(270°, 360°)$, $\omega_e < \omega_w$. While if a USV heads towards wave direction, i.e. $\chi_w \in (90°, 270°)$, $\omega_e > \omega_w$. In the simulation of Fig. 4.10, we assume the vehicle has the maximum moving speed of 1 m/s. When the moving speed is lower than 1 m/s, it has been demonstrated that ω_e is not varied as much from ω_w as shown in Fig. 4.10.

Note that in the safety analysis chapter, we will investigate the relationship between the excited USV motion amplitude and the wave encounter frequency ω_e.
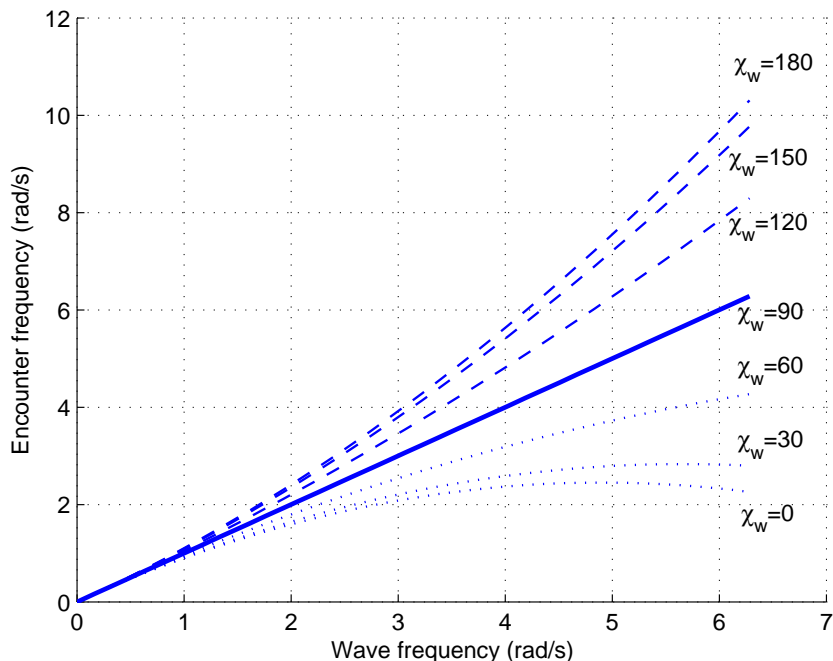
Figure 4.10: The relationship between wave frequency and wave encounter frequency for different wave directions relative to the USV heading angle, assuming a constant surge speed of 1 m/s.

4.3.2 Roll and Pitch Excitation Moments

In this section, we investigate the formulation of the excitation moment for a USV's roll and pitch motion. A complete derivation can be found in [53] and [54], and here we only provide a brief overview.

The potential of fluid velocities contributed from the sinusoidal wave on a USV body can be expressed as

$$\varphi_w = \varphi_I + \varphi_D$$

where φ_I denotes incident waves potential and φ_D is the potential of the fluid velocities

caused by the diffracted waves from the USV hulls. If we assume that the incident wave elevation has the same form as Eq. 4.15, the pressure acting on the USV body caused by φ_w can be written as

$$p_w = \varphi_w \rho \zeta_A \omega_w \sin(\omega_w t) \tag{4.21}$$

where ρ is the fluid density, ζ_A is the wave amplitude, ω_w is the incident wave frequency and t denotes the time instant. Note that Eq. 4.21 is derived using the Bernoulli's equation and maintaining only the first order terms. The dimension of the studied USV is Length×Width=1.5 m×1.0 m and we are considering the wind waves that have a wavelength of over 10 m. Since the size of the USV is small compared to the wavelength, we can apply the Froude-Krylov hypothesis and neglect the influence of the hull body on the pressure field of the incident waves, i.e. $\varphi_D = 0$. Thus, the wave exciting moment is calculated by integration of the wave pressure p_w acting over the surface S_B of the USV hull as

$$
\begin{aligned}
\overrightarrow{M}_w^{FK} &= \iint_{S_B} p_w(\overrightarrow{r} \times \overrightarrow{n})dS \\
&= \rho \iint_{S_B} \varphi_I \zeta_A \omega_w \sin(\omega_w t)(\overrightarrow{r} \times \overrightarrow{n})dS
\end{aligned}
\tag{4.22}
$$

where $\overrightarrow{r}$ is the position vector of a unit area on the hull body with respect to the center of gravity and $\overrightarrow{n}$ is the unit normal vector on the body surface directed into the body.

Based on Eq. 4.22, the roll and pitch excitation moment about the center of gravity can be derived as [54]

$$K = \rho g V_0 k \zeta_A \overline{GM_T} \sin(\chi_w) \sin(\omega_w t)$$

and

$$M = -\rho g V_0 k \zeta_A \overline{GM_L} \cos(\chi_w) \sin(\omega_w t) - 2\rho \zeta_A x_{GF} g \cos(\omega_w t) A_{WP}.$$

where x_{GF} is the distance between the center of gravity and the center of flotation along the

longitudinal direction and A_{WP} defines the water plane area for one hull. If it is assumed that the metacentric height $\overline{GM_T}$ and $\overline{GM_L}$ are constant while the USV operates in the seaway, a compact form representation can be formulated

$$
\begin{aligned}
K &= I_r \alpha_A \omega_{n4}^2 \sin(\chi_w) \sin(\omega_w t) \\
&= K_0 \sin(\omega_w t)
\end{aligned}
\tag{4.23}
$$

where

$$
K_0 = I_r \alpha_A \omega_{n4}^2 \sin(\chi_w),
\tag{4.24}
$$

and

$$
\begin{aligned}
M &= -I_p \alpha_A \omega_{n5}^2 \cos(\chi_w) \sin(\omega_w t) - \rho \zeta_A x_{GF} g \cos(\omega_w t) 2 A_{WP} \\
&= -M_0 \sin(\omega_w t + \varepsilon')
\end{aligned}
\tag{4.25}
$$

where

$$
M_0 = \sqrt{(I_p \alpha_A \omega_{n5}^2 \cos(\chi_w))^2 + (\rho \zeta_A x_{GF} g 2 A_{WP})^2},
\tag{4.26}
$$

$$
\varepsilon' = \tan^{-1} \frac{\rho \zeta_A x_{GF} g 2 A_{WP}}{I_p \alpha_A \omega_{n3}^2 \cos(\chi_w)}
$$

and α_A is the amplitude of wave slope, which is given as

$$
\alpha_A = k \zeta_A.
$$

According to Eq. 4.24 and Eq. 4.26, we can compute the wave excitation moment amplitude for roll and pitch motion with respect to wave direction and wave frequency. The wave amplitude is still assumed to be $0.2~m$. The roll exciting moment amplitude in the polar coordinate system has been depicted in Fig. 4.11a. It clearly shows that when a USV heads towards or follows the sea waves direction, K_0 is close to zero regardless of the wave frequency. The unsafe condition occurs when there are beam waves, and if

$\chi_w = 90°$ or $270°$, K_0 increases rapidly with the increment of the wave frequency. We can also show the result from another point of view in the Cartesian coordinates as shown in Fig. 4.11b. In general, the roll exciting moment amplitude is small when the wave frequency is low, and with the increment of the wave frequency it starts to grow fast. The beam sea condition features the fastest increment of the exciting moments.

As for the pitch exciting moment amplitude M_0, the adverse condition happens when a USV is heading towards or following the sea wave direction, which has been shown in Fig. 4.12. In the Cartesian coordinates of Fig. 4.12b, with the increment of the wave frequency, the pitch exciting moment amplitude increases quickly, especially for the case when $\chi_w = 0°$ or $180°$. Again, if a USV operates with a surge velocity of u in the horizontal plane, when calculating K and M, we need to employ the encounter wave frequency as in Eq. 4.20 instead of ω_w for the cosinusoidal term in Eq. 4.23 and Eq. 4.25.

4.4   General Chapter Summary

The oscillatory motion of a USV is closely related to its operational safety, but it is often omitted by researchers. In this chapter, we introduced the decoupled linear and nonlinear oscillatory motion model, and through performing the experiments, the model parameter values had been successfully identified by following different routines depending on varied model structures. The primary environmental disturbances come from the ocean waves, and we provided detailed discussion about how we could mathematically model the hull-wave interaction including computing the exciting forces and moments for heave, roll and pitch motion. In the next chapter, we will start investigating the safety of a USV under different wave conditions. We hope to discover the safe operational boundary conditions that can be conveniently integrated into a USV's guidance and control system so that we can realize a USV's safe and reliable ocean survey mission.
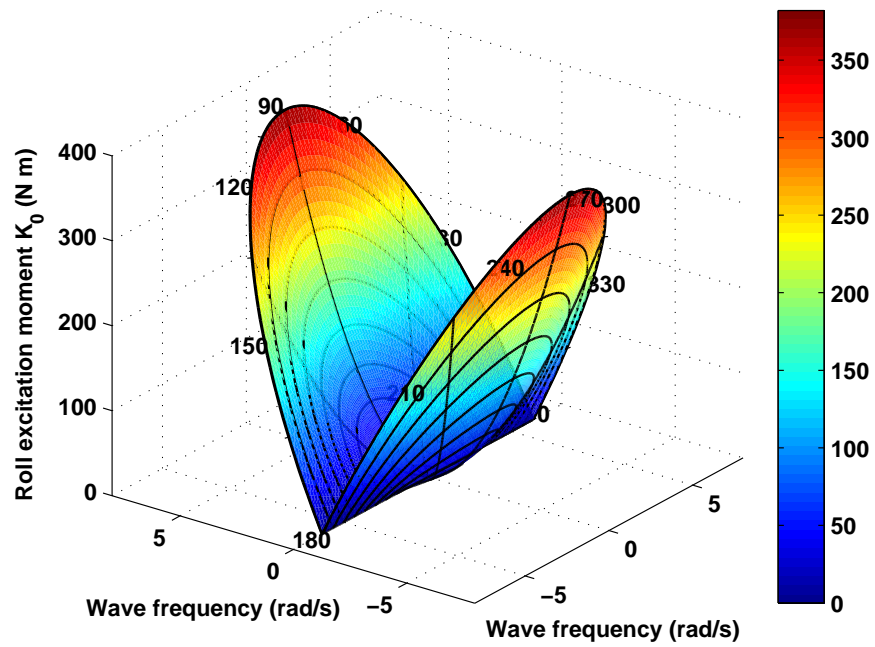
(a) Polar coordinate system
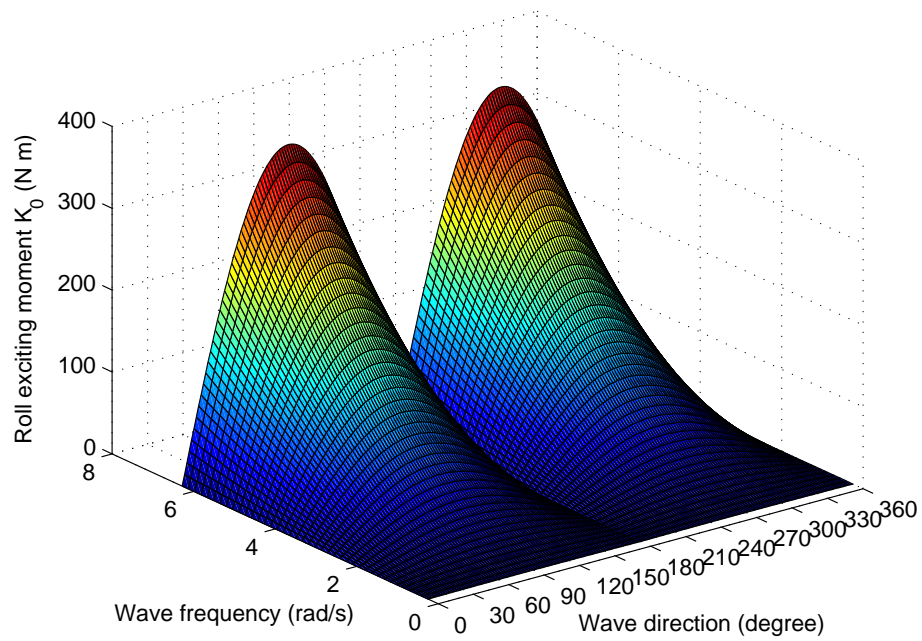
(b) Cartesian coordinate system

Figure 4.11: Roll exciting moment amplitude K_0 with respect to the wave frequency and wave direction represented in the polar and Cartesian coordinate systems.
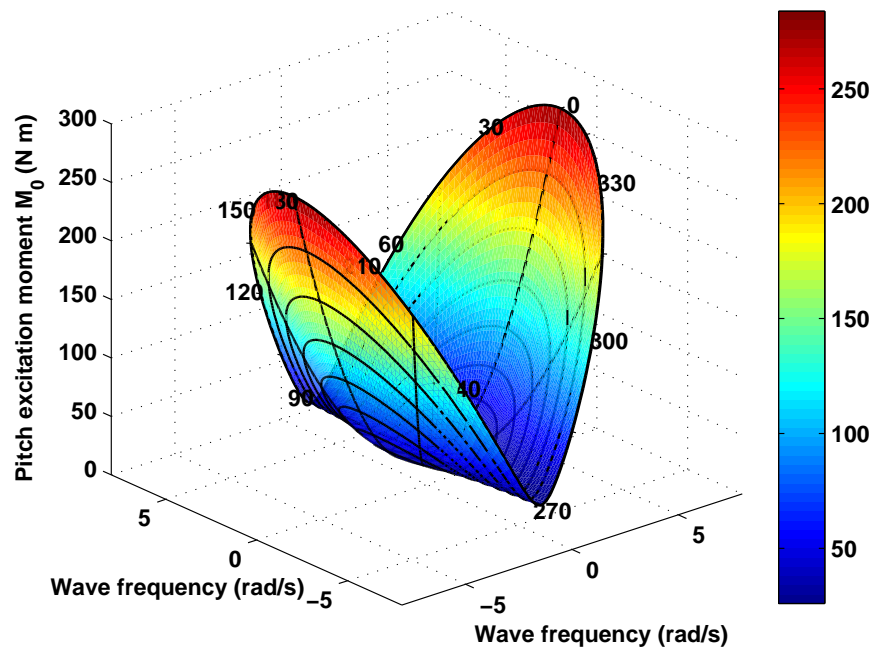
(a) Polar coordinate system
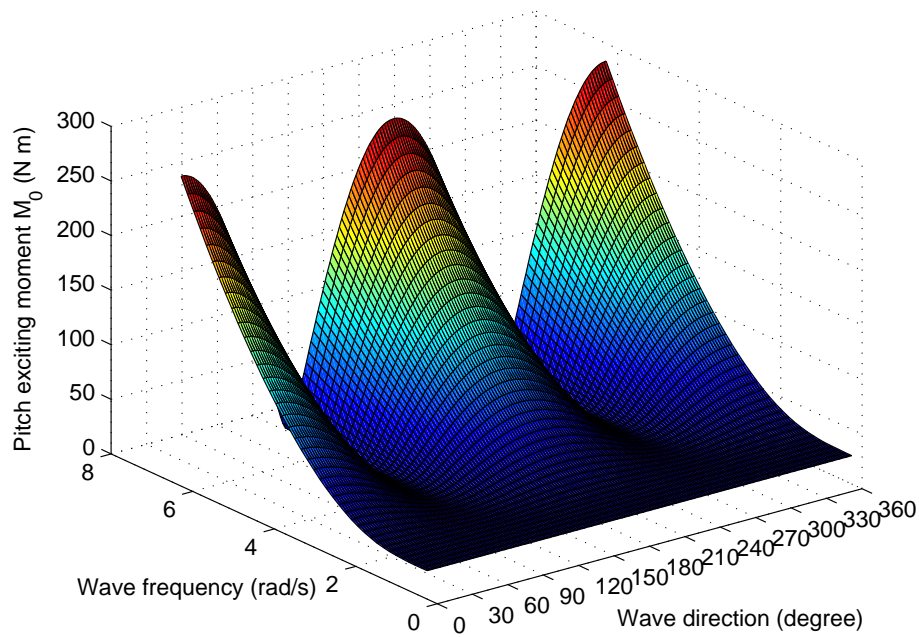
(b) Cartesian coordinate system

Figure 4.12: Pitch exciting moment amplitude M_0 with respect to the wave frequency and wave direction represented in the polar and Cartesian coordinate systems.

Chapter 5

Safety Analysis

A USV operating on the ocean surface has to be able to survive fast-changing ocean environments. A fundamental question is how we can assess the vehicle's safety in real-time considering the primary disturbances from ocean waves. This is a prerequisite for a successful USV mission. In this chapter, depending on our introduced heave, roll and pitch motion model from chapter 4, we perform the safety analysis of a USV considering various ocean wave conditions. Three well-known methods, i.e. Analytical Method, Melnikov's Method and Erosion Basin Method, for the linear and nonlinear oscillatory motion dynamics analysis have been implemented on a USV platform for the first time. Extensive simulations are performed, and the safe operation boundary condition for a USV running a mission in harsh ocean environments has been established. The presented safe operational condition can be conveniently integrated into a USV's path-planning system to enable a safe and enduring survey mission.

5.1   Analysis Tools

In this section, we introduce the Analytical Method, Melnikov's Method and Erosion Basin Method for analyzing the oscillatory motion dynamics of a USV that operates

in harsh ocean environments. When considering about the linear heave, roll and pitch model, a linear analytical solution is enough for determination of the worst operating conditions. However, as for the nonlinear roll and pitch motion dynamics, we need to employ advanced analysis tools. As we know, the nonlinearity in the oscillatory motion model leads to some well-known complicated phenomena, such as jumping and system chaos [29]. For instance, due to the nonlinearity of the roll restoring moments, the region around the roll resonant frequency may have multiple steady-state roll response solutions [33]. In the following, we first introduce the linear and nonlinear analytical methods. It is noteworthy that through solving for the nonlinear analytical solutions, we can demonstrate the complicated behaviour of the vehicle roll and pitch motion considering different wave conditions. Further, to provide an insightful analysis of the complicated motion dynamics, we introduce the Melnikov's Method and Erosion Basin Method, based on which the safe operational boundary condition is finally achieved. By convention, during our discussion the regular ocean waves are considered [28, 31, 55].

5.1.1   Analytical Method

Various analytical methods have been discussed in the literature depending on different oscillatory motion model structures [29]. For the linear oscillatory motion model, a close-form solution can be generated. Whereas, as for the nonlinear case, only an analytical approximation of the steady-state response solutions can be formulated. Some typical nonlinear analytical methods include Perturbation Method and Harmonic Balance Method [34], and they have demonstrated their effectiveness in the dynamic motion's main resonance region.

5.1.1.1 Linear Model

In section 4.2.1, we have already introduced the linear model for a USV's heave, roll and pitch motion. In Eq. 4.3, if $\tau_i \neq 0$, the motion is termed as forced and damped oscillation. In a simple case, we can assume that the excitation forces and moments result from a specific incident wave with an encounter frequency of ω_e, and they can be written as

$$\tau_i = \tau_{0i} \cos(\omega_e t),$$

so the analytical solution can be formulated as [32]

$$\eta_i = A_{mi} e^{-v_i t} \sin(\omega_{di} t + \delta_i) + \eta_{ai} \cos(\omega_e t + \delta_i) \ (i = 3, 4, 5) \tag{5.1}$$

where η_{ai} is the motion amplitude as a result of the excitation forces and moments and δ_i is the phase angle of the forced motion related to the exciting forces and moments. Compared to Eq. 4.9, we can conclude that the analytical solution in Eq. 5.1 is a summation of the free damped oscillation solution and the steady-state oscillatory motion solution due to the encountered waves.

In this section, it is assumed that a wave of a certain length and amplitude passes along rather slowly so that the USV is in position to balance itself statically on the wave at every instant of its passage. Hence, the USV will encounter a static amplitude of heave, roll and pitch while it rises and falls slowly according to the incident wave. We define this static amplitude as

$$\eta_{ist} = \frac{\tau_{0i}}{R_{i1}},$$

so the magnification factor is given as [32]

$$\mu_i = \frac{\eta_{ai}}{\eta_{ist}} = \frac{1}{\sqrt{(1 - \Lambda^2)^2 + 4\kappa^2 \Lambda^2}}.$$

where Λ is the tuning factor

$$\Lambda = \frac{\omega_e}{\omega_{ni}},$$

κ is the damping factor

$$\kappa = \frac{\upsilon_i}{\omega_{ni}},$$

and the phase angle δ_i is

$$\delta_i = \tan^{-1} \frac{2\kappa\Lambda}{1 - \Lambda^2}.$$

Using the identified linear model parameter values of heave, roll and pitch from Table 4.1, we perform the dynamic response analysis as shown in Fig. 5.1. In the figure, we display the dynamic response of the three oscillatory motion together, and it can be seen that when the wave encounter frequency is less than 1 rad/s, the magnification factor is close to unity in all three cases. When the wave encounter frequency is higher than 4 rad/s for roll and pitch or higher than 6 rad/s for heaving motion, the magnification will decrease to lower than unit magnification. Owing to the small damping value of υ_i for heave, roll and pitch, when the wave encounter frequency is close to the corresponding natural frequency, the magnification factor becomes really large. Therefore, according to our investigation of the linear model, it is clear that the resonance condition is adverse for a USV's safe operation and should be avoided.

5.1.1.2 Nonlinear Model

However, for a USV that operates in dynamic ocean environments, the oscillatory motion dynamics is hardly close to linear. When considering about the nonlinear roll and pitch motion model, there are no analytical solutions available in the closed form, and only approximate methods can be used. In this section, we will implement the well-accepted harmonic balance method (HBM) for the nonlinear motion dynamics analysis. Due to the similarity of the formulated roll and pitch model, we can focus on the rolling motion,
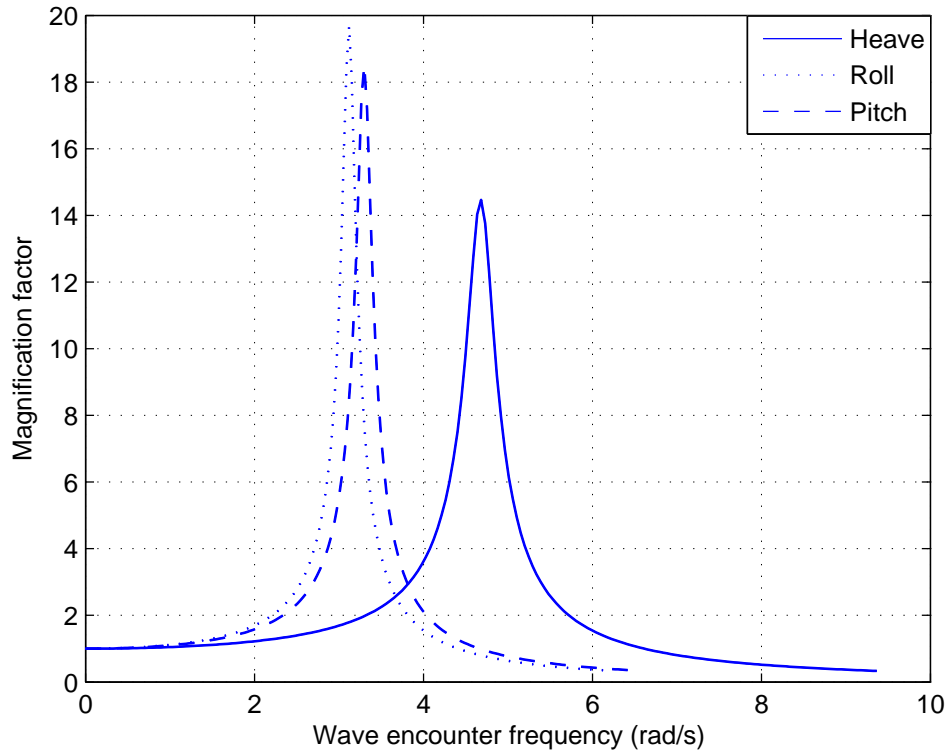
Figure 5.1: The dynamic response of the studied USV's heave, roll and pitch motion implementing the identified linear dynamic motion models.

and the pitching motion can be investigated following a similar procedure. HBM is only applicable for the linear damping case, and thus the employed roll motion model for analysis is given as

$$I_r\ddot{\phi} + D_{41}\dot{\phi} + R_{41}\phi + R_{43}\phi^3 = K_0\cos(\omega_e t) \tag{5.2}$$

where the model parameters have already been determined in chapter 4. Note that we consider a vehicle moving with surge speed u in the horizontal plane, and thus we need to use the wave encounter frequency ω_e on the right hand side of Eq. 5.2. If we divide

both sides of Eq. 5.2 by I_r, we get

$$\ddot{\phi} + d_{41}\dot{\phi} + r_{41}\phi + r_{43}\phi^3 = k_0 \cos(\omega_e t) \tag{5.3}$$

where we define k_0 as the non-dimensional roll exciting moment amplitude. Note that Eq. 5.3 has a similar form as the well-known Duffing oscillator with the external oscillatory influences [56]. Assuming that the steady-state response of the system is

$$\phi(t) = \phi_a \cos(\omega_e t + \delta_2),$$

we can substitute the steady-state solution back to Eq. 5.3. By equating the coefficients of the orthogonal functions $\cos(\omega_e t)$ and $\sin(\omega_e t)$ on both sides of the equation, we get

$$k_0 = [(r_{41} - \omega_e^2)\phi_a + 0.75 r_{43}\phi_a^3] \cos(\delta_2) - d_{41}\phi_a\omega_e \sin(\delta_2) \tag{5.4}$$

and

$$0 = -[(r_{41} - \omega_e^2)\phi_a + 0.75 r_{43}\phi_a^3] \sin(\delta_2) - d_{41}\phi_a\omega_e \cos(\delta_2) \tag{5.5}$$

By squaring and summation of Eq. 5.4 and Eq. 5.5, the relationship between the non-dimensional exciting moment amplitude k_0, the roll motion amplitude ϕ_a and wave encounter frequency ω_e can be formulated as

$$k_0^2 = [(r_{41} - \omega_e^2)\phi_a + 0.75 r_{43}\phi_a^3]^2 + d_{41}^2\phi_a^2\omega_e^2. \tag{5.6}$$

This equation can be expanded and arranged as

$$\omega_e^4 + (d_{41}^2 - 2r_{41} - 1.5 r_{43}\phi_a^2)\omega_e^2 + (r_{41} + 0.75 r_{43}\phi_a^2)^2 - (\frac{k_0}{\phi_a})^2 = 0. \tag{5.7}$$

Since Eq. 5.7 is quadratic in ω_e^2, we can solve for the two positive solutions as

$$\omega_{e1,2} = \sqrt{r_{41} + \frac{3}{4}r_{43}\phi_a^2 - \frac{1}{2}d_{41}^2 \pm \sqrt{\frac{1}{4}d_{41}^2(d_{41}^2 - 4r_{41} - 3r_{43}\phi_a^2) + \frac{k_0^2}{\phi_a^2}}}. \tag{5.8}$$

In order to have the real solutions for ω_e, the following two conditions need to hold

$$\frac{1}{4}d_{41}^2(d_{41}^2 - 4r_{41} - 3r_{43}\phi_a^2) + \frac{k_0^2}{\phi_a^2} \geq 0 \tag{5.9}$$

and

$$r_{41} + \frac{3}{4}r_{43}\phi_a^2 - \frac{1}{2}d_{41}^2 \pm \sqrt{\frac{1}{4}d_{41}^2(d_{41}^2 - 4r_{41} - 3r_{43}\phi_a^2) + \frac{k_0^2}{\phi_a^2}} \geq 0. \tag{5.10}$$

Using the approximate solutions in Eq. 5.8, we can generate the frequency response curve for the nonlinear roll motion as shown in Fig. 5.2. It is noteworthy that the subscript 1 and " $+$ " sign in Eq. 5.8 refer to the right branch of the response curve, while the subscript 2 and " $-$ " sign refer to the left branch. The x axis is defined as the normalized wave encounter frequency as

$$\omega_{ne} = \frac{\omega_e}{\omega_{n4}}.$$

The thick curve line in Fig. 5.2 is called the backbone curve [54], and it is achieved by setting the damping and exciting amplitude as zero. The roll motion frequency response curves bend to the left according to the backbone curve, and this phenomenon is quite different from the linear case in Fig. 5.1. This complicated nonlinear characteristic leads to the jump phenomenon [33], which has been proved by researchers through performing capsize tests. To further illustrate the jump phenomenon, we extract one of the frequency response curves ($k_0 = 0.32$) and show it in Fig. 5.3. If ω_{ne} starts from zero and keeps
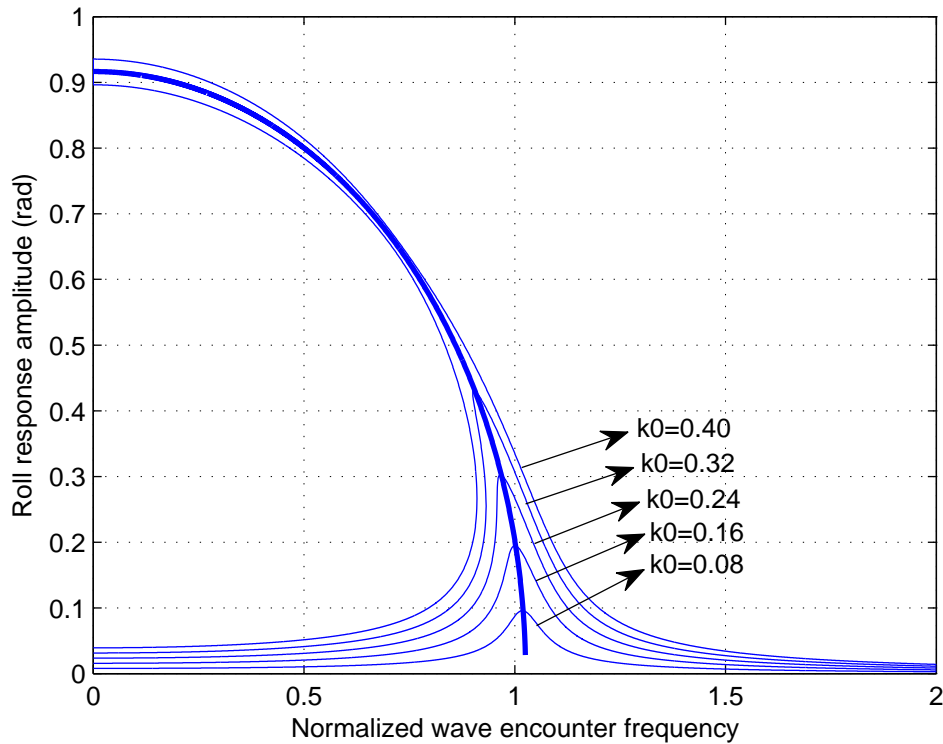
Figure 5.2: The dynamic response of the USV's roll motion considering the restoring moments nonlinearity. The x axis is the normalized wave encounter frequency ω_{ne}, and the y axis is the steady-state roll response amplitude.

increasing, there exists a jump-up point, highlighted as a star point, where the roll amplitude jumps instantly from the left to the right branch. After the jump-up point, the amplitude starts to decrease. On the contrary, if ω_{ne} decreases from a large value, there will be a jump-down point where the amplitude reduces quickly to the left branch. The jump-up and jump-down points bring in the discontinuity of the roll motion response with the variation of encounter wave frequency. It is noteworthy that between the two jump points, three roll amplitude solutions exist for a given value of ω_{ne}. In this range, it has been demonstrated that the final steady-state rolling motion depends on the provided initial conditions [33].

As shown in Fig. 5.2, when $k_0 = 0.4$ the two branches will not intersect. To explain
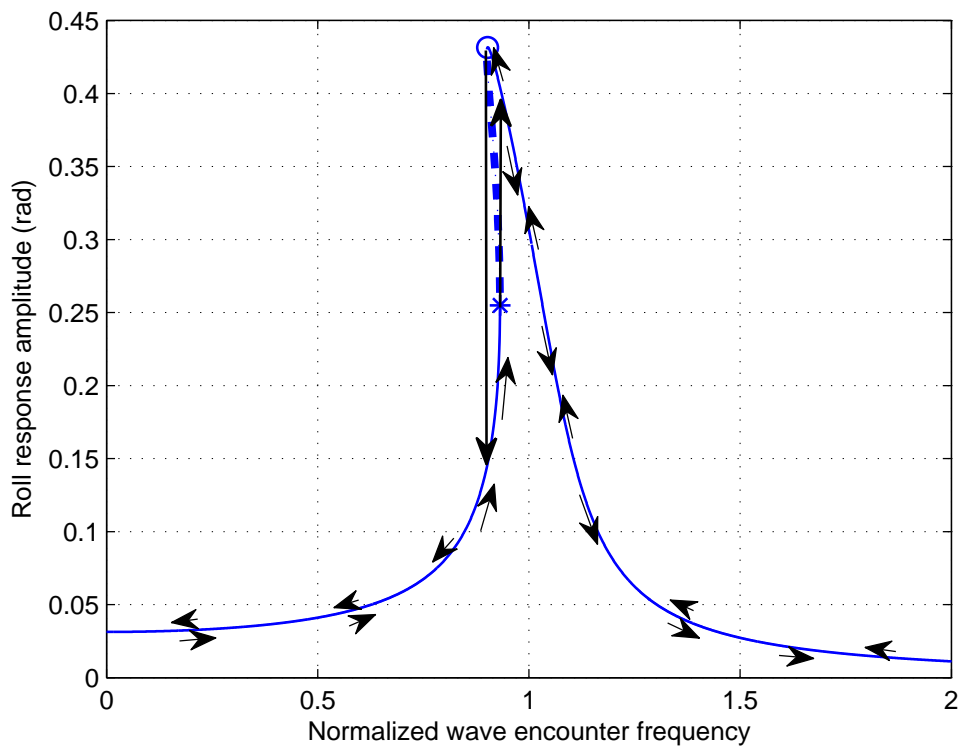
Figure 5.3: The nonlinear roll motion frequency response when $k_0 = 0.32$. The arrows indicate the amplitude changes with the variation of the normalized wave encounter frequency. The jump-up and jump-down points are highlighted using star and circle, respectively. The dash line indicates the unstable roll motion where multiple solutions exist.

this phenomenon, we can employ the approximation of the jump-up and jump-down frequencies as [57]

$$\omega_{ju} = \omega_0(1 - \frac{1}{2}(\frac{3}{2})^{4/3}|\Gamma|^{1/3}) \qquad (5.11)$$

and

$$\omega_{jd} = \omega_0\sqrt{\frac{1}{2} + \sqrt{\frac{1}{4} + \frac{3\Gamma}{16\Upsilon^2}}} \qquad (5.12)$$

where

$$\omega_0 = \sqrt{\frac{R_{41}}{I_r}},$$

$$\Gamma = \frac{I_r^2 R_{43}}{R_{41}^3} k_0^2$$

and

$$\Upsilon = \frac{D_{41}}{2\sqrt{I_r R_{41}}}.$$

In order for the jump-down point to exist $1 + \frac{3\Gamma}{4\Upsilon^2} \geq 0$, and thus the non-dimensional wave exciting amplitude $k_0 \leq 0.3855$.

The nonlinear pitch motion model has a similar form as the roll model

$$I_p\ddot{\theta} + D_{51}\dot{\theta} + R_{51}\theta + R_{53}\theta^3 = M_0 \cos(\omega_e t), \tag{5.13}$$

and by dividing both sides of Eq. 5.13 with I_p, we can get

$$\ddot{\theta} + d_{51}\dot{\theta} + r_{51}\theta + r_{53}\theta^3 = m_0 \cos(\omega_e t)$$

where m_0 is denoted as the non-dimensional pitch exciting moment amplitude. The frequency response curve has been depicted in Fig. 5.4, and it is noteworthy that the backbone and the response curves all bend towards left. Similar to the roll motion case, we can refer to Eq. 5.11 and Eq. 5.12 to compute the jump-up and jump-down frequency. Through calculation, we find out that when the pitch excitation amplitude $m_0 > 0.3968$, there will be no jump-down points, and this scenario has been demonstrated in Fig. 5.4 when $m_0 = 0.40$.

Based on the aforementioned discussion, we can see a USV operating in harsh ocean environments has highly nonlinear roll and pitch dynamics, and many complicated phenomena exist. In order to further investigate these oscillatory motions and generate the safe operational condition, we will introduce more advanced tools including Melnikov's Method and Erosion Basin Method.
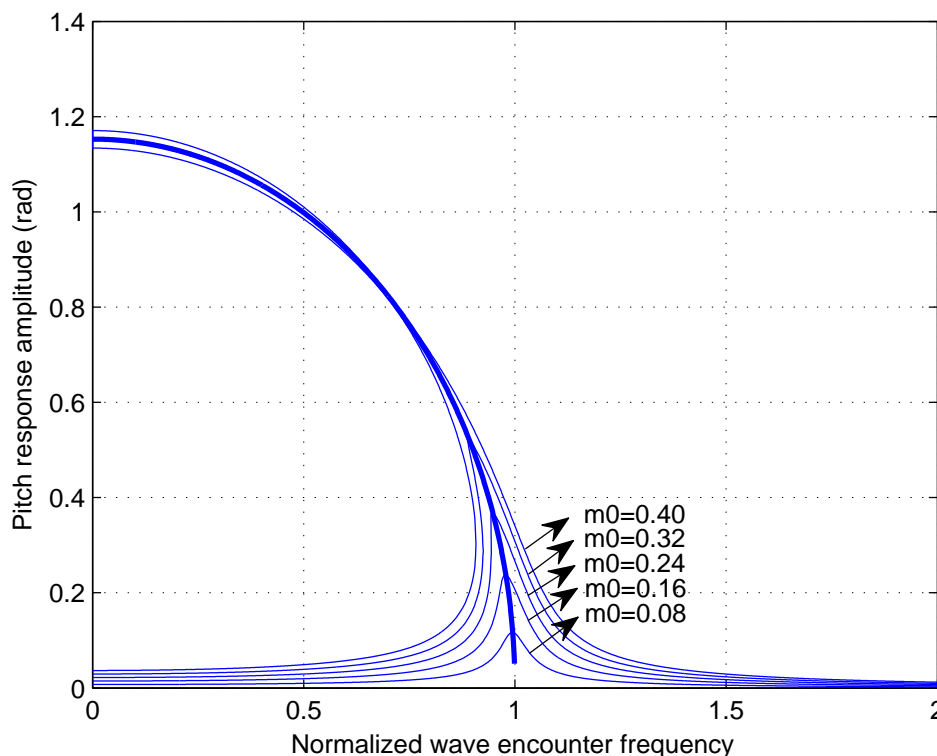
Figure 5.4: The dynamic response of the USV's pitch motion considering the restoring moments nonlinearity..

5.1.2 Melnikov's Method

In this section, we employ the geometric global analysis method, i.e. Melnikov's Method, for investigation of the USV's nonlinear oscillatory motion. When using the nonlinear analytical approximation in section 5.1.1.2, we can only investigate the roll and pitch motion model with linear damping, otherwise the analytical solutions are not tractable. However, while performing the Melnikov's analysis, we can also take into account the quadratic damping terms that make our analysis more realistic. The studied roll and pitch motion models have already been formulated in Eq. 4.5 and Eq. 4.6, and their model parameters have been successfully identified.

Before moving on to analyse the motion model using the Melnikov's Method, we first
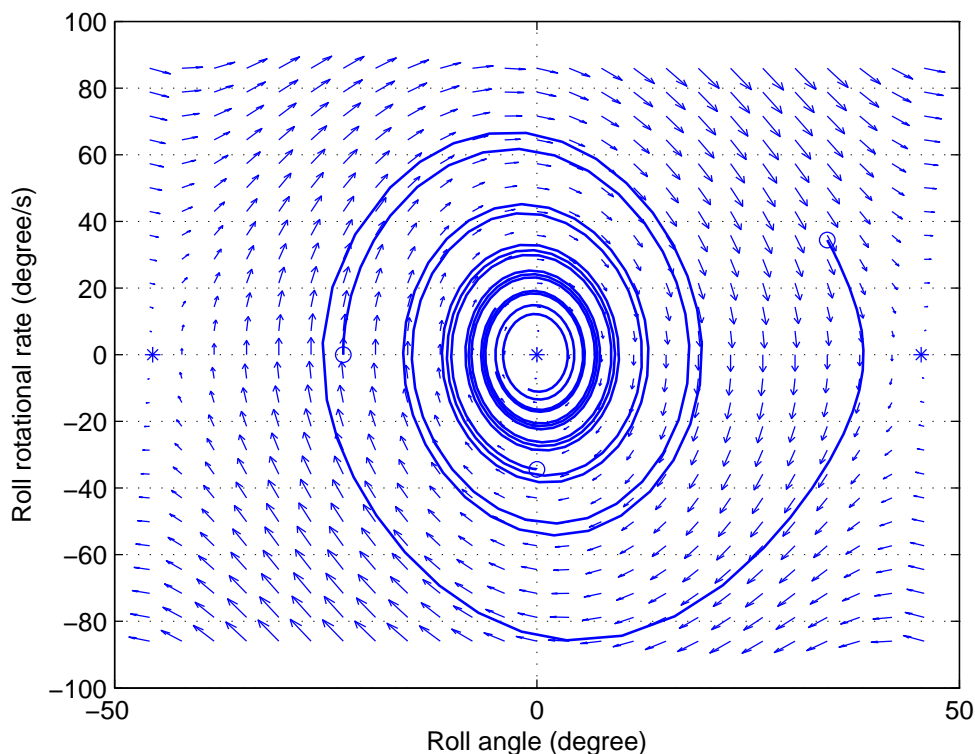
Figure 5.5: An example of the phase portrait for the nonlinear roll motion without excitation moments. The circles indicate three different initial conditions for the simulation, while the star points represent the roll motion equilibrium positions. The arrows in the phase plane represent the tendency at a specific phase plane point which guides the evolution of the roll motion dynamics.

introduce the concept of the phase plane [58], which serves as a foundation for the following discussion. As we know, while the vehicle undergoes rolling or pitching, it is both the angle and angular velocity that determine the operational safety of the USV. For instance, provided a USV's roll angle passed over the critical angle, if we do not consider the roll angular velocity, we can readily decide that the USV will certainly capsize. Whereas, if for some reason the USV captured a roll angular velocity that could bring the vehicle back to the upright position, the vehicle would still be operating safely. On a phase plane, each point represents a particular angle and angular velocity at the specific time instant, and with the evolution of the system motion in time, the phase trajectory is formed.

An intuitive example is depicted in Fig. 5.5, where the roll motion model of Eq. 4.5 without excitation moments is used. Three different initial conditions are considered and they are indicated as circles in the figure, i.e. $(\phi,\ \dot{\phi})$=(34.38°, 34.38°/s), (0°, -34.38°/s) and (-22.92°, 0°/s). Depending on the roll motion formula in Eq. 4.5, we can calculate the equilibrium positions by setting the roll restoring moments as zero. The three equilibrium points are highlighted as the star points, in which (0°, 0°/s) represents the upright equilibrium position, while the ($\pm$45.47°, 0°/s) are the critical roll angles or the angles of vanishing stability.

The stability of the equilibrium positions can be evaluated by applying a small perturbation and check if the system returns back to that position. Multiple methods are available to be used, which include evaluating the eigenvalues of the linearized equation around the equilibrium position or using the Lyapunov Direct Method. More details about these methods can be found in [54]. As for the studied USV, the upright position is validated to be a stable position, and the other two equilibrium points are unstable and are called the saddle points. As shown in Fig. 5.5, in all three simulation cases the USV will finally converge to the safe upright equilibrium position, i.e. $(\phi,\ \dot{\phi})$=(0°, 0°/s). In the physical world, there are another two equilibrium positions located at ($\pm$180°, 0°/s) that have not been shown in the figure, and they are the upside-down or unsafe stable positions for a USV.

We start with the nonlinear roll motion model analysis. For calculation convenience, the original roll motion model with harmonic wave excitation moments given in

$$I_r\ddot{\phi} + D_{41}\dot{\phi} + D_{42}\dot{\phi}|\dot{\phi}| + R_{41}\phi + R_{43}\phi^3 = K_0\cos(\omega_e t)$$

has been written in the non-dimensional form as

$$\ddot{x}_\phi + \epsilon\sigma_1\dot{x}_\phi + \epsilon\sigma_2\dot{x}_\phi|\dot{x}_\phi| + x_\phi - \alpha x_\phi^3 = \epsilon f(t') \tag{5.14}$$

where the second and first-order derivative is with respect to the new timescale $t' = \omega_{n4}t$, and the other terms are defined as [28]

$$
\begin{aligned}
&x_\phi = \phi, \ \omega_{n4} = \sqrt{\frac{R_{41}}{I_r}}, \ \epsilon\sigma_1 = \frac{D_{41}\omega_{n4}}{R_{41}}, \ \epsilon\sigma_2 = \frac{D_{42}}{I_r}, \\
&\alpha = -\frac{R_{43}}{R_{41}}, \ \epsilon f(t') = \frac{K_0}{R_{41}}\cos(\omega_{ne}t'), \ \omega_{ne} = \frac{\omega_e}{\omega_{n4}}.
\end{aligned}
\tag{5.15}
$$

The damping and wave excitation moments are assumed to be small and they are multiplied by a small parameter ϵ. Using this representation, we can still investigate the large roll motions of the vehicle since the roll angle and the restoring moments are not scaled. We can also formulate Eq. 5.14 in the first-order form as

$$
\begin{aligned}
&\dot{x}_\phi = y_\phi \\
&\dot{y}_\phi = -x_\phi + \alpha x_\phi^3 + \epsilon(f(t') - \sigma_1\dot{x}_\phi - \sigma_2\dot{x}_\phi|\dot{x}_\phi|)
\end{aligned}
\tag{5.16}
$$

where the terms multiplied by ϵ can be regarded as the small perturbation into the system. When the perturbation is zero, i.e. $\epsilon=0$, the remaining first-order equations become the integrable Hamiltonian type and the closed form solutions can be represented using the Jacobi elliptic functions as

$$
\begin{aligned}
&x_\phi = \sqrt{\frac{2k^2}{\alpha(1+k^2)}} sn(\frac{t'}{\sqrt{1+k^2}}, k) \\
&y_\phi = \pm\sqrt{\frac{2}{\alpha}}\frac{k}{1+k^2} cn(\frac{t'}{\sqrt{1+k^2}}, k) dn(\frac{t'}{\sqrt{1+k^2}}, k).
\end{aligned}
\tag{5.17}
$$

In Eq. 5.17, sn, cn and dn are Jacobi elliptic functions, and $k \in [0, 1]$ defines the modulus for the elliptic function, which represents the energy level of the system.

As shown in Fig. 5.6, the solutions with different k values have been plotted as the orbits around the upright equilibrium position. When k reaches its highest value of 1, it corresponds to the two thick boundary curves, i.e. separatrixes or heteroclinic

Figure 5.6: Phase portrait of the nonlinear roll motion without damping and excitation moments. The stars mark the three equilibrium positions, and the thick curves represent the heteroclinic orbit that separates the safe and unsafe oscillatory motions.

orbit, that connect the two saddle points, i.e. $(\phi, \dot{\phi})=(\pm 45.47°, 0°/s)$. When the initial condition for the roll motion is within the two boundary curves, the USV will be safe since bounded oscillatory motions will occur. Otherwise, when outside of the separatrixes, the vehicle motion will be unbounded and tend to capsize. It is important to note that the separatrixes can be regarded as an overlay of the unstable and stable manifolds of the two saddle points [54]. There are another two stable equilibrium positions, i.e. $(\phi, \dot{\phi})=(\pm 180°, 0°/s)$, that are not shown in Fig. 5.6. These two points represent a USV's upside-down motion status.

When damping is nonzero in Eq. 5.16, the roll motion phase portrait will change, and the results are depicted in Fig. 5.7. The original heteroclinic orbits split and form the
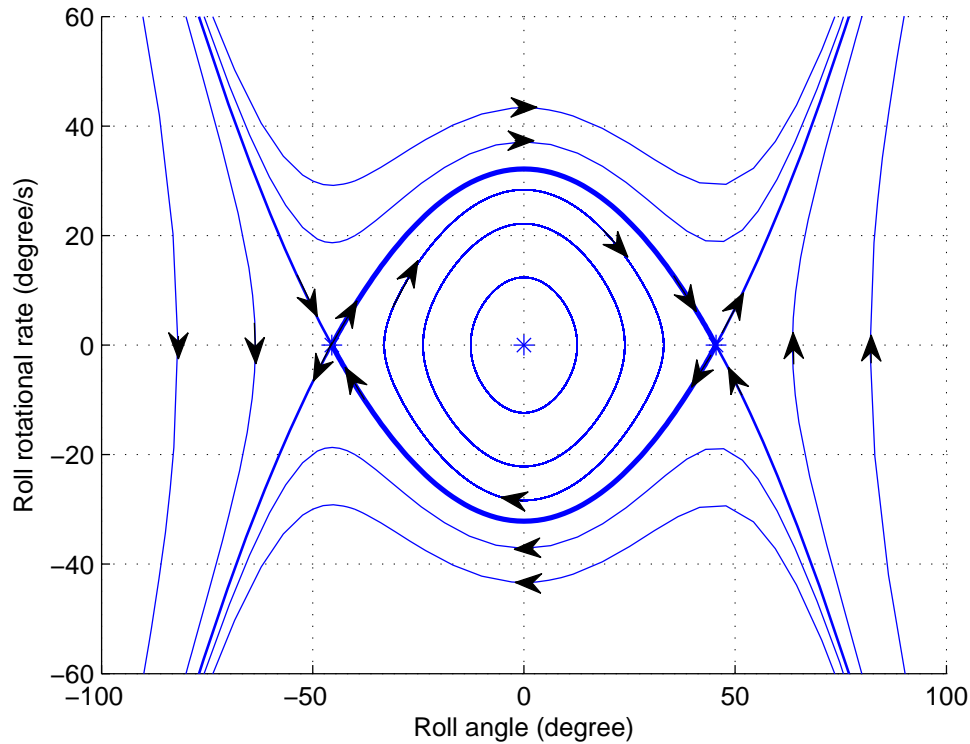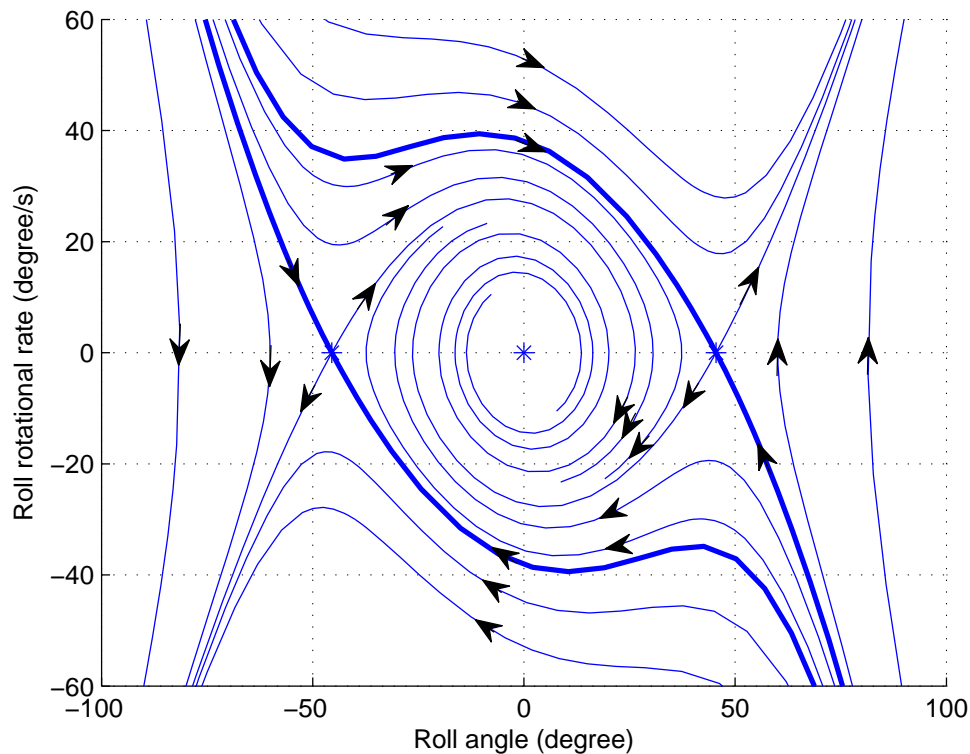
Figure 5.7: Phase portrait of the nonlinear roll motion when there is damping but no excitation moments. The stars mark the three equilibrium positions and the thick curves indicate the boundary curves that separate the safe and unsafe oscillatory motions.

new boundary curves. Through comparison with Fig. 5.6, we can conclude that when there is damping the stable and unstable manifolds of the two saddle points get separated, and the boundary curves are formed by the stable manifolds. Inside the region bounded by the new boundary curves, the roll motion will converge to the upright position, while on the outside, a USV will converge to the upside-down equilibrium position, i.e. capsize.

If wave excitation is also present in Eq. 5.16, the equilibrium points of the roll motion model become oscillatory. Under this circumstance, the safe roll motion will be those that converge to an oscillation around the upright position with a small amplitude, while the unsafe roll motion will be those that result in vehicle capsizing.

The area within the boundary curves is called the safe basin [37]. With the increment

of the wave excitation amplitude, the safe basin area will shrink and the boundary lines can become fractal [29]. The reduction of the safe basin area is adverse for a USV's safe operation, because some original safe initial conditions turn unsafe. Therefore, finding out the parameter condition that can predict the onset of the fractal basin boundary can be regarded as a criteria to determine a USV's roll motion safety. The occurrence of the fractal boundaries comes from the intersection of the stable and unstable manifolds. Through implementing Melnikov's method, we can analytically calculate the separation of the two manifolds. For detailed derivation of the Melnikov function, interested readers can refer to [35], and here we only provide a general overview. We start with the integrable Hamilton system in Eq. 5.16 with $\epsilon = 0$. According to Eq. 5.17, when $k = 1$ the separatrixes that connect the two saddle points are given as

$$x_{\phi s} = \sqrt{\frac{1}{\alpha}} \tanh(\frac{t'}{\sqrt{2}})$$

$$y_{\phi s} = \pm\sqrt{\frac{1}{2\alpha}} sech^2(\frac{t'}{\sqrt{2}})$$

where $\pm$ denotes the upper and lower separatrixes, respectively. It is also noteworthy that $|y_{\phi s}| = \dot{x}_{\phi s}$. The Melnikov integration is along the two separatrixes, and the Melnikov's function can be formulated as

$$
\begin{aligned}
M_s(t_0') &= \int_{-\infty}^{+\infty} y_{\phi s}(f(t' + t_0') - \sigma_1 y_{\phi s} - \sigma_2 y_{\phi s}|y_{\phi s}|)dt' \\
&= \sqrt{\frac{2}{\alpha}}\frac{K_0}{R_{41}}\pi\omega_{ne}\frac{\cos(\omega_{ne}t_0')}{\sinh(\frac{\pi\omega_{ne}}{\sqrt{2}})} - \frac{2\sqrt{2}}{3\alpha}\sigma_1 - \frac{8}{15}(\frac{1}{\sqrt{\alpha}})^3\sigma_2
\end{aligned}
\tag{5.18}
$$

where t_0' denotes an arbitrary initial time on the separatrix loop. The detailed derivation of Eq. 5.18 can be found in [55] and [59], and note that in our study we set $\epsilon = 1$. When the separation measure $M_s(t_0')$ changes sign as the point moves along the separatrix loop, the stable and unstable manifolds intersect with each other. This is a sufficient condition

for the existence of the fractal basin boundaries.
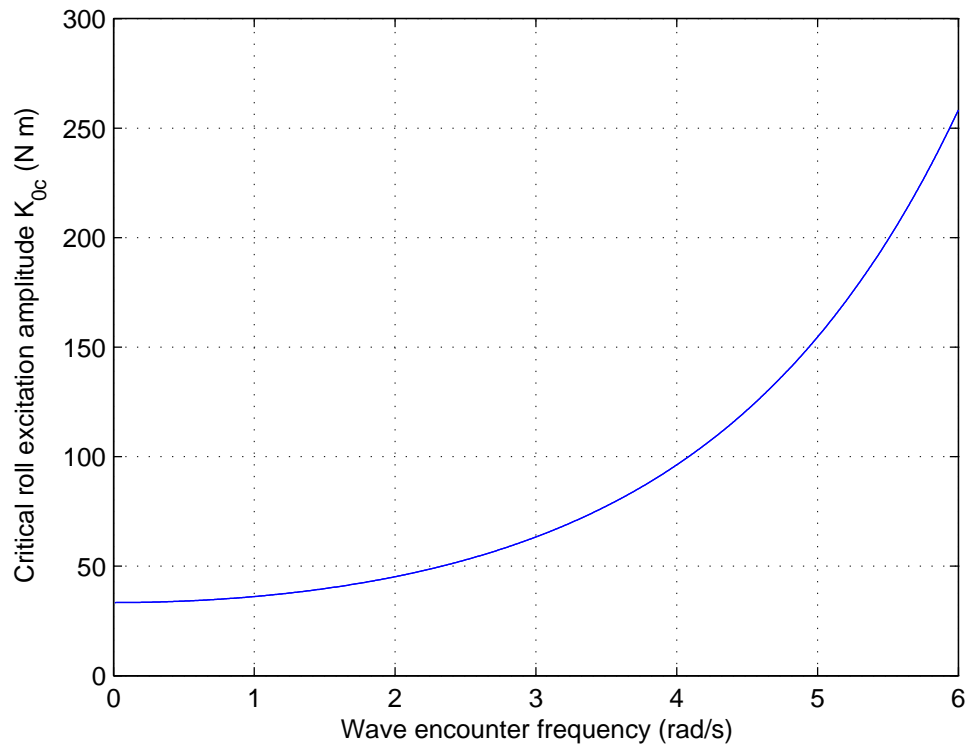
Figure 5.8: The critical roll excitation amplitude K_{0c} under different wave encounter frequencies.

Therefore, by setting $M_s(t'_0) = 0$ and $\partial M_s(t'_0)/\partial t'_0 = 0$, we can solve for this critical condition as

$$K_{0c} = \frac{\frac{2\sqrt{2}}{3\alpha}\sigma_1 + \frac{8}{15}\left(\frac{1}{\sqrt{\alpha}}\right)^3\sigma_2}{\sqrt{\frac{2}{\alpha}}\pi\omega_{ne}}R_{41}\sinh\left(\frac{\pi\omega_{ne}}{\sqrt{2}}\right) \quad (5.19)$$

where K_{0c} is the critical wave excitation amplitude and it sets the boundary condition for the safe basin to shrink and become fractal. As illustrated in [36], the derived criteria is a conservative one, and it can be conveniently used for this research because we need to define a conservative operational condition for the operational safety of a USV. According to Eq. 5.19, the critical wave amplitude is directly related to the wave encounter frequency. This relationship has been plotted as shown in Fig. 5.8, and it shows that when the

wave excitation amplitude is above the boundary curve, the USV will have an increasing probability of capsizing through rolling motion.

The Melnikov analysis of the pitch motion follows the same routine. The phase portrait of the unforced and undamped pitch motion has been depicted in Fig. 5.9. Again, the integration along the separatrixes gives the measure of the distance between the stable and unstable manifolds, which serves as a prospect criteria for determination of a USV's unsafe operational condition regarding its pitch motion. The critical pitch excitation amplitude M_{0c} versus the wave encounter frequency has been depicted in Fig. 5.10.
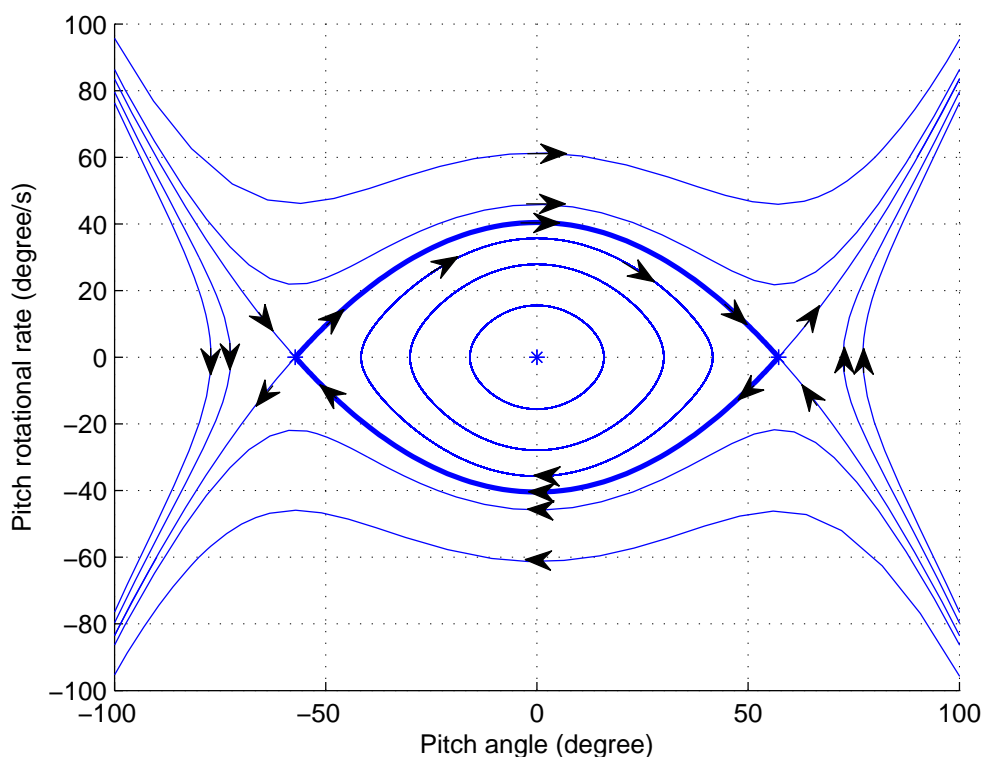
Figure 5.9: Phase portrait of the pitch motion without damping and excitation moments. The stars mark the three equilibrium positions and the thick curves indicate the heteroclinic orbit.
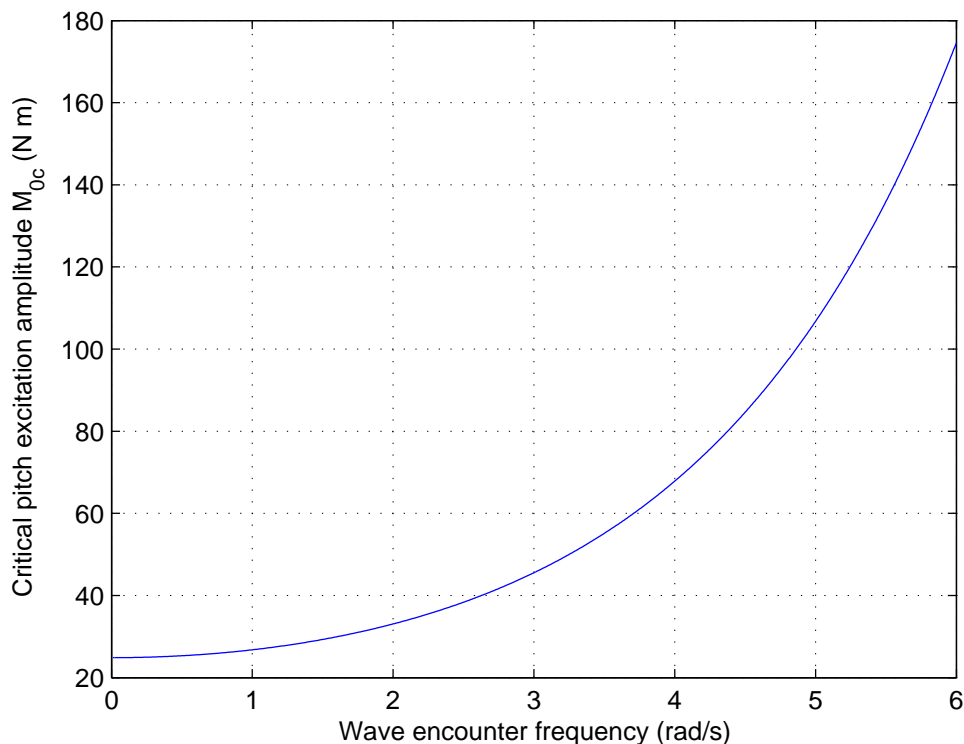
Figure 5.10: The critical pitch excitation amplitude M_{0c} under different wave encounter frequencies.

5.1.3   Erosion Basin Method

Taking advantage of recent advances in computing power, numerical methods have been extensively employed for analysing the ship's nonlinear dynamic motion. In this section, we will implement the erosion basin technique [30, 31, 60] to investigate the nonlinear roll and pitch motion dynamics of a USV in regular seas. It has been demonstrated by several researchers [29] that with the increment of the wave exciting amplitude, the area of the safe basin will reduce or erode. When this happens, the probability of a ship capsizing increases. It is noteworthy that through our analysis using the Melnikov's function, we have already determined the condition for the basin erosion to set in. Therefore, the investigation using another method can complement and validate our previous study in section 5.1.2.

The stability of a nonlinear dynamic system is very sensitive to the initial conditions. We can use the phase portrait in Fig. 5.7 as an example. Assuming that in the phase plane, there are two points that are located close to each other, and one is inside the boundary cure while the other is on the outside. We can imagine quite different motion behaviours, since the inside one leads to the upright safe position, while the other one will cause the capsizing. The erosion basin method is advantageous, because it helps to examine all possible initial conditions in the phase plane.

We employ the non-dimensional model in Eq. 5.14 for the roll motion erosion basin analysis. Unlike in section 5.1.1.2, here we formulate the non-dimensional roll excitation amplitude k_0 as

$$k_0 = K_0/R_{41}$$

according to Eq. 5.15. It is important to note that as a lumped parameter k_0 (K_0) already takes into account the wave direction information according to Eq. 4.24. While implementing the erosion basin method, the studied phase plane area is divided into equal sized small grids, and the center of each grid is regarded as a particular initial condition, i.e. initial roll angle and angular rate, for the roll motion simulation. The numerical solution is calculated based on these initial conditions. Based on the boundedness of each simulated solution, different zones of safe and unsafe initial conditions in the phase plane can be determined. In this study, the graphs only plot the safe zones. If we vary the wave excitation amplitude k_0 (K_0), we can investigate the process of the safe basin erosion.

The basin erosion process for a particular example has been depicted in Fig. 5.11. In this series of simulation, the wave encounter frequency is defined as ω_e=2.6 rad/s and the non-dimensional roll excitation amplitude, k_0, is varied from 0.4 to 1.8. In each plot, the studied roll motion area is $\phi \in [-80°, 80°]$ and $\dot{\phi} \in [-80°/s, 80°/s]$ and it has been divided into 161×161 equal sized grids. The center of each grid is used as the initial condition for the integration and the simulation time is defined as 100 s. The numerical solution is

solved by using the fourth-order Runge-Kutta algorithm. After the integration, if the final roll motion converges to the vicinity of the upright roll position, i.e. $(\phi, \dot{\phi}) = (0°, 0°/s)$, this initial condition is safe and will be plotted out in the final phase plane. Otherwise, if the simulation indicates the divergence, that initial condition is unsafe and will be left blank. It shows clearly in Fig. 5.11 that with the increment of k_0, the boundary becomes fractal and shrinks quickly at some point. There are actually two trends in Fig. 5.11. When $k_0 \in [0, 1)$, the safe basin will reduce from all directions simultaneously. Whereas, if $k_0 \geq 1.0$, the safe basin erodes irregularly. In other words, even the area that is close to the upright position turns out to be unsafe.

To demonstrate this tendency, we generate a plot based on the proportion of the safe initial conditions. When there is no exciting moments, the safe region or the safe initial points reach the maximum number N_m. While in the simulation where there is wave excitation, we calculate the number of the safe points N_s and normalize it by N_m, i.e. the safe region proportion is defined as N_s/N_m. This result has been depicted in Fig. 5.12. It can be concluded that the safe region starts to shrink around $k_0 = 0.6$, and it reduces slowly until $k_0 = 1.0$. When $k_0 > 1.0$, the safe region decreases at a much faster rate. This phenomenon is clearly indicated by the last two plots in Fig. 5.11, and it has been suggested by [61] that system chaos may have occurred.

The safe region proportion N_s/N_m can be employed for representation of a USV's rolling motion safety. With the increment of the wave exciting amplitude or the sea state, the safe region will reduce, which indicates a more severe operational environmental condition. To examine the relationship between N_s/N_m and different wave encounter frequencies, more erosion basin simulations have been performed. A summary of these results have been provided in Table 5.1.

We plot the data in Cartesian coordinates as shown in Fig. 5.13, where the x and y axes are the wave encounter frequency and k_0, respectively, and z axis is the safe region
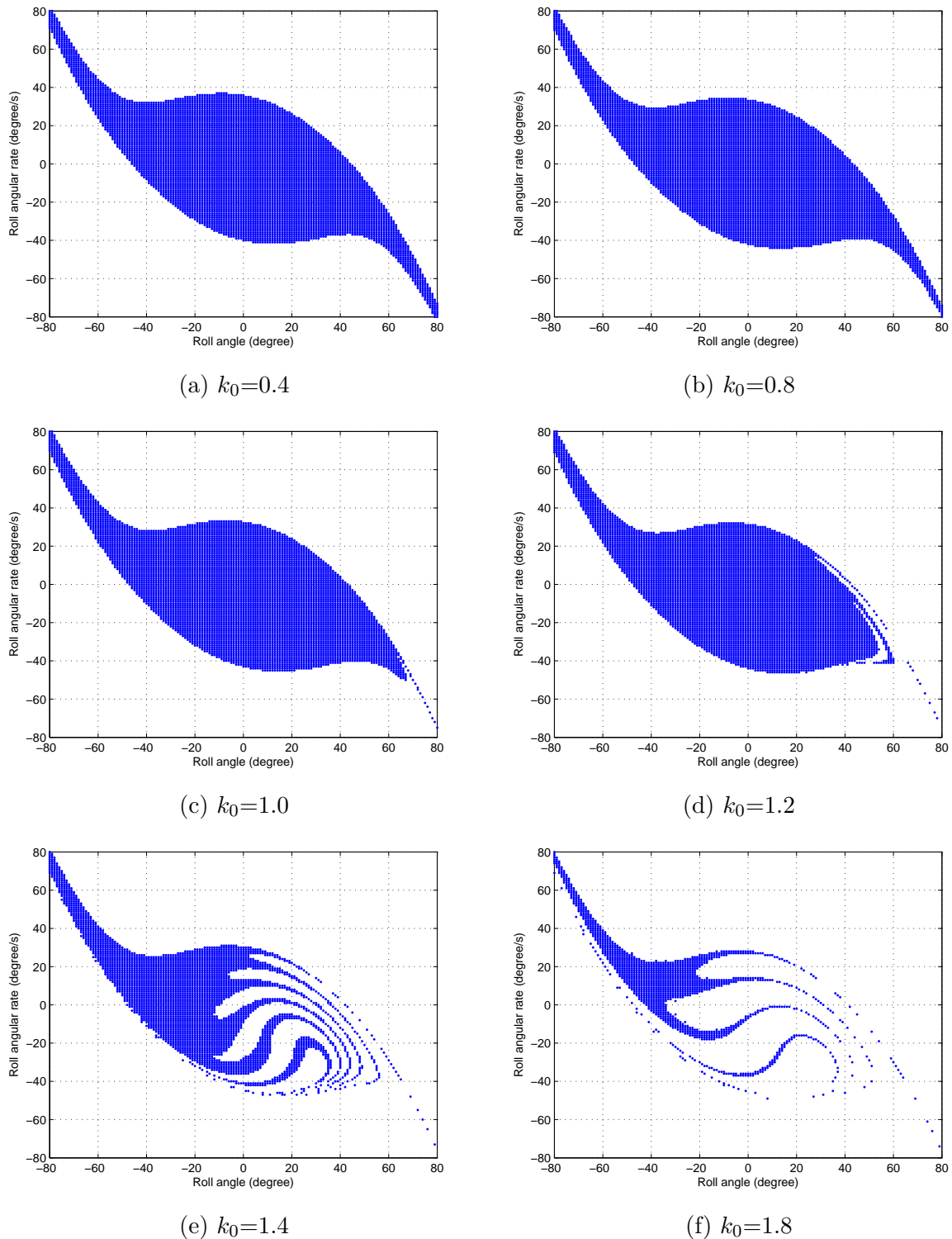
Figure 5.11: Erosion basin of the dynamic roll motion model with the wave encounter frequency of ω_e=2.6 rad/s or $\omega_{ne} = 0.8334$. Note that k_0 is the non-dimensional roll exciting amplitude.
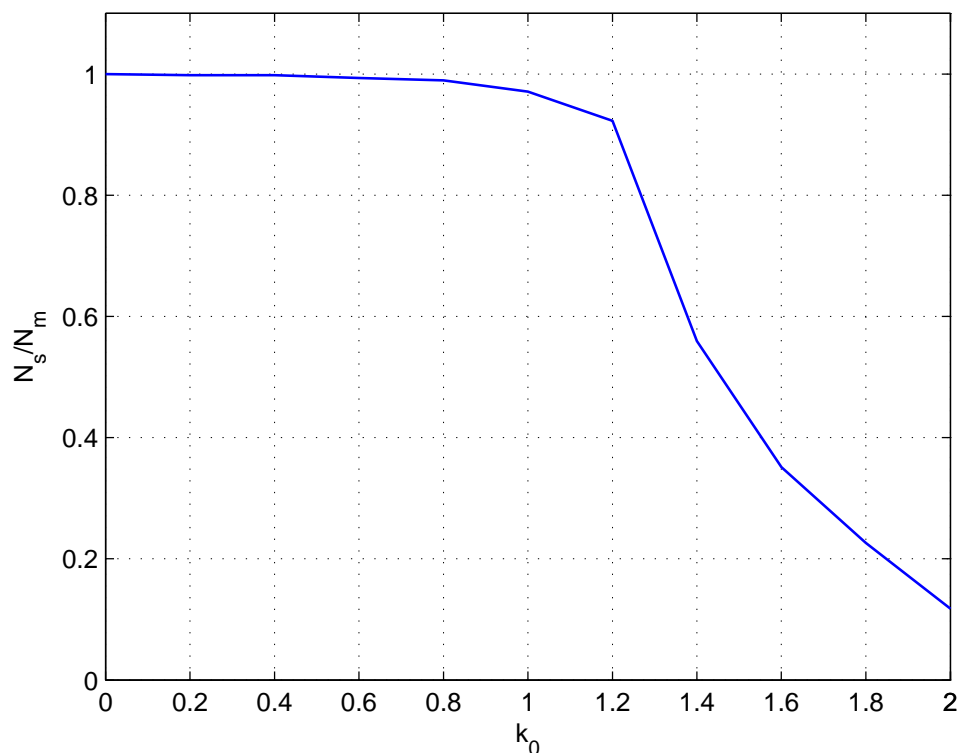
Figure 5.12: The proportion of the safe region versus the non-dimensional wave excitation amplitude k_0 when the wave encounter frequency is 2.6 rad/s.

proportion. It can be seen that when $k_0 < 0.5$, the safe region will not reduce a lot, but with the increment of k_0 the basin erosion becomes more evident. The worst case is when the wave encounter frequency is around 2.2 rad/s, which features the fastest decrement among all the simulations. This simulation result complies well with our analytical analysis in section 5.1.1.2, where we find out that the nonlinear roll resonance bends towards the low frequency range as shown in Fig. 5.2. This theoretically explains why the worst case occurs when the encounter frequency is lower than the natural roll frequency that is around 3.12 rad/s.

The erosion basin results can be used to verify our Melnikov's analysis. For example, since both erosion basin and Melnikov methods are based on the phase plane, we can overlay their results together and check the safe basin boundary. This result has been

Table 5.1: Safe region proportion under different wave encounter frequencies and non-dimensional wave exciting amplitudes

ω_e \ k_0	0	0.4	0.8	1.0	1.2	1.4	1.6	1.8	2.0
0.2	1.0000	0.9761	0.8324	0.6971	0.5897	0.4946	0.4139	0.3405	0.2754
0.6	1.0000	0.9831	0.9296	0.8827	0.8170	0.7168	0.6019	0.5252	0.4572
1	1.0000	0.9916	0.9626	0.9255	0.8482	0.6755	0.5451	0.4413	0.3534
1.4	1.0000	0.9954	0.9805	0.8974	0.8000	0.6695	0.5032	0.3505	0.2495
1.8	1.0000	0.9987	0.9980	0.8354	0.6822	0.5084	0.3365	0.1797	0.0663
2.2	1.0000	0.9997	0.9970	0.9874	0.4467	0.1586	0.0013	0	0
2.6	1.0000	0.9982	0.9896	0.9711	0.9226	0.5592	0.3512	0.2263	0.1176
3	1.0000	0.9966	0.9795	0.9605	0.9378	0.9011	0.8301	0.7036	0.5605
3.4	1.0000	0.9950	0.9782	0.9630	0.9448	0.9253	0.9028	0.8628	0.8185

depicted in Fig. 5.14, where the phase portrait is directly taken from Fig. 5.7, and the shaded area is achieved from the erosion basin analysis assuming no wave excitation moments. We can conclude that through using two different methods, we actually achieve the same boundary condition to distinct the safe and unsafe regions.

Further, we can use the erosion basin analysis results to validate the critical wave excitation amplitude computed using the Melnikov function. According to Table 5.1, the contour plot has been generated as shown in Fig. 5.15, and it has been overlaid with the critical excitation amplitude curve, i.e. thick line, in Fig. 5.8. The numbers on each contour represent the safe region proportion. It is evident that the critical amplitude curve generated from the Melnikov method provides a good estimate of the boundary conditions for the roll motion. When the exciting moment amplitude K_0 has the value above the critical curve, the safe region will reduce quickly. Again, this plot clearly shows the worst wave encounter frequency for the USV's roll motion is around 2.2 rad/s. The critical exciting amplitude curve is close to the contour that represents the 90% safe region proportion, especially in the high encounter frequency range. Note that using the results from Fig. 5.15, we can also define a boundary condition based on the 80% safe region proportion contour or even lower ones. However, it is better to be more conservative on
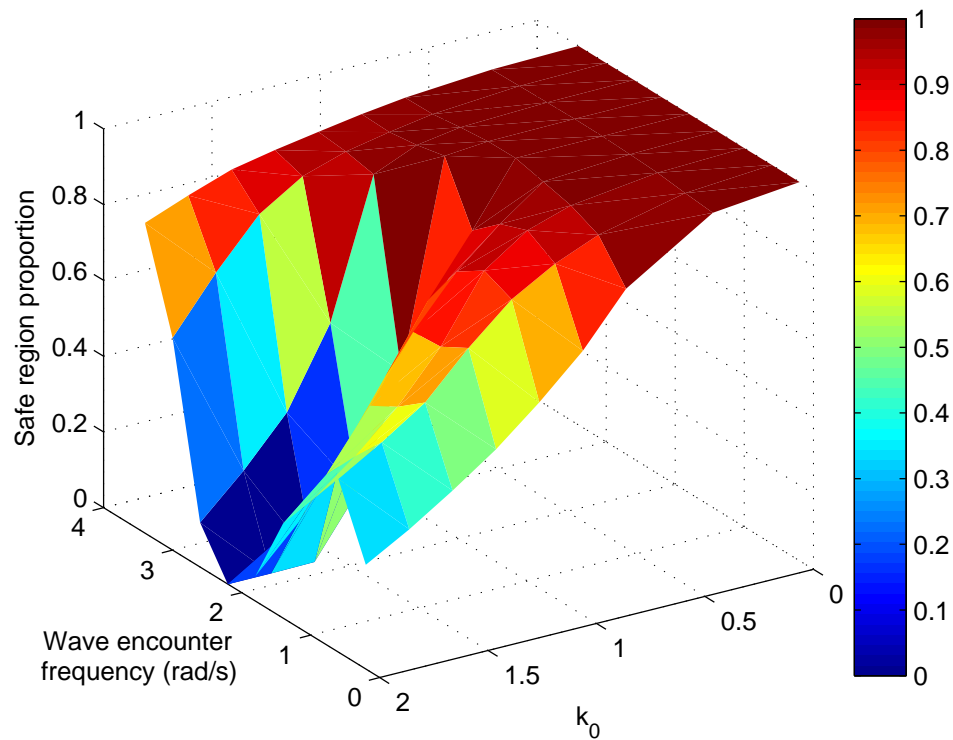
Figure 5.13: The safe region proportion versus k_0 and the wave encounter frequency expressed in the Cartesian coordinates.

the safety of a USV operating in harsh ocean environments. In summary, the boundary condition suggested by Melnikov's Method is a conservative condition, and it can be employed as the safety criteria for the roll motion. As for the nonlinear pitch motion, the analysis is similar, and to be concise no erosion basin analysis results are included. However, according to our previous analysis, the conservative critical condition in Fig. 5.10 can be used as the pitch motion safety criteria.

5.2 Safe Operational Condition

We have already studied the USV's heave, roll and pitch motion using three different analysis tools, i.e. linear and nonlinear analytical methods, Melnikov's method and ero-
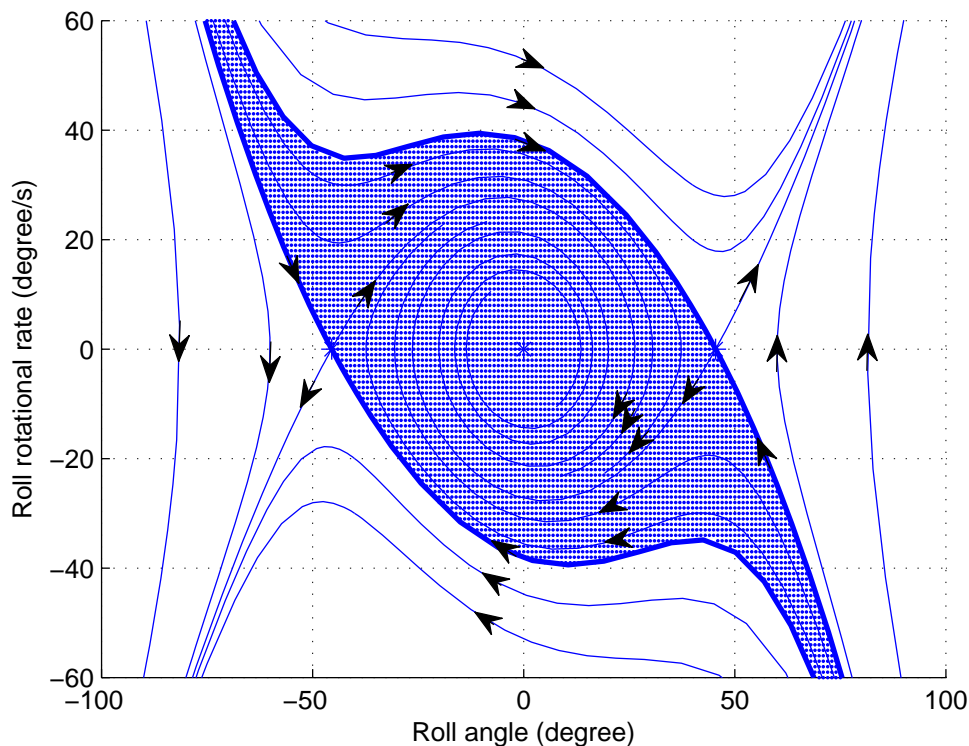
Figure 5.14: Overlay of the erosion basin analysis results and the phase portrait achieved from the Melnikov's analysis. Note that in both simulations, we assume that the wave excitation moments are zero.

sion basin method. Using the linear model, we can achieve the close-form solution and analytically compute the resonance frequency for heave, roll and pitch motion. Considering a USV that operates in harsh ocean environments, the nonlinear oscillatory motion models are more reasonable. However, by using the analytical tool, we can only formulate an approximated analytical solution. Melnikov's function can be implemented to analyze the complicated nonlinear oscillatory motion, and it has been employed to compute the critical wave exciting moment amplitude for a USV's nonlinear rolling and pitching movement. By performing the erosion basin simulation, we further validate the critical conditions suggested by the Melnikov's analysis. In this section, we will use the achieved critical condition to discover a USV's safe operational condition under ocean
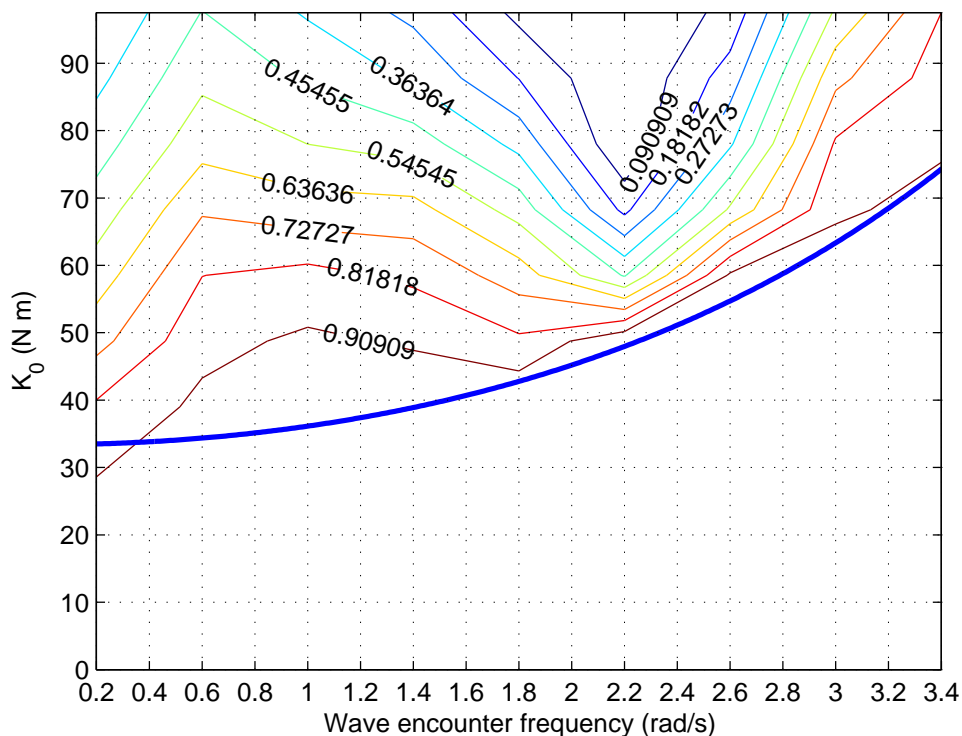
Figure 5.15: The contour plot compared with the critical exciting moment amplitude for roll motion based on the Melnikov analysis. The thick line indicates the Melnikov suggested critical value of K_0.

wave influences. In the following discussion, it must be borne in mind that the studied USV platform is underactuated, and only the USV's moving speed and heading angle (or course angle) are controllable.

First, we determine the safe operational region for the roll motion. We assume the wave amplitude is $0.2\ m$, the USV's moving speed is $0.5\ m/s$ and the vehicle heads towards the sea waves. We can plot the critical exciting amplitude K_{0c} in the polar coordinates as a function of wave frequency ω_w and wave direction χ_w and overlay it on top of the wave-induced roll exciting moments in Fig. 4.11a of section 4.3.2. Note that the critical roll exciting moment amplitude is related to the wave encounter frequency (Fig. 5.8), and thus it has to be converted to the wave frequency using Eq. 4.20 before generating the

3D surface plot in the polar coordinates.

The results have been depicted in Fig. 5.16, and it shows that the two surfaces intersect with each other. Therefore, the safe (unsafe) region can be defined as where the wave-induced roll exciting moment is below (above) the critical wave exciting amplitude, i.e. the surface of K_{0c}. We can imagine that by varying the wave conditions or the vehicle operation status, the safe regions will change depending on the intersection of the two surfaces.
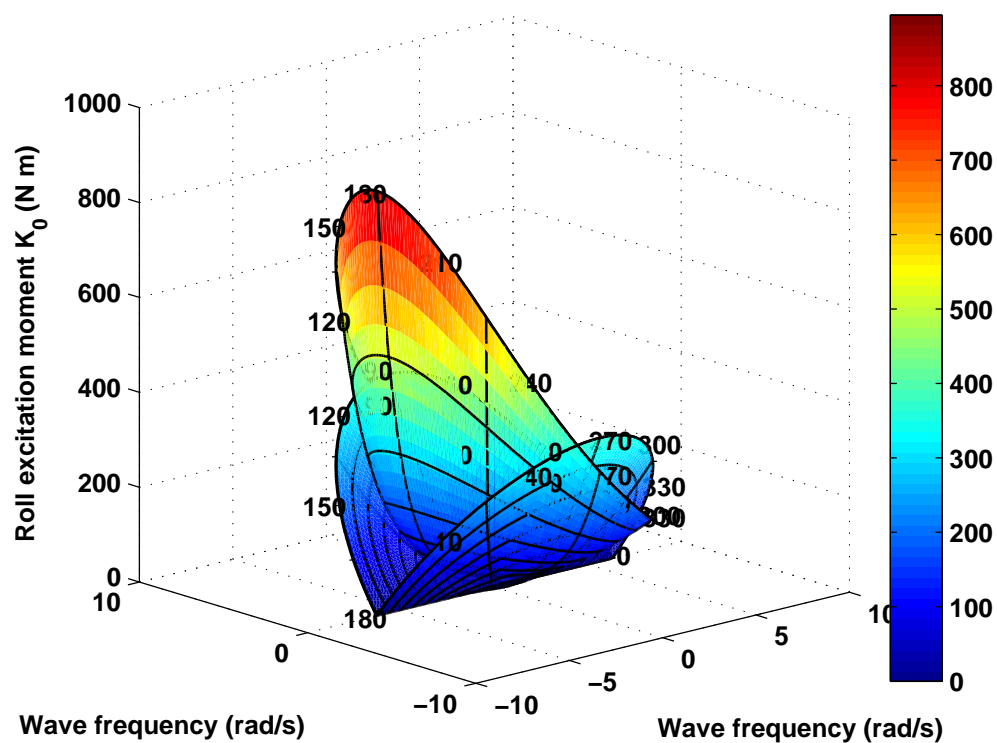
Figure 5.16: Roll excitation moment amplitude and the critical roll excitation moment amplitude plotted together in the polar coordinates.

To clearly show the safe operational region and make it usable for a USV's guidance and control system, we choose to use the contour plot and only draw the unsafe regions using polar coordinates. Two sea states are considered, i.e. when $\zeta_A = 0.2\ m$ and when $\zeta_A = 0.5\ m$, and the two groups of plots with varied vehicle moving speed are depicted

in Fig. 5.17 and Fig. 5.18. In each graph, χ_w is measured from the vehicle's heading direction and the value is in the range of $\chi_w \in [0°, 360°)$. Again, $\chi_w = 0°$ represents the following sea condition, while $\chi_w = 180°$ stands for the head sea condition. The radial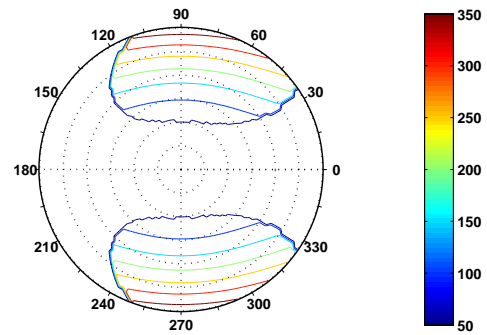 distance is measured with respect to the polar origin in each graph, and it denotes the wave frequency in the range of $\omega_w \in [0, 2\pi]$ rad/s with each division representing $\pi/3$ rad/s.

As shown in Fig. 5.17, the USV's moving speed is varied from 0 m/s to 1.0 m/s with a step of 0.2 m/s, and the unsafe area in the polar coordinates are highlighted with contours. The wave-induced roll exciting moment amplitude (K_0) is represented according to the color bar on the right of each graph. In Fig. 5.17a, when $u = 0$ it clearly shows that the beam sea waves are the most dangerous case for a USV's roll motion safety. We can see when $\omega_w > 2\pi/3$ rad/s and the wave direction belongs to the range of $\chi_w \in [75°, 135°]$ and $\chi_w \in [225°, 315°]$, the vehicle will operate in the unsafe regions. Inside the unsafe regions, with the increment of ω_w the wave exciting moment increases quickly, and the vehicle will have a higher probability of capsizing. On the contrary, if the wave comes from other directions, i.e. the safe operational region, the vehicle will operate safely without any need to consider about the roll safety issues even ω_w is high. Through comparing the series of graphs in Fig. 5.17, we can conclude that the unsafe operational region changes dynamically according to the vehicle's moving speed. For instance, when $u = 0.6$ m/s, the unsafe wave direction changes to $\chi_w \in [15°, 100°]$ and $\chi_w \in [260°, 345°]$. As suggested by the drawn graphs, when the vehicle runs at high speed, it is a reasonable choice to drive the vehicle in head sea condition, since large safe operational region can be found around $\chi_w = 180°$.

When the sea state increases, the unsafe region will expand evidently, which has been demonstrated in Fig. 5.18. In Fig. 5.18a, if $\omega_w <= 2\pi/3$ rad/s, a USV can survive the ocean waves from any directions. However, if $\omega_w > 2\pi/3$ rad/s, the vehicle can

(a) u=0 m/s, ζ_A=0.2 m

(b) u=0.2 m/s, ζ_A=0.2 m

(c) u=0.4 m/s, ζ_A=0.2 m

(d) u=0.6 m/s, ζ_A=0.2 m

(e) u=0.8 m/s, ζ_A=0.2 m
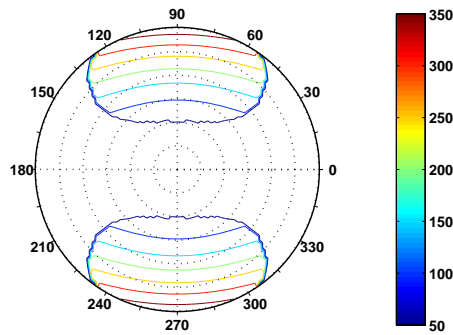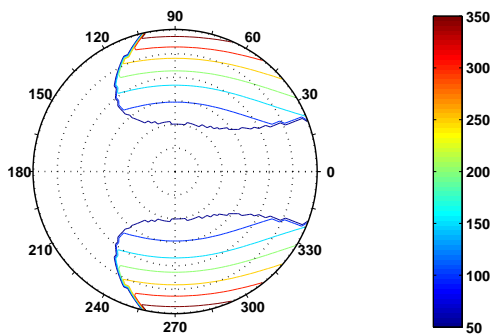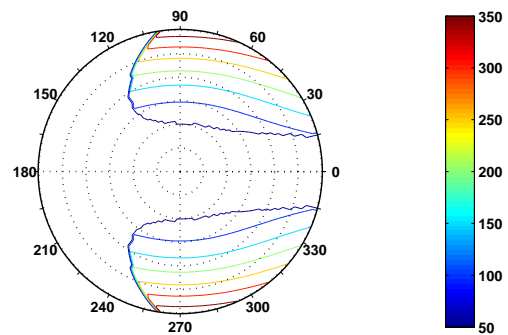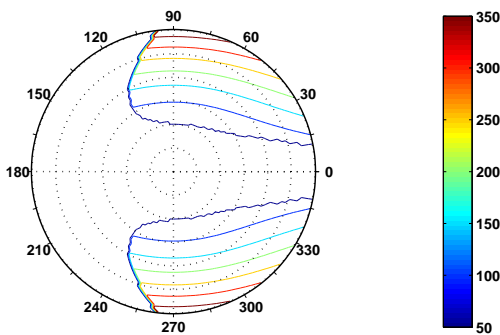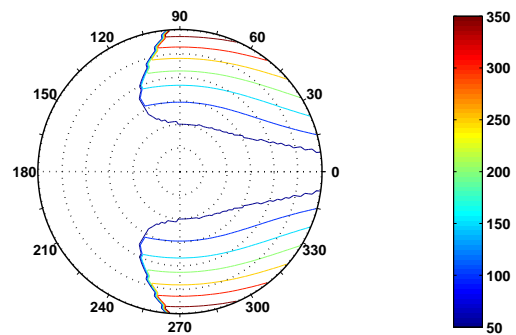
(f) u=1.0 m/s, ζ_A=0.2 m

Figure 5.17: The unsafe (safe) operational region for a USV's roll motion while the vehicle operates in the seaway with different moving speeds. In this group of simulation, the wave amplitude ζ_A=0.2 m, and the unsafe region is indicated by the contours.

(a) u=0 m/s, ζ_A=0.5 m

(b) u=0.2 m/s, ζ_A=0.5 m

(c) u=0.4 m/s, ζ_A=0.5 m

(d) u=0.6 m/s, ζ_A=0.5 m

(e) u=0.8 m/s, ζ_A=0.5 m
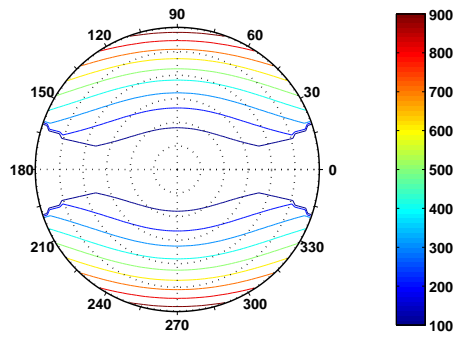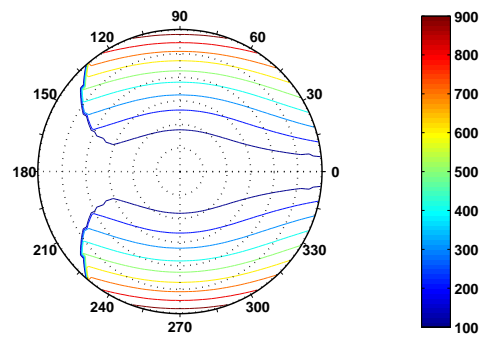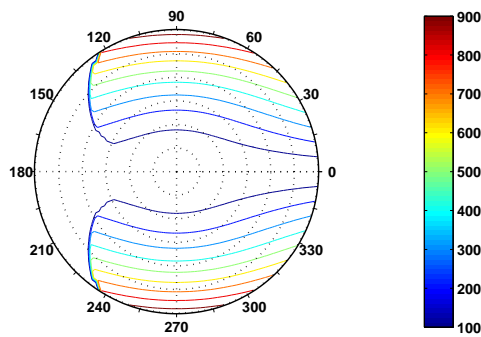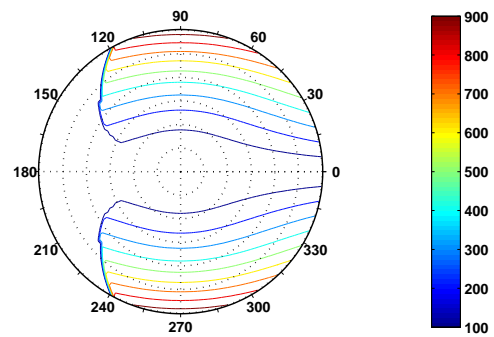
(f) u=1.0 m/s, ζ_A=0.5 m

Figure 5.18: The unsafe (safe) operational region for a USV's roll motion while the vehicle operates in the seaway with different moving speeds. In this group of simulation, the wave amplitude ζ_A=0.5 m, and the unsafe region is indicated by the contours.

easily enter the unsafe region with a high probability of capsizing. With an increment of the vehicle speed, it is more favorable if a USV operates at the head sea condition, i.e. $\chi_w = 180°$.

Similarly, we can investigate the safe operational condition for the pitch motion following the same routine. In Fig. 5.19, we overlay the critical pitch exciting amplitude $M_{0c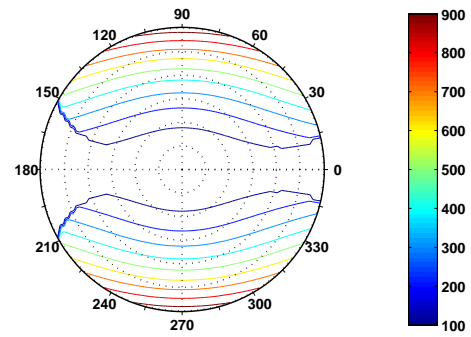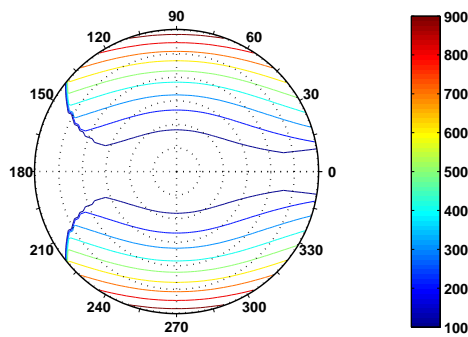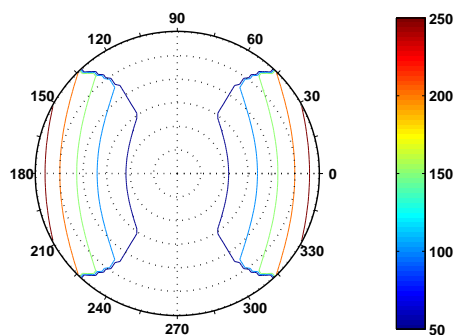}$ surface on top of the achieved wave-induced pitch exciting moment amplitude. In this group of graphs, we assume the head sea condition with the wave amplitude of $\zeta_A = 0.2\ m$ and the vehicle's moving speed as $0.5\ m/s$. The two surfaces intersect with each other, based on which we can determine the safe and unsafe operational regions.

Again, the 2D contour plots in polar coordinates are generated to better show the results. The pitch unsafe (safe) operational regions under varied vehicle moving speed, wave frequency ω_w and wave direction χ_w have been shown in Fig. 5.20 and Fig. 5.21 with the wave amplitude of $\zeta_A = 0.2\ m$ and $\zeta_A = 0.5\ m$, respectively. As shown in Fig. 5.20, the most harmful waves are those that come from the head sea or follow sea directions, i.e. $\chi_w = 180°$ or $\chi_w = 0°$, which is just opposite to the roll motion safety. Interestingly, when the moving speed increases, the unsafe region around $\chi_w = 0°$ expands. On the contrary, the area around $\chi_w = 180°$ reduces significantly until only a small portion of unsafe region is left. When the sea state increases, i.e. $\zeta_A = 0.5\ m$ in Fig. 5.21, the unsafe region expands significantly, and only a small region around beam sea directions is safe. When the vehicle captures a high speed, the original large unsafe region around the head sea direction $\chi_w = 180°$ reduces.

Finally, we can combine the unsafe regions of roll and pitch together so that we can determine the thorough safe operational condition. The results are shown in Fig. 5.22 where the wave amplitude is assumed as $0.2\ m$. In general, the vehicle is suitable to operate in an environment with low-frequency ocean waves, preferably below $\omega_w < 2\pi/3$ rad/s. With the increment of ω_w, the exciting moment exceeds the roll and pitch boundary

Figure 5.19: Pitch excitation moment amplitude and the critical pitch excitation moment amplitude plotted together in the polar coordinates.

condition and the vehicle tends to capsize. When a USV operates at high speed though, the unsafe region will converge to the following sea directions, i.e. the area where $\chi_w = 0°$, and thus the heading sea operation is the most reasonable choice to make the platform operate safely.

5.3   Safety-Based Path-Planning

The ocean environment is very dynamic and becomes harsh sometimes, so it is very important for a researcher to determine a USV's safety according to the environmental conditions before running a survey mission. More importantly, if a USV is equipped with powerful computing capability, it is of great value if the vehicle can assess its safety on-line

(a) u=0 m/s, ζ_A=0.2 m

(b) u=0.2 m/s, ζ_A=0.2 m

(c) u=0.4 m/s, ζ_A=0.2 m

(d) u=0.6 m/s, ζ_A=0.2 m

(e) u=0.8 m/s, ζ_A=0.2 m

(f) u=1.0 m/s, ζ_A=0.2 m

Figure 5.20: The unsafe (safe) operational region for a USV's pitch motion while the vehicle operates in the seaway with different moving speeds. In this group of simulation, the wave amplitude ζ_A=0.2 m, and the unsafe region is indicated by the contours.

(a) *u=0 m/s, ζ_A=0.5 m*

(b) *u=0.2 m/s, ζ_A=0.5 m*

(c) *u=0.4 m/s, ζ_A=0.5 m*

(d) *u=0.6 m/s, ζ_A=0.5 m*

(e) *u=0.8 m/s, ζ_A=0.5 m*
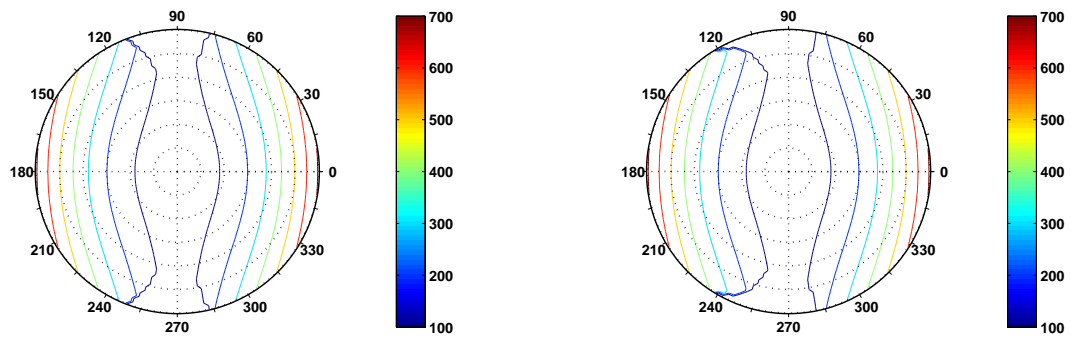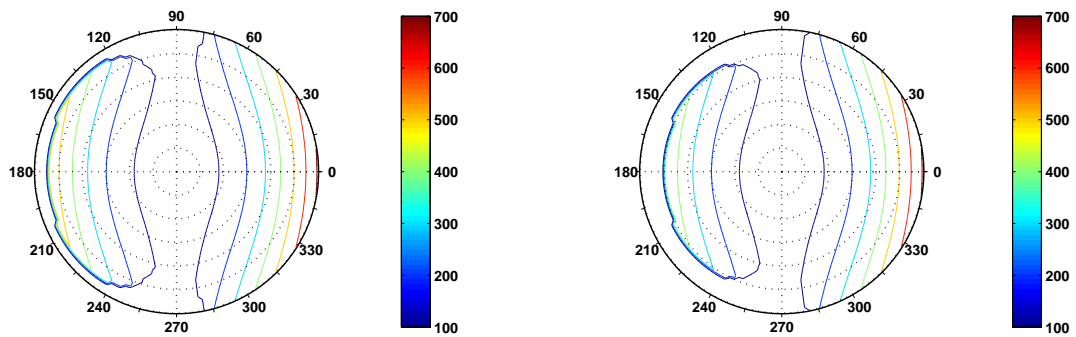
(f) *u=1.0 m/s, ζ_A=0.5 m*

Figure 5.21: The unsafe (safe) operational region for a USV's pitch motion while the vehicle operates in the seaway with different moving speeds. In this group of simulation, the wave amplitude ζ_A=0.5 m, and the unsafe region is indicated by the contours.

(a) u=0 m/s, ζ_A=0.2 m

(b) u=0.2 m/s, ζ_A=0.2 m

(c) u=0.4 m/s, ζ_A=0.2 m

(d) u=0.6 m/s, ζ_A=0.2 m

(e) u=0.8 m/s, ζ_A=0.2 m
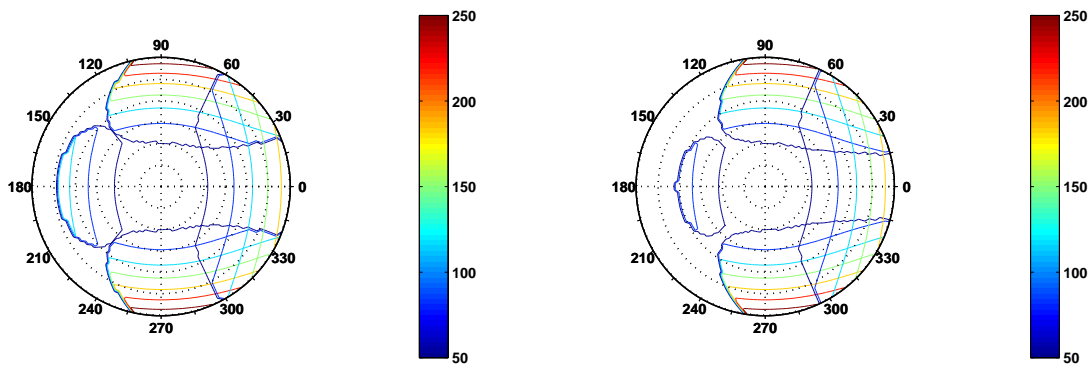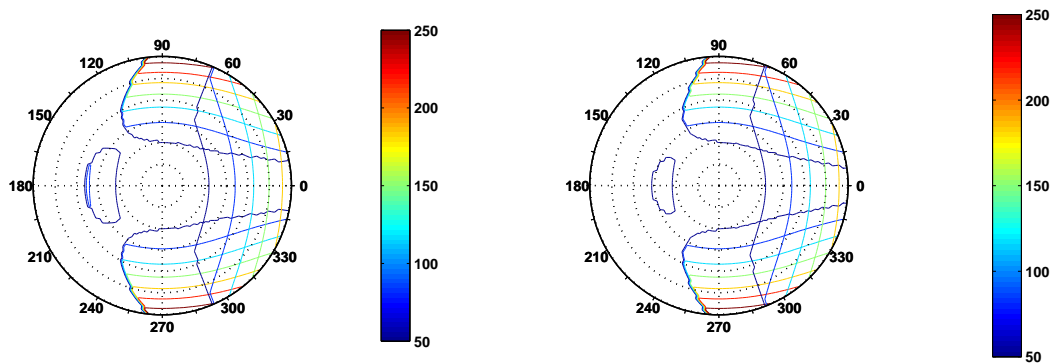
(f) u=1.0 m/s, ζ_A=0.2 m

Figure 5.22: The unsafe (safe) operational region for a USV's roll and pitch motion while the vehicle operates in the seaway with different moving speeds. In this group of simulation, the wave amplitude ζ_A=0.2 m, and the unsafe region is indicated by the contours.

during a mission. In this section, we discuss how we can integrate our defined safe (unsafe) operational condition into a USV's path-planning system to improve its survivability.

To provide a concrete example, we assume that the depth information of a polygon-shape survey area, defined with the four waypoints in Fig. 3.40a, is required to be sa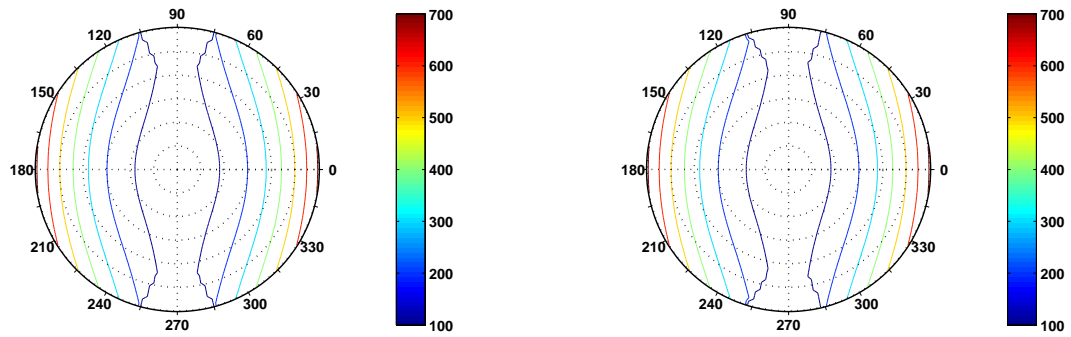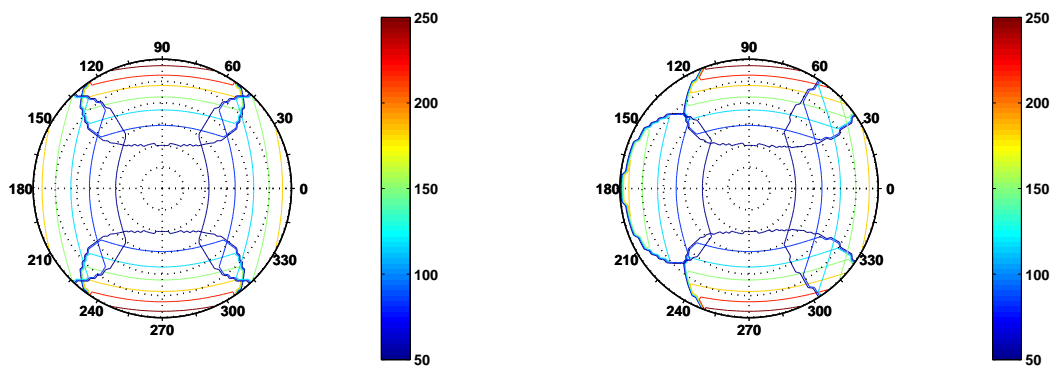mpled by a USV. To fully cover this survey area, the Coverage Path Planning (CPP) algorithm is normally employed [62, 63]. An example of the generated survey paths has been depicted in Fig. 5.23, where the scanning path direction is $\chi_{sc} = -45°$ with respect to true north and the interval between the parallel scanning lines is decided to be d_{in}=10 m. The group of parallel straight lines will intersect with the polygonal boundary lines at different points. These points will be combined together with the polygon vertices to form an orderly waypoint list for a USV to follow. Through implementing one of the three path following control algorithms from chapter 3, the vehicle will be capable of covering the desired region and generating the required seabed image. Note that we have already introduced the guidance and control system architecture and program flow chart in chapter 3, and the CPP algorithm can be conveniently executed in the initialization stage as shown in Fig. 5.24.

There are multiple choices of the scanning direction χ_{sc} to complete the survey mission, but the question is how we can guarantee that the vehicle can successfully complete the mission safely in dynamic environments. The ocean wave conditions, i.e. dominant wave amplitude and wave direction, can be acquired by either on-board sensors, such as radar, or from the ocean forecasting network. In the following discussion, we will assume these environmental conditions are known.

5.3.1 Case Study 1

In this case, we assume the wave amplitude ζ_A=0.2 m, the designated vehicle speed $u = 0.8 \ m/s$ and the wave frequency $\omega_w < 2\pi/3 \ rad/s$. Hence, we can refer to Fig. 5.25
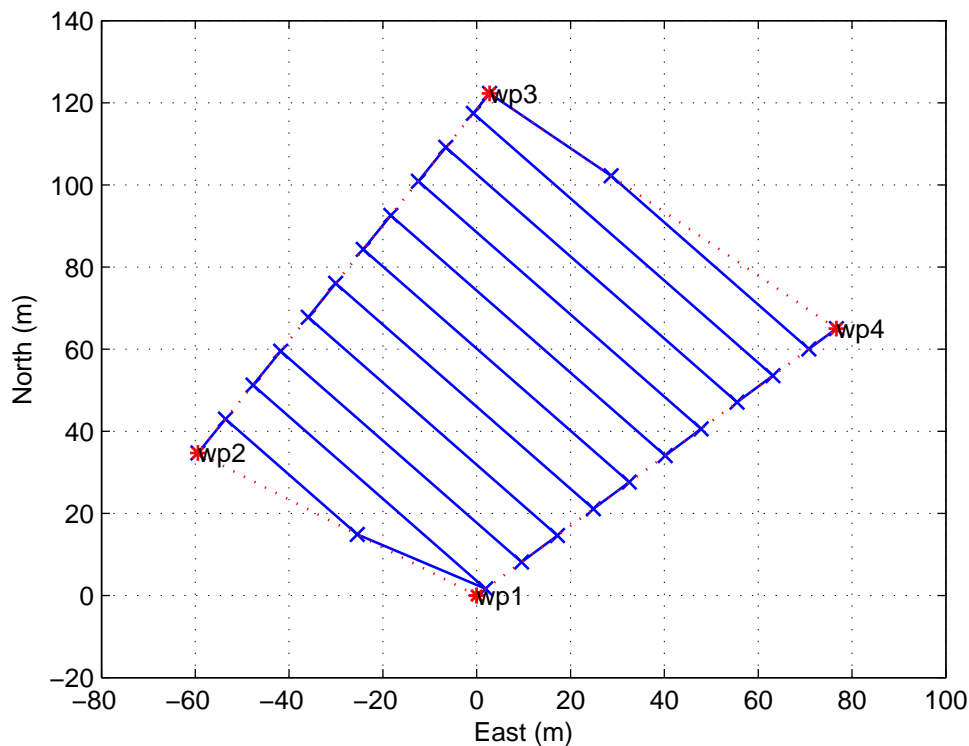
Figure 5.23: An illustration of the generated waypoints and paths based on the coverage path planning algorithm.

to determine the safe (unsafe) operational condition of the studied USV. As shown in Fig. 5.25, inside the circular region CS_1 where $\omega_w < 2\pi/3\ rad/s$, the vehicle can operate safely with any heading directions. In this scenario, the user or the vehicle itself can freely choose the survey direction. According to Fig. 5.22, the vehicle's moving speed can also be assigned to a higher or lower value without any safety issues.

5.3.2 Case Study 2

If the wave amplitude and vehicle speed are kept the same while the wave frequency increases to $\pi\ rad/s$ (circle of CS_2), there will not be many choices of the survey direction. As depicted in Fig. 5.25, for the safety of the studied platform, the survey direction needs to be within the range of $\chi_w \in [128°,\ 138°]$ and $[218°,\ 228°]$. If we refer to the series of
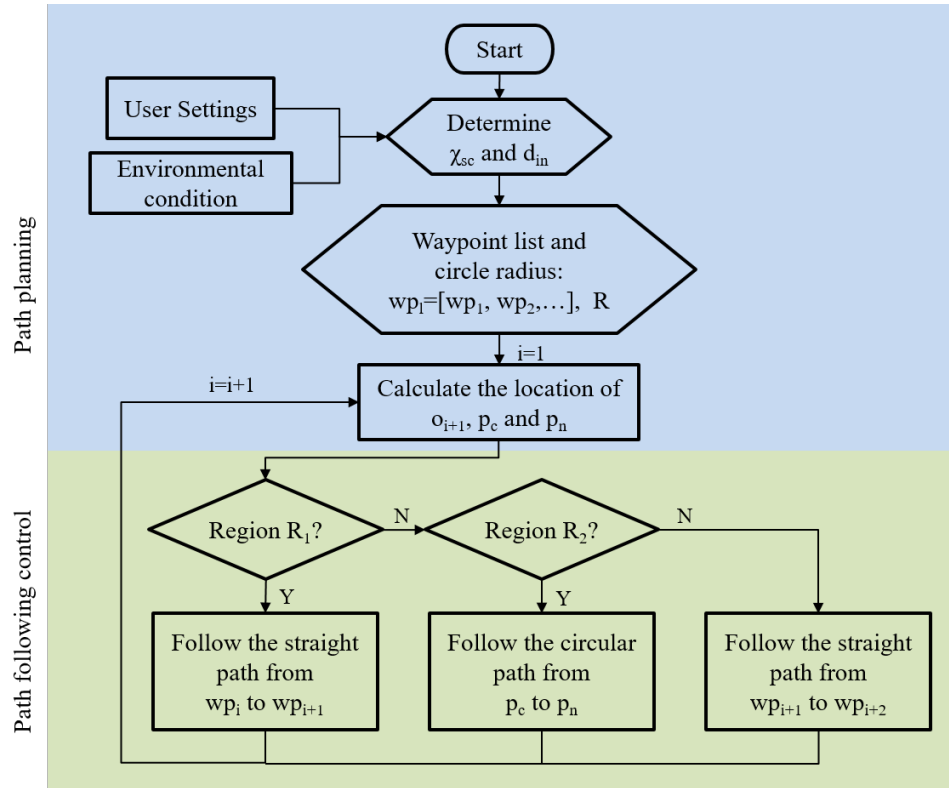
Figure 5.24: The flowchart indicates the generation of the coverage waypoint paths and the implementation of the path following control algorithms, i.e. switching between the straight and circular path following control.

plots in Fig. 5.22, the vehicle speed needs to be greater than 0.4 m/s, or there will be no safe heading direction for the USV. However, CPP requires the vehicle to track the path using the lawn-mower pattern. As shown in Fig. 5.25, although we can choose $\chi_w = 135°$ as one survey direction (marked with a cross), when the vehicle travels back, χ_w becomes 315°, and the vehicle inevitably enters the unsafe operational region. The user or the USV itself can compute the wave excitation moments, and in this case, we calculate the value as 64.95 Nm. According to Eq. 4.20, using the wave frequency π rad/s, wave direction 315° and vehicle speed 0.8 m/s, we can compute the wave encounter frequency as 2.57 rad/s. Until this point, by referring to Fig. 5.15, we can determine that the safe region proportion for roll motion is around 54.5%, and this operation will be at a high risk of the USV's capsizing, about which the user should be aware of. This is a relatively
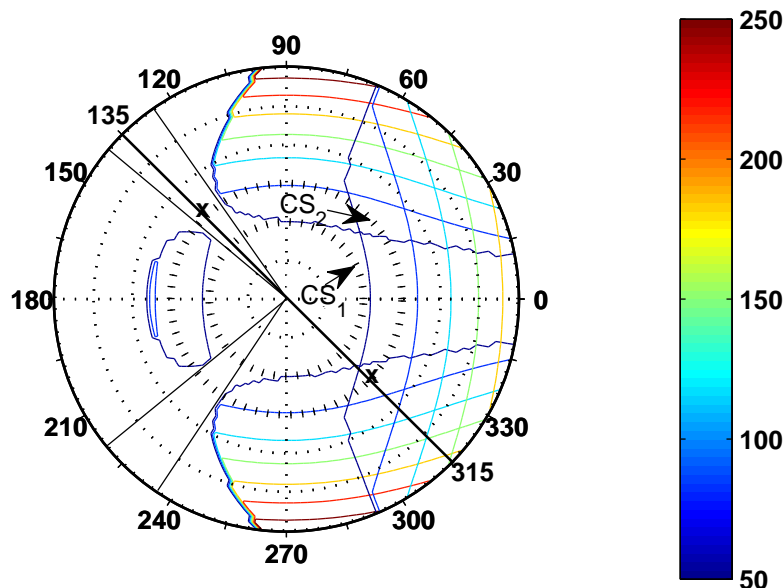
Figure 5.25: The unsafe (safe) operational region for a USV's roll and pitch motion while the vehicle runs at 0.8 m/s in the seaway. The wave amplitude ζ_A=0.2 m, and the unsafe region is indicated by the contours.

unsafe condition, because a USV can not guarantee its safety during the whole mission. Under this circumstance, a user can choose different operation conditions according to Fig. 5.25 and find the one that provides the maximum safe region proportion. Otherwise, it is necessary to cancel the designated survey mission. It is important to note that wave conditions, i.e. wave frequency and amplitude, are known beforehand by using either on-board radar or collecting information from the forecasting network. Therefore, the safety analysis actually provides a prediction of the vehicle's operational status in a future time, and users have enough time to retrieve the vehicle or drive the USV to a new place with acceptable safety analysis results.

5.4   General Chapter Summary

In this chapter, we introduced three mathematical methods, i.e. analytical method, Melnikov's method and erosion basin method, to analyze a USV's complicated nonlinear roll and pitch motion. Through formulating the nonlinear analytical solution, we investigated and demonstrated the well-known jump phenomenon for the rolling and pitching motion. Melnikov's function was used to calculate the distance between stable and unstable manifolds, using which the onset of the system's chaotic behavior could be predicted. This conservative condition had been employed as the USV's safe operation boundary condition, and the results had been further proved by using the erosion basin technique. The wave-induced excitation amplitude analysis in chapter 4 had been combined together with the boundary condition to establish the basis for derivation of a USV's safe (unsafe) operational conditions. These results are quite novel in the USV's research community, and it is helpful for USV practitioners to decide on if a USV's survey mission should be carried on or aborted. Towards the end of this chapter, we discussed the possibility of integration of the safe operational condition into a particular path planning system.

Chapter 6

Conclusions and Future Work

In this chapter, we will provide a general review of this research and highlight the significance of our results, based on which we provide our suggestions for future USV practitioners.

6.1 General Summary and Significant Results

Unmanned Surface Vehicles (USVs) have demonstrated significant value for ocean exploration missions. To be fitted for these missions, a USV has to be capable of operating in the dynamic and sometimes harsh marine environment. Presently available research mainly concentrates on a USV's planar motion control using advanced guidance and control algorithms. However, most work only experiments with the developed strategies in optimal weather conditions, which makes it difficult for USV researchers to determine the efficiency and robustness of these algorithms. Further, a USV that operates in the seaway experiences all six degrees of freedom (DOF) motion, and the oscillatory motion dynamics in heave, roll and pitch are vital factors for a vehicle's operational safety. Unfortunately, only very little work has been done alleviating this potentially disastrous problem.

In this thesis, we provide a comprehensive treatment of USV operations including

a USV's 6 DOF motion dynamics modeling and validation, path-following control algorithms investigation and real-world testing, as well as a complete safety analysis of a USV. We hope that our accomplished work can support and inspire future USV practitioners to choose appropriate motion dynamics models, develop more efficient and robust path-following algorithms, and incorporate more accurate safety analysis results for mission planning to improve a USV's robustness and survivability during a specific survey task. Some of our significant research results are summarized as follows.

The need for high-performance control of USVs motivates us to research high-fidelity planar motion modeling and parameter identification methods. The investigated planar motion dynamics model in surge, sway and yaw is derived from the general 6 DOF rigid body motion equations considering the hydrodynamics and major external influences. In order to identify an accurate motion model, a hybrid model parameter identification method that combines tow tank tests and the on-board sensor based identification routine has been introduced. An accurate bilinear thruster model has been identified by performing the tow tank tests. Using this model, the remaining model parameters are successfully identified through carrying out the field experiments. Using the collected field trial data we evaluate the self-propulsion points and validate the surge damping value from the tow tank tests. We are also able to generate the generic surge and yaw motion model, which stands out from the presently available researches. These models bring great convenience for construction of the simulation model and development of advanced control algorithms. Although the chosen planar motion model structures are highly simplified, through evaluation of the model using the collected zigzag experimental data, we can determine that the achieved model can approximate the vehicle's actual motion with reasonably good performance.

Much effort has been put into the research of path-following control for mobile robots. However, as for USVs, most attention has only been paid on the Line-of-Sight Method

(LOS), and the evaluation experiments are performed in ideal weather in most cases. To compare with the LOS method and extend the options for future USV practitioners, we comprehensively investigate three mainstream path-following control algorithms, i.e. Vector Field Method (VF), Carrot Chasing Method (CC) and the well-accepted LOS method. To the best of the author's knowledge, VF and CC are tested on a USV platform for straight-line and circular path-following control study for the first time. Each algorithm has been analytically derived, and based on the parameter space exploration results, we theoretically investigate their different path-following control characteristics. Although VF and CC are generated from quite different perspectives, we have revealed the mathematical relationship between them. An integral gain can be integrated into the conventional CC algorithm (CCI) with considerable improved path-following control robustness. To evaluate the performance of each algorithm on an actual dynamic system, we perform the preliminary simulation tests using the identified USV's planar motion dynamics. A Matlab/Simulink model has been developed incorporating the USV's motion dynamics and the guidance and control system architecture. Using this model, we successfully carry out the straight-line, circular and waypoint path-following experiments using VF, CCI and LOS methods. By performing the simulation tests, we gain valuable experience in tuning the low-level controllers as well as each path-following control algorithms. The achieved results have been used to validate the exploration of the parameter space results. Eventually, field trial experiments are performed on the real USV platform in adverse weather conditions to further evaluate the efficiency and robustness of each individual path-following method. Similar to the simulation case, we still perfom the straight-line, circular and waypoint path-following control tests. Although the actual testing platform has varied motion dynamics compared to the simulated model, our experimental results show a relatively good consistency with those from the simulation. For instance, we validate that all three methods can drive the vehicle to track the straight-line

path successfully, among which VF has a little bit better performance. However, similar to the simulation, we discover VF is not good at controlling a USV to track the small circular paths and there will be steady-state cross track errors; LOS, on the other hand, will control the USV to track the circular path from inside of a circular path; CCI has a better performance than VF, but it requires a relatively long time before the vehicle can converge to the circular path. The final waypoint path-following control experiments that resemble a real ocean survey mission are carried out in bad weather conditions. In general, all three methods provide a reasonably good performance to complete the desig-nated survey mission under the adverse weather influences. To complete the same survey task, LOS is the fastest with an average path-tracking error of less than 1 m and VF requires the lowest total control energy. Although we predict that CCI will have a much better performance in the real-world tests, it turns out that the integral gain will bring in large path tracking overshoot when the vehicle transits between the straight-line and circular path segments.

The introduced path-following methods can control a USV to operate reliably in the horizontal plane in the adverse weather conditions. However, the uncontrollable oscilla-tory motion in heave, roll and pitch are critical for a USV's operational safety, and this topic is not very well addressed in the USV research community. To make the problem tractable, we follow the convention and introduce decoupled linear and nonlinear models for the three oscillatory motion analysis. The linear model parameters can be identified using nonlinear least-squares solver based on the collected free decay data. As for the nonlinear model, we need to employ additional tank tests, the hydrostatics software and the energy method to correctly determine the model parameter values. The identified models have been successfully validated through comparison with the actual measured data. To investigate a USV's operational safety, we consider the primary influences from the ocean waves and construct the model to represent the wave-hull interaction forces

and moments. This highly nonlinear interactive dynamics are quite complicated, and we implement three well-accepted tools, i.e. Analytical Method, Melnikov's Method and Erosion Basin Method, to perform the safety analysis. Through formulating the approximation of the nonlinear analytical solution, we investigate the jump phenomenon for the roll and pitch motion and demonstrate their distinctive characteristic compared to the linear solutions. Melnikov's method has been employed to analyze the onset of the chaotic behavior of a USV's rolling and pitching motion as a result of the excitation waves. Using Melnikov's function, we can determine a conservative critical condition to predict the occurrence of the chaotic motion, and the fractal boundary can be regarded as a USV's safe operation boundary condition. The erosion basin numerical analysis has been implemented as a supplement of the Melnikov's method, and the results prove the fidelity of the boundary condition and show that the achieved boundary condition corresponds to the 90% safe region proportion contour. The boundary condition computed by Melnikov's method has been plotted in 3D polar coordinates has been overlayed on top of the wave-induced excitation moments to determine the safe (unsafe) operational region for a USV. To clearly show the results, unsafe region contours are depicted in the 2D polar coordinates. We find out that the wave amplitude plays a key role in changing the size of the safe (unsafe) operational region. Further, through alternating a USV's moving speed and heading direction (wave direction), the safe region will change dynamically in the 2D polar coordinate frame. A USV practitioner can use the measured wave frequency information and refer to the generated 2D polar graph for determination of the safe configuration, i.e. speed and heading, for a USV to complete a specific mission. In the cases that the vehicle enters the unsafe region, we can also evaluate the safe region proportion to decide whether it is worth risking the safety of the vehicle to finish the specific mission. Through our analysis, we find that although the small catamaran-type USV has been a popular research platform for different research institutions across the world, it is only

capable of operating in coastal and some low sea-state conditions. The small platform will start to suffer serious limitations in terms of its operational safety in realistic open sea conditions.

6.2   Suggestions for Future Work

With the fast development of Unmanned Surface Vehicle (USV) technology, now we are more capable of exploring the vast ocean. These robotic platforms are cost-effective and can be deployed for persistent observation of the ocean even in the most challenging environments without endangering humans. In this work, we provide a complete study of a USV's motion dynamics modeling, guidance and control system development and safety analysis. Our suggestions for the future USV practitioners are summarized as follows.

The presented planar motion model and parameter identification methods are applicable for the displacement-style USVs with slow motion dynamics. In terms of the planing hull ones, to accurately identify the model parameter values, a varied model structure and a faster motion data sampling rate is needed. Although the affine thruster model has been widely used, we recommend the usage of bilinear thruster model since it takes into account the thrust deduction and hull thruster interaction, which can better represent the generated propulsive forces. Owing to the simplicity and fidelity of the achieved generic surge and yaw motion models, they can be conveniently implemented for further development of advanced motion control algorithms.

The investigated three geometric path-following control algorithms, namely Vector Field Method (VF), Carrot Chasing Method (CC) and Line-of-Sight Method (LOS), can be successfully implemented on a USV platform. However, it is important for the future researchers to note that VF and conventional CC have the same mathematical basis, which will lead to similar path tracking results. While implementing each algorithm, the

controller parameters need to be fine tuned to gain the best performance. It will also be an interesting research topic about the comparison of these algorithms with optimization-based path-following control methods. The slow motion dynamics of the USV platform is a key element when choosing the low-level control algorithm, and it will be helpful to investigate feed-forward control and other advanced control schemes to speed up the system response time in the future. When planning a USV mission, such as survey of restricted area, it is also important to take into account these dynamics limit.

The operational safety of a USV is vital in successful completion of a designated mission, and thus it is of great importance for future researchers to pay more attention to this subject. We have introduced a convenient and simple experimental method, i.e. free decay tests, to identify the oscillatory motion model parameters. To identify the nonlinear damping terms, we implement the energy method, but if there is required equipment and available funding, forced oscillation in calm water is suggested for more accurate results. The wave-hull interaction is a highly nonlinear complicated problem, and our analysis makes the assumption of regular waves from a specific direction. We have implemented Melnikov's function to calculate the critical wave amplitude, and the erosion basin method has demonstrated the correctness of this safe operational boundary condition. However, more tank experiments with various wave conditions are needed to further validate this critical condition in future work. The generated safe (unsafe) region contour plot in 2D polar coordinates has practical value for USV practitioners. Before a specific mission, depending on the current wave condition, researchers can determine a proper survey trajectory for a USV to follow. On the other hand, if the platform can acquire the wave condition information on-line, the safe (unsafe) region plots can be recorded on-board the vehicle so that the system itself can make correct decisions to maximize its mission execution safety. In this research, we only provide a simple coverage path planning case for discussion. To achieve fully autonomous safety awareness, researchers will need to

develop new algorithms to optimize the process of searching for the best USV speed and heading settings. It is also important to note that to further increase the region of safe operations, researchers can develop and incorporate fin stabilizers or roll and pitch stabilization mechanisms according to the USV payload capacity and project budget.

Bibliography

[1] M. Caccia, R. Bono, G. Bruzzone, G. Bruzzone, E. Spirandelli, G. Veruggio, A. Stortini, and G. Capodaglio, "Sampling sea surfaces with SESAMO: an autonomous craft for the study of sea-air interactions," *IEEE Robotics Automation Magazine*, vol. 12, pp. 95–105, Sept. 2005.

[2] J. Manley, "Development of the autonomous surface craft ACES," in *OCEANS '97. MTS/IEEE Conference Proceedings*, vol. 2, pp. 827–832, Oct. 1997.

[3] W. Naeem, T. Xu, R. Sutton, and A. Tiano, "The design of a navigation, guidance, and control system for an unmanned surface vehicle for environmental monitoring," *Proceedings of the Institution of Mechanical Engineers, Part M: Journal of Engineering for the Maritime Environment*, vol. 222, pp. 67–79, June 2008.

[4] J. Manley, "Unmanned surface vehicles, 15 years of development," in *OCEANS 2008*, Sept. 2008.

[5] V. Bertram, "Unmanned Surface Vehicles - A Survey," 2008.

[6] R. Hine, S. Willcox, G. Hine, and T. Richardson, "The Wave Glider: A Wave-Powered autonomous marine vehicle," in *OCEANS 2009, MTS/IEEE Biloxi - Marine Technology for Our Future: Global and Local Challenges*, pp. 1–6, Oct. 2009.

[7] M. Caccia, M. Bibuli, R. Bono, G. Bruzzone, G. Bruzzone, and E. Spirandelli, "Aluminum hull USV for coastal water and seafloor monitoring," in *OCEANS 2009 - EUROPE*, pp. 1–5, May 2009.

[8] N. Smith, R. Bachmayer, Z. Li, and F. Luchino, "Development of a semi-submersible unmanned surface craft," in *Oceans - St. John's, 2014*, pp. 1–7, Sept. 2014.

[9] C. R. Sonnenburg and C. A. Woolsey, "Modeling, Identification, and Control of an Unmanned Surface Vehicle," *Journal of Field Robotics*, vol. 30, pp. 371–398, May 2013.

[10] T. Huntsberger, H. Aghazarian, A. Howard, and D. C. Trotz, "Stereo vision based navigation for autonomous surface vessels," *Journal of Field Robotics*, vol. 28, pp. 3–18, Jan. 2011.

[11] T. I. Fossen, *Handbook of Marine Craft Hydrodynamics and Motion Control.* Chichester, West Sussex: Wiley, May 2011.

[12] F. Caron, E. Duflos, D. Pomorski, and P. Vanheeghe, "GPS/IMU data fusion using multisensor Kalman filtering: introduction of contextual aspects," *Information Fusion*, vol. 7, pp. 221–230, June 2006.

[13] J. Curcio, J. Leonard, and A. Patrikalakis, "SCOUT - a low cost autonomous surface platform for research in cooperative autonomy," in *Proceedings of MTS/IEEE OCEANS, 2005*, pp. 725–729 Vol. 1, 2005.

[14] M. Benjamin and J. Curcio, "COLREGS-based navigation of autonomous marine vehicles," in *Autonomous Underwater Vehicles, 2004 IEEE/OES*, pp. 32–39, June 2004.

[15] Z. Yu, X. Bao, and K. Nonami, "Course Keeping Control of an Autonomous Boat using Low Cost Sensors," *Journal of System Design and Dynamics*, vol. 2, pp. 389–400, 2008.

[16] H. Ashrafiuon, K. Muske, L. McNinch, and R. Soltan, "Sliding-Mode Tracking Control of Surface Vessels," *IEEE Transactions on Industrial Electronics*, vol. 55, pp. 4004–4012, Nov. 2008.

[17] A. S. K. Annamalai, R. Sutton, C. Yang, P. Culverhouse, and S. Sharma, "Robust Adaptive Control of an Uninhabited Surface Vehicle," *Journal of Intelligent & Robotic Systems*, pp. 1–20, May 2014.

[18] M. Caccia, G. Bruzzone, and R. Bono, "A Practical Approach to Modeling and Identification of Small Autonomous Surface Craft," *IEEE Journal of Oceanic Engineering*, vol. 33, pp. 133–145, Apr. 2008.

[19] C. Sonnenburg, A. Gadre, D. Horner, S. Kragelund, A. Marcus, D. Stilwell, and C. Woolsey, "Control-Oriented Planar Motion Modeling of Unmanned Surface Vehicles," in *OCEANS 2010*, Sept. 2010.

[20] T. I. Fossen, *Guidance and Control of Ocean Vehicles.* Chichester ; New York: Wiley, Sept. 1994.

[21] M. Nomoto and M. Hattori, "A deep ROV "DOLPHIN 3k": Design and performance analysis," *IEEE Journal of Oceanic Engineering*, vol. 11, pp. 373–391, July 1986.

[22] J. H. Milgram, "Strip theory for underwater vehicles in water of finite depth," *Journal of Engineering Mathematics*, vol. 58, no. 1-4, pp. 31–50, 2007.

[23] M. Caccia, G. Indiveri, and G. Veruggio, "Modeling and identification of open-frame variable configuration unmanned underwater vehicles," *IEEE Journal of Oceanic Engineering*, vol. 25, pp. 227–240, Apr. 2000.

[24] P. Ridao, A. Tiano, A. El-Fakdi, M. Carreras, and A. Zirilli, "On the identification of non-linear models of unmanned underwater vehicles," *Control Engineering Practice*, vol. 12, pp. 1483–1499, Dec. 2004.

[25] T. I. Fossen, S. I. Sagatun, and A. J. Sørensen, "Identification of dynamically positioned ships," *Control Engineering Practice*, vol. 4, pp. 369–376, Mar. 1996.

[26] I. Morrison, A.T. and D. Yoerger, "Determination of the hydrodynamic parameters of an underwater vehicle during small scale, nonuniform, 1-dimensional translation," in *OCEANS '93. Engineering in Harmony with Ocean. Proceedings*, pp. II277–II282 vol.2, Oct. 1993.

[27] D. A. Smallwood and L. L. Whitcomb, "Adaptive identification of dynamically positioned underwater robotic vehicles," *IEEE Transactions on Control Systems Technology*, vol. 11, pp. 505–515, July 2003.

[28] J. M. Falzarano, S. W. Shaw, and A. W. Troesch, "Application of global methods for analyzing dynamical systems to ship rolling motion and capsizing," *International Journal of Bifurcation and Chaos*, vol. 02, pp. 101–115, Mar. 1992.

[29] K. J. Spyrou and J. M. T. Thompson, "The Nonlinear Dynamics of Ship Motions: A Field Overview and Some Recent Developments," *Philosophical Transactions: Mathematical, Physical and Engineering Sciences*, vol. 358, pp. 1735–1760, June 2000.

[30] I. Senjanovic, G. Cipric, and J. Parunov, "Survival analysis of fishing vessels rolling in rough seas," *Philosophical Transactions of the Royal Society of London A: Mathematical, Physical and Engineering Sciences*, vol. 358, pp. 1943–1965, June 2000.

[31] Z.-J. Long, S.-K. Lee, and J.-Y. Kim, "Estimation of survival probability for a ship in beam seas using the safe basin," *Ocean Engineering*, vol. 37, pp. 418–424, Mar. 2010.

[32] R. Bhattacharyya, *Dynamics of Marine Vehicles*. New York: John Wiley & Sons Inc, June 1978.

[33] B. Cotton and K. J. Spyrou, "AN EXPERIMENTAL STUDY OF NONLINEAR BEHAVIOUR IN ROLL AND CAPSIZE," *International Shipbuilding Progress*, vol. 48, pp. 5–18, Jan. 2001.

[34] M. N. Hamdan and T. D. Burton, "On the Steady State Response and Stability of Non-Linear Oscillators Using Harmonic Balance," *Journal of Sound and Vibration*, vol. 166, pp. 255–266, Sept. 1993.

[35] J. Guckenheimer and P. J. Holmes, *Nonlinear Oscillations, Dynamical Systems, and Bifurcations of Vector Fields*. New York: Springer, 1st ed. 1983. corr. 6th printing 2002 edition ed., Feb. 2002.

[36] W. Wu and L. McCue, "Application of the extended Melnikov's method for single-degree-of-freedom vessel roll motion," *Ocean Engineering*, vol. 35, pp. 1739–1746, Dec. 2008.

[37] J. M. T. Thompson, "Loss of Engineering Integrity due to the Erosion of Absolute and Transient Basin Boundaries," in *Nonlinear Dynamics in Engineering Systems*, International Union of Theoretical and Applied Mechanics, pp. 313–320, Springer Berlin Heidelberg, 1990.

[38] Z. Li, *Design of a Robust Autonomous Surface Craft for Deployment in Harsh Ocean Environment*. Master Thesis, Memorial University of Newfoundland, Mar. 2013.

[39] K. Etschberger, *Controller Area Network*. Weingarten, Germany: IXXAT Automation GmbH, Aug. 2001.

[40] T. I. Fossen, M. Breivik, and R. Skjetne, "Line-of-sight path following of underactuated marine craft," in *Proc. 6th IFAC Conf. Manoeuvring Control Marine Craft*, pp. 244–249, Sept. 2003.

[41] R. Bachmayer, L. Whitcomb, and M. Grosenbaugh, "An accurate four-quadrant nonlinear dynamical model for marine thrusters: theory and experimental validation," *IEEE Journal of Oceanic Engineering*, vol. 25, pp. 146–159, Jan. 2000.

[42] R. W. Schafer, "What Is a Savitzky-Golay Filter? [Lecture Notes]," *IEEE Signal Processing Magazine*, vol. 28, pp. 111–117, July 2011.

[43] L. E. Dubins, "On Curves of Minimal Length with a Constraint on Average Curvature, and with Prescribed Initial and Terminal Positions and Tangents," *American Journal of Mathematics*, vol. 79, no. 3, pp. 497–516, 1957.

[44] S. Amir Hossein Tabatabaei, A. Yousefi-Koma, M. Ayati, and S. Mohtasebi, "Three dimensional fuzzy carrot-chasing path following algorithm for fixed-wing vehicles," pp. 784–788, Oct. 2015.

[45] D. Nelson, D. Barber, T. McLain, and R. Beard, "Vector field path following for miniature air vehicles," *IEEE Transactions on Robotics*, vol. 23, pp. 519–529, June 2007.

[46] P. Sujit, S. Saripalli, and J. Borges Sousa, "Unmanned aerial vehicle path following: a survey and analysis of algorithms for fixed-wing unmanned aerial vehicless," *IEEE Control Systems*, vol. 34, pp. 42–59, Feb. 2014.

[47] M. A. Johnson and M. H. Moradi, eds., *PID Control: New Identification and Design Methods*. New York: Springer, 2005 edition ed., May 2005.

[48] M. Bikdash, B. Balachandran, and A. Navfeh, "Melnikov analysis for a ship with a general roll-damping model," *Nonlinear Dynamics*, vol. 6, pp. 101–124, July 1994.

[49] E. V. Lewis, ed., *Principles of Naval Architecture*. Society of Naval Architects &, second revised edition, June 1988.

[50] "Hydrostatics and Stability Orca3d Naval Architecture Software [Online]." `http://orca3d.com/modules/hydrostatics-and-stability/`

[51] J. B. Roberts, "Estimation of nonlinear ship roll damping from free-decay data," June 1983.

[52] R. V. Wilson, P. M. Carrica, and F. Stern, "Unsteady RANS method for ship motions with application to roll for a surface combatant," Computers & Fluids, vol. 35, pp. 501–524, June 2006.

[53] J. N. Newman, *Marine hydrodynamics*. Cambridge, Mass.: MIT Press, 1977.

[54] V. L. Belenky and N. B. Sevastianov, *Stability and Safety of Ships: Risk of Capsizing*. Jersey City, NJ: The Society of Naval Architects and Marine Engineers, second edition, Jan. 2007.

[55] S.-R. Hsieh, A. W. Troesch, and S. W. Shaw, "A Nonlinear Probabilistic Method for Predicting Vessel Capsizing in Random Beam Seas," *Proceedings: Mathematical and Physical Sciences*, vol. 446, pp. 195–211, July 1994.

[56] A. H. Nayfeh and N. E. Sanchez, "Bifurcations in a forced softening duffing oscillator," *International Journal of Non-Linear Mechanics*, vol. 24, no. 6, pp. 483–497, 1989.

[57] M. J. Brennan, I. Kovacic, A. Carrella, and T. P. Waters, "On the jump-up and jump-down frequencies of the Duffing oscillator," *Journal of Sound and Vibration*, vol. 318, pp. 1250–1261, Dec. 2008.

[58] J.-J. Slotine and W. Li, *Applied Nonlinear Control.* Englewood Cliffs, N.J: Prentice Hall, 1 edition ed., Oct. 1990.

[59] C. Jiang, A. Troesch, and S. Shaw, "Highly nonlinear rolling motion of biased ships in random beam seas," *Journal of Ship Research*, vol. 40, no. 2, pp. 125–135, 1996.

[60] E. Üçer, "Examination of the stability of trawlers in beam seas by using safe basins," *Ocean Engineering*, vol. 38, pp. 1908–1915, Dec. 2011.

[61] J. M. T. Thompson, R. C. T. Rainey, and M. S. Soliman, "Ship Stability Criteria Based on Chaotic Transients from Incursive Fractals," *Philosophical Transactions: Physical Sciences and Engineering*, vol. 332, pp. 149–167, July 1990.

[62] H. Choset and P. Pignon, "Coverage path planning: The boustrophedon cellular decomposition," in *Field and Service Robotics*, pp. 203–209, Springer, 1998.

[63] E. Galceran and M. Carreras, "A survey on coverage path planning for robotics," *Robotics and Autonomous Systems*, vol. 61, pp. 1258–1276, Dec. 2013.